

Electrospun carbon hybrid fibers as binder-free electrodes for electrochemical energy storage

Dissertation
zur Erlangung des Grades
des Doktors der Naturwissenschaften
der Naturwissenschaftlich-Technischen Fakultät
der Universität des Saarlandes

von
Aura Tolosa

Saarbrücken
2018

Tag des Kolloquiums: 27.11.2018

Dekan: Prof. Dr. G. Kickelbick

Berichterstatter: Prof. Dr. V. Presser
Prof. Dr. G. Kickelbick

Vorsitz: Prof. Dr. T. Kraus

Akad. Mitarbeiter: Dr.-Ing. D. Foetz

"The best way to predict the future is to invent it."

Alan Kay

Table of contents

Acknowledgments	I
Abstract	III
Zusammenfassung	IV
Symbols and Abbreviation	V
1. Introduction	1
1.1 Electrochemical energy storage	3
1.1.1 Electrochemical energy storage mechanisms	3
1.1.2 Electrochemical energy storage devices	7
1.1.3 Supercapacitors	8
1.1.4 Rechargeable batteries	15
1.2 Carbon and hybrid materials for energy storage	22
1.2.1 Approaches for the synthesis of hybrid materials for energy storage	23
1.3 Sol-gel process	26
1.4 Electrospinning	29
2. Approach and overview	33
3. Results and discussion	37
3.1 Electrospinning and electrospraying of silicon oxycarbide-derived nanoporous carbon for supercapacitor electrodes	39
3.2 Niobium carbide nanofibers as a versatile precursor for high power supercapacitor and high energy battery electrodes	53
3.3 Binder-free hybrid titanium-niobium oxide/carbon nanofiber mats for lithium-ion battery electrodes	69
3.4 Continuous silicon oxycarbide fiber mats with tin nanoparticles as high capacity anode for lithium-ion batteries	83
3.5 Electrospun hybrid vanadium oxide/carbon fiber mats for lithium and sodium-ion battery electrodes	99

3.6	Design of carbon/metal oxide hybrids for electrochemical energy storage.....	113
4.	Conclusions and outlook.....	127
	References.....	133
	Appendixes	143
	Appendix A: Supporting Information to Chapter 3.1.....	144
	Appendix B: Supporting Information to Chapter 3.2.....	152
	Appendix C: Supporting Information to Chapter 3.3	166
	Appendix D: Supporting Information to Chapter 3.4.....	180
	Appendix E: Supporting Information to Chapter 3.5	190

Acknowledgments

The work of this thesis was carried out in the INM-Leibniz Institute for New Materials in Saarbrücken under the supervision of Prof. Volker Presser, head of the Energy Materials group. The work was funded by the German Federal Ministry for Research and Education (BMBF) in support of the nanoEES3D project (award number 03EK3013) as part of the strategic funding initiative energy storage framework.

They are many who make this thesis possible, and I wish to express my most profound gratitude to all of them. First, to my thesis advisor Prof. Presser, who gave me the opportunity to continue with this interesting research topic in his group. I am very grateful for his mentoring and constructive feedback, guiding me through each step of my research. For the full help and support, thank you, dear *Doktorvater*.

I want to thank Prof. Guido Kickelbick for being my scientific supervisor from Saarland University, for the fruitful discussions and for revising my thesis. This thesis would not have been possible without the great support of the Energy Materials group. I met here great people, I am grateful for the enjoyable time at the lab, and outside work. It was a wonderful opportunity to learn from and with each of them. I would like to say special thanks to Jennifer S. Atchison for introducing me to electrospinning, and for each advice, she gave me when I started in this research group. Also, thank you Dr. Daniel Weingarth, Dr. Soumyadip Choudhury, and Dr. Mesut Aslan for transmitting your knowledge, and being always so kind. To my colleagues, thank you for the time together: Dr. Marco Zeiger, Dr. Nicolas Jäckel, Anna Schreiber, Simon Fleischmann, Benjamin Krüner, Pattarachai Srimuk, Juhan Lee, Hwirim Shim and my dear office mate Öznil Budak, for the lovely time together. I would also like to thank the support and help of Robert Drumm, Dr. Ingrid Grobelsek, Andrea Jung, and Marcus Koch, all at INM, for your kind help with measurements and technical advice. Particularly thanks to the Jazz sextet! I enjoyed the time with you, and I am very grateful for the opportunity. Outside INM, I would like to thank Prof. Cekdar Vakifahmetoglu, Dr. John Griffin, Dr. Antje Quade, Jemma Rowlandson and Mathias Widmaier for your scientific input in this work, and your very kind help. To my family and my life partner, I owe you everything that I am, thank you for your love and unconditional support.

Abstract

There is a great need for the development and improvement of electrochemical energy storage devices for applications ranging from energy and power management to portable electronic devices. My work explores electrode materials for devices with higher energy storage capacity and rate handling, namely electrical double-layer capacitors, lithium-ion batteries, and sodium-ion batteries. To this end, I report the synthesis and properties of electrospun fiber mats composed of nanoporous carbon, transition metal oxide/carbon hybrid material, or silicon oxycarbide. Based on a comprehensive array of structural and chemical analysis and electrochemical benchmarking, this work evaluates the potential and drawbacks of electrospun materials as electrodes.

Key findings demonstrate that electrospinning of molecular precursor is an attractive approach for the synthesis of carbon and hybrid fiber mats as free-standing electrodes. By following a one-pot synthesis approach, material properties such as phase composition, crystal structure, and phase distribution are well tuned to achieve the desired electrochemical properties. Compared to polymer-bound free-standing electrodes, the continuous fiber network yields a superior gravimetric electrochemical performance, related to the absence of additives and the continuous path for electron transport. However, the large interfiber space and low electrode density limit the usefulness of adopting electrospun fiber mats to size-sensitive applications.

Zusammenfassung

Mobile Anwendungen und Strommanagement erfordern verstärkt die Entwicklung verbesserter elektrochemischer Energiespeicher. Diese Dissertation erforscht vor diesem Hintergrund elektrogesponnene Fasern als hochleistungsfähige Elektroden für elektrische Doppelschichtkondensatoren, Lithium-Ionen-Batterien und Natrium-Ionen-Batterien. Hierzu kommen Fasern aus nanoporösen Kohlenstoff, Kohlenstoff/Metalloxid-Hybridmaterialien oder Siliziumoxykarbid zum Einsatz. Diese werden umfangreicher Materialanalyse und elektrochemischer Charakterisierung unterzogen um die Grenzen und Chancen für den Einsatz als Elektroden aufzuzeigen.

Meine Ergebnisse zeigen, dass Elektrosponnen eine vielversprechende Methode ist um nanoskalige Fasermatten zu erzeugen, die direkt ohne weitere Beaufschlagung mit Leitadditiv oder Polymerbinder als Elektroden für elektrochemische Energiespeicher verwendet werden können. Durch die dargestellte one-pot Synthese können wichtige Eigenschaften wie Phasenzusammensetzung, Kristallstruktur und Phasenverteilung gezielt auf die gewünschten elektrochemischen Eigenschaften hin optimiert werden. Im Vergleich zu polymergebundenen freistehenden Elektroden liefert das hochvernetzte Fasernetzwerk eine höhere gravimetrische Leistung. Der große freie Raum zwischen den einzelnen Fasern führt jedoch zu einer geringen Leistung bezogen auf das Elektrodenvolumen, wodurch die Verwendung von Fasermatten als Elektroden für platzsensitive elektrochemische Energiespeicher eingeschränkt wird.

Symbols and Abbreviation

Abbreviation

ALD	Atomic layer deposition
BET	Brunauer-Emmett-Teller theory
CDC	Carbide-derived carbon
CVD	Chemical vapor deposition
DFT	Density functional theory
DMC	Dimethyl carbonate
EC	Ethylene carbonate
EDLC	Electrical double-layer capacitor
EDX	Energy-dispersive X-ray spectroscopy
EES	Electrochemical energy storage
FT-IR	Fourier transform infrared spectroscopy
HOMO	Highest occupied molecular orbital
HVPS	High-voltage power supply
LIB	Lithium-ion battery
LUMO	Lowest unoccupied molecular orbital
Ni/MH	Niquel metal hydride battery
NIB	Sodium-ion battery
PC	Propylene carbonate
SEI	Solid electrolyte interphase
SEM	Scanning electron microscopy
SHE	Standard hydrogen electrode
SSA	Specific surface area
TEM	Transmission electron microscopy

Symbols

a_i	Activity of the species
C	Capacitance
C_{eff}	Coulombic efficiency
d	Distance between two opposite charged surfaces
E_F	Energy at the Fermi level
E_{redox}	Energy of redox couple

e	Elementary charge of an electron
F	Electric field strength
F_{Tc}	Electric field strength at the Taylor cone
I	Current
M	Molar mass
N_A	Avogadro constant
Ox	Oxidized specie
P	Specific Power
Q	Stored or released charge
q	Point charge
R	Ratio of the curvature of the round off cone apex
Red	Reduced specie
U	Voltage
W	Specific energy
W_{eff}	Energy efficiency
z	Number of electrons transferred during the redox reaction
γ	Surface tension of the spinning dope
δ^+	Positive partial charge
δ^-	Negative partial charge
ε	Relative permittivity of a dielectric medium
ε_0	Permittivity of vacuum
ζ	Zeta potential
ν_i	Stoichiometric number of a species i
v	Voltage scan rate
φ	Electrode potential of the half-cell reaction
φ^θ	Standard electrode potential of the half-cell reaction
φ_{HP}	Helmholtz potential
φ_L	Electrolyte potential
φ_M	Metal electrode potential

1. Introduction

In the year 1745, Pieter van Musschenbroek developed the first device to store electrical energy: the Leyden jar. This device employs electrostatic energy storage at two metal plates separated by glass, thereby, a capacitor (not a battery) was at the beginning of the development of electrochemical storage devices. Fifty years later, Alessandro Volta created the voltaic pile. This pile consisted of pairs of copper and zinc plates stacked on top of each other and separated by a cloth soaked in brine (the electrolyte), where energy storage was achieved by faradaic reactions between the electrodes and the electrolyte. Over the last 300 years, these two different storage mechanisms have diversified the portfolio of energy devices, yielding today a rich field of electrochemical energy storage (EES) systems. Many of these systems are complementary in their performance metrics, and their combination and synergy are desired to achieve sustainable EES technologies.

Electrical energy is a fundamental requirement for industry and society, and it must be available at any time and place. We need to be able to transport the energy with us and to use it at any time of the day. Currently, most of the electrical energy is being produced from non-renewable energy sources; however, our energy consumption should be met by renewable sources. For example, in 2015 only 16.4% of the energy consumed in the European Union (EU)-28 did not come from fossil fuels and nuclear source.¹ In the same year, 33.6% of the energy in Germany was produced from renewable sources, increasing to 38.4% in 2017.² The EU is engaged with the transition to renewable sources and aims to achieve an increase in the share of renewable energy to 45% by 2030.³ The transition to renewable sources is marked by ambitious plans in all continents, which make part of the fascinating energy revolution we are currently experiencing.

When transitioning from energy production-on-demand (e.g., coal power plants near cities or factories) to energy production-when-possible via renewable sources, the unpredictable generation capacity is a key challenge when maintaining a stable power grid. A critical tool to manage energy from renewable sources is the ability to store and recover energy, thereby matching the supply fluctuations to the changing demand.⁴ Besides energy management for renewable sources, the storage of energy plays a crucial role in several applications, among them: power management, portable electronic

devices, and electric cars.⁴ Each of these applications has different storage requirements which can only be met by the combined use of various devices and technologies. For high power applications, energy can be effectively supplied using devices where mainly ion electrosorption takes place; while high energy applications may use devices in which faradaic reactions take place.

Each and every technology has certain limitations with important consequences for the selection of suitable applications. Electrical double-layer capacitors, for example, can be used for high power applications when high power pulses need to be stored or released. These devices also present a high device life but a low specific energy. Lithium-ion and sodium-ion batteries provide a high specific energy but suffer from a low specific power and limited cycle life. So far, there is no single energy storage solution or technology which fits all these requirements. With the steady increase in the power and capacity requirements for advanced applications, the continued technological development and need for improvements will continue.

Finding improved ways to meet the demand for advanced energy storage devices with higher specific energy and power is a core motivation of this thesis. My work aims to obtain electrodes with higher capacity and rate handling. The approach consists of the synthesis and electrochemical benchmarking of fiber mats, which are free of additives and offer a continuous path for electron transport. In the next chapters, this thesis reports the potential and drawbacks of electrospun materials as electrodes for devices with high energy and power.

1.1 Electrochemical energy storage

1.1.1 Electrochemical energy storage mechanisms

Currently, electrochemical energy storage (EES) systems with high specific energy (batteries) and power (supercapacitors) are available, and their different performance metrics make them suitable for distinct applications. These systems consist of one or several pairs of electrodes, which are physically and electrically separated by an electrolyte and a permeable membrane. According to the properties of the various components (electrode materials, electrolytes), the fundamental principles for the energy storage can be separated.

The stored charge is time-dependent as a function of the current (I), as described in Eq 1. The time-dependent charge (Q) and voltage (U) yield different metrics for the specific energy (W) and power (P). From an applications point of view, energy and power are usually normalized by either device mass or volume. Dependent on the application, the size or the mass of a device may be more important to consider.

$$Q = \int I \cdot dt \quad (\text{Eq. 1})$$

$$P = \frac{W}{t} = \frac{\int U \cdot dQ}{t} \quad (\text{Eq. 2})$$

When a potential difference is applied between two electrodes, a charge separation will be formed between the charged electrode and ions in the electrolyte, forming an electrical double-layer.⁵ Here, the charge is stored at the electrode/electrolyte interface,⁶ for solid electrodes in contact with liquid electrolytes and mobile ions. As described by Helmholtz,⁷ a rough estimation of the capacitance assumes a plate capacitor where a single layer of ions is electrosorbed onto the electrode surface. Similar to capacitors, charge storage is achieved by a potential difference between two plates with an area A , separated by a distance d , by a dielectric medium. The absolute permittivity of the dielectric medium consists of the product of the vacuum permittivity (ϵ_0) and the relative permittivity of the medium (ϵ). The stored charge is the product of the capacitance (C) and the voltage.

$$C = \frac{\epsilon \cdot \epsilon_0 \cdot A}{d} \quad (\text{Eq. 3})$$

$$Q = U \cdot C \quad (\text{Eq. 4})$$

$$W = \int \frac{Q}{C} \cdot dQ = \frac{1}{2} C U_{max}^2 \quad (\text{Eq. 5})$$

In this case, the charge is stored by electrosorption of ions at the electrode/electrolyte interface. A higher voltage leads to higher energy and more charge stored, limited only by the electrochemical stability of the electrolyte,⁸ such as 1.2 V, 2.7 V, and >3 V for aqueous solvents, organic solvents, and ionic liquids, respectively.⁹ Also, a higher surface area will also increase the energy stored, according to Eq. 3-5. This is true within a certain limit since above $1200 \text{ m}^2\cdot\text{g}^{-1}$ the average pore wall thickness approaches the screening length of the electric field.¹⁰

Electrostatic energy storage leads to a low specific energy when compared to faradaic reactions. In this process, Faraday's law quantifies the charge stored (Eq. 6), where z is the number of electrons transferred during the redox reaction (Eq. 7) per 1 mol of reacting species; *Ox* and *Red* are the oxidized and reduced species, respectively. M corresponds to the molar mass and m to the mass of the component undergoing an electrochemical reaction, N_A the Avogadro constant and e the elementary charge of an electron.

$$Q = zeN_A \frac{m}{M} \quad (\text{Eq. 6})$$



For an electron transfer to occur, the energy of the electron orbitals must be between the donor (*Red*) and acceptor (*Ox*).⁶ Meaning that the *Ox|Red* has an associated energy (E_{redox}). In a battery, there is an electron transfer between the electrolyte and the electrode, corresponding to half-reaction of the complete cell. For the half-reaction, these energy levels correspond to the Fermi energy level of the electrode and the orbital of the valence electron in the electrolyte.⁶ The Nernst equation (Eq. 8) describes the electrode potential of the half-cell (φ), at the desired temperature (T), related to the standard electrode potential of the half-cell (φ^θ), the stoichiometric number (ν_i) and the activity (a_i) of the species. This equation considers the influence of the species concentration, and the temperature on the reaction potential. Furthermore, the mechanism of electron transfer at an electrode consists of several steps: (i) the diffusion of the species at the reaction spot, (ii) the rearrangement of the ionic atmosphere, (iii) the rearrangement of the solvent dipoles (iv) electron transfer, (v) and relaxation.⁶

$$\varphi = \varphi^\theta - \frac{RT}{nF} \sum \nu_i \ln a_i \quad (\text{Eq. 8})$$

By modifying the potential of the electrode, we influence the highest occupied electronic level in the electrode, which corresponds to the Fermi level, and its associated energy (E_F).⁶ The electrode has to supply electrons to the oxidized species or remove electrons from the reduced species, as represented in **Figure 1**.

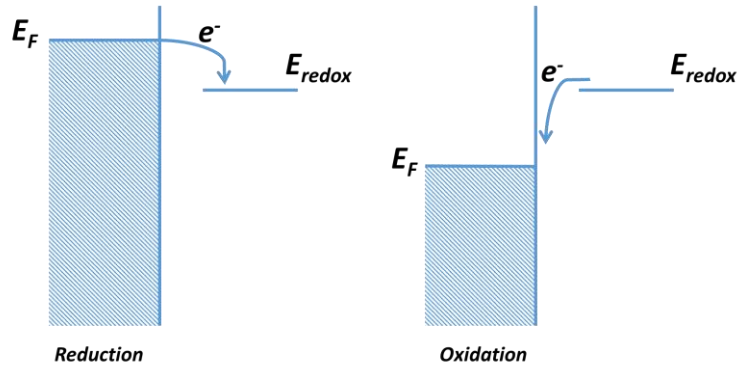


Figure 1. Electron transfer at an inert metallic electrode. Adapted from Ref. ⁶.

Several resistivity contributions restrict the transformation of chemical energy into electrical energy. Therefore, the redox event is experimentally observed at a different potential to the described by the Nernst equation. An overpotential must be applied, and the applied potential for reduction and oxidation (charge and discharge) differ.¹¹ The difference in the applied potential causes that the potential efficiency and the energy efficiency (W_{eff}) are less than 100 %.¹¹ Also, the presence of non-reversible reactions at the electrode will decrease the charge efficiency (C_{eff} , coulombic efficiency). For practical development, energy efficiency is the most crucial factor for large-scale batteries, because it translates into the final cost of the energy supplied.¹² Therefore, a complete electrochemical evaluation is required since a high charge efficiency does not directly correlate to a high energy efficiency, but also depends on the applied voltage (Eq. 2).

$$C_{eff} = \frac{Q_{discharge}}{Q_{charge}} \quad (\text{Eq. 9})$$

$$W_{eff} = \frac{W_{discharge}}{W_{charge}} \quad (\text{Eq. 10})$$

In the case of faradaic charge transfer, the potential at which the electron transfer occurs depends on the potential of the half-cell reaction and the Fermi energy level of the electrode. For faradaic systems, a higher voltage does not correspond to a higher stored charge, since it is limited to the standard potential of the reaction, or to the voltage window where redox reactions take place (Eq. 6). A higher voltage, however, will lead to

an increase in stored energy (Eq. 2). Contrary to faradaic systems, during electrical double-layer formation, a higher voltage will lead to a higher stored charge and stored energy (Eq. 4-5).

These two different charge storage mechanisms present different electrical responses, which are directly observed by galvanostatic and potentiostatic methods as shown in **Figure 2**.

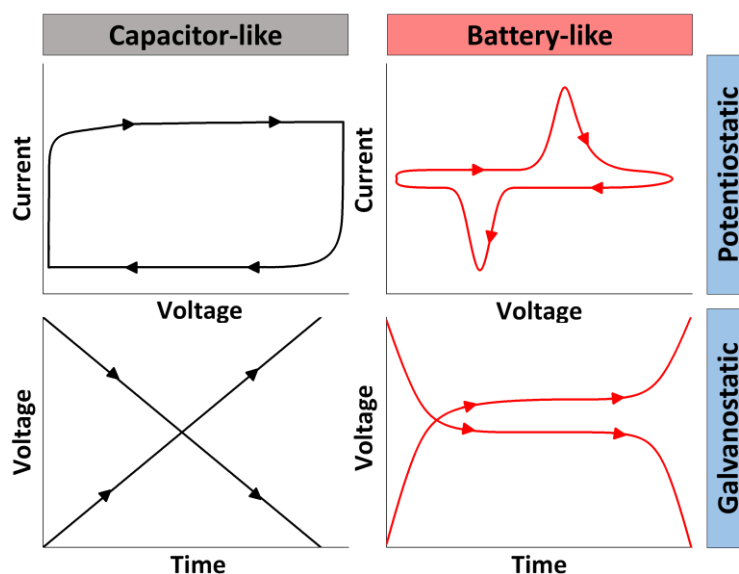


Figure 2. The electrical response of different energy storage mechanisms, by potentiostatic and galvanostatic methods. Adapted from Ref. ¹³⁻¹⁴.

As described by Eq. 4, the stored charge at the electrical double-layer and the voltage follow a linear relationship at constant current. In the case of a constant voltage scan rate, a rectangular voltammogram can be observed. The electrode materials presenting this electrochemical response are called capacitor-like.⁸ In the case of charge storage by faradic reactions, the voltammogram presents anodic and cathodic peaks, indicating the presence of oxidation and reduction reactions, respectively. The fact that electrons are transferred only at the E_{redox} is also observed as a voltage plateau in the galvanostatic curve. This plateau indicates the presence of two phases: one oxidized and one reduced.¹³ The electrode materials presenting this electrical response are battery-like.⁸

1.1.2 Electrochemical energy storage devices

The choice for suitable energy storage devices depends on the application and its specific requirements. Depending on these requirements, different electrode materials with different energy storage mechanisms may be selected. One key aspect is the required duration of energy storage, where charging time and self-discharge of the system are important parameters. The self-discharge of a device, while stored in the charged state, corresponds to the voltage drop over time either by chemical reactions or physical processes.¹⁵ In the case of medium-term energy storage, between hours and weeks, batteries are the primary and best choice. For short-term storage, between minutes and seconds, supercapacitors are a more suitable choice, storing more energy than other devices in the short time frame. The essential parameters to evaluate the practical performance of these devices are the specific energy and specific power.

The very different energy storage mechanisms and electrical responses of batteries and supercapacitors determine the operation range of each device. The so-called Ragone Plot (**Figure 3**) illustrates the highest power and energy range of the devices.¹⁶ Each device can reach a maximum possible specific power which also determinates the time range for operation, and leads to the characteristic curves.¹⁷⁻¹⁸

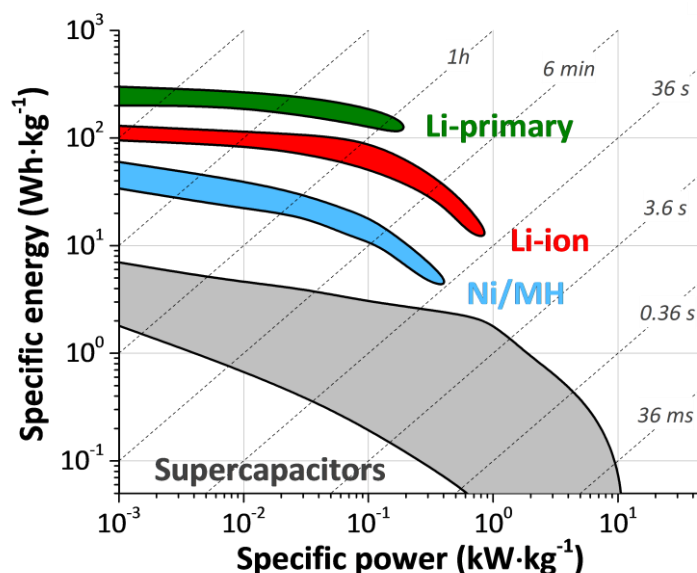


Figure 3. Ragone plot, representation of specific power against specific energy for supercapacitors, nickel metal hydride batteries (Ni/MH) and lithium-based batteries. Operation times are calculated by dividing the specific energy by the power. Data from Ref. 16, 18.

Considering the charging time presented in the Ragone plot, at short times scales (0.01-30 s), the higher contribution of resistive losses in the battery cell lead to low energy values, while a supercapacitor offers stable specific energy.¹⁴ By increasing the specific energy of supercapacitors, or improving the specific power of batteries, the performance gap between supercapacitors and batteries can be reduced.

1.1.3 Supercapacitors

1.1.3.1 Electrical double-layer capacitors (EDLC)

In EDLC systems, the energy is mainly stored via reversible ion adsorption at the electrode/electrolyte interface,¹⁹ while electrochemical redox reactions are of minor or no importance.¹¹ Common EDLC devices consist of a pair (or multiple pairs) of symmetric highly porous carbon electrodes, separated by a membrane, and soaked in an electrolyte (**Figure 4**). Highly porous materials are the most commonly used electrodes owing to the high surface area, low electronic resistivity, and chemical stability over a broad voltage range.²⁰

When a potential difference is applied between the two electrodes, an electrical double-layer is formed at each electrode and the electrolyte in contact with it.²¹ The capacitance of the EDLC (C_{EDLC}) can be approximated with Eq. 11 where C_{DL} is the capacitance of each electrode. Compared to a capacitor, an EDLC presents a much higher specific energy but a lower specific power, which is attributed to the high surface area of the electrodes used ($700\text{-}3000\text{ m}^2\cdot\text{g}^{-1}$). **Figure 4** and Eq. 11 present a simplified model for the potential development of the electrode and electrolyte. This model assumes that the bulk and surface properties of the electrode are equal, and no dilution phenomena in the electrolyte occur. In real surfaces, an imbalance of charges is present, which results in a probability of finding electrons beyond the surface plane.²² For the polarized electrode in contact with the electrolyte, charges accumulate at the interface due to the mobility of the charge carriers (electrons and ions). Traditionally for solvent-based electrolytes, the formed electrical double-layer consists of several layers, dependent on the separation to the polarized electrodes, the electrolyte composition and process conditions.²³

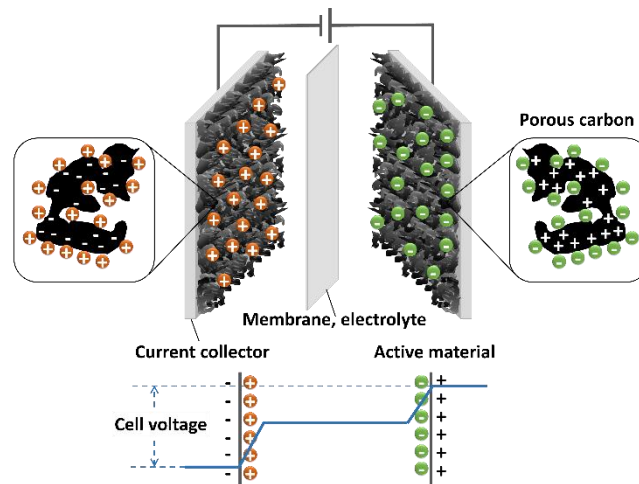


Figure 4. Configuration of an EDLC and simplified voltage development in the cell.

$$\frac{1}{C_{EDLC}} = \frac{1}{C_{DL1}} + \frac{1}{C_{DL2}} \quad (\text{Eq. 11})$$

The understanding of the electrical double-layer formation is crucial for the development of devices with improved electrochemical performance. Several models have been proposed to describe the formation of the electrical double-layer and the potential development in it. The Helmholtz model suggested a traditional plate capacitor, where two layers with opposite polarity are formed at the interface between the electrode and electrolyte.⁷ Thereby, charged electrodes immersed in an electrolyte repel co-ions of the same charge and attract counter ions to their surface.⁷ Gouy and Chapman proposed a diffuse layer with exponential decay of the potential from the electrode surface to the potential of the bulk electrolyte. These two models were consolidated in the Gouy-Chapman-Stern model, indicating that specifically absorbed ions form a dense layer near to the electrode,²⁴ forming an electrical double-layer as suggested by the Helmholtz model (**Figure 5**).⁷ In this layer, the potential decays linearly, which is followed by a diffuse layer extending into the bulk solution according to Gouy-Chapman model.²⁴ The diffuse layer develops outside of the Helmholtz layer, and the concentration of ions decreases exponentially to the distance from the electrode surface.

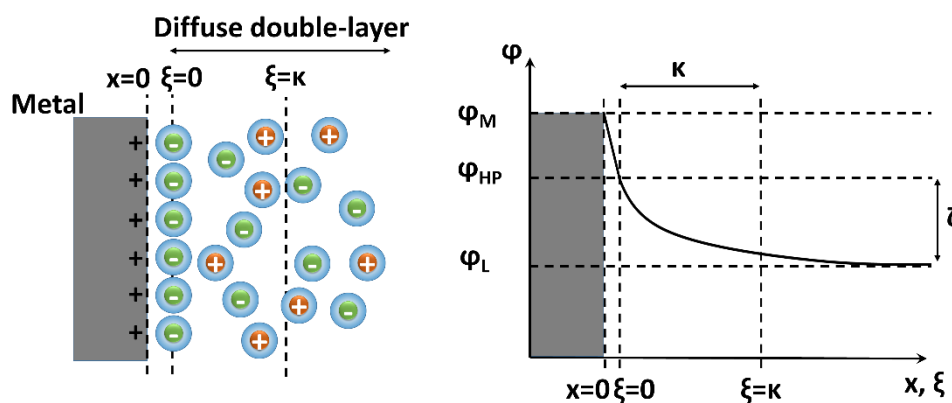


Figure 5. Representation of the Stern model, describing the ion concentration in the electrical double-layer, and the potential through it. ζ = zeta potential, κ = thickness of the diffuse layer, φ_M metal electrode potential, φ_{HP} Helmholtz potential and φ_L electrolyte potential. Adapted from Ref. ^{6, 24}.

The Gouy-Chapman-Stern model is based on several simplifications: ions are modeled as point charges, only coulombic interactions are considered, and constant values are assumed for dielectric permittivity and viscosity of the electrolyte. Later, Bockris et al.²⁵ suggest that the dielectric permittivity is not constant but decreases in the vicinity of the electrode. The Stern model also does not consider the interaction between the solvent and the solute. The electrical double-layer depends on the ion concentration; for example, a higher concentration leads to a decrease in the thickness of the diffuse layer, and the electrical double-layer follows the model described by Helmholtz. Also, depending on the electrolyte and ion concentration, it is significant to consider the ion-ion interactions which affect the potential development and the structure of the electrical double-layer, due to the screening of charges by neighboring ions with opposite charges.²² Finally, studies on molecular dynamics have shown that the structure of the electrical double-layer fluctuates as a dynamic process being dependent on the applied potential.²⁶

The models mentioned so far were conceptualized for a metallic electrode with an infinite amount of available charge carriers on the electrode side. In the case of a carbon electrode with a finite density of states, there is no constant potential at the electrode but a decay close to the surface. Also, the behavior of a flat metallic plate is different to highly porous carbon used in commercial electrodes. In the case of a flat plate, the initial premise was that ions could only be adsorbed on a surface maintaining the solvation shell entirely, due to the high solvation energy. For highly porous carbon, past studies demonstrated an increase in the capacitance when the pore sizes are below the diameter of the solvated

ions.²³ The seminal work by the Béguin Group²⁷ followed by the works of the Simon/Gogotsi Groups^{23, 28} analyzed porous carbon with tailored porosity and observed an increase in the capacitance normalized to the specific surface area (SSA) especially for pores smaller than the solvated ions, the SSA was estimated applying a Brunauer-Emmett-Teller (BET) model. The partial removal or distortion of the solvation shell and the increased confinement of the ions could explain the capacitance increase.²³ Centeno et al.²⁹ used simultaneously up to eight different techniques to quantify the ion-accessible surface area and observed no dependence of capacitance on pore size.²⁹ They attributed the different behaviors to the use of the BET model for surface area characterization, which is unreliable in the case of microporous carbons with pores below 2 nm.²⁹ Despite these differences, both models confirm that ion desolvation takes place in pores with an average size smaller than the solvated ion. The Presser group found that the electrode capacitance cannot be directly correlated with the average pore size, and it is also not constant with the voltage.³⁰ In this study, the volume-weighted average pore size was determined by gas sorption, and DFT (density functional theory) models were employed. Here, the average pore size was not considered but separated into two pore size ranges: pore sizes between the size of the bare ion and partially solvated ions, and pores sizes larger than the complete solvated ions. Pore sizes smaller than the bare ion were excluded since they are not accessible for the ions. Each pore size range contributes to the overall capacitance, and this contribution depends on the pore size/ion size, the applied voltage, and the solvation energy.³⁰

The efforts of developing EDLCs with higher specific energy and power are not limited to the tuning of the pore structure and available surface area. Several other aspects are also crucial, such as applied voltage and electrical resistivity. A higher applied voltage increases the energy stored but should not exceed the stability limit of the electrolyte. For example, in neutral aqueous solutions above a potential difference of 1.23 V water splitting will take place.³¹⁻³² This potential difference can be extended between 1.6 V to 2.0 V mainly due to reversible hydrogen electrosorption on the negative electrode. Also, different parameters contribute to a higher stability limit, as demonstrated for neutral aqueous media using ions with a strong solvation shell,³²⁻³³ or by tuning the pH at each electrode to modify the water equilibrium potential, as described by the Pourbaix diagram.³⁴ To further increase the operation voltage, aqueous electrolytes can be replaced by organic electrolytes or ionic liquids, which present higher voltage limits (2.5-3.5 V).

These electrolytes present a higher electrochemical stability window in an appropriate range of temperatures, but exhibit a lower ionic conductivity than aqueous electrolytes, increasing the ohmic losses of the system.

Various carbon materials have been explored as EDLC electrode materials, including microporous carbon (activated carbons,³⁵ and carbide-derived carbons³⁶) and nanocarbons (graphene,³⁷ carbon onions,³⁸ and carbon nanotubes³⁹). Microporous carbon materials (with pore size smaller than 2 nm) exhibit typically higher specific surface areas and are produced either from organic or inorganic precursors. Activated carbons can be made from organic materials with high carbon content, such as coconut shells and heavy petroleum products.^{9, 40} These materials exhibit a broad distribution of pore sizes, and the carbon material properties cannot be precisely controlled since it is highly dependent on the biological material used. Using an inorganic material like metal carbides as the carbon precursor is attractive for the synthesis of reproducible carbon materials with tunable porosity. The metal or metalloid atoms are removed by chemical etching with chlorine gas, leaving behind porous carbons with tunable pore size distribution, carbide-derived carbon (CDC).^{36, 41}

1.1.3.2 Pseudocapacitors

As seen in **Figure 2**, different energy storage mechanisms lead to different current-versus-voltage responses. Contrary to EDLCs, pseudocapacitors employ an electroactive material which undergoes chemical changes with faradaic charge transfer, but with an electrical response like a capacitor.⁸ Pseudocapacitance develops when the charge required or delivered is a linear function of the voltage, meaning that redox-reactions take place continuously over a broad voltage range.³¹ In this case, reversible redox reactions occur at or near the surface of the electrode material and present a high degree of reversibility.¹⁴ Therefore, pseudocapacitive materials are expected to achieve higher specific energy than EDLC due to the electron transfer reactions, and to deliver higher power density and cycle life than batteries, since the ion diffusion into the bulk material does not limit the process.¹³⁻¹⁴

The characteristics of a pseudocapacitive material are:

- The current is constant or almost constant when applying a constant voltage scan rate. If peaks are present, they are broad and exhibit a small peak-to-peak voltage separation (**Figure 6A**).
- The voltage varies linearly at a constant charge or discharge current with similar charge/discharge voltage curves (**Figure 6B**).
- The Nyquist plot of the impedance experiment presents a vertical line at low frequencies with a phase angle of 90° or less (**Figure 6C**). For a capacitor and EDLC, a phase angle close to 90° is obtained.

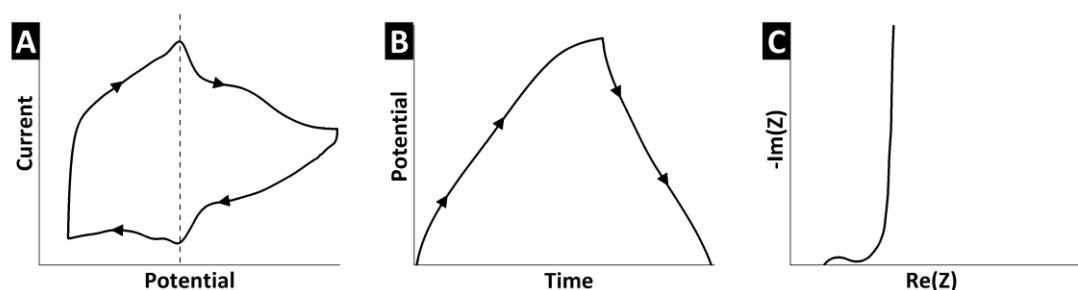


Figure 6. The characteristic electrochemical behavior of pseudocapacitive materials, by cyclic voltammetry (A), galvanostatic cycling (B), and impedance spectroscopy (C). Adapted from Ref. ¹⁴.

Examples of materials with pseudocapacitive properties are transition metal oxides (RuO_2 , MnO_2),^{31, 42-43} metal dichalcogenides,⁴⁴ MXenes,⁴⁵ metal nitrides,⁴⁶ hydrous metal oxides,⁴⁷ and conductive polymers.⁸ Also, some nitrogen- and oxygen-containing functional groups may provide a reversible pseudocapacitive contribution.⁴⁸⁻⁴⁹

One of the first pseudocapacitive materials studied was RuO_2 ,⁵⁰ which shows a capacitor-like response when used as a thin film electrode in aqueous media or protonic ionic liquids. Compared to the bulk material, a nanoscale structure and the presence of structural water led to an improvement in the rate handling performance.⁵¹ Depending on the crystal structure, pseudocapacitance is achieved in $\text{RuO}_2 \cdot \text{H}_2\text{O}$ and MnO_2 by redox reactions near the surface and intercalation into the bulk material.^{47, 52} In the case of redox reactions near the surface, ions are electrochemically adsorbed at the surface, together with a faradaic charge-transfer. In the case of pseudocapacitance by intercalation, ions intercalate into the layers of redox-active materials, accompanied by a faradaic charge transfer, but without a phase change.¹⁴ In the case of some metal oxides with layer

structures, like orthorhombic Nb_2O_5 and layered V_2O_5 , Li^+ intercalation yields a pseudocapacitive behavior. No phase change takes place, and ion insertion occurs with a minimal lattice volume change.⁵³⁻⁵⁴ This behavior is observed for a wide range of particle sizes and morphologies below 200 nm and corresponds to an intrinsic property of the material.

Compared to common battery materials, pseudocapacitive materials can be fully charged/discharged at much higher rates in the order of seconds to minutes. Yet, sluggish redox processes in battery systems can also be accelerated by structural design of the electrode materials. The short transportation paths for ions and electrons leads to effective energy storage at high rates but maintaining a battery-like electrical response with clear voltage plateaus.^{13, 55} For some materials with a particle size below 10 nm, the electrical response may change from battery-like to capacitor-like response; this is named as extrinsic pseudocapacitance. This capacitor-like electrical response emerges from a large amount of lithium storage sites in the near-surface region, being not diffusion limited.¹³ The structural disorder of the crystal layers near the surface provides a broad range of Li^+ insertion energies instead of one well-defined energy threshold.¹⁴ In some cases, even the phase transformation during the faradaic reaction is suppressed, for example, LiCoO_2 present a capacitor-like behavior at particle sizes around 6 nm, while a well-defined plateau appears for particles larger than 17 nm.⁵⁶ Extrinsic pseudocapacitance emerges through appropriate nanostructuring, while intrinsic pseudocapacitance is present for a wide range of particle sizes.

A faradaic reaction can be diffusion-limited (battery-like response) or surface-limited (capacitor-like response), this is however not only due to a material property but also a system operation property. Accordingly, it is essential to take into account the dynamic nature of the process. The current-versus-voltage response varies with the applied potential window and the applied voltage scan rate. Therefore, for any material a general relationship between the current at a particular voltage $I(U)$ and the voltage scan rate v is described by Eq. 12, where k_1 and k_2 are constants.¹⁴ For surface-limited faradic reactions at the electrode, the current response varies linearly with the voltage scan rate. For diffusion-limited faradic reactions at the electrode, the current response varies linearly with the $v^{1/2}$.¹⁴

$$I(U) = k_1v + k_2v^{1/2} \quad (\text{Eq. 12})$$

1.1.4 Rechargeable batteries

The lithium-ion battery is a very common rechargeable battery technology, being the primary option on the market of consumer electronics.⁵⁷⁻⁵⁸ In a conventional setup, a lithium-ion battery consists of two electrodes, separated by a membrane (typically polypropylene/polyethylene) soaked in an organic electrolyte. Typically used electrolytes are lithium salts containing hexafluorophosphate (PF_6^-) or perchlorate (ClO_4^-) as the anion, dissolved in alkyl organic carbonates in different ratios, such as ethylene (EC), propylene (PC), and dimethyl (DMC) carbonates. The separator prevents the electrical contact between both electrodes and allows the transport of ions during the charging and discharging processes via the electrolyte. The reversible lithium insertion in the two electrodes is exemplified for graphite as anode and LiCoO_2 as a cathode (**Figure 7A**), which are among the most common commercially used electrode materials.⁵⁹

During polarization, the potential of one of the electrodes will be increased (positive electrode) and of the other decreased (negative electrode) creating a potential difference (cell voltage). During the polarization step, the negative electrode is reduced, and the positive electrode is oxidized according to Eq. 13-14. In the depolarization step, the opposite process will take place, leading to the standard convention for anode and cathode for cell discharge process: free electrons travel through the external circuit from the anode (oxidized electrode) to the cathode (reduced electrode; **Figure 7B**).

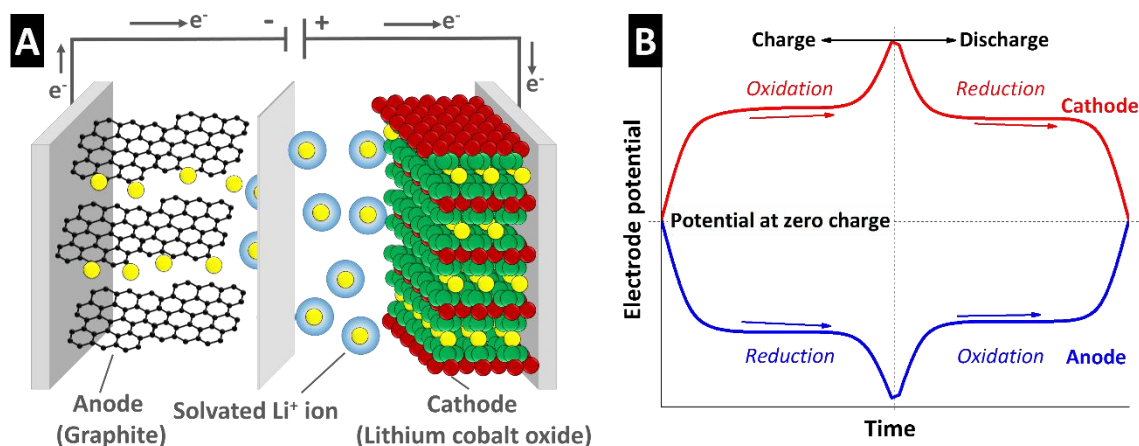


Figure 7. Schematic representation of a conventional lithium-ion battery (A), and voltage profile of the full-cell during charging and discharging processes (B).

Graphite is the most commonly used anode material, due to the high cycle life and low cost, although the low operation voltage leads to safety issues and presents a moderate reversible capacity ($372 \text{ mAh}\cdot\text{g}^{-1}$).⁶⁰ Additionally, the diffusion rate of lithium in graphite is low (10^{-12} - $10^{-6} \text{ cm}^2\cdot\text{s}^{-1}$).⁶¹ The low operation voltage (below 1.0 V vs. Li/Li⁺) causes the reductive decomposition of the organic electrolytes, followed by the formation of a passivating film (solid electrolyte interphase, SEI). For charging and discharging under the presence of the SEI, heterogeneous deposition and dissolution of lithium takes place, eventually leading to high surface area lithium (dendrites).⁶² At these dendrites, the electrolyte further decomposes during cycling. When the dendrites grow across the electrolyte to the cathode, short-circuit of the cell may happen.⁶² Substitute materials are currently being developed, focusing in either a material operating above the reduction potential of the electrolyte, or a material operating at the same potential of graphite but with a higher theoretical capacity. Alternative anode materials include group IV materials (e.g., Si, Ge, Sn),⁶³⁻⁶⁵ metal oxides (e.g., Nb₂O₅, TiO₂, LiTi₄O₅)⁶⁶⁻⁶⁸, metal sulfides (e.g., NiS, Fe₃S₄)⁶⁹⁻⁷⁰, and metal nitrides (e.g., Cu₃N, CoN)⁷¹⁻⁷².

The disadvantages of using LiCoO₂ as a cathode electrode relate to the high cost of cobalt,⁷³ and the low capacity of the electrode material, $148 \text{ mAh}\cdot\text{g}^{-1}$.⁵⁹ Therefore, several alternative materials have been investigated for higher specific power and higher specific energy, along with excellent cycle life. Some of the alternative cathode materials are metal oxides (e.g., LiNiO₂, LiMnO₂)⁷⁴⁻⁷⁵ and transition metals containing complex anions (e.g., Fe₂(SO₄)₃, LiFePO₄)⁷⁶⁻⁷⁷.

1.1.4.1 Cation insertion mechanisms

Depending on the material used as an electrode, the selected cation (Li⁺ or Na⁺), and operation voltage range, different reaction mechanisms can take place at the electrodes. In this chapter, the two major types of reaction mechanisms are outlined, exemplified for Li⁺: reconstitution reactions and insertion reactions.⁷⁸

In reconstitution reactions, the initial phase disappears, and a new phase grows during Li⁺ addition. The microstructure of the material get significantly changed or is reconstituted.⁷⁹ The growth of a new phase is a consequence either of an alloying reaction (formation reaction) or a displacement reaction. During alloying reactions, the Li⁺ ions add to the reactant phase *M*, which is often metal or metalloid.⁵⁹ The phase *M*

electrochemically alloys and forms compound phases with lithium, according to Eq. 15. Alloying reactions typically lead to high capacity values, for example, 993 mAh·g⁻¹ and 4200 mAh·g⁻¹ for Li_{4.4}Sn and Li_{4.4}Si, respectively. A drawback is the low Li⁺ diffusion of 10⁻¹⁰-10⁻¹⁴ cm²·s⁻¹ for Sn and Si thin films and nanoparticles,⁸⁰⁻⁸² which translated to low current handling.⁸³ A high volumetric expansion takes place to accommodate a large number of Li⁺ ions, leading to deterioration of the electrode (e.g., cracking and pulverization), a short cycle life, and high capacity loss.⁸³⁻⁸⁴



In displacement reactions, lithium displaces the species *B* from the initial binary system *AB_y*, forming *Li_xA* and a new phase *B* is created, according to equation Eq. 16.^{79, 83} The initial phase can be a binary intermetallic, a transition metal oxide or a transition metal chalcogenide. For a binary intermetallic, this approach depends on selecting intermetallic alloys which show a robust structural relationship with the lithiated products, such as Cu₆Sn₅ and Cu₂Sb.⁸⁵⁻⁸⁶ The element which is displaced can be active with lithium or inactive. In the case of *B* being reactive, usually, this reaction takes place at lower potentials with lithium, leading to an alloying reaction after the main displacement reaction.⁸³ If the formed *B* is not reactive with lithium, and the displacement reaction is not reversible, the *B* metal can be extruded as nanoparticles and provide a host framework for the subsequent cycles, limiting the volume expansion.⁸³ So far, these systems suffer from low cyclability due to irreversible reactions and moderate volume expansion (40-60%), and they have proven to maintain capacities as high as 300-360 mAh g⁻¹ after 200 cycles.⁸⁷⁻⁸⁸ Compared to alloying reactions, lower volume expansion occurs during displacement reactions, causing less strain and corresponding structural degradation.⁸³



A subtype of displacement reactions is conversion reactions. For these reactions, lithium entirely reduces the material according to Eq. 17. This reaction-type occurs for a wide range of transition metal oxides and transition metal chalcogenides. Binary transition metal oxides with the rock salt structure (CoO, CuO, and NiO)⁸³ and metalloid oxides (SiO and SnO)⁸⁹⁻⁹⁰ are completely reduced, forming Li₂O. In the case of 2D nanosheets of MoS₂, the complete reduction of the initial phase leads to the formation of LiS₂.⁹¹ For these

systems, the formed lithium compound is more stable than the initial material (MO), and a thermodynamic force drives a displacement reaction.⁷⁹ The complete reduction leads to the formation of metallic nanodomains engulfed in an amorphous Li_2O or LiS_2 matrix.⁸³ In the case of SnO , the formation of Li_2O is not fully reversible, representing a high capacity loss in the initial cycles.⁹² The formed Sn domains will form $Li-Sn$ alloys in a secondary step.⁹² These systems present a very high charge storage capacity compared to graphite ($1000-1300 \text{ mAh}\cdot\text{g}^{-1}$) and yield a higher cycle life than alloying materials (Si, Sn).



Insertion reactions involve the insertion of Li^+ into a stable host material as described by Eq. 18.⁷⁹ Although the chemical composition of the host material changes during the process, the crystal structure of the host material remains unchanged.⁷⁹ In most of the cases, the insertion of Li^+ causes a change in the lattice volume. According to the host material and the insertion path, insertion reactions are sometimes called solid solution reactions or intercalation reactions. The term “solid solution reactions” refers to the insertion of a solute (Li^+) topotactically into the host material which is the solvent.⁷⁹ During the topotactic transition, Li^+ ions incorporate into unoccupied interstitial sites and also partially substitute the atoms in the lattice of the host, but the final lattice is related to that of the original host.⁹³ The term “intercalation reactions” refers to the reversible insertion of Li^+ ions into the interlayer vacant sites of the layer-type crystal structures.^{78, 93-94} Some examples of materials undergoing intercalation reactions are layered transition metal oxides (orthorhombic- Nb_2O_5 and layered V_2O_5)⁹⁵, metal dichalcogenides (TiS_2 and MoS_2)⁹⁶, MXene,⁹⁷ and graphite⁹⁸. Intercalation materials are highly attractive, since they provide high rates among solid electrodes for batteries,⁷⁸ and therefore some of them have been explored as electrode materials for pseudocapacitors.¹⁴ On the other hand, the host material presents a limited capacity to hold the lithium into the interlayer vacant sites of its structure, typically storing maximum one Li^+ ion per formula unit.⁷⁸ These materials offer high reversibility due to the small structural changes, lower structural degradation, and improved rate handling, but present a low capacity (typically $100-300 \text{ mAh}\cdot\text{g}^{-1}$).



In the case of some conversion-type anode materials, conversion occurs at a sufficiently low potential typically below 1 V vs. Li/Li⁺, whereas at higher voltages intercalation reactions take place. For example, MoS₂ undergoes intercalation reactions at 1.8 V vs. Li/Li⁺, and conversion reactions start to take place at ~1.2 V vs. Li/Li⁺ leading to the formation of LiS₂.⁹¹ The conversion reactions lead to a higher specific capacity and energy compared to the intercalation reactions, but also to a higher structural degradation and lower rate handling. Therefore, when considering the use of an electrode material for energy storage devices, it is important to be aware of the selected electrode material, cation (Li⁺ or Na⁺), current rate, and applied voltage window. These parameters determine which reaction mechanisms take place, and therefore the electrochemical performance metrics (specific energy, specific power, and cycle life).

1.1.4.2 Solid electrolyte interphase

Essential aspects of battery design are the operation voltage of each electrode and the voltage window at which the electrolyte is stable. If the Fermi level of the negative electrode is higher than the lowest unoccupied molecular orbital (LUMO) of the electrolyte, electrons will be transferred to the electrolyte, causing its reduction. If the Fermi level of the positive electrode is lower than the highest occupied molecular orbital (HOMO) of the electrolyte, electrons will be transferred from the electrolyte causing its oxidation.⁹⁹⁻¹⁰⁰ Organic carbonates are the most common type of electrolytes and have oxidation and reduction potentials of around 4.7 V and 1 V vs. Li/Li⁺. The Fermi level of Na/Na⁺ and Li/Li⁺ is higher than the LUMO of the electrolyte, causing the reduction of the electrolyte.¹⁰⁰ The electrolyte reduction also occurs for several anode materials such as graphite, Si, or SiOC (standard reduction potential: 0.6-0.01 V vs. Li/Li⁺). The products of the electrolyte reduction form a solid electrolyte interphase (SEI) at the electrode surface. This layer is electrically insulating and presents a thickness of 3-100 nm.^{79, 100}

The SEI layer affects the short-term and long-term performance of the device. During the first cycle, the formation of the SEI at the anode leads to a non-reversible cathodic current and consumes Li⁺ ions and electrolyte. The insulating character of the SEI avoids further reduction of the electrolyte and allows only the transport of Li⁺ ions.⁷⁹ Ideally, the layer formation enables a reversible capacity in the next cycles.¹⁰⁰ However, the volumetric expansion of the anode materials during Li⁺ insertion, causes the expansion and cracking of the SEI, causing a continued irreversible capacity.¹⁰¹ An ideal SEI layer should consume

minimal amounts of Li^+ and electrolyte during the formation, should be flexible enough to overcome the volumetric expansion of the electrode; and reduce the capacity fading during long-term operation.¹⁰⁰ Yet, the selection of systems that do not require or exhibit the formation of an SEI layer would ideally be preferred.

1.1.4.3 Sodium-ion batteries

Despite the advanced development of lithium-ion battery technology, there remain issues regarding safety, lifetime, sustainability, and cost.^{73, 102} Contrary to lithium, sodium is much more abundant on Earth's crust and presents a low cost,⁷³ yet many materials have the ability for reversible sodiation/desodiation upon electrochemical cycling.⁵⁷ From the performance point of view, sodium-ion batteries might be competitive with lithium-ion batteries, at least for certain applications.¹⁰³

Compared to lithium, sodium has a much higher mass (300% larger) and ionic radius (40% larger). The characteristics of the host electrode materials and its affinity to the cation determine the specific capacity. Therefore, the difference in mass might not have a significant effect on the gravimetric capacity.¹⁰³ In the case of using metallic sodium as an anode, a lower specific energy is obtained due to the higher standard reduction potential than lithium (0.3 V higher), and the lower gravimetric capacity (30% of lithium capacity; **Table 1**).¹⁰³⁻¹⁰⁴

	<i>Lithium</i>	<i>Sodium</i>
<i>Shannon's ionic radii (\AA)</i>	0.76	1.02
<i>Atomic weight ($\text{g}\cdot\text{mol}^{-1}$)</i>	6.9	23.0
<i>Coordination preference</i>	Octahedral and tetrahedral	Octahedral and prismatic
<i>Capacity metal ($\text{mAh}\cdot\text{g}^{-1}$)</i>	3861	1166
<i>φ^\ominus vs. SHE (V)</i>	-3.04	-2.71
<i>Melting point ($^\circ\text{C}$)</i>	180.5	97.7
<i>Abundance (ppm)</i>	20	23600

Table 1. Comparative data of physical properties and abundance in earth's crust for lithium and sodium. Standard potential vs. standard hydrogen electrode (SHE) is reported. Data from Ref. ¹⁰⁴.

To meet the demands of future applications, the development of suitable electrode materials for sodiation is necessary. For example, successful reversible intercalation materials must possess interstitial sites to host the larger Na^+ ion and high ionic and electronic conductivity. Moreover, sodium-ion batteries are facing similar technical barriers as lithium-ion batteries, such as the high reactivity with the electrolyte, dendrite formation, and safety issues.¹⁰⁵ For the transition from lithium-ion to sodium-ion batteries, initially similar host materials were explored due to the similarity of the chemical properties. However, the differences in ion size, electronegativity, and diffusion properties, lead to different interactions between the host material and the cations.⁵⁷

Graphite is the most commonly used anode material for lithium-ion batteries but does not easily intercalate Na^+ ions.¹⁰⁶ Jache and Adelheim demonstrated that by forming ternary graphite intercalation compounds, solvated Na^+ ions are intercalated (co-intercalation) into graphite.¹⁰⁶ As an alternative, different carbonaceous materials have been examined, which are not entirely graphitic but contain graphene layers in its structure.¹⁰⁷ Carbon materials such as carbon black and pitch-based carbon have demonstrated reversible Na^+ insertion where the presence of nanopores and cavities for the ion insertion plays an important role.¹⁰⁴ Anode materials explored for sodium-ion batteries so far include transition metal oxides (e.g., TiO_2 , NiCo_2O_4 , NaTi_3O_7)¹⁰⁸⁻¹¹⁰, intermetallic alloys (e.g., SnSb)¹¹¹, and metal sulfides (e.g., Ni_3S_2 , SnS , Cu_2S)¹¹²⁻¹¹⁴.

Another difference between the electrode materials for lithium-ion and sodium-ion batteries is the coordination of both atoms (**Table 1**). Sodium prefers six-fold-coordination in an octahedral or prismatic arrangement, while tetrahedral-coordination does not occur.¹⁰³ The coordination of sodium will determinate the type of structures available for electrode materials. Some examples of cathode for sodium-ion batteries include transition metal oxides (e.g., $\text{Na}_{0.44}\text{MnO}_2$, $\alpha\text{-V}_2\text{O}_5$, NaCoO_2)¹¹⁵⁻¹¹⁷, metal sulfides (e.g., TiS_2 , TaS_2)¹¹⁸, metal fluorides (e.g., FeF_3)¹¹⁹, and metal phosphates (e.g., NaVPO_4F , $\text{Na}_3\text{V}_2(\text{PO}_4)_3$)¹²⁰⁻¹²¹.

1.2 Carbon and hybrid materials for energy storage

An essential aspect of the development of devices with improved performance metrics is the design of electrode materials that enable a combination of high specific energy, specific power, and cycle life. EDLC and battery technologies offer different performance metrics and could complement each other to achieve improved overall performance metrics. Suitable electrode materials for EDLC provide a large surface area for ion adsorption and high electrical conductivity. Battery electrode materials undergo Faradaic reactions with the ions in the electrolyte, leading to high charge transfer. Therefore, the combination of EDLC and battery materials is becoming increasingly popular in the field of electrochemical energy storage as novel electrode materials with both high specific energy and power.¹²²

The first step in this direction is the integration of nanoporous carbon and redox-active particles, typically transition metal oxides, in a macroscopic electrode material: either as composite or hybrid.¹²³ In the case of a composite, particles of these materials are mechanically mixed and bound together with a polymer; therefore, discrete structural units of the components are observed (**Figure 8**). When the size of each phase is reduced to the nanometer level, and the phase moieties are blended on a molecular scale, more homogeneous materials are obtained (i.e., hybrid materials; see **Figure 8**).¹²⁴

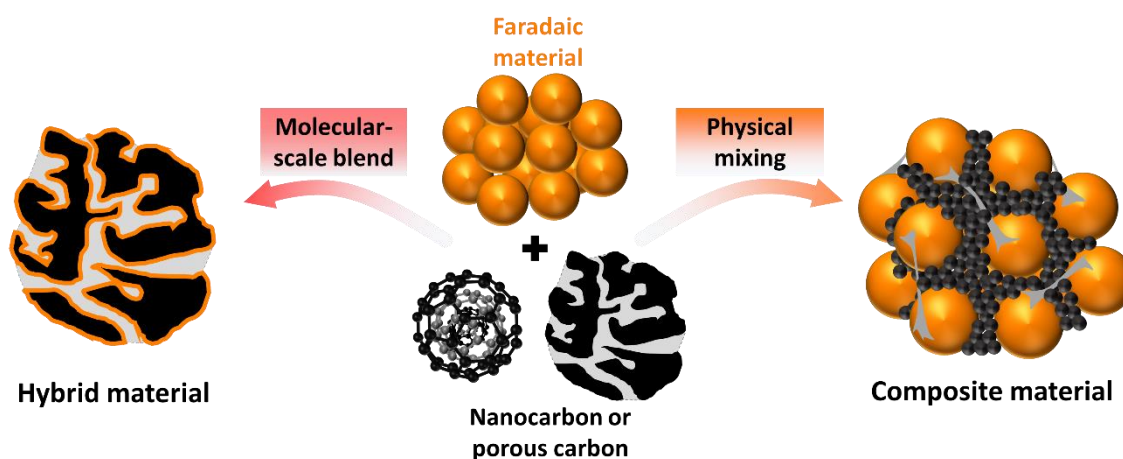


Figure 8. Schematic representation of hybrid and composite electrode material. In hybrid materials both carbon and redox-active material are blended at the molecular-scale, while in composites discrete units are physically mixed. Copyright Wiley-VCH Verlag GmbH & Co. KGaA. Reproduced with permission.¹²²

In hybrid materials, an intimate interface between two components is formed, leading to enhanced charge transfer.^{123, 125} The term hybrid material is also often used when describing the blending of an organic and an inorganic phase, but not limited to this case.^{124, 126} This work follows the definition proposed for hybrid materials in energy storage devices,¹²²⁻¹²³ where “hybrid material” refers to materials containing partially graphitized carbon and redox-active phases blended on a molecular scale. The synthesis of hybrid materials allows tuning the material properties to more precisely meet the requirements of a particular application, resulting in characteristics positioned between the two primary components or even new properties.¹²⁴

1.2.1 Approaches for the synthesis of hybrid materials for energy storage

Hybridization requires careful design to create synergistic effects for an increased electrochemical performance and to avoid detrimental effects inherent to each technology.¹²² Several approaches for the synthesis of hybrid materials are represented in **Figure 9**, and we can differentiate the building-block approach and the in situ synthesis.¹²³⁻¹²⁴


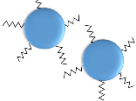

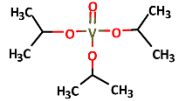
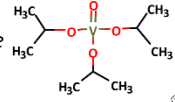
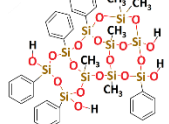
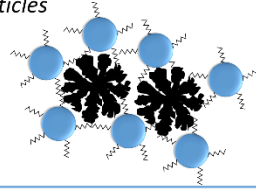
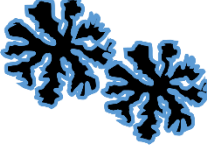
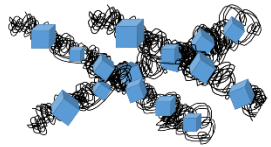
	(A) Assembly of building-blocks	(B) In situ formation of components	
		Deposition	Co-synthesis
Precursor	Carbon nanoparticles  Metal oxide with surface modifiers 	Carbon substrate  Metal alkoxide 	Metal alkoxide  Organic/inorganic polymer 
Processing	Chemical mixing, capping agents	ALD, CVD, hydrothermal synthesis	Sol-gel reaction, shaping, thermal treatment
Product	Particles 	Coated substrate 	Precursor-derived ceramic 
Advantages	Higher control of structure for each phase	Small diffusion distances in thin film coatings	Shaping at low temperatures, and in different morphologies
Disadvantages	Involves chemical modification	Possible pore blocking	Needs post-thermal treatment

Figure 9. Schematic representation of synthesis approaches for hybrid materials containing carbon and transition metal oxides, either by the assembly of building-blocks (A) or in situ formation of the components (B). Modified from Ref. ¹²².

In the building-block approach, pre-formed building-blocks react with each other to form the final hybrid material. In the first step, the components are synthesized separately and later the surface is chemically modified to achieve a blending on a molecular scale.¹²⁴ Throughout the formation of the hybrid material, the building-blocks keep their structural integrity at least partially, which means that the initially formed units are also present in the final material. The advantage of this approach is that different thermal conditions and synthesis methods for each component can be used, allowing good control of structure, size, and shape of the separated phases. The disadvantage is the need of surface modifiers such as capping agents or anchoring groups. Also, the process is limited to particle processing and single layer coatings.¹²³

In situ formation of components is the most commonly used approach for the synthesis of hybrid electrode materials for electrochemical energy storage.¹²³ During in situ synthesis, either one (deposition) or both (co-synthesis) structural units are formed from molecular precursors which are later transformed into a novel structure. The main advantage of the deposition approach is that the metal oxide phase can be added to various morphologies of carbon substrates, including amorphous or semi-crystalline layers of nanoparticles, by using a variety of techniques, both in the liquid and in the gas phase.¹²³ Common synthesis techniques to assure a homogenous coating include wet-chemical approaches⁴⁷ and non-line-of-sight vapor deposition techniques¹²⁷⁻¹²⁹. Here, transition metal oxides are incorporated at the internal or external surface of the carbon substrate; consequently, the porosity of the substrate has a strong influence on the structure and properties of the hybrid material.⁴⁷ The deposition of metal oxides can lead to pore blocking and insulating coatings, which is unwanted for hybrid electrodes since it prevents the access for ions and the transport of electrons. In this regard, atomic layer deposition (ALD) allows a higher control of the deposition layer thickness and a controlled multilayer deposition, compared to wet-chemical approach or chemical vapor deposition (CVD).^{122, 129} The nanoscopic size of the Faradaic materials incorporated in the accessible (open) carbon pores leads to short pathways for ion diffusion; also the high contact with the conductive substrate enables high charge/discharge rates, compared to bulk and composite electrodes.^{14, 53}

For co-synthesis, hybrid electrodes are obtained from in situ synthesis of both phases using one pot or one precursor. The hybridization can be performed using either gas reactions with solid precursors or wet-chemical methods. For example, using only one

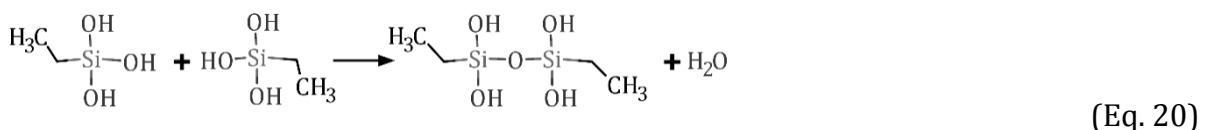
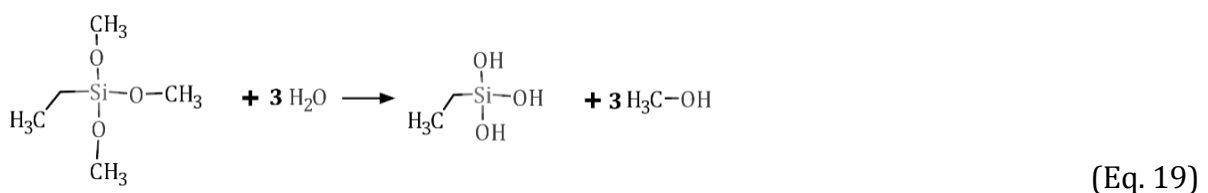
precursor (in this case: vanadium carbide), hybrid carbon/vanadium oxide particles have been obtained as described by Zeiger et al.¹³⁰ In the first step, vanadium was etched from the outside towards the inside of the vanadium carbide particles by chlorine gas treatment, resulting in a shell of highly porous carbon and a vanadium carbide core. In the second step, the remaining VC was calcinated under an oxidizing atmosphere to form a V_2O_5 core while choosing such oxidation parameters that the carbon is largely maintained.

The co-synthesis of hybrid materials by wet-chemical approaches yields hybrid carbon/metal oxide particles with a uniform distribution. Metal oxide/carbon hybrid material have been produced by a block-copolymer assisted self-assembly synthesis, starting from dissolved organic and inorganic polymers.¹³¹ The thermal decomposition of the block-copolymer phase produced a carbon material surrounding the metal oxide phase. In a different approach, starting from metal alkoxides as precursors, metal oxide/carbon hybrids have been produced by water-in-oil microemulsion, where the carbonization of the emulsifier produced a carbon shell.¹³² For both synthesis approaches, the advantage of the hybridization approach over pristine metal oxide particles was demonstrated by comparison of their electrochemical properties. One of the benefits of using a wet-chemical method for co-synthesis is that different polymer processing techniques can be applied at room temperature, such as fibers, layers, or particles. For this, either two separate molecular precursors can be used, or only one precursor containing both organic and inorganic moieties; the latter is the case of polysilsesquioxanes. In polysilsesquioxanes, the inorganic component is an oligomeric or polymeric siloxane chain, branched structure or network to which the organic functionalities are attached through a Si-C bond.¹²⁴ Shaping techniques are applied at room temperature, and the material maintains its shape after thermal treatment at high temperatures, at which a ceramic material is formed. For example, hybrid silicon dioxide/carbon materials are produced from polysilsesquioxanes. Either for the preparation of these polymers or in the synthesis starting from molecular precursors, one of the most prominent processes is sol-gel.

1.3 Sol-gel process

Sol-gel processing allows controlling the structure of a material on a nanometer scale from the earliest stages of processing. The sol-gel process is chemically related to an organic polycondensation reaction in which small molecules form polymeric structures by the loss of substituents.¹²⁴ Thereby, the synthesis process offers important advantages: higher material purity and homogeneity, low processing temperature, and shaping techniques can be applied to create unique morphologies such as ultra-fine fibers.

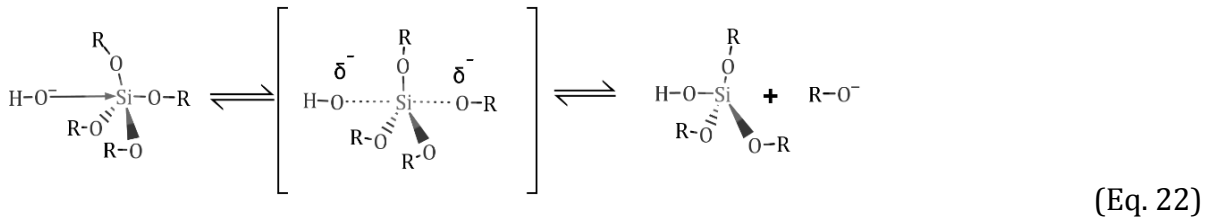
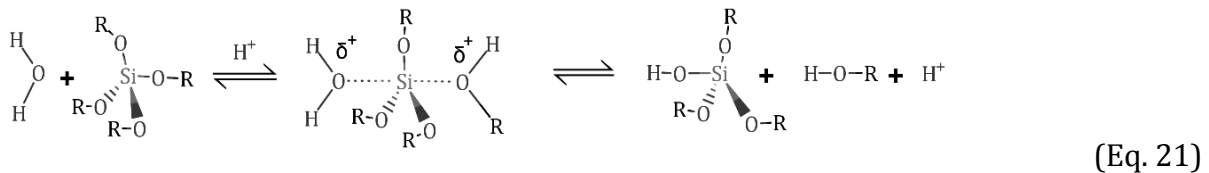
The concept of molecular manipulation for the processing of ceramics requires the understanding and application of chemical properties. The silicon-based sol-gel process has been studied extensively in past studies; therefore, the fundamental reaction principles are discussed using this process as a model system. The process starts with metal organic compounds, such as metal alkoxides or metal salts. Generally, $R_{4-n}SiX_n$ compounds ($n = 1-4$, $X = OR'$ or halogen) are used as molecular precursors, in which the Si-X bond is unstable towards hydrolysis reactions (Eq. 19), forming unstable silanols (Si-OH) that react and lead to Si-O-Si bonds (Eq. 20). During hydrolysis, the positively charged metal centers are attacked by water in a nucleophilic addition reaction. Later, the negatively charged alkoxides attack the protons from the water molecule, leading to an intermolecular proton transfer followed by a nucleophilic substitution reaction. During the condensation, the hydrolyzed metal alkoxide attacks the metal center from another metal alkoxide. This process can occur either by addition of water, in situ water formation, or reaction pathways with alkoxides that do not require water.¹³³ Linkage of additional $\equiv Si-OH$ occurs as a polycondensation and eventually results in a metal oxide network.¹²⁴ Si-C bonds have enhanced stability against hydrolysis, which is not the case for all metal-carbon bonds.¹²⁴ The stability of the Si-C bonds allows the modification of a preformed network by the attachment of organic moieties on the surface of an inorganic network.¹²⁴



As the reactions proceed, initial oligomer and polymer, as well as cyclic compounds, are created and dispersed in the solvent, subsequently resulting in a colloid (sol). The size of the dispersed particles is at least in one dimension roughly between 1 nm and 100 nm.¹³⁴⁻¹³⁵ When the colloidal particles grow and collide, condensation reactions occur, and microparticles are formed. In this stage, the individual particles interact with each other rather weakly. The viscosity of a solution undergoing hydrolysis and polycondensation reactions is time-dependent and also relates to the size of the particles. During this stage, shaping techniques for polymers can be applied to form layers, particles, or fibers, and for these techniques, good control on the viscosity must be assured.

At a high enough reaction yield, there will be a large increase in the viscosity and a transition to gel will occur (gelation point).¹³⁵ A non-fluid colloidal network or 3D polymer network expands through the bulk volume, and it can support stress elastically.¹³⁶ This polymer network can be either covalently linked or physically aggregated and the polymeric chains present an average length greater than a micrometer with pores of submicrometer dimensions. The term “gel” embraces a diversity of substances as discussed by Flory et al.¹³⁷ including well-ordered lamellar structure, covalent polymeric networks, and polymer networks formed by segregation.

The structure of the gel depends on several variables including temperature, pressure, precursor, solvent, and electrolyte (acid, base). These variables affect the rates of the hydrolysis and condensation reactions, which co-occur in the solution.¹³⁵ The presence of acid or base species has a high influence on the gel structure. The presence of H_3O^+ ions increases the rate of the hydrolysis reaction, and mostly linear structures are obtained, with a low degree of crosslinking due to steric crowding.¹³⁵ At acidic conditions (Eq. 21), the proton is attracted by the oxygen atom of the alkoxide, causing a shift of the electron cloud of the Si-O bond toward oxygen. The positive charge of the Si increases and a water molecule can attack the Si atom, forming a transition state.¹³⁵ In the case of base catalysis, the OH^- ion has a high nucleophilic character and attacks the metal center directly since it carries the highest positive charge.¹³⁵ Under basic conditions, the rate of condensation reactions increases together with the degree of crosslinking, therefore species with a broad distribution of molecular weights, and branched polymers are obtained.¹³⁵



The reaction rate of the sol-gel process also depends on the activity of the metal alkoxide, and different alkoxides have distinct behavior. The nature of the alkoxy groups influences the rate constant: as a general rule, the larger the substituents, the lower the reaction rate due to steric hindrance.¹²⁴ Also, the electronegativity of the metal or metalloid center affects the reaction rate. Metal and transition-metal alkoxides are more reactive towards hydrolysis and condensation reactions compared to silicon.¹³⁸⁻¹³⁹ Transition metal alkoxides present a lower electronegativity being more electrophilic and less stable towards hydrolysis. Also, the large coordination sphere of transition metal ions allows ligand exchanging and bridging reactions with other metal alkoxides, which impact on the reactivity of the metal alkoxides.^{124, 140} If bridging reactions occur with acidic anions, monodentate (acetate) or bidentate (acetic anhydride) ligands are formed, and some coordination sites of the metal ion are blocked,¹²⁴ leading to the formation of less active complexes.¹⁴¹

After gel formation, its structure and properties continue to change long after the gelation point; this process is called aging.¹³⁵ At this stage, polycondensation proceeds within the gel network as long as neighboring silanols are sufficiently close to react. Bridging bonds increase, and the gel tends to reduce the solid-liquid interfacial area. During this step, the gel shrinkages and expulses the solvent molecules from the pores. During Ostwald ripening, dissolution and precipitation processes take place leading to a decrease of the surface.¹³⁵

After gel aging the polymer forms an infusible 3D network, which is typically heat treated at high temperatures (500-2000 °C) for the transformation of the gel into a ceramic material as represented in **Figure 10**. Heat treatment at elevated temperatures substantially reduces the number of pores and leads to an increase in material density. The composition and structure of the ceramic material will be influenced by parameters such as electronegativity of the metal atom, organic functional groups linked to the oxo metal units and thermal treatment conditions.

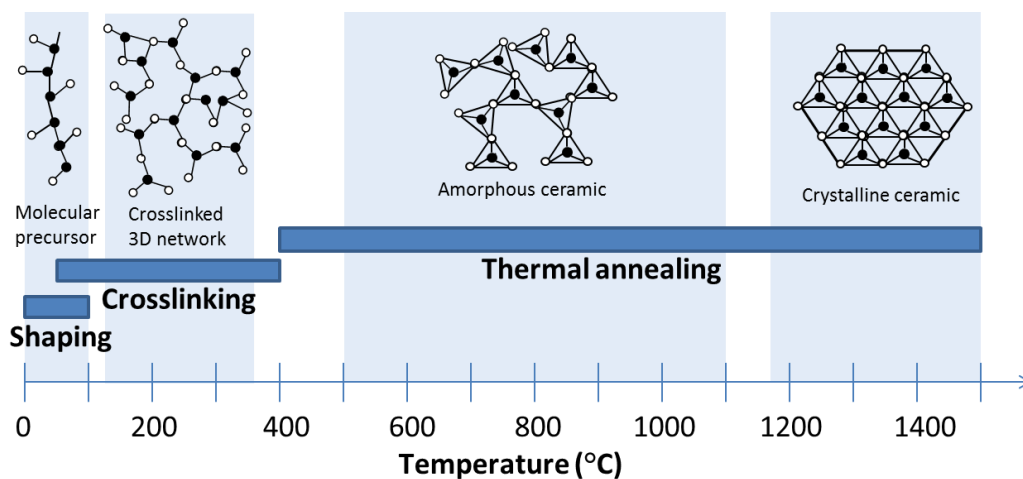


Figure 10. Schematic representation of the synthesis of ceramic materials from a molecular precursor, as a function of temperature.

1.4 Electrospinning

By applying the processing concepts explained in *Chapter 1.2-1.3*, different kinds of particles can be synthesized and used as electrode materials. Most of the electrodes are prepared as processable films by mechanically admixing of the electrochemically active material, conductive additives (if needed), and the polymer binder. Nevertheless, this process presents several disadvantages:

- The polymer binder does not contribute to the electrochemical energy storage and increases the electrical resistivity.
- The electrical conductivity highly depends on the contact sites between the electrochemically active and the conductive additive particles.
- The different hydrophobic/hydrophilic behavior of the particles may cause agglomeration and inhomogeneous material distribution.

The synthesis of non-woven mats eliminates the need for polymer binders and creates a continuous network for electron transport.¹⁴²⁻¹⁴⁴ These mats can be synthesized as hybrid materials containing the electrochemically active and conductive phase, as schematically represented in **Figure 11C**. Compared to composite and hybrid polymer-bound electrodes in **Figure 11A-B**, these fiber mats present an improved rate handling capability, a significant inter-fiber space which facilitates ion transport, and a short diffusion distances for insertion of ions.

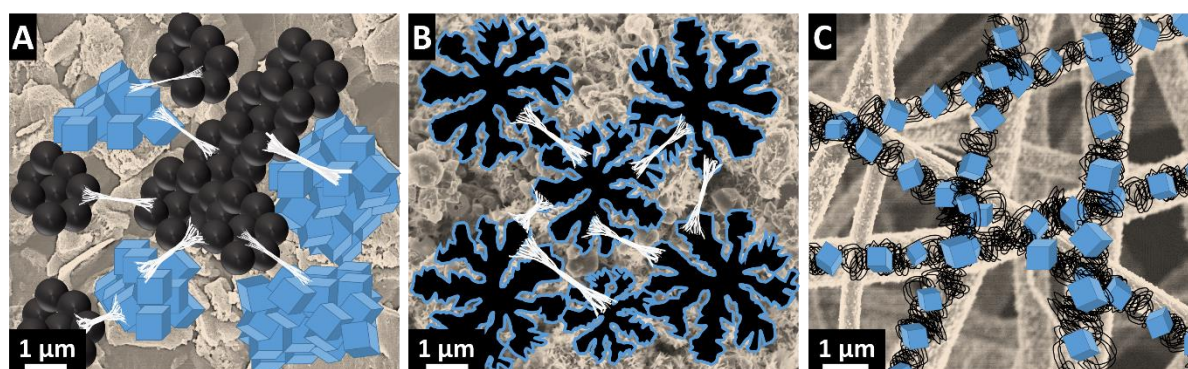


Figure 11. Schematic representation and scanning electron micrographs of polymer-bound electrodes either as a composite electrode with carbon and metal oxide particles (A) or hybrid carbon/metal oxide particles (B), compared to the binder-free hybrid fiber mat (C). Adapted from Ref.¹²².

Several methods based on wet-chemical approaches allow the production of ultrafine ceramic fibers (i.e., diameter of 20-1000 nm).¹⁴⁵⁻¹⁴⁶ These methods include self-assembly,¹⁴⁷ drawing,¹⁴⁸ phase separation,¹⁴⁹ template synthesis,¹⁵⁰ and electrospinning.¹⁵¹ Among them, electrospinning offers several advantages related to scalability for the production of continuous fiber mats from a variety of polymers.¹⁵¹ The process of electrospinning was first patented by J. F. Cooley in 1900.¹⁵² In later years, commercialization of the process started and several improvements were accomplished especially by Anton Formals.¹⁵³⁻¹⁵⁵ Electrospinning has been explored since then in more detail as a viable nano-fabrication technique.¹⁵⁶⁻¹⁵⁷

The basic setup for electrospinning (**Figure 12**) consists of a high-voltage power supply (HVPS; 5-35 kV) connected to a syringe containing the spinning dope (mainly a dissolved organic or inorganic polymer), and a grounded conductive collector. A motorized pump continuously supplies the dope at a rate of 0.2-2.0 mL·h⁻¹ through the spinneret, which is typically a needle with a diameter of 0.2-1.0 mm. A pendant droplet at the needle tip is

formed due to the surface tension of the solution with the surrounding environment. As a high voltage is applied between the needle and the grounded collector, the polymeric droplet will be inductively charged. The induced charges build up on the droplet surface in the direction of the electric field, undergoing Coulombic repulsion and charge redistribution; as a result, a tapered shape arises called, the Taylor cone.¹⁵⁸ The deformation will continue due to the higher charge density at the cone point, and a liquid jet is formed when the force of the applied field exceeds the force of the surface tension. As studied by Doshi and Reneker, the electric field strength (F_{Tc}) measured at the Taylor cone, meaning, the strength to launch a liquid jet, is described by Eq. 23 as a function of the surface tension of the spinning dope (γ), the permittivity of the vacuum (ϵ_0), and the ratio of the curvature of the round off cone apex (R).¹⁵⁷

$$F_{Tc} = \sqrt{\frac{4\gamma}{\epsilon_0 R}} \quad (\text{Eq. 23})$$

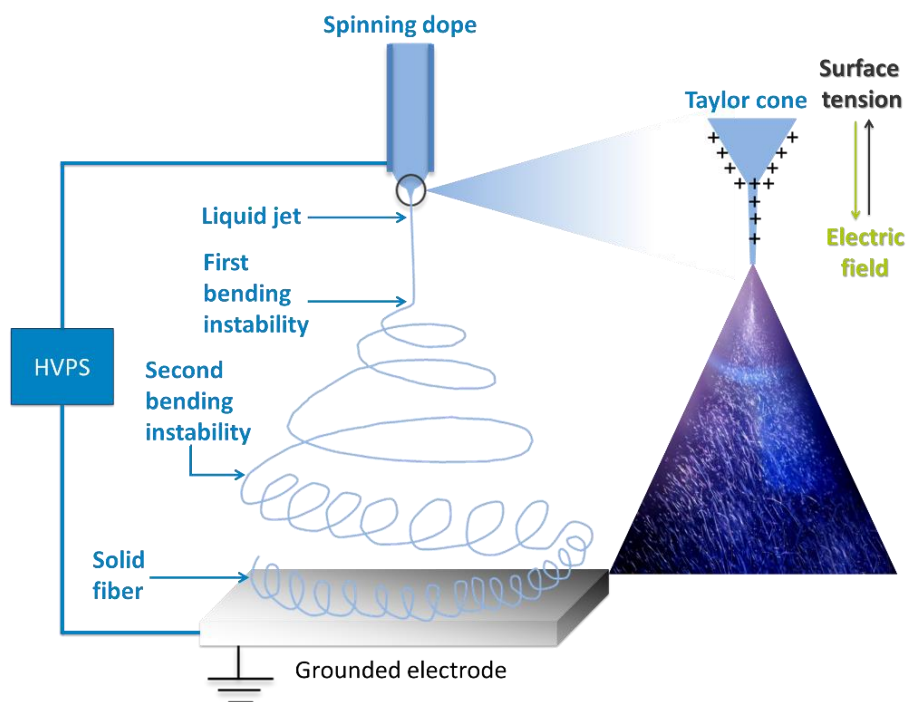


Figure 12. Schematic representation of the electrospinning process. The main components of the process, and a more detailed illustration of the formation of the Taylor cone. A photograph of the transition zone between the liquid and the solid fibers.

As the jet travels through the field towards the grounded electrode, it follows a rectilinear trajectory initially. By Joule heating and contact of the liquid jet with the air, the solvent evaporates from the jet stream. The charges in the jet are redistributed, introducing instabilities which can occur either symmetric or non-symmetric to the electric field.¹⁵⁹⁻¹⁶⁰ The first corresponds to the classical Rayleigh instability which produces beads or beaded fibers.¹⁶¹ This process is promoted by surface tension, decreased by the viscosity of the spinning dope, and suppressed at the high electric fields.¹⁶² The non-axis-symmetric instabilities introduce bending moments causing the fibers to whip in a helix. The whipping motion has several beneficial effects to obtain fibers with lower diameters: it first decreases the velocity in the direction of the electric field, increases the time for further fiber stretching, and reduces the fiber diameter.¹⁶²⁻¹⁶³ It is in this region of instability that the initially liquid jet is mechanically drawn to its final diameter as solid fibers.

Several stages are involved in the formation of ultrafine fibers from a polymeric solution, and during these stages, the process parameters and spinning dope properties interact having a strong influence on the final fiber morphology. Solution parameters determine the spinnability of the solution and the final fiber diameter. High surface tension will promote the formation of beads or beaded fibers; while a low surface tension will lead to uniform and even thinner fibers. A high viscosity will increase the resistance of the solution to flow, either under forces promoted by the surface tension or the electric field. As a consequence, a higher viscosity will reduce the formation of beaded structures, and it will lead to fibers with higher diameters. Moreover, increasing the conductivity of the solution, and therefore the surface charge density decreases the fiber diameter.¹⁶⁴

$$|F| = \frac{1}{4\pi\epsilon_0} \frac{|q|}{d^2} \quad (\text{Eq. 24})$$

Process parameters, such as voltage and flying distance, influence the strength of the electric field. As derived from the Coulomb's law (Eq. 24),⁶ the electric field is proportional to the built charge at the spinneret (q) and irreversibly proportional to the distance (d) to the ground collector. A large enough distance must be assured so that the polymer has enough time to dry and obtain solid fibers. Also, the applied voltage should correspond at least with the threshold voltage for the Taylor cone formation. However, no clear trend has been observed between these process parameters and the fiber diameter, but the behavior changes depending on the type of solvent and polymer used.¹⁶³

2. Approach and overview

Electrospinning is a promising technology for the synthesis of electrodes with higher energy and power because it eliminates the need of a polymer binder and conductive additives, and the presence of a continuous network allows for effective and rapid electron transport. Although the synthesis of microporous carbon fibers from organic precursors has been investigated in the literature,¹⁶⁵⁻¹⁶⁶ very little attention has been given to the synthesis and electrochemical characterization of continuous hybrid fibers from molecular precursors. Therefore, this work explores carbon and hybrid fiber mats as electrodes for energy storage devices and will provide a comparison with conventional powder electrodes. The fiber mats are produced from a one-pot synthesis from molecular precursors. My work aims: (1) identification of suitable synthesis conditions for hybrid fibers, and (2) electrochemical benchmarking of the fiber mats as electrodes for electrical double-layer capacitors (EDLC), lithium-ion batteries (LIB), and sodium-ion batteries (NIB). The key results of this work are presented in *Chapter 3*, and **Figure 13** shows a schematic representation of the content of this chapter.

Motivated by the need of materials with a high and accessible surface area and a tunable porosity, the first part of this work explores the synthesis and characterization of CDC materials for EDLCs. The pore structure of CDC materials depends mainly on the crystal structure of the carbide and the chlorine treatment conditions;³⁶ therefore, two different carbide precursors were synthesized (SiOC and NbC) and thermally treated with chlorine gas for the selective removal of the metal or metal (carb)oxide domains. *Chapter 3.1* presents the synthesis of highly porous carbon from carbon-rich SiOC ultrafine fibers, and *Chapter 3.2* the synthesis of highly porous carbon from NbC/C hybrid nanofibers. In the first part, the effect of the electrode morphology in the electrochemical performance is studied. By comparing free-standing fiber mat electrodes and polymer-bound CDC bead films, we achieved a better understanding of the importance of the morphology, system resistivity and interparticle contact in the electrochemical performance. Also, the effect of the chlorine treatment conditions (temperature and time) on the microstructure and electrochemical performance of the CDC materials was studied.

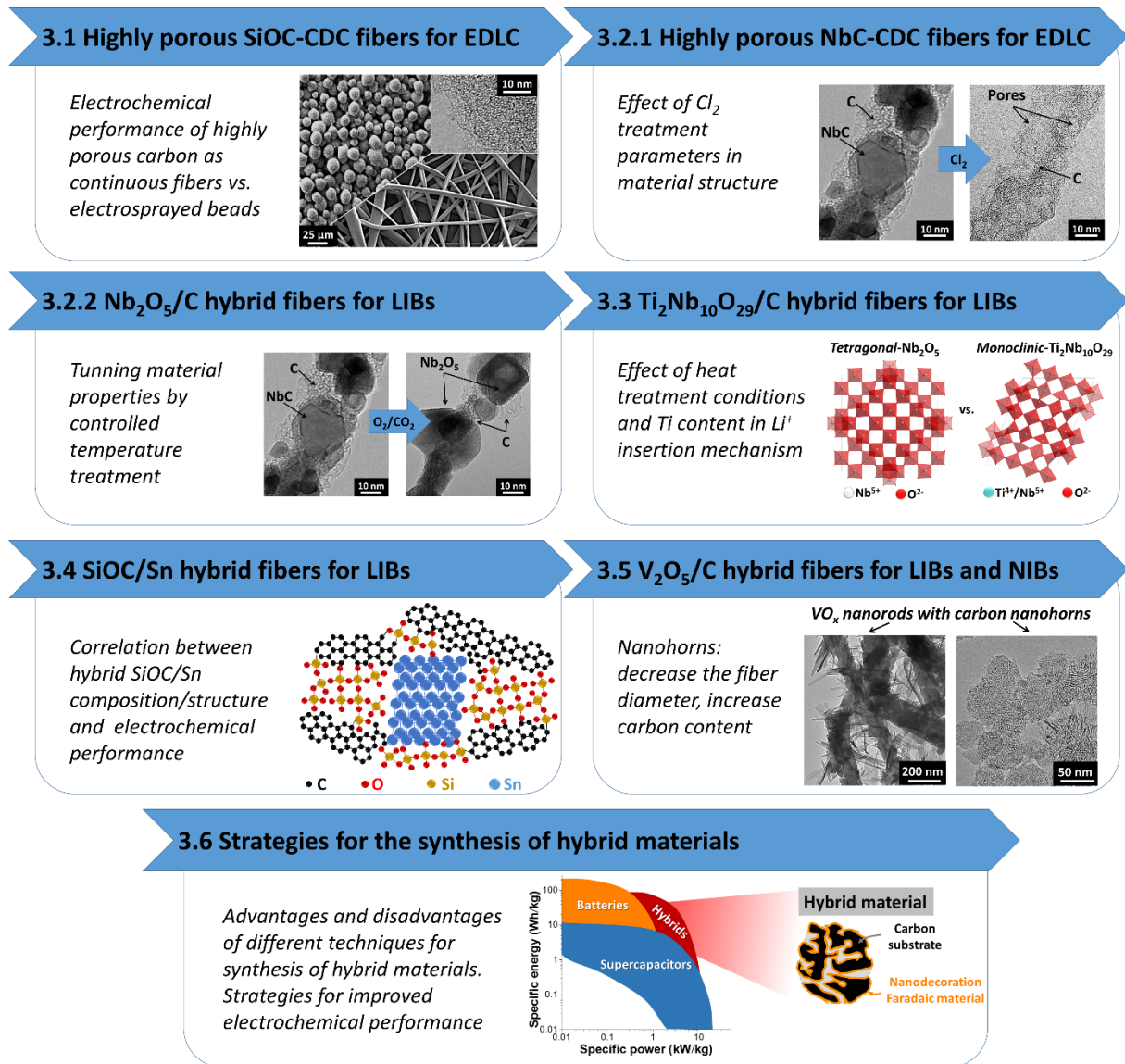


Figure 13. Key topics of the thesis work.

The second part of the work explores the synthesis and electrochemical characterization of metal oxide/carbon hybrid fibers as electrodes for LIBs and NIBs. Initially, my work focuses on anode materials with different electrochemical performance, based on insertion (Nb_2O_5 , $\text{Ti}_2\text{Nb}_{10}\text{O}_{29}$) or reconstitution reactions (SiOC, Sn). *Chapter 3.2* presents an optimization study for the synthesis of Nb_2O_5 /carbon hybrid fibers and evaluates the effect of the thermal treatment conditions on the material properties. Following this work, *Chapter 3.3* presents the synthesis of niobium oxide electrodes with higher specific energy by the combination of crystal structures with higher lithium insertion capacity (tetragonal, monoclinic) and the addition of titanium to the system. This chapter assesses the influence of titanium addition and heat treatment conditions in the material properties.

Compared to titanium-niobium oxide, alloy electrode materials such as Si and Sn present a much higher capacity but suffer from a higher degradation due to the large volume expansion (200-400%).^{64, 167} Therefore, a critical parameter in the electrode preparation is the selection of a polymer binder stable in the voltage operation window (0.01-2.0 V vs. Li/Li⁺), which can support the large volume expansion.¹⁶⁸ These considerations motivated the synthesis and characterization of polymer-binder free SiOC-Sn fiber electrodes in *Chapter 3.4*. This chapter presents a systematic study of the composition and chemical structure of the hybrid fibers, together with a correlation with the electrochemical performance.

In *Chapter 3.5* the synthesis and characterization of continuous mats of hybrid vanadium oxide/carbon fibers are explored as cathodes for LIBs and NIBs. In this chapter, the addition of separately synthesized (commercially available) carbon nanohorns is evaluated, compared to the one-pot synthesis approach followed in *Chapter 3.1-3.4*. The chapter presents a systematic study of the effect of nanostructuring, vanadium oxide crystal phase and carbon content on the electrochemical performance as lithium- and sodium-ion battery electrode.

As presented in *Chapter 3.2-3.5*, hybrid continuous fiber mats are promising electrode materials for energy storage devices. *Chapter 3.6* gives an overview of different approaches for the synthesis of hybrid materials, compared to the hybrid fibers produced in this thesis. The synthesis of hybrid materials requires careful design to create synergistic effects in the electrochemical performance; therefore, the last chapter highlights the advantages and disadvantages of each approach and proposes strategies for materials with improved electrochemical behavior.

3. Results and discussion

The major scientific findings within the cumulative part of this thesis are reported in the following publications:

3.1 *Electrospinning and electrospraying of silicon oxycarbide-derived nanoporous carbon for supercapacitor electrodes*

3.2 *Niobium carbide nanofibers as a versatile precursor for high power supercapacitor and high energy battery electrodes*

3.3 *Binder-free hybrid titanium-niobium oxide/carbon nanofiber mats for lithium-ion battery electrodes*

3.4 *Continuous silicon oxycarbide fiber mats with tin nanoparticles as high capacity anode for lithium-ion batteries*

3.5 *Electrospun hybrid vanadium oxide/carbon fiber mats for lithium and sodium-ion battery electrodes*

3.6 *Design of carbon/metal oxide hybrids for electrochemical energy storage*

3.1 Electrospinning and electrospraying of silicon oxycarbide-derived nanoporous carbon for supercapacitor electrodes

Aura Tolosa,^{a,b} Benjamin Krüner,^{a,b} Nicolas Jäckel,^{a,b} Mesut Aslan,^a
Cekdar Vakifahmetoglu,^c and Volker Presser^{a,b}

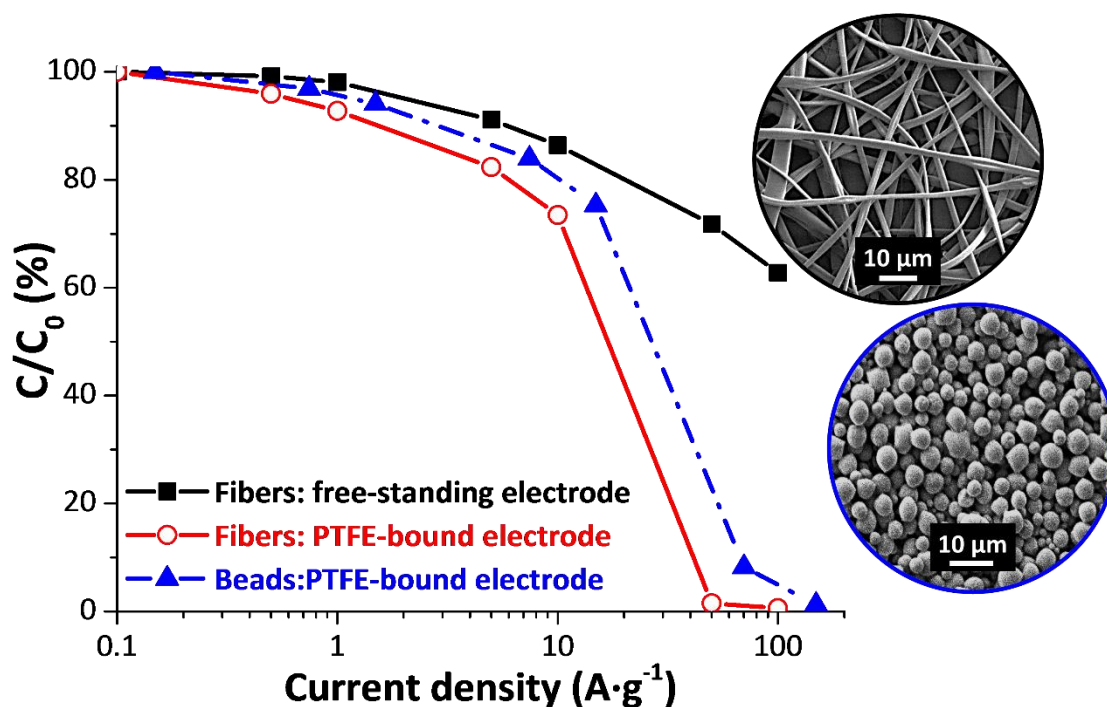
^a INM - Leibniz Institute for New Materials, 66123 Saarbrücken, Germany

^b Department of Materials Science and Engineering, Saarland University, 66123 Saarbrücken, Germany

^c Department of Mechanical Engineering, Istanbul Kemerburgaz University, 34217 Istanbul, Turkey

Published in: Journal of Power Sources, 313 (2016), 178-188

DOI: 10.1016/j.jpowsour.2016.02.077



Own contribution: Project management; paper writing; material synthesis; data analysis; measurements: SEM, TEM, EDX, FT-IR, Raman spectroscopy, electrochemical characterization



Contents lists available at ScienceDirect

Journal of Power Sources

journal homepage: www.elsevier.com/locate/jpowsour

Electrospinning and electrospaying of silicon oxycarbide-derived nanoporous carbon for supercapacitor electrodes



Aura Tolosa ^{a, b}, Benjamin Krüner ^{a, b}, Nicolas Jäckel ^{a, b}, Mesut Aslan ^a,
Cekdar Vakifahmetoglu ^{c, **}, Volker Presser ^{a, b, *}

^a INM - Leibniz Institute for New Materials, 66123 Saarbrücken, Germany

^b Department of Materials Science and Engineering, Saarland University, 66123 Saarbrücken, Germany

^c Department of Mechanical Engineering, Istanbul Kemerburgaz University, 34217 Istanbul, Turkey

H I G H L I G H T S

- First report on carrier polymer free electrospun carbide derived carbon fibers.
- Use of low-cost silicon oxycarbide precursor materials.
- Synthesis of ultrafine fibers or beads by adjusting synthesis parameters.
- Comparative study of freestanding fiber mats vs. PTFE-film electrodes.
- High rate handling ability of freestanding, binder-free fiber mats.

A R T I C L E I N F O

Article history:

Received 23 December 2015

Received in revised form

17 February 2016

Accepted 23 February 2016

Available online 19 March 2016

Keywords:

Silicon oxycarbide

Electrospinning

Electrospaying

Carbide-derived carbon

Electrical double-layer capacitors

A B S T R A C T

In this study, carbide-derived carbon fibers from silicon oxycarbide precursor were synthesized by electrospinning of a commercially available silicone resin without adding a carrier polymer for the electrospinning process. The electrospun fibers were pyrolyzed yielding SiOC. Modifying the synthesis procedure, we were also able to obtain electrospayed SiOC beads instead of fibers. After chlorine treatment, nanoporous carbon with a specific surface area of up to 2394 m² g⁻¹ was obtained (3089 m² g⁻¹ BET). Electrochemical characterization of the SiOC-CDC either as free-standing fiber mat electrodes or polymer-bound bead films was performed in 1 M tetraethylammonium tetrafluoroborate in acetonitrile (TEA-BF₄ in ACN). The electrospun fibers presented a high gravimetric capacitance of 135 F g⁻¹ at 10 mV s⁻¹ and a very high power handling, maintaining 63% of the capacitance at 100 A g⁻¹. Comparative data of SiOC-CDC beads and fibers show enhanced power handling for fiber mats only when the fiber network is intact, that is, a lowered performance was observed when using crushed mats that employ polymer binder.

© 2016 Elsevier B.V. All rights reserved.

1. Introduction

Electric double-layer capacitors (EDLCs), also known as supercapacitors, are energy storage devices which present unique properties such as high rate handling and long cycle lifetime, but exhibit only a moderate energy density [1,2]. In these systems,

energy is stored by electrostatic adsorption of ions to the large surface area of nanoporous carbon electrodes [3]. Common supercapacitor electrodes consist of nanoporous carbon powder, possibly a conductive additive like carbon black, and a polymer binder [4,5]. While necessary for mechanical stability, the polymer binder increases the electrical resistance and blocks access to a certain fraction of the carbon nanopores [4]. These limitations can be overcome by employing free-standing electrodes, like buckypaper or graphene sheets [6,7]. Alternatively, continuous mats of highly interconnected ultrafine fibers (and in many cases even nanofibers) is possible via electrospinning. This way, free-standing and binder-free fiber mats can be obtained for direct use as supercapacitor electrodes [8,9]. Continuous fibers in a non-woven mat form a

* Corresponding author. INM - Leibniz Institute for New Materials, 66123 Saarbrücken, Germany.

** Corresponding author. Department of Mechanical Engineering, Istanbul Kemerburgaz University, 34217 Istanbul, Turkey.

E-mail addresses: cekdar.vakifahmetoglu@kemerburgaz.edu.tr (C. Vakifahmetoglu), volker.presser@leibniz-inm.de (V. Presser).

percolated network which is expected to facilitate high power handling by exhibiting very high electrical conductivity (commonly factor 10 higher than for powder electrodes) [10].

For a high supercapacitor performance, careful optimization of the porosity is required to combine high power (transport-optimization) and high energy ratings (maximization of suitable micropores) [1]. Among the large group of carbon nanomaterials, including graphene, carbon nanotubes, and carbon onions, commercial supercapacitors almost exclusively employ nanoporous activated carbon [11]. Particularly attractive tunable carbon nanomaterials belong to the family of carbide-derived carbons (CDCs) [12]. For CDC synthesis, metal carbides [13], carboxides [14,15], or carbonitrides [16] are chemically etched with halogens (most commonly gaseous Cl_2). This way, non-carbon atoms are effectively removed from the precursor as volatile metal chlorides. The resulting carbon structure depends on the temperature, structure of the precursor, and further synthesis conditions. Also, the resulting degree of carbon ordering, pore size distribution, and porosity characteristics can be finely tuned and optimized for different electrolyte systems [17,18]. So far, the conformal nature and versatility of the CDC synthesis process has been adapted for the synthesis of powders [19], thin films [20], nanobeads [21], and ultrafine fibers [22,23].

Although CDC had been widely synthesized from metal carbides powders such as TiC [24], SiC [25], B_4C [26], VC [27,28], SiOC [29], and NbC [30], less attention was given to the synthesis of these materials with a specific morphology such as fiber shape. Metal carbide fibers can be produced in the form of non-woven mats by electrospinning of metal carbide molecular precursors at room temperature, which are later transformed into metal carbides by pyrolysis above 1200 °C [31]. By this approach, the only two systems explored have been TiC-CDC [32], [22], and SiC-CDC [23]. The latter was produced using polycarbosilane (PCS) as precursor and did not present uniform morphology.

Cost considerations are of high importance when employing advanced processing such as electrospinning. SiOC precursors, namely polysiloxanes and polysilsesquioxanes, are commercially available for relative low costs and have been positively evaluated as CDC precursor, but not yet for electrospun CDC fibers [14]. Therefore, in this study we focus on the production of SiOC-CDC fibers using a low cost commercially available polysilsesquioxane as precursor.

SiOC fibers had been produced by melt spinning of polysiloxanes [33] and by mechanical drawing of sol-gel systems [34], yielding fiber diameters between 10 and 30 μm . In order to obtain thinner fibers electrospinning has been explored and for this method, adjusting the rheological parameters of the solution is of critical importance [35]. To achieve beneficial spinnability, commonly a carrier polymer is added to the spinning dope. So far, all reported electrospun SiOC fibers from preceramic polymers have made use of carrier polymer [36]. By introducing a polymer which can be easily electrospun, uniform, and smooth fibers can be obtained. The electrospinning of PCS and tetraethyl orthosilicate (TEOS) has been accomplished by adding polyvinyl butyral (PVB) or polystyrene (PS), obtaining fibers in the range of 0.5–1.5 μm [37]. Guo et al. [38] have reported the production of electrospun SiOC fibers from silicone resins, using polyvinylpyrrolidone (PVP) as a carrier polymer. The as-spun fibers, containing 75 mass% silicone resin and 25 mass% PVP, showed fiber diameters between 1.0 and 2.7 μm . In order to transform the as-spun fibers into ceramic fibers, a latent catalyst was added helping to maintain the fiber shape during the thermic process for transformation to SiOC. However, adding a carrier polymer, such as PVP or PAN, severely increases the process cost and produces undesired products by the decomposition of the carrier polymer.

Our work presents for the first time an approach to obtain continuous SiOC electrospun fibers without adding any carrier polymer. We also take advantage of the versatile transition from fiber-synthesis via electrospinning to obtain beaded materials via electrospinning by adjusting the process parameters. The obtained fibers and beads were then transformed into SiOC-CDC and evaluated as electrodes for supercapacitors. To the best of our knowledge, this study is also the first to present CDC beads from electrospay synthesis. The performance of the fiber mat was compared to rolled electrodes containing polymer binder, one containing milled SiOC-CDC fibers and another containing SiOC-CDC beads. This enables us to gain important insights in the electrochemical performance and power handling ability when comparing, for the same material, different shape (beads vs. fibers) and electrode design (interconnected fibers and binder-free vs. broken fibers with binder).

2. Experimental

2.1. Materials

Ethanol ($\geq 99.8\%$) and *N,N*-dimethylformamide (anhydrous, 99.8%) were purchased from Sigma Aldrich. Commercial silicone resin, namely H44 (polymethylphenyl-silsesquioxane) was purchased from Wacker Chemie. Moisture sensitive catalysts zirconium(IV)acetylacetonate (ZrAcAc), and zinc acetylacetonate hydrate powder (ZnAcAc) were purchased from Sigma Aldrich and stored in moisture free N_2 atmosphere in a glove box (H_2O , $\text{O}_2 < 0.1$ ppm). All chemicals were used as-received.

2.2. Synthesis of SiOC fibers and beads

Before preparing the spinning dope, H44 was partially crosslinked by heating as-received powder to 200 °C in air. The pre-crosslinked resin H44 was cooled to room temperature and ground into a powder using an agate mortar and pestle.

The spinning dopes were prepared at ambient conditions, containing 56 mass% of silicone resin and 6 mass% of ZnAcAc in ethanol and/or DMF. All solutions were stirred for 24 h. Electrospinning and electrospaying were carried on a MECC Co. NF-103V nanofiber system. The spinning dope was pumped at 1 mL h^{-1} through a spinneret (inner diameter: 510 μm), which was inductively charged at 28 kV. The fibers and beads were collected on a stationary grounded target at a distance of 21 cm from the spinneret. The collected material was then heated at 100 °C for 24 h to stabilize the fiber/bead shape. Complete crosslinking of the silicone resin was accomplished by heat treatment at 200 °C for 2 h.

The pyrolysis of the crosslinked silicone resin was achieved by heating the material at 5 °C \cdot min $^{-1}$ to 1200 °C for 2 h, under argon in a graphite heated high temperature furnace (Thermal Technologies, Model: 1100). After heat treatment SiOC nonwoven mat and beads were cooled at a rate of 20 °C min^{-1} to room temperature.

2.3. Chlorine gas treatment

Carbide-to-carbon conversion by chlorine gas treatment (CDC process) was carried on a quartz tube furnace HTRH, Gero, constantly purged with argon (50 cm^3 min^{-1}). The SiOC produced was heated at a rate of 15 °C min^{-1} to 1200 °C, and treated with chlorine gas for 3 h (10 cm^3 min^{-1}). During cooling, a post annealing process with hydrogen gas (10 cm^3 min^{-1}) was applied at 600 °C for 3 h in order to remove residual chlorine and chloride species present in the sample. The mass of the sample was measured before and after the chlorine treatment.

2.4. Materials characterization

The molar mass of the silicone resin was determined by high performance liquid chromatography-gel permeation chromatography (HPCL-GPC) using automatic injection (Agilent 1260 Infinity). The calibration was carried out with PDMS-standards in toluene. The melting of the silicone resin and the decomposition of the catalysts were determined by differential scanning calorimetry (DSC). All measurements were carried in air at $5\text{ }^{\circ}\text{C min}^{-1}$. Thermogravimetric analysis (TGA) of the metal acetonates was carried out in O_2 with a SDT Q26 system, TA instruments, using a heating rate of $10\text{ }^{\circ}\text{C min}^{-1}$.

The morphology of the sprayed or spun material was examined by a JEOL JSM 7500F field emission scanning electron microscope (FE-SEM). All samples were fixed on steel sample holders with sticky carbon tape. The as-spun and crosslinked fibers were sputter coated prior to the imaging with a thin layer of platinum in a JEOL Autofine Coater. ImageJ software [39] was used to process the SEM images and diameters of at least 150 individual fibers or beads were measured. High resolution transmission electron microscope images (TEM) were carried in a JEOL JEM-2100F system at 200 kV in vacuum. TEM samples were prepared by dispersing and sonicating the fibers in ethanol and drop casting them on a copper grid with a lacey carbon film. The composition of the fibers was measured by energy dispersive X-ray spectroscopy (EDX) using a X-Max-150 detector from Oxford Instruments attached to the SEM chamber. Using an accelerating voltage of 5 kV and an emission current of $10\text{ }\mu\text{A}$, the spectra of 10 different fibers or beads were measured and the average values were calculated.

X-ray diffractograms were collected with a Bruker D8 Discover diffractometer using $\text{Cu-K}\alpha$ radiation (0.154 nm) with a step size of 0.02° and a measurement time of 1 s per step. The system was calibrated with an alumina standard.

Infrared vibrational spectroscopy was performed with a diamond total attenuated reflectance crystal (ATR) using a Bruker Tensor 27 FTIR system (Fourier transform infrared spectroscopy). Raman spectra were recorded with a Renishaw InVia Raman system using a laser with a 532 nm excitation wavelength and 0.5 mW power on the sample with a spectral resolution of ca. 1.2 cm^{-1} , using a $50\times$ objective (numeric aperture: 0.9). Peak analysis and peak fitting were performed assuming four Voigt peak fitting between 500 and 2000 cm^{-1} .

Nitrogen gas sorption measurements at $-196\text{ }^{\circ}\text{C}$ were carried out with an Autosorb iQ system (Quantachrome). The samples were outgassed at $300\text{ }^{\circ}\text{C}$ for 10 h under vacuum conditions (about 10^2 Pa) to remove adsorbed water and other volatile surface functionalities. The relative pressure range was sampled from $5\cdot 10^{-7}$ to 1.0 in 68 steps. The specific surface area (SSA) was calculated with the ASiQwin software using the Brunauer-Emmett-Teller (BET) equation [40] in the linear relative pressure range 0.05–0.2. We also calculated the SSA and pore size distribution (PSD) via quenched-solid density functional theory (QSDFT) [41] with assuming slit-shaped pores and pore size between 0.56 and 37.5 nm. Values for the total pore volume correspond to $p/p_0 = 0.95$. CO_2 gas sorption measurements were carried out at $0\text{ }^{\circ}\text{C}$ in the relative pressure range from $1\cdot 10^{-4}$ to $1\cdot 10^{-2}$ in 40 steps. SSA and PSD values were calculated for pore sizes between 0.3 and 1.0 nm with the ASiQwin software using nonlocal density functional theory (NLDFT) for CO_2 sorption [42,43].

2.5. Electrochemical characterization

For the electrochemical characterization, free-standing fiber mats and film electrodes containing polymer binder were used. The polymer binder containing electrodes were prepared using SiOC-

CDC beads or SiOC-CDC ground fibers. SiOC-CDC fibers and beads were ground with an agate mortar in ethanol until obtaining a homogeneous slurry, to which 13 mass% polytetrafluoroethylene (PTFE, 60 mass% solution in water, Sigma Aldrich) was added. The obtained paste was rolled until $140 \pm 20\text{ }\mu\text{m}$ thick electrodes were obtained (MTI HR01 rolling machine, MTI). Prior to use, the electrodes were dried at 2 kPa, $120\text{ }^{\circ}\text{C}$ for 48 h.

The performance of the electrodes was evaluated using a half- and full-cell setup in 1 M tetraethylammonium tetrafluoroborate (TEA-BF_4) in electrochemical grade acetonitrile (ACN) from BASF. The electrodes were tested in custom-built polyether ether ketone (PEEK) cells with spring loaded titanium pistons. Half-cell tests were performed with an oversized counter electrode (YP-50, Kuraray Chemicals). The working electrode discs with 8 mm diameter were punched out of the PTFE-bound electrodes and the free-standing fiber mats. The electrode pair was separated by a glass-fiber separator (GF/D from Whatmann) and placed between 12 mm diameter carbon-coated aluminum current collectors (Zflo 2653, Exopack technologies, USA). YP-50F with 5 mass% PTFE was used as the reference. The assembled cells were dried at 2 kPa, $120\text{ }^{\circ}\text{C}$ for 24 h. After cooling down the cells were placed in an inert gas glove box (MBraun Labmaster 130, O_2 and $\text{H}_2\text{O} < 1\text{ ppm}$), and filled with 1 M TEA-BF_4 in ACN.

Electrochemical measurements were carried out with a potentiostat/galvanostat (VSP300 from Bio-Logic), by cyclic voltammetry (CV) and galvanostatic cyclic potential limitation (GCPL). CVs were recorded at 10 mV s^{-1} scan rate in the potential range from 0 V to $+2.7\text{ V}$ for full-cell and from -1 V to $+1\text{ V}$ in half-cell versus carbon. Galvanostatic cycling was carried from -1 V to $+1\text{ V}$ in a three-electrode setup (i.e., half-cell) at 2 A g^{-1} with a holding time of 10 min. The capacitance was calculated by use of Eq. (1), with C_{sp} specific capacitance, t_0 starting time, t_{end} end time of discharge and, U cell voltage. The specific capacitance corresponds to the capacitance related only to the active mass material (mass of polymer binder was not considered). The parameter X corresponds to 1 for a half-cell and to 4 for a full-cell (i.e., two-electrode system) [2].

$$C_{sp} = \frac{X}{m} \cdot \left(\frac{\int_{t_0}^{t_{end}} I dt}{U} \right) \quad (1)$$

Performance stability tests were carried out over 10,000 cycles of voltage cycling at 2.7 V at 50 mV s^{-1} . Electrical impedance spectra were recorded in symmetrical full cells for 100 kHz to 100 mHz at 0 V with 10 points per decade and averaged over 5 measurements.

3. Results and discussion

3.1. Electrospinning of polymethylphenyl-silsesquioxane fibers

In order to electrospin H44, we first had to establish optimized processing parameters, such as a suitable solvent (ethanol) and polymer concentration (60 mass%; see ESI, Fig. S1). After the electrospinning process, the fibers are transformed into an infusible thermoset, which for silicone resin typically occurs by heating above $200\text{ }^{\circ}\text{C}$. However, at $42\text{ }^{\circ}\text{C}$ the as-received H44 melts (Table 1) and the fiber integrity is lost before complete crosslinking is achieved at $200\text{ }^{\circ}\text{C}$.

Reduced softening or promoting of crosslinking at lower temperatures can be achieved by adding latent catalysts such as metal acetylacetonates [38,44]. According to Smith [45], the decomposition products of metal acetylacetonates may be the active species which activate the crosslinking of the polymer at lower

Table 1

Melting point and molecular weight (M_w ; M_n : number average molecular weight) of as received and pre-crosslinked silicone resins.

Sample	Melting point (°C)	M_w (g·mol ⁻¹)	M_w/M_n
H44 as-received	42	1084	4.1
H44-22	51	1458	4.3
H44-26	58	1746	4.6

temperatures. Each metal acetylacetonate will decompose at a different temperature; however, the decomposition occurs typically above the melting point of the silicone resin, for example for ZnAcAc and ZrAcAc (see *ESI*, Fig. S2). When adding 0.05 parts of latent catalyst per part of silicone resin, fiber melting is observed before the activation of the catalyst (see *ESI*, Fig. S3). Thus, direct pyrolysis after electrospinning of H44 fibers is not possible and a modified approach needs to be applied, the most attractive one being pre-crosslinking.

3.1.1. Pre-crosslinking

The melting behavior of the polymers can be modified when the molecular weight of the polymer is increased by partial crosslinking. In such cases, the higher entanglement and interaction between the chains will restrict translational movements of the chains, and more energy is required for the melting of the polymer [46,47]. We explored pre-crosslinking of the H44 precursor prior to electrospinning in order to ensure the integrity of the fibers during curing process. After electrospinning, stabilization of the fiber shape can be accomplished at a temperature below the melting point of the polymer which is still sufficiently high to promote the catalytic activity of the metal acetylacetonate, such as ZnAcAc. H44 was pre-crosslinked at 200 °C for 2 h (H44-22) and 6 h (H44-26) and the change on molecular weight and the melting point compared to the as-received state of H44 is given in Table 1.

An increase of 60% in the average molecular weight lead to an increase of 16 °C in the melting point in the case of H44-26. Further increase in the molecular weight comes at the cost of decrease in the solubility of the precursor polymer. In order to compare the effect of pre-crosslinking on the microstructural evolution, spinning dopes were prepared containing 60 mass% of silicone resin in ethanol using H44 and H44-26 resin. A total of 0.1 parts of latent catalyst (ZnAcAc) per part of silicone resin was added, for a solution with a concentration of 56 mass% silicone resin and 6 mass% ZnAcAc. The melting behavior of the spun fibers was confirmed by SEM as shown in Fig. 1 and by DSC of dried spinning dopes, in both cases after stirring the spinning dope for 24 h (see *ESI*, Fig. S4). It can be observed that the catalyst concentration and the pre-crosslinking have an influence in the melting point of the fibers. For as-received H44, by adding 0.1 parts of catalyst per part of silicone resin (Fig. 1a), the fibers partially melted at 80 °C, while fibers had completely melted when adding just 0.05 parts of catalyst (see *ESI*, Fig. S3d). When adding 0.1 parts of catalyst to the as-received and pre-crosslinked resin (Fig. 1), the pre-crosslinking increased the melting point of the system. The H44-26 fibers maintained the shape by heating to 100 °C with a melting point of the system of about 120 °C, which is ca. 30 °C higher than for the H44 fibers (see *ESI*, Fig. S4). The thermal decomposition of ZnAcAc occurs in the range of 100–120 °C (see *ESI*, Fig. S4), meaning that crosslinking reactions can be promoted at ca. 100 °C and the fiber shape can be maintained in consequence.

3.1.2. Optimization of fiber diameter

Aiming to produce fibers as thin as possible, two parameters were modified separately: (i) polymer concentration, and (ii)

dielectric constant of the solvent. While each parameter can promote the formation of thinner fibers, an increase in the surface tension or a decrease in the viscosity promotes the formation of beads.

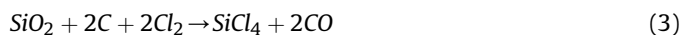
First, the polymer concentration was decreased relative to the solvent from 60 to 50 and 40 mass% (see *ESI*, Fig. S5). By doing so, symmetrical instabilities were promoted due to the low viscosity of the system and high surface tension, leading to beaded fibers and beads formation. The bead's collapsed skin was related to the rapid loss of the solvent [48]. By keeping the polymer concentration constant at 60 mass% relative to the solvent, the dielectric constant was then modified by adding a solvent with a higher dielectric constant than ethanol (EtOH). Dimethylformamide (DMF) presents a higher dielectric constant but yields also higher surface tension [49]; therefore, spinning dopes were prepared from the blends of DMF/EtOH. The obtained morphologies are shown in Fig. 2.

Different DMF/EtOH mass ratios between 0 and 1 were evaluated. When using more than 0.1 of DMF, the surface tension of the system increased by such a large amount that beaded fibers were formed. When using 1/0 and 0.5/0.5 ratios of DMF/EtOH, electrospinning occurred yielding beads with an average size of $3.3 \pm 0.8 \mu\text{m}$ and $2.5 \pm 0.6 \mu\text{m}$ were obtained, respectively (Fig. 2c). The as-spun fibers by using only ethanol presented a fiber diameter of $5.0 \pm 2.5 \mu\text{m}$ (Fig. 2f). By using 0.1/0.9 of DMF/EtOH, the fiber diameter decreased to $2.2 \pm 1.4 \mu\text{m}$ (Fig. 2d) which was the smallest diameter we were able to obtain. In addition to the change in fiber diameter, also the fiber morphology was modified. When using just ethanol, the observed fiber morphology was mostly ribbon-like, and increasing the DMF content caused an increase in the formation of cylindrical cross sectioned fibers. The presence of ribbons is related to the interaction phenomena of mechanical forces and the solvent evaporation at scales above 1 μm [48].

3.2. From polymethylphenyl-silsesquioxane to SiOC and SiOC-CDC

After optimizing the crosslinking of the system and fiber morphology, two different systems were chosen: (1) free-standing fiber mats produced using 0.1/0.9 of DMF/EtOH and (2) beads produced using 1/0 of DMF/EtOH. The mats and beads were further treated at 200 °C for 2 h to ensure complete crosslinking prior to the pyrolysis. They were later transformed to SiOC by pyrolysis under Ar at 1200 °C for 2 h. The process resulted in a cumulative mass loss of 29%, and led to SiOC, where an excess of carbon relative to stoichiometric SiOC precipitates (called as “free carbon”; stoichiometric SiOC:SiO₂(1-x)C_x, see Table 2) [50].

The fibers and beads were then treated with chlorine gas to remove non-carbon atoms from the material [12]. During thermal chlorine treatment of SiOC, the SiC and SiO₂ domains react in the presence of carbon according to Eqs. (2)–(3), removing the silicon and oxygen as volatile species, and leading to a highly porous carbon [32].



The chlorine treatment for the fibers and beads yielded a mass loss of 82–85 mass%, leaving behind almost pure carbon. As seen from Table 2, the material contained ca. 2 at% of oxygen, but no other elements were detected. The beads showed small amounts of residual silicon (0.2 at%) and chlorine (2 at%) as a result of the much larger bead diameter, indicating slightly incomplete transformation to CDC.

With FTIR, we tracked the solvent evaporation, and hydrolysis and condensation reactions during crosslinking (Fig. 3a). A broad

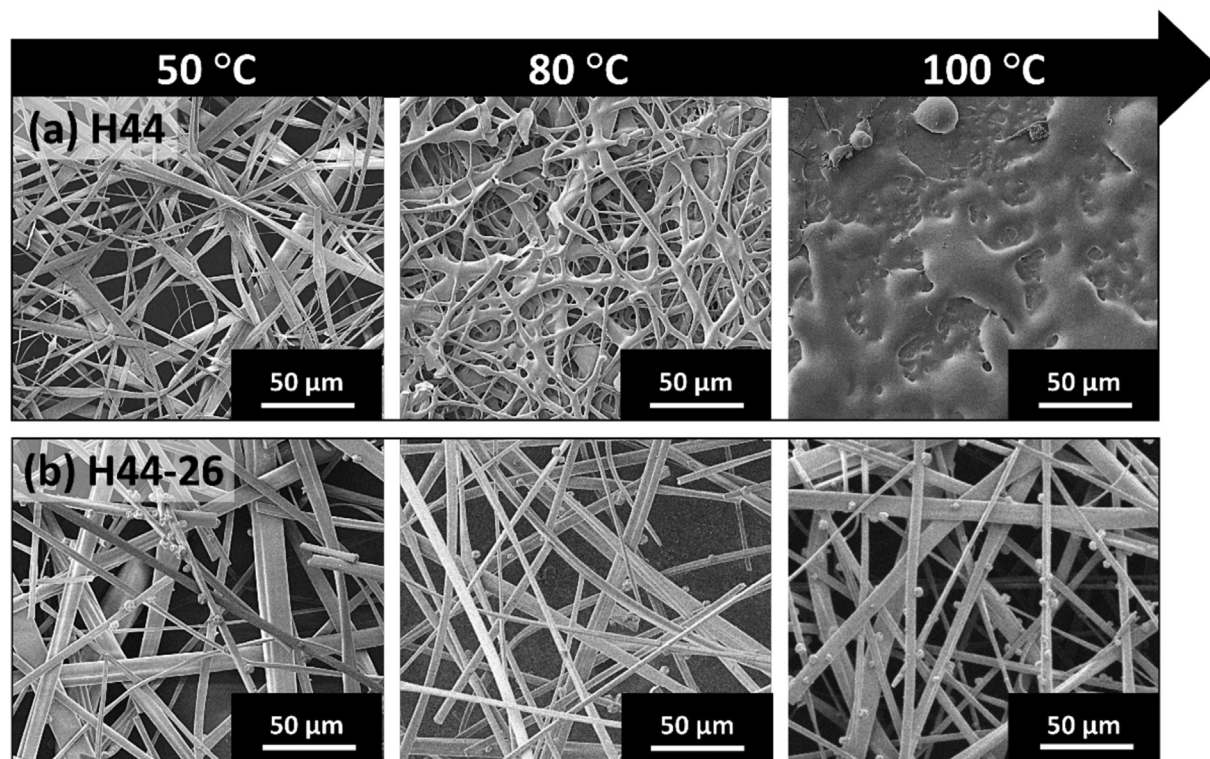


Fig. 1. SEM images of electrospun mats of H44 (a) and H44-26 (b), treated at different temperatures.

peak centered at 3330 cm^{-1} related to terminal O–H bonds present in ethanol and in the silicone resin disappeared in the crosslinked fibers [51]. The Si–O stretching vibration in the Si–O–Si ladder structure appeared between 1041 and 1026 cm^{-1} [52], overlapping with a peak present at 1084 cm^{-1} related to C–N bridging vibrations in DMF, and a peak at 1130 cm^{-1} related to phenolic groups present in the silicone resin [51]. Peaks observed at 1268 , 2970 , and 2927 cm^{-1} are related to the C–H vibration modes from the methyl groups [51]. Absorbance of the bridging bond Si–C in the Si–CH₃ was observed at 734 cm^{-1} [52]. In the pyrolyzed sample, the only visible bands correspond to Si–O–Si (980 cm^{-1}) and Si–C (715 cm^{-1}) [52]. This confirms the formation of SiOC ceramic material. Both signals disappear after chlorine gas treatment, related to the removal of Si atoms as SiCl₄ and the emergence of highly pure carbon, with hydroxyl groups bonded to the carbon, related to the broad peak at 3330 cm^{-1} . However, a broad and small peak can be seen at 980 cm^{-1} in the spectra of SiOC-CDC beads, confirming the incomplete transformation to CDC.

Raman spectroscopy allows to characterize the degree of ordering of the free carbon phase within in the SiOC matrix and the structure of SiOC-CDC. The measured spectra (Fig. 3b) showed two peaks characteristic for incompletely graphitized carbons, namely the D-mode between 1335 cm^{-1} and 1346 cm^{-1} and the G-mode between 1599 cm^{-1} and 1607 cm^{-1} . In addition, we see combination modes and overtones between 2500 cm^{-1} and 3000 cm^{-1} . D- and G-mode relate both to sp²-hybridized carbon; the G-mode is related to the bond stretching of pairs of sp²-hybridized carbon atoms in rings and chains [53], and the D-mode is due to the activation of the breathing modes of six carbon atoms rings when a defect is present [54]. The shift of the G peak from 1581 cm^{-1} for pure graphite to 1600 cm^{-1} is related to the coexistence of amorphous carbon (1550 cm^{-1}), nanocrystalline graphite, and sp²-hybridized carbon chains [54]. For the characterization of the D- and G-mode, a four peak Voigt fitting was applied (see ESI, Fig. S6) to

deconvolute the peaks related to amorphous carbon and *trans*-polyacetylene (TPA, between 1200 cm^{-1} and 1260 cm^{-1}), in addition to the dominant D- and G-mode. The combined data of the integral I_D/I_G ratio and full-width at half-maximum (FWHM) for SiOC and SiOC-CDC (Table 2) give information about the degree of carbon ordering. The free carbon in SiOC fibers and beads presents an in-plane correlation length L_a (often seen as domain or crystalline size) of 3.4 nm and 3.6 nm respectively, calculated by the Tuinstra-Koenig relation [55,56]. After chlorine gas treatment, a new carbon phase is formed. Considering the high chlorine gas treatment temperature (1200 °C), graphitization is promoted for the formed carbon phase and the already existing phase, meaning a lower presence of amorphous carbon but a smaller average in correlation length of the nanocrystalline carbon (L_a ca. 3.0 nm and 2.8 nm for fibers and beads respectively). This observation aligns well with the measured FWHM decrease for both modes.

X-ray diffraction (XRD) and TEM analysis allow to follow the structural transition from the amorphous as-spun fibers after thermal stabilization at 200 °C to the SiOC ceramic material with a highly disordered structure after pyrolysis to partially graphitic carbon (SiOC-CDC) after chlorine gas treatment (Fig. 4). Additionally, SEM allows us to observe the changes in the fiber morphology caused by the process. After the treatment of H44-26 at 200 °C , a partial melting was observed between the points of contact of the fibers (Fig. 4b), but the open percolated network and the characteristic fiber morphology was maintained. The open percolated morphology was also maintained after pyrolysis (Fig. 4c) and thermal chlorine gas treatment (Fig. 4d).

XRD pattern of the polymer H44-26 (Fig. 4a) allow to characterize the ladder structure of the polymer [57]. The peak at $8.4^\circ 2\theta$ indicates a plane-to-plane distance corresponding a chain-to-chain distance of $d_1 = 1.05\text{ nm}$. The peak at $19.7^\circ 2\theta$ represents a thickness of the molecular chains of $d_2 = 0.45\text{ nm}$ [57]. The XRD pattern of SiOC is typical for an amorphous material in agreement with TEM

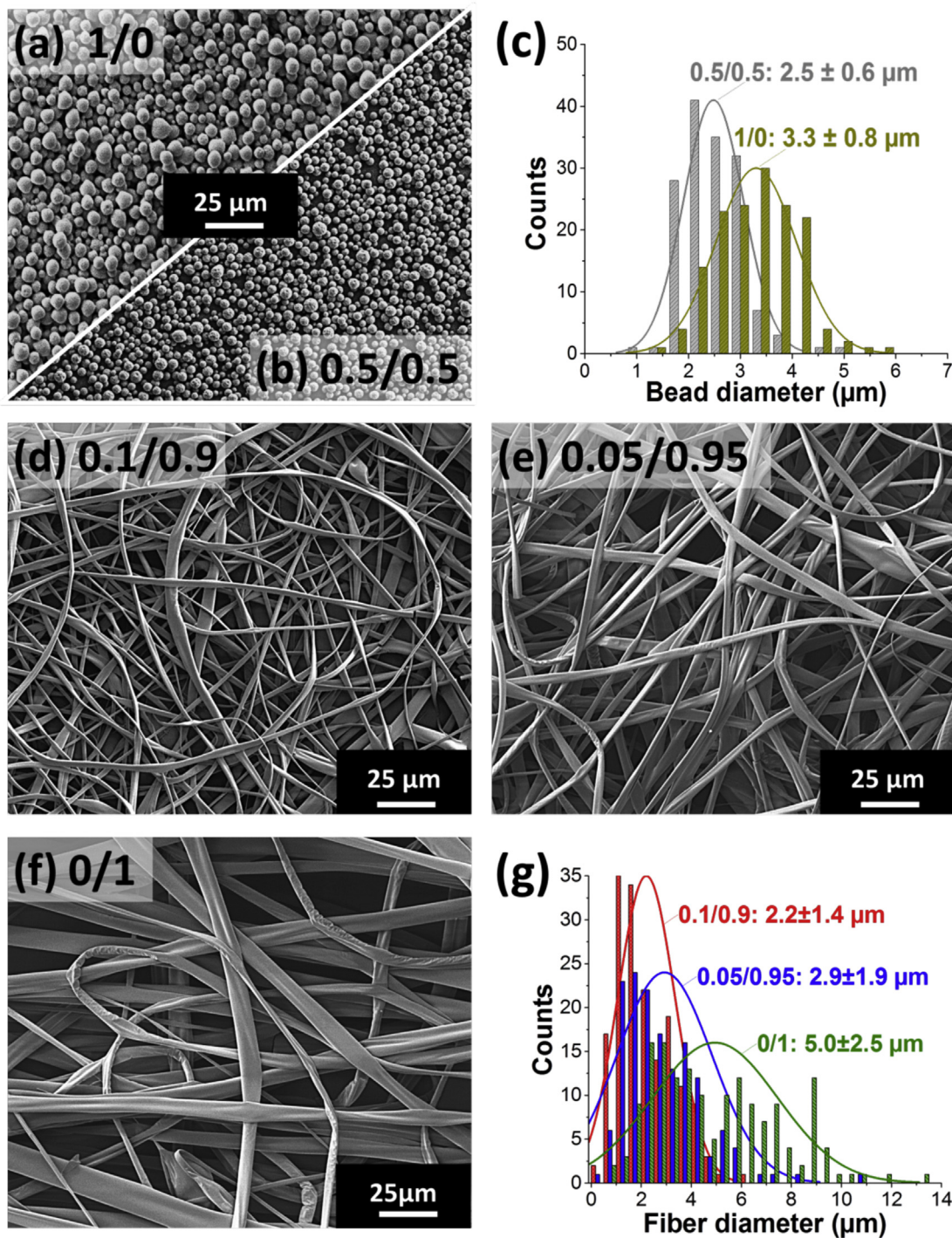


Fig. 2. SEM micrographs of H44-26 in DMF/EtOH at different mass ratios. Electrospun beads formed at ratios 1/0 (a) and 0.5/0.5 (b). Bead diameter distribution (c). Electrospun fibers/ribbons formed at ratios 0.1/0.9 (d), 0.05/0.95 (e) and 0/1 (f). Fiber diameter distribution of as spun fibers (g), the Gaussian lines are inserted to guide the eye.

Table 2

Overview of the results of the chemical composition determined by EDX, porosity data from gas sorption analysis using the BET equation, and structural data from Raman peak analysis.

Sample	Composition	BET SSA ($\text{m}^2 \cdot \text{g}^{-1}$)	I_D/I_G -ratio	FWHM D-mode (cm^{-1})	FWHM G-mode (cm^{-1})
SiOC fibers	$\text{SiO}_{1.6}\text{C}_{0.2} + 2.4 \text{C}_{\text{free}}$	11	1.46	169.1 ± 2.1	68.7 ± 0.8
SiOC beads	$\text{SiO}_{1.6}\text{C}_{0.2} + 2.3 \text{C}_{\text{free}}$	10	1.35	141.4 ± 2.3	65.0 ± 0.8
SiOC-CDC fibers	$\text{C} + 0.02 \text{O}$	3089	1.63	75.2 ± 0.8	59.5 ± 0.9
SiOC-CDC beads	$\text{C} + 0.02 \text{O} + 0.02 \text{Cl}$	2227	1.78	68.0 ± 0.7	65.8 ± 1.0

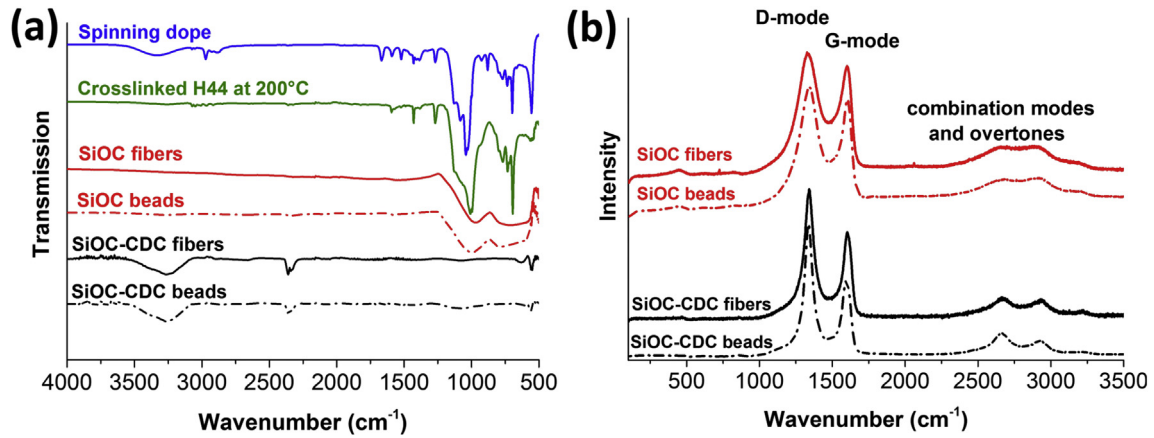


Fig. 3. Fourier transformed infrared (FTIR) spectra of spinning dope, crosslinked H44, SiOC and SiOC-CDC fibers and beads (a). Raman spectra of SiOC and SiOC-CDC fibers and beads (b).

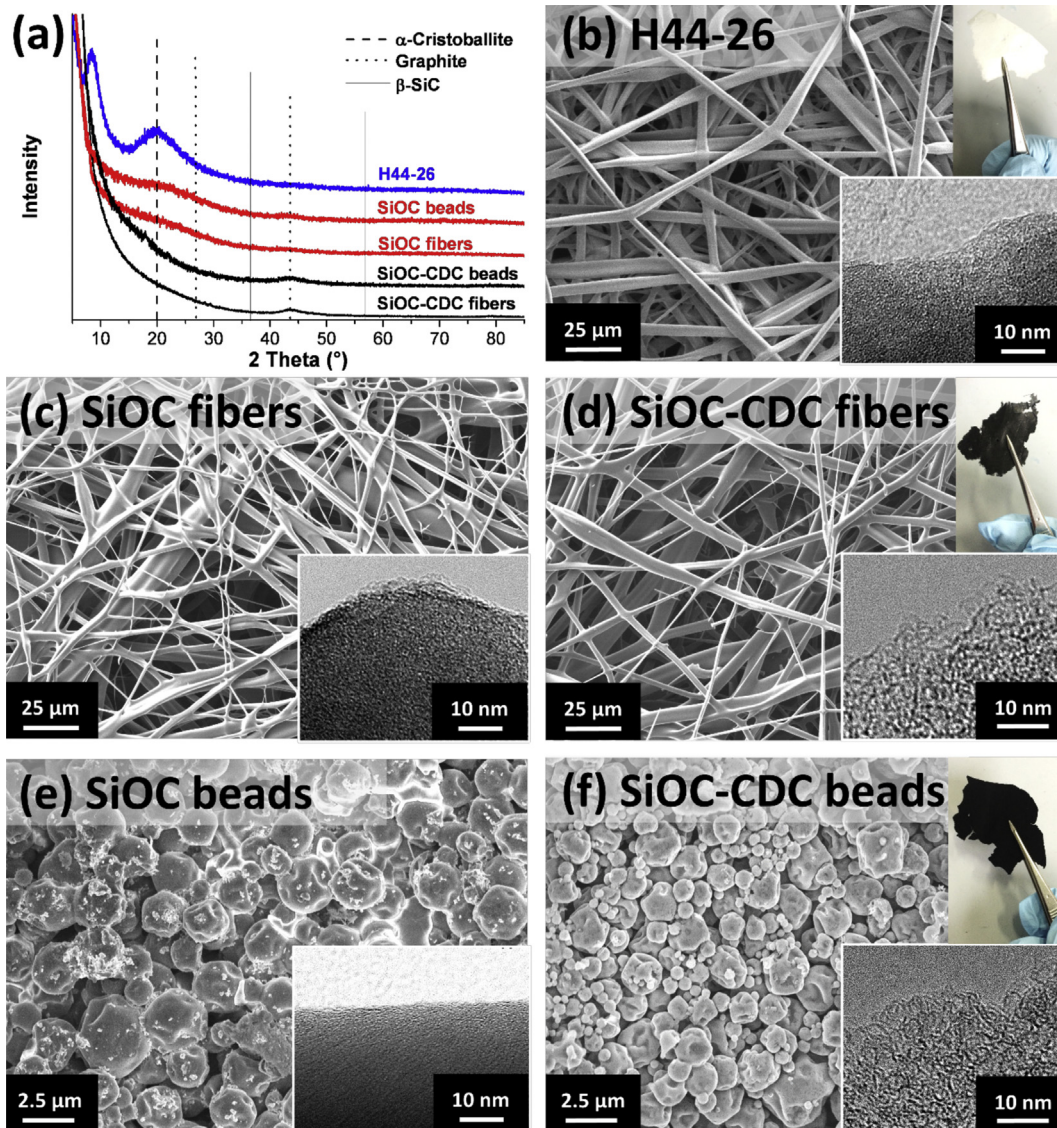


Fig. 4. (a) XRD patterns and SEM and TEM micrographs of polymer H44-26 (b), SiOC (c,e), and SiOC-CDC (d,f). The insets show digital photographs of the free-standing fiber mats before and after pyrolysis, and beads PTFE-bound electrode.

(Fig. 4c and e). For SiOC, no distinguishable peaks can be identified related to α -cristobalite or β -SiC due to highly disordered character of the material at such pyrolysis temperatures. After chlorine treatment, the decrease in density resulting from etching non-carbon species is evidenced by TEM micrographs (Fig. 4d and f). The XRD pattern for SiOC-CDC is characteristic of amorphous/disordered carbon with a distinguishable peak around $44^\circ 2\theta$ related to the (10)-reflection from the graphene layer plane [58]. Applying the Scherrer equation [59], the average in-plane coherence length is estimated to be around 3–4 nm for the SiOC-CDC fibers and beads, which is similar to the value obtained from the Raman spectra when applying the Tuinstra-Koenig equation [56]. The lack of a distinct (002)-graphite reflection at around $26^\circ 2\theta$ is related to a lack of stacking of the graphite layers or a high disorder of the stacking [58].

Furthermore, SiOC and SiOC-CDC samples were characterized by gas sorption analysis with N_2 and CO_2 for the determination of the pore structure (Fig. 5). According to the N_2 sorption isotherms (Fig. 5a), SiOC presents a Type II isotherm characteristic of nonporous solids [60]. After chlorine treatment, the material corresponds to a highly microporous material, characterized by a Type I(b) isotherm, presenting a broader range of micropores and narrow mesopores [60,61]. The pore size distribution of the material was characterized by N_2 gas sorption for pores of 0.9–35 nm and by CO_2 gas sorption for pores <0.9 nm. The cumulative pore volume increased from around $0.01 \text{ cm}^3 \text{ g}^{-1}$ for SiOC to $1.78 \text{ cm}^3 \text{ g}^{-1}$ and $1.41 \text{ cm}^3 \text{ g}^{-1}$ after chlorine gas treatment, for the fiber and beads respectively. The SiOC-CDC fibers present a very high BET specific surface area of $3089 \text{ m}^2 \text{ g}^{-1}$ (QSDFT: $2394 \text{ m}^2 \text{ g}^{-1}$), and the SiOC-CDC beads present a BET specific area of $2227 \text{ m}^2 \text{ g}^{-1}$ (QSDFT: $1679 \text{ m}^2 \text{ g}^{-1}$). Both SiOC-CDC presented similar average pore size (ca. 1.6 nm), but beads exhibit a lower cumulative pore volume and specific surface area considering the incomplete CDC transformation. The BET surface area of SiOC-CDC fibers belongs to the highest values reported for CDCs so far [14,29,62], currently only surpassed slightly by SiC-CDC of Rose et al. [23] (BET $3116 \text{ m}^2 \text{ g}^{-1}$).

3.3. Electrochemical performance of SiOC-CDC electrodes

The electrochemical performance of the SiOC-CDC electrodes was evaluated by cyclic voltammetry and galvanostatic cycling. By comparing different particle morphologies, we aim to establish a better understanding of the advantages of a continuous material network versus a non-continuous material for electrodes. We provide for the first time comparative data for SiOC-CDC fibers used as binder-free, free-standing electrode mats (Fig. 4d, inset) or as

PTFE-bound films using either SiOC-CDC beads (Fig. 4f, inset) or crushed fibers. The reported specific capacitance values are based only on the active material for a fair comparison between binder-free electrodes and PTFE-bound films.

Cyclic voltammograms of the half-cell setup recorded at 10 mV s^{-1} in 1 M TEA-BF₄ in ACN are shown in Fig. 6a and galvanostatic charge-discharge capacitance values vs. electrode potential (vs. carbon) are plotted in Fig. 6b. Negative or positive polarization led to a constant increase of the capacitance with electrode potential. This effect is well-known and related to the increase in density of states in the nanocrystalline graphite [63]. The increase corresponds to 175–200% of the value at 0 V and was observed in all electrodes. A higher capacitance was observed in half-cell setup for positive potentials related to difference in size of the anion and cation, leading to a higher confinement for BF₄⁻ than for TEA⁺ [64]. Using Eq. (1), a specific capacitance of 135 F g^{-1} or 110 F g^{-1} at 1 V vs. carbon was obtained for free-standing fiber mat and PTFE-bound beads, respectively. Using GCPL (Fig. 6b), the fibers electrodes present a specific capacitance at +1 V of 120 F g^{-1} (binder-free) and 114 F g^{-1} (PTFE-bound) compared to 112 F g^{-1} for SiOC-CDC beads. All these values fall within a $\pm 10\%$ range of statistical variation. Even though normalized to the mass of carbon (i.e., correcting for the binder-content), the PTFE-bound fiber electrode still shows a lower capacitance value. This can be explained by pore blocking due to the presence of binder compared to the binder-free free-standing fiber mat electrodes [5].

While the near-equilibrium performance (i.e., at low rate) of binder-free and binder-bound electrodes are very similar, the behavior is very different for the power handling ability. We already see the much faster response of the binder-free fiber electrode in the CV shown in Fig. 6a with the steep increase and weakly pronounced resistive knee at the vortex potentials. Furthermore, the impedance of the free-standing fiber mat is different from the PTFE-bound electrodes (Fig. 6c). The electrical serial resistance (ESR) of the fiber mat is $0.62 \Omega \text{ cm}^2$, which is smaller than for the PTFE-bound electrodes ($0.82 \Omega \text{ cm}^2$, Table 3). The difference in the ESR value is related to the lower internal resistance of the continuous fibers and a higher particle-particle contact resistance for the PTFE-bound electrodes. The electrical distribution resistance (EDR) is $0.09 \Omega \text{ cm}^2$ for the free standing fibers. This behavior changes for the PTFE-bound electrode, where the EDR is larger (0.17 and $0.15 \Omega \text{ cm}^2$, for fibers and beads, respectively) because of the higher particle packing and the larger diffusion length of ions. Regarding very low frequencies, the constant phase element (CPE) of the free standing fiber mat is more pronounced, having an exponent of 0.83 and we explain this by the very inhomogeneous thickness of the

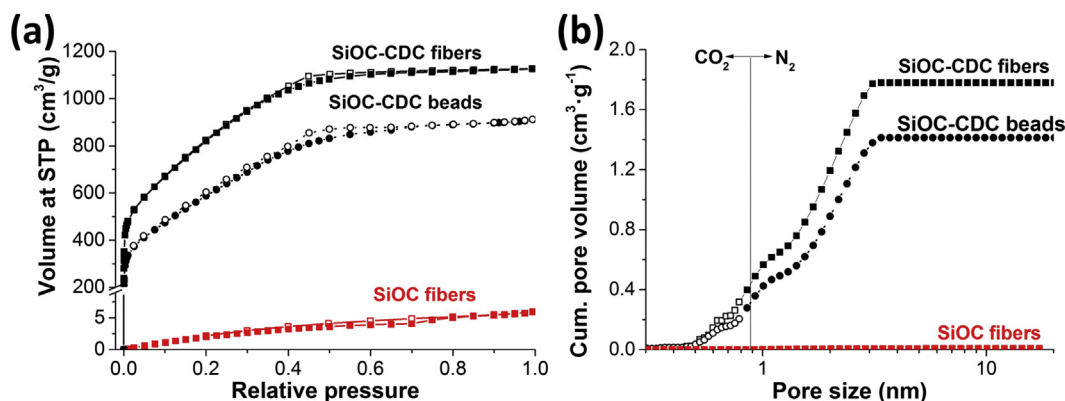


Fig. 5. (a) N_2 gas sorption isotherms for SiOC and SiOC-CDC fiber and beads. (b) Cumulative pore volume distribution using NLDFT and QSDFT models for CO_2 and N_2 adsorption, respectively.

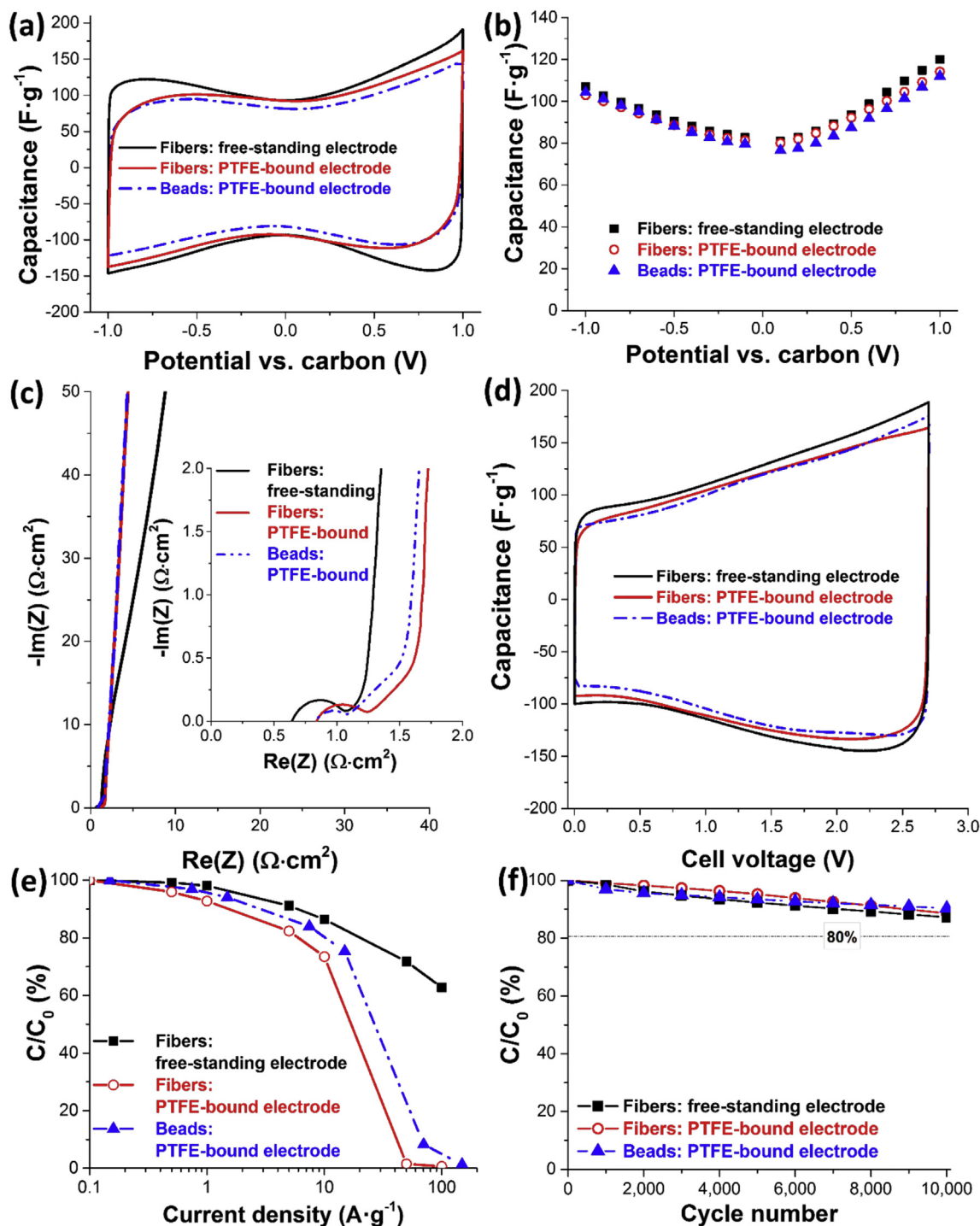


Fig. 6. Electrochemical performance of the free-standing SiOC-CDC fiber mat electrode and PTFE containing electrodes. (a) Cyclic voltammograms at 10 mV s⁻¹ and (b) specific capacitance by GCPL at 2 A g⁻¹ with a holding time of 10 min for half-cell configuration. (c) Nyquist plot (inset shows a zoomed range). (d) Cyclic voltammograms at 10 mV s⁻¹ for a full-cell. (e) Rate handing capability in full-cell by GCPL at 1 V. (f) Electrochemical performance stability surveyed by voltage sweeping up to a cell voltage of 2.7 V. The dashed line represents a capacitive fade of 20% (failure criterion in industry) and was not crossed by any material.

fiber mat in comparison to the homogeneously compacted and rolled particles in the PTFE-bound electrode [65]. The exponent of the CPE for the polymer-bound electrodes is very close to 1 related to an ideal capacitive behavior (Table 3).

When evaluating the rate capability for full-cell by GCPL between 0.1 A g⁻¹ to 100 A g⁻¹ a drastic difference between the electrodes is observed (Fig. 6e). At 10 A g⁻¹, the free-standing fiber

mat electrode retains 86% of the capacitance at 0.1 A g⁻¹, while the PTFE-containing electrodes retain 80% and 73% of the capacitance. At 100 A g⁻¹, the PTFE-containing electrodes had completely lost the capacitance, while the fiber mat was still able to maintain 63% of the initial.

When comparing SiOC-CDC fibers with and without binder, we see although using the same carbon with the same porosity, pore

Table 3

Equivalent distributed resistance (EDR), equivalent serial resistance (ESR) and the exponent of the constant phase element (CPE) of free-standing fiber electrode and PTFE-bound electrodes. Values were calculated from Nyquist plots.

Electrode	ESR ($\Omega \cdot \text{cm}^2$)	EDR ($\Omega \cdot \text{cm}^2$)	CPE exponent
Fibers: free-standing	0.62	0.09	0.83
Fibers: PTFE-bound	0.82	0.17	0.95
Beads: PTFE-bound	0.81	0.15	0.96

structure, and particle size, an enhanced power handling can only be capitalized in the case of a continuous carbon fiber network. When comparing the two binder-containing electrode systems, we found a lower rate handling ability for the fibers compared to the SiOC-CDC beads (Fig. 6e). This can be explained by the higher number of micropores found in SiOC-CDC fibers (i.e., inaccessible pores for ions), and also the better compaction of the beads compared to ground fibers. These considerations can also be seen for full-cell tests at 10 mV s^{-1} (Fig. 6d), where a specific capacitance of 130, 116, and 117 F g^{-1} (maximum value at 2.7 V: 188, 176, and 164 F g^{-1}) was obtained for the fiber mat, PTFE-bound beads, and PTFE-bound fibers, respectively. It can be seen that fibers and beads electrodes present similar capacitance values, showing that an enhanced porosity does not necessarily translate to an increased capacitance in organic media. Korenblit et al., for example, obtained larger capacitance values ($125\text{--}150 \text{ F g}^{-1}$) for SiC-CDC powder electrodes, which present a lower SSA value than the material synthesized in this work [62].

In the full-cell, all electrodes showed a good performance stability over 10,000 of charge/discharge cycles at 50 mV s^{-1} at 2.7 V (Fig. 6f). Within the scatter of the method, we cannot see a statistically significant difference between the electrode materials' cycling stability. All samples showed after 10,000 cycles a decrease of just ca. 11%. Yet, a comparison with the literature is difficult because the stability of SiOC-CDC powder electrodes in the same electrolyte had only been measured by voltage cycling at 2 V with a value of 95% after 10,000 cycles [29]. Considering slightly smaller values but after cycling to much higher cell voltages provides a positive perspective for the longevity of SiOC-CDC electrodes.

4. Conclusions

In our study we have presented a novel approach to produce ultrafine SiOC electrospun fibers without using any carrier polymer. This new approach, based on the pre-crosslinking of silicone resin, and utilization of a latent catalyst, resulted in the stabilization of the fiber shape prior to heat treatment at high temperatures. After pyrolysis at $1200 \text{ }^\circ\text{C}$, non-porous SiOC fibers were obtained. The material was evaluated as precursor for highly porous SiOC-CDC fibers, leading to partially graphitized carbon with average correlation length of ca. 3 nm and a BET specific surface area of $3089 \text{ m}^2 \text{ g}^{-1}$. Transitioning from electrospinning to electrospraying, SiOC-CDC beads were produced with a diameter of around $3 \mu\text{m}$. The beads, using the same chlorine gas treatment parameters as the fibers, showed a lower specific pore volume related to incomplete CDC transformation.

The synthesized fiber mats were evaluated as binder-free electrode for supercapacitors and compared to the performance of PTFE-bound electrodes composed of crushed fiber mats or beads. The specific capacitance was similar for the fibers with PTFE and for the bead electrodes but higher for the freestanding fiber mat. This is indicating the pore blocking effect by the polymer binder. The binder-free free-standing fiber mat presented a much higher power handling ability, retaining at 100 A g^{-1} still 63% of the capacitance at 0.1 A g^{-1} compared to an almost complete loss of the energy

storage ability of binder-containing electrode films at such high rates.

In all cases, the SiOC-beads, present similar electrochemical performance as the fibers, but a lower specific surface area. Obviously, an enhanced porosity does not necessarily translate to an increased capacitance in organic media when using nanoporous carbons with such a high specific surface area. These findings perfectly align with what has been shown by Barbieri et al. [66] The SiOC-CDC present a higher capacitance in organic electrolyte (135 F g^{-1} , Fig. 6a) compared to other metal carbide-derived carbon fibers synthesize (120 F g^{-1}) [22], and to other metal carbide-derived carbon powders ($100\text{--}130 \text{ F g}^{-1}$) [29,67,68].

Acknowledgments

The INM team acknowledges funding from the German Federal Ministry for Research and Education (BMBF) in support of the nanoEES^{3D} project (award number 03EK3013) as part of the strategic funding initiative energy storage framework. This work was supported by the CREATE-Network Project, Horizon 2020 of the European Commission (RISE Project No. 644013). C.V. gratefully acknowledges the support of TÜBITAK under the project Grant No: CAYDAG-113Y533. We acknowledge Robert Drumm for the TGA and DSC measurements of the latent catalysts. The authors thank Prof. Eduard Arzt (INM) for his continuing support.

Appendix A. Supplementary data

Supplementary data related to this article can be found at <http://dx.doi.org/10.1016/j.jpowsour.2016.02.077>.

References

- [1] P. Simon, Y. Gogotsi, *Nat. Mater.* 7 (2008) 845–854.
- [2] S. Zhang, N. Pan, *Adv. Energy Mater.* 5 (2015) 1401401.
- [3] M. Lu, F. Beguin, E. Frackowiak, *Supercapacitors: Materials, Systems and Applications*, Wiley-VCH, 2013.
- [4] N. Jäckel, D. Weingarth, M. Zeiger, M. Aslan, I. Grobelsek, V. Presser, *J. Power Sources* 272 (2014) 1122–1133.
- [5] M. Aslan, D. Weingarth, N. Jäckel, J.S. Atchison, I. Grobelsek, V. Presser, *J. Power Sources* 266 (2014) 374–383.
- [6] J. Che, P. Chen, M.B. Chan-Park, *J. Mater. Chem. A* 1 (2013) 4057–4066.
- [7] L.T. Le, M.H. Ervin, H. Qiu, B.E. Fuchs, W.Y. Lee, *Electrochem. Commun.* 13 (2011) 355–358.
- [8] B.-H. Kim, K.S. Yang, H.-G. Woo, K. Oshida, *Synth. Met.* 161 (2011) 1211–1216.
- [9] C. Tran, V. Kalra, *J. Power Sources* 235 (2013) 289–296.
- [10] M. Zeiger, D. Weingarth, V. Presser, *ChemElectroChem* 2 (2015) 1117–1127.
- [11] E. Frackowiak, *Phys. Chem. Chem. Phys.* 9 (2007) 1774–1785.
- [12] V. Presser, M. Heon, Y. Gogotsi, *Adv. Funct. Mater.* 21 (2011) 810–833.
- [13] W.A. Mohun, in: *Proceedings of the 4th Biennial Conference on Carbon Pergamon*, Oxford, 1959, pp. 443–453.
- [14] C. Vakifahmetoglu, V. Presser, S.-H. Yeon, P. Colombo, Y. Gogotsi, *Micropor. Mesopor. Mater.* 144 (2011) 105–112.
- [15] L. Borchardt, C. Hoffmann, M. Oschatz, L. Mammitzsch, U. Petasch, M. Herrmann, S. Kaskel, *Chem. Soc. Rev.* 41 (2012) 5053–5067.
- [16] J.K. Ewert, D. Weingarth, C. Denner, M. Friedrich, M. Zeiger, A. Schreiber, N. Jäckel, V. Presser, R. Kempe, *J. Mater. Chem. A* (2015) 18906–18912.
- [17] L. Borchardt, M. Oschatz, S. Kaskel, *Mater. Horizons* 1 (2014) 157–168.
- [18] W. Gu, G. Yushin, *Wiley Interdiscip. Rev. Energy Environ.* 3 (2014) 424–473.
- [19] S.R. Varanasi, S.K. Bhatia, *J. Phys. Chem. C* 119 (2015) 17573–17584.
- [20] P. Huang, M. Heon, D. Pech, M. Brunet, P.-L. Taberna, Y. Gogotsi, S. Lofland, J.D. Hettinger, P. Simon, *J. Power Sources* 225 (2013) 240–244.
- [21] M. Oschatz, M. Zeiger, N. Jäckel, P. Strubel, L. Borchardt, R. Reinhold, W. Nickel, J. Eckert, V. Presser, S. Kaskel, *J. Mater. Chem. A* 3 (2015) 17983–17990.
- [22] Y. Gao, V. Presser, L. Zhang, J.J. Niu, J.K. McDonough, C.R. Pérez, H. Lin, H. Fong, Y. Gogotsi, *J. Power Sources* 201 (2012) 368–375.
- [23] M. Rose, E. Kockrick, I. Senkovska, S. Kaskel, *Carbon* 48 (2010) 403–407.
- [24] C.R. Pérez, S.-H. Yeon, J. Ségalini, V. Presser, P.-L. Taberna, P. Simon, Y. Gogotsi, *Adv. Funct. Mater.* 23 (2013) 1081–1089.
- [25] T. Fey, B. Zierath, A.M. Kern, P. Greil, B.J.M. Etzold, *Carbon* 70 (2014) 30–37.
- [26] R.K. Dash, A. Nikitin, Y. Gogotsi, *Micropor. Mesopor. Mater.* 72 (2004) 203–208.
- [27] A. Jänes, T. Thomborg, E. Lust, *Carbon* 45 (2007) 2717–2722.
- [28] L.G.B. Camargo, B.G. Palazzo, G. Taylor, Z.A. Norris, Y.K. Patel, J.D. Hettinger, L. Yu, *J. Electrochem. Soc.* 162 (2015) H811–H815.

- [29] A. Meier, M. Weinberger, K. Pinkert, M. Oschatz, S. Paasch, L. Giebeler, H. Althues, E. Brunner, J. Eckert, S. Kaskel, *Micropor. Mesopor. Mater.* 188 (2014) 140–148.
- [30] J. Xu, R. Zhang, P. Chen, D. Shen, X. Ye, S. Ge, *Carbon* 64 (2013) 444–455.
- [31] J.S. Atchison, M. Zeiger, A. Tolosa, L.M. Funke, N. Jackel, V. Presser, *RSC Adv.* 5 (2015) 35683–35692.
- [32] J.R. Martin, L. Borchart, M. Oschatz, G. Mondin, S. Kaskel, *Chem. Ing. Tech.* 85 (2013) 1742–1748.
- [33] F.I. Hurwitz, L. Hyatt, J. Gorecki, L. D'Amore, in: 11th Annual Conference on Composites, Advanced Ceramics, and Composite Materials Cosponsored by the American Ceramic Society, DOD, and NASA, Cocoa Beach, Florida, 1987.
- [34] D.-S. Ruan, Y.-L. Li, L. Wang, D. Su, F. Hou, *J. Sol-Gel Sci. Technol.* 56 (2010) 184–190.
- [35] C. Vakifahmetoglu, *Adv. Appl. Ceram.* 110 (2011) 188–204.
- [36] S. Cavaliere, *Electrospinning nanofibers for low-temperature PEMFC*, in: *Electrospinning for Advanced Energy and Environmental Applications*, CRC Press, Taylor and Francis Group, 2015, pp. 37–38.
- [37] Y.E. Roginskaya, A.D. Shepelev, T.K. Tenchurin, E.D. Politova, B.A. Loginov, N.V. Kozlova, T.L. Kulova, A.M. Skundin, *Russ. J. Phys. Chem. A* 85 (2011) 2013–2019.
- [38] A. Guo, M. Roso, M. Modesti, J. Liu, P. Colombo, *J. Appl. Polym. Sci.* 131 (2014) 39836.
- [39] C.A. Schneider, W.S. Rasband, K.W. Eliceiri, *Nat. Methods* 9 (2012) 671–675.
- [40] S. Brunauer, P.H. Emmett, E. Teller, *J. Am. Chem. Soc.* 60 (1938) 309–319.
- [41] G.Y. Gor, M. Thommes, K.A. Cychoz, A.V. Neimark, *Carbon* 50 (2012) 1583–1590.
- [42] P.I. Ravikovitch, G.L. Haller, A.V. Neimark, *Adv. Colloid Interface Sci.* 76–77 (1998) 203–226.
- [43] A. Vishnyakov, P.I. Ravikovitch, A.V. Neimark, *Langmuir* 15 (1999) 8736–8742.
- [44] F. Wolff, C. Kugler, H. Münstedt, *Rheol. Acta* 51 (2012) 71–80.
- [45] J.D.B. Smith, *J. Appl. Polym. Sci.* 26 (1981) 979–986.
- [46] P.J. Flory, A. Vrij, *J. Am. Chem. Soc.* 85 (1963) 3548–3553.
- [47] A.B. Strong, *Fundamentals of Composites Manufacturing: Materials, Methods and Applications*, second ed., Society of Manufacturing Engineers, 2008.
- [48] S. Koombhongse, W. Liu, D.H. Reneker, *J. Polym. Sci. Part B Polym. Phys.* 39 (2001) 2598–2606.
- [49] B.P. Whim, P.G. Johnson, *Directory of Solvents*, Springer Netherlands, 2012.
- [50] P. Colombo, G. Mera, R. Riedel, G.D. Sorarù, *J. Am. Ceram. Soc.* 93 (7) (2010) 1805–1837.
- [51] G. Socrates, *Infrared and Raman Characteristic Group Frequencies: Tables and Charts*, Wiley, 2004.
- [52] T. Oh, C. Choi, *J. Korean Phys. Soc.* 56 (4) (2010) 1150–1155.
- [53] A.C. Ferrari, *Solid State Commun.* 143 (2007) 47–57.
- [54] A.C. Ferrari, D.M. Basko, *Nat. Nano* 8 (2013) 235–246.
- [55] G.A. Zickler, B. Smarsly, N. Gierlinger, H. Peterlik, O. Paris, *Carbon* 44 (2006) 3239–3246.
- [56] F. Tuinstra, J.L. Koenig, *J. Chem. Phys.* 53 (1970) 1126–1130.
- [57] L. Zhang, D. Dai, R. Zhang, *Polym. Adv. Technol.* 8 (1997) 662–665.
- [58] K. Faber, F. Badaczewski, M. Oschatz, G. Mondin, W. Nickel, S. Kaskel, B.M. Smarsly, *J. Phys. Chem. C* 118 (2014) 15705–15715.
- [59] P. Scherrer, *Nachrichten von der Gesellschaft der Wissenschaften zu Göttingen, Mathematisch-Physikalische Klasse*, 1918, pp. 98–100.
- [60] M. Thommes, K. Kaneko, A.V. Neimark, J.P. Olivier, F. Rodriguez-Reinoso, J. Rouquerol, K.S.W. Sing, in: I.D. Gruyter (Ed.), 2015.
- [61] P.B. Balbuena, K.E. Gubbins, *Langmuir* 9 (1993) 1801–1814.
- [62] Y. Korenblit, M. Rose, E. Kockrick, L. Borchart, A. Kvit, S. Kaskel, G. Yushin, *ACS Nano* 4 (2010) 1337–1344.
- [63] D. Weingarth, M. Zeiger, N. Jäckel, M. Aslan, G. Feng, V. Presser, *Adv. Energy Mater.* 4 (2014) 1400316.
- [64] J. Chmiola, C. Largeot, P.-L. Taberna, P. Simon, Y. Gogotsi, *Angew. Chem. Int. Ed.* 47 (2008) 3392–3395.
- [65] R. Kötz, M. Carlen, *Electrochim. Acta* 45 (2000) 2483–2498.
- [66] O. Barbieri, M. Hahn, A. Herzog, R. Kötz, *Carbon* 43 (2005) 1303–1310.
- [67] R. Dash, J. Chmiola, G. Yushin, Y. Gogotsi, G. Laudisio, J. Singer, J. Fischer, S. Kucheyev, *Carbon* 44 (2006) 2489–2497.
- [68] C. Portet, G. Yushin, Y. Gogotsi, *J. Electrochem. Soc.* 155 (2008) A531–A536.

3.2 Niobium carbide nanofibers as a versatile precursor for high power supercapacitor and high energy battery electrodes

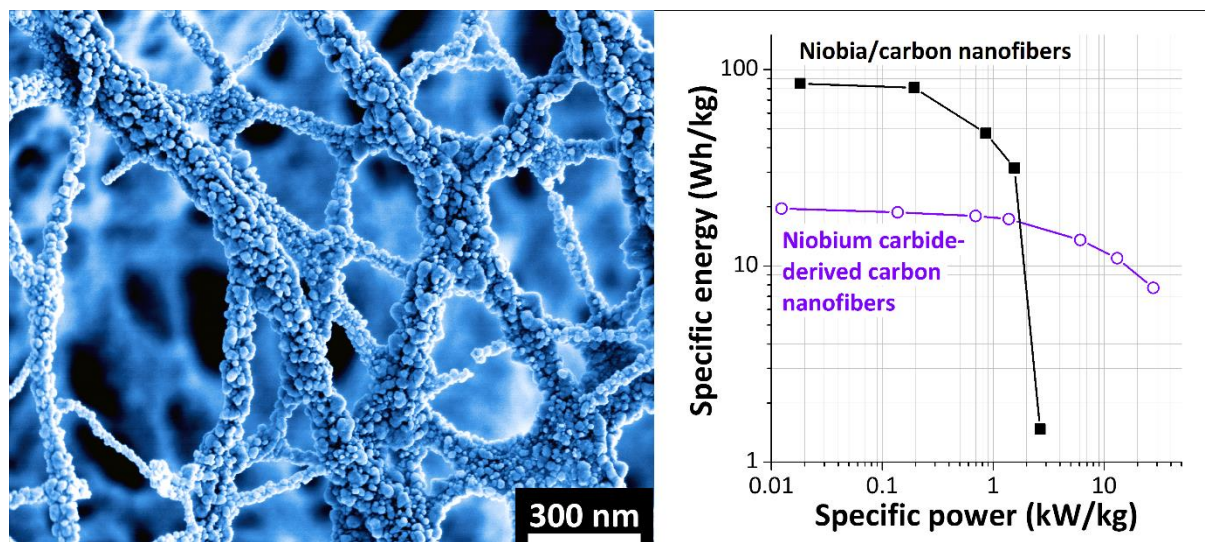
Aura Tolosa,^{a, b} Benjamin Krüner,^{a, b} Simon Fleischmann,^b Nicolas Jäckel,^{a, b}
Marco Zeiger,^{a, b} Mesut Aslan,^a Ingrid Grobelsek,^a and Volker Presser^{a, b}

^a INM - Leibniz Institute for New Materials, 66123 Saarbrücken, Germany

^b Department of Materials Science and Engineering, Saarland University, 66123 Saarbrücken, Germany

Published in: Journal of Materials Chemistry A, 4 (2016), 16003-16016

DOI: 10.1039/c6ta06224e



Own contribution: Project management; paper writing; material synthesis; data analysis; measurements: TEM, EDX, FT-IR, Raman spectroscopy (ex situ and in situ), electrochemical characterization

Cite this: *J. Mater. Chem. A*, 2016, 4, 16003

Niobium carbide nanofibers as a versatile precursor for high power supercapacitor and high energy battery electrodes†

Aura Tolosa,^{ab} Benjamin Krüner,^{ab} Simon Fleischmann,^b Nicolas Jäckel,^{ab} Marco Zeiger,^{ab} Mesut Aslan,^a Ingrid Grobelsek^a and Volker Presser^{*ab}

This study presents electrospun niobium carbide/carbon (NbC/C) hybrid nanofibers, with an average diameter of 69 ± 30 nm, as a facile precursor to derive either highly nanoporous niobium carbide-derived carbon (NbC–CDC) fibers for supercapacitor applications or niobium pentoxide/carbon (Nb₂O₅/C) hybrid fibers for battery-like energy storage. In all cases, the electrodes consist of binder-free and free-standing nanofiber mats that can be used without further conductive additives. Chlorine gas treatment conformally transforms NbC nanofiber mats into NbC–CDC fibers with a specific surface area of $1508 \text{ m}^2 \text{ g}^{-1}$. These nanofibers show a maximum specific energy of 19.5 W h kg^{-1} at low power and 7.6 W h kg^{-1} at a high specific power of 30 kW kg^{-1} in an organic electrolyte. CO₂ treatment transforms NbC into T-Nb₂O₅/C hybrid nanofiber mats that provide a maximum capacity of 156 mA h g^{-1} . The presence of graphitic carbon in the hybrid nanofibers enabled high power handling, maintaining 50% of the initial energy storage capacity at a high rate of 10 A g^{-1} (64 C-rate). When benchmarked for an asymmetric full-cell, a maximum specific energy of 86 W h kg^{-1} was obtained. The high specific power for both systems, NbC–CDC and T-Nb₂O₅/C, resulted from the excellent charge propagation in the continuous nanofiber network and the high graphitization of the carbon structure.

Received 22nd July 2016
Accepted 15th September 2016

DOI: 10.1039/c6ta06224e

www.rsc.org/MaterialsA

Introduction

Energy storage systems with high power and high energy ratings are in high demand for a variety of applications; ranging from mobile devices to power leveling for wind and solar energy installations.¹ In particular, electrochemical energy storage (EES) has emerged as a highly promising and efficient technology.² With EES, energy can be stored by several mechanisms, ranging from physical ion electrosorption (electrical double-layer capacitors, EDLCs, also known as supercapacitors) and fast surface redox processes to ion intercalation (batteries).^{3,4} The process of electrical double-

layer formation is a non-faradaic interface mechanism, enabling high specific power and long cycling lifetime, but rather low specific energy.⁵ Ion intercalation batteries accomplish charge storage and recovery by faradaic charge transfer between the electrolyte ions and the electrode materials.⁶ By this way, high specific energy can be obtained, while the cycling lifetime and power handling are limited by mechanical/structural degradation and diffusion processes through bulk materials.⁶ The ultimate goal is to achieve a combination of high power and high energy ratings. This is sought to be achieved by the development of hybrid technologies, such as lithium ion capacitors,⁷ and employment of rapid pseudocapacitive materials⁸ or redox-active electrolytes.^{9,10}

A particularly attractive group of electrode materials are binder-free and free standing fiber mats.^{11,12} The open-mesh percolated network and the possibility of creating a continuous active material are highly attractive to achieve an improved power performance. Commonly, different precursor materials and electrode architectures are employed when exploring supercapacitor or battery-like systems. The challenge is to satisfy the very different requirements for these two applications: (1) nanoporous carbon with a highly tailorable and controllable pore size distribution and (2) a redox-active material enabling, for example, rapid and reversible Li-ion intercalation.

Nanoporous carbon fibers have been extensively explored for supercapacitor applications, especially those derived from high

^aINM – Leibniz Institute for New Materials, 66123 Saarbrücken, Germany. E-mail: volker.presser@leibniz-inm.de

^bDepartment of Materials Science and Engineering, Saarland University, 66123 Saarbrücken, Germany

† Electronic supplementary information (ESI) available: Comprehensive Raman data (including peak deconvolution analysis), additional high resolution transmission and scanning electron micrographs, additional fiber diameter distribution analysis, additional gas sorption data, comprehensive data analysis (SEM, Raman, XRD, gas sorption analysis, and electrochemistry) for CDC materials obtained for 1 h of chlorine gas treatment (compared to 3 h in the manuscript), complementary thermogravimetric analysis and thermodynamic calculations with FACTSAGE, and additional electrochemical galvanostatic benchmarking of a half-cell and full-cell setup for the battery-system. See DOI: 10.1039/c6ta06224e



carbon yield polymers such as polyacrylonitrile (PAN) and polymer blends such as polyvinylpyrrolidone and methylacrylate as pore formers.¹³ To achieve a large surface area, physical or chemical activation of such PAN fibers can be employed.^{13,14} An alternative approach, which allows more control over the size and size distribution of nanopores, is the selective removal of metal atoms from metal carbide fibers.¹⁵ This can be done *via* thermal treatment with chlorine gas, yielding highly nanoporous carbon (carbide-derived carbon, CDC).¹⁶ So far, this approach has only been employed with electrospun fibers of TiC–CDC^{12,17} and SiC–CDC.^{18,19} More detailed work has been carried out on the synthesis of CDC powders, including systems such as NbC,²⁰ TiC,^{21,22} or B₄C,²³ with surface areas between 1000 and 3000 m² g⁻¹ and pore volumes between 0.5 and 2 cm³ g⁻¹.

Carbon hybrid fibers containing redox-active materials have been proposed for pseudocapacitors, redox-hybrids, and battery-like energy storage.^{24,25} Different approaches have been reported, including functionalization of carbon fibers with quinones,²⁶ coating with pseudocapacitive oxides (mainly MnO₂),^{27,28} and synthesis of composite fibers with RuO₂ or NiO.^{29,30} The hybridization of carbon and redox-active materials combines two synergetic aspects: the high electrical conductivity of carbon with the high faradaic charge storage capacity of redox-active materials. The latter often lack a good electron propagation ability, which makes the presence of a conductive phase mandatory in order to achieve a high power performance. A very promising metal oxide that has not been explored so far for carbon-hybrid fibers is niobium pentoxide (Nb₂O₅). Niobium pentoxide presents a high specific energy and power capability related to fast lithium ion intercalation within (110) or (001) planes, depending on the crystal phase.^{8,31,32} There are several Nb₂O₅ crystal phases based on octahedrally coordinated niobium atoms and the most common phases are TT-Nb₂O₅ (pseudohexagonal), T-Nb₂O₅ (orthorhombic), M-Nb₂O₅ (tetragonal), and H-Nb₂O₅ (monoclinic).³³ The monoclinic phase is the most thermodynamically stable (formed above 1000 °C), while the TT-phase is the least thermodynamically stable and is formed at lower temperatures (400–500 °C).³³

First studies showed that Nb₂O₅ presents Li-ion intercalation at a potential below 2.0 V *vs.* Li/Li⁺,³⁴ and it was initially explored as a cathode material in secondary lithium batteries using a Li-metal anode.³⁵ Different polymorphs have later been investigated as electrode materials not just for Li-ion batteries,³⁶ but also for carbon/Nb₂O₅ hybrid systems.^{8,37} It has been observed that the energy storage capacity of Nb₂O₅ for lithium-ion batteries highly depends on its crystalline structure; H-Nb₂O₅ shows the highest specific energy, delivering a second cycle discharge capacity of 242 mA h g⁻¹, compared to 152 mA h g⁻¹ for TT-Nb₂O₅.^{35,36} For battery-like systems, TT-, T- and M-Nb₂O₅ have been widely studied. T-Nb₂O₅ has shown superior power handling due to fast two dimensional Li⁺ transport within the crystal structure that causes no phase transition during the electrochemical reaction.^{8,37} So far, polymer-bound electrodes have been mainly produced by mixing Nb₂O₅ fibers,³⁶ nano-sheets,³⁸ and nanoparticles^{8,31} with conductive additives. Thin electrodes without conductive additives have also been explored

by direct drop casting of Nb₂O₅ nanoparticles on the current collector³² or from thin mesoporous films.³⁹ However, this approach remains limited with regards to scalability.

Our work presents, for the first time, electrospun NbC/C hybrid nanofibers as a versatile precursor to derive either (1) NbC–CDC nanofibers for high power, capacitive energy storage or (2) Nb₂O₅/C hybrid nanofibers for high energy, battery-like energy storage. We will first establish the synthesis process and optimum processing parameters, and then provide comprehensive material characterization. Supercapacitor performance was benchmarked in an organic electrolyte (1 M TEA-BF₄ in acetonitrile), and the battery-like system is investigated in 1 M LiClO₄ in ethylene carbonate/dimethyl carbonate electrolyte. The choice of different electrolytes was motivated by enabling high ion mobility for the supercapacitor system, while a large voltage stability window and lithium intercalation were needed for the battery-like system. A key feature of our system is the ability to directly use free-standing, binder-free nanofiber mats; hence, the need for a binder (*i.e.*, dead mass) is eliminated, the possible blocking of pores by the polymer binder is avoided, and an improved electrical conductivity of the electrode can be obtained, as shown in our recent study.¹⁸

Experimental description

Materials synthesis

Niobium carbide/carbon hybrid nanofibers were synthesized following a sol–gel synthesis, as described in our previous work.⁴⁰ Niobium *n*-butoxide (NbBO) (99% metal basis) was purchased from Alfa Aesar, while acetic anhydride (Ac₂O) (≥99% purity), anhydrous *N,N*-dimethylformamide (DMF) (99.8% purity), and polyvinylpyrrolidone (PVP) (*M_w* ≈ 1 300 000 g mol⁻¹) were purchased from Sigma Aldrich. The spinning dope was prepared by mixing 9 mass% NbBO and 2 mass% Ac₂O for 2 min. Then, 79 mass% of DMF (solvent) and 10 mass% of PVP (carrier polymer) were added. The spinning dope was stirred for 48 h prior to electrospinning, until a translucent solution was obtained. The fiber mats were produced by electrospinning in a MECC nanofiber system. The solution was pumped at 0.5 mL h⁻¹ through a spinneret (inner diameter: 400 μm), inductively charged at 23 kV. The fibers were collected at a distance of 165 mm from the spinneret. The humidity and the temperature were maintained between 10 and 20% and 25 and 30 °C.

Post spinning, the as-spun fibers were exposed at room humidity for 72 h, to promote further hydrolysis and condensation reactions. Annealing was performed under 99.5% argon in a graphite heated furnace, Thermal Technology. The fibers were heated at 5 °C min⁻¹ to 400 °C for 3 h, and then heated to 1500 or 1700 °C for 4 h for carbothermal reduction.

Synthesis of niobium carbide-derived carbon nanofibers. The NbC/C fibers pyrolyzed at 1500 °C (NbC-1500) were used for carbide-to-carbon conversion. Chlorine gas treatment was carried out in a quartz tube furnace (Gero HTRH) which was constantly purged with Ar (50 cm³ min⁻¹). NbC-1500 fibers were heated at 15 °C min⁻¹, until reaching the temperature of the treatment (400, 600, or 900 °C), and treated with Cl₂ for 1 or 3 h (flow rate: 10 cm³ min⁻¹). A post annealing process with



hydrogen gas ($10 \text{ cm}^3 \text{ min}^{-1}$) was applied at $600 \text{ }^\circ\text{C}$ for 3 h to remove residual chlorine species present in the sample. Then, the samples were cooled to room temperature.

Synthesis of niobium pentoxide–carbon hybrid nanofibers.

The NbC/C fibers pyrolyzed at $1700 \text{ }^\circ\text{C}$ (NbC-1700) were used for carbide-to-oxide conversion. Two different oxidative atmospheres were studied, CO_2 and air. NbC-1700 fibers were thermally annealed between 450 and $500 \text{ }^\circ\text{C}$ in a VG Scienta GP-CVD tube furnace under synthetic air (flow rate: $50 \text{ cm}^3 \text{ min}^{-1}$) at $5 \text{ }^\circ\text{C min}^{-1}$ for 3 h. Thermal annealing under CO_2 ($50 \text{ cm}^3 \text{ min}^{-1}$) was done at $850 \text{ }^\circ\text{C}$ in a Xerion XROTATE tube furnace at $5 \text{ }^\circ\text{C min}^{-1}$ for 1 h.

Materials characterization

Structural and chemical characterization. The morphology of the fibers was examined with a JEOL JSM 7500F field emission scanning electron microscope (SEM). All samples were fixed on steel sample holders with sticky carbon tape. The Nb_2O_5 containing fibers were coated prior to the imaging with a thin layer of platinum in a JEOL Autofine Coater. ImageJ software was used to process the SEM micrographs and diameters of at least 100 individual fibers were measured. For high resolution analysis of the fibers, a JEOL JEM-2100F high resolution transmission electron microscope (TEM) was employed at 200 kV. In the TEM, selected area electron diffraction (SAED) was carried out for the Nb_2O_5 containing fibers. TEM samples were prepared by sonicating the fibers in ethanol for 3 min, and drop casting them on a carbon film on a copper grid.

The composition of the fibers was determined by energy dispersive X-ray spectroscopy (EDX) using an X-Max-150 detector from Oxford Instruments attached to the SEM chamber. The spectra of 10 fibers were measured using an accelerating voltage of 10 kV, in uncoated fibers attached to a sticky carbon tape. A silicon standard was used for standardization.

XRD diffractograms were recorded with a Bruker D8 Discover diffractometer using $\text{Cu}_{K\alpha}$ radiation (0.154 nm ; without a monochromator) with a step size of 0.02° and a measurement time of 1–3 s per step. The system was calibrated with a corundum alumina standard. The samples were pestled and placed on a sapphire single crystal for the measurement. The full width at half maximum (FWHM) was measured by using EVA software from Bruker. The values of the average coherence length (roughly corresponding with the domain size) were obtained using the Scherrer equation.⁴¹

Raman spectra were recorded with an InVia Raman system, from Renishaw, using a laser with 532 nm excitation wavelength and 0.5 mW power on the sample with a spectral resolution of $ca. 1.2 \text{ cm}^{-1}$, using a $50\times$ objective (numeric aperture: 0.9). Peak analysis was performed by baseline correction and assuming four Voigt peak fittings between 500 and 2000 cm^{-1} . *In situ* Raman spectra were recorded during thermal treatment under synthetic air (heating rate $5 \text{ }^\circ\text{C min}^{-1}$) by using a temperature controlled Linkam T95-HT heating stage. A laser with 532 nm excitation wavelength was used, which exposed the sample to a power of 0.5 mW at the focal point.

Thermogravimetric analysis (TGA) was carried out in synthetic air or CO_2 with a heating rate of $5 \text{ }^\circ\text{C min}^{-1}$ with a TG 209 F1

Libra system (Netzsch). Nitrogen gas sorption measurements were carried out at $-196 \text{ }^\circ\text{C}$ with an Autosorb iQ system (Quantachrome), after outgassing at $300 \text{ }^\circ\text{C}$ for 10 h under vacuum conditions (about 10^2 Pa) to remove volatile surface functionalities present in the sample. The specific surface area (SSA) was calculated with the Quantachrome ASiQwin software using the Brunauer–Emmett–Teller (BET) equation⁴² in the linear relative pressure range of 0.05–0.2. Using the quenched-solid density functional theory (QSDFT),⁴³ the SSA and pore size distribution (PSD) were calculated assuming slit-shaped pores and pore sizes between 0.56 and 37.5 nm . The values of the total pore volume correspond to $p/p_0 = 0.95$. The values of the mean pore size are volume-weighted. Thermodynamic calculations were carried out with FactSage 7.0 (GTT-technologies).

Electrochemical measurements. Electrochemical measurements were carried out with a potentiostat/galvanostat (VSP300 from Bio-Logic), using cyclic voltammetry (CV) and galvanostatic cycling with potential limitation (GCPL). The electrodes were tested in custom-built polyether ether ketone (PEEK) cells with spring loaded titanium pistons as a three electrode system. 8 mm diameter working electrode discs ($1\text{--}2 \text{ mg}$, $80 \text{ }\mu\text{m}$ thickness) were punched out of the free-standing fiber mats. Activated carbon (type YP-50F, Kuraray Chemicals) with 5 mass% polytetrafluoroethylene (PTFE) films was used as a quasi-reference electrode.⁴⁴ Working and counter electrodes were separated by a 13 mm diameter glass-fiber separator (GF/D from Whatman) and placed between 12 mm diameter carbon-coated aluminum current collectors (Zflo 2653, Exopack technologies). After assembling, the cells were dried at 2 kPa , $120 \text{ }^\circ\text{C}$ for 12 h. After cooling down, the cells were placed in an argon glove box (MBraun Labmaster 130, O_2 and $\text{H}_2\text{O} < 1 \text{ ppm}$), and filled with the corresponding electrolyte.

For electrochemical characterization of electrical double-layer capacitor cells, the performance of NbC–CDC electrodes was characterized in half- and symmetric full-cell setups employing 1 M tetraethylammonium tetrafluoroborate (TEA-BF_4) in electrochemical grade acetonitrile (ACN) from BASF as the electrolyte. Half-cell tests were performed with an oversized activated carbon (AC) counter electrode (10 mm diameter, 15 mg mass; YP-80F from Kuraray Chemicals with 5 mass% PTFE). Symmetric full-cell tests used two NbC–CDC fiber electrodes of the same mass. CVs were recorded at 10 mV s^{-1} scan rate in the potential range from -1.0 V to $+1.0 \text{ V}$ vs. carbon in half-cells and from 0 to $+2.7 \text{ V}$ cell voltage for full-cells. Galvanostatic cycling for half-cells was carried out from -1.0 V to $+1.0 \text{ V}$ vs. carbon at 2 A g^{-1} with a holding time of 10 min. The specific capacitance (C_{sp}) was calculated by integrating the discharge current between t_0 , the discharge starting time, and t , the end time of discharge, divided by U (voltage vs. carbon or applied cell voltage, for half- and full-cells, respectively) via eqn (1).⁴⁵ m corresponds to the mass of the CDC electrode for the half-cells, and for the full-cells it corresponds to the mass of both electrodes divided by four.

$$C_{\text{sp}} = \frac{1}{m} \frac{\left(\int_{t_0}^t I dt \right)}{U} \quad (1)$$



Rate handling was quantified with the *IR* drop corrected voltage measured after 5 s resting time. Electrical impedance spectroscopy (EIS) was performed in the range of 100 kHz to 100 mHz at 0 V with 10 points per decade and averaged over 5 measurements. Performance stability tests were carried out in full-cells by galvanostatic cycling over 10 000 cycles to 2.5 V at 1 A g⁻¹.

For electrochemical characterization of battery-like cells, Nb₂O₅/C electrodes were characterized by using half- and asymmetric full-cell setups in 1 M lithium perchlorate (LiClO₄) in electrochemical grade ethylene carbonate (EC)/dimethyl carbonate (DMC) from Sigma-Aldrich (volume ratio 1 : 1). Half-cell tests were performed with an oversized AC counter electrode (10 mm diameter, 15 mg mass; YP-80F from Kuraray Chemicals with 5 mass% PTFE) and asymmetric full-cell tests by combining a Nb₂O₅/C hybrid electrode with an AC electrode (YP-80F with 5 mass% PTFE). Charge balancing for asymmetric full-cells was achieved by mass balancing, according to the capacity values obtained by half-cell measurements at 0.1 A g⁻¹. The lower gravimetric capacity of the AC electrode compared to the Nb₂O₅/C electrode was compensated by using electrodes with different masses. The mass of the AC electrode was between 1.5 and 2.5 times higher than the mass of the Nb₂O₅/C electrode. The cell voltage was chosen in order to achieve a maximum potential of -2.0 V vs. carbon at the negative electrode (Nb₂O₅/C). For Nb₂O₅/C fiber electrodes, CVs were recorded at 1 mV s⁻¹ scan rate in the potential range from 0 to -2.0 V vs. carbon in half-cells and from 0 to +3.6 V cell voltage in full-cells. Rate handling for half- and asymmetric full-cells was carried out by GCPL, using the same potential ranges, from 0.1 to 40 A g⁻¹ with a holding time of 10 min. Capacity (Q_{sp}) was calculated by integrating the discharge current between t_0 , the discharge starting time, and t , the end time of discharge, and normalized to the electrode mass, m , via eqn (2):

$$Q_{\text{sp}} = \frac{1}{m} \left(\int_{t_0}^t Idt \right) \quad (2)$$

Performance stability tests were carried out by galvanostatic cycling over 5000 cycles from 0 to -2.0 V vs. carbon and 3.0 V cell voltage at 1 A g⁻¹ for half- and asymmetric full-cells, respectively.

Data from the electrodes with the best electrochemical performance for electrical double-layer capacitors or battery-like systems are presented in a Ragone plot. Using GCPL data of full-cells (asymmetric and symmetric), specific energy (E_{sp}) and specific power (P_{sp}) were calculated, using eqn (3) and (4), respectively, with U and I as the voltage and current applied to the full-cell, and M corresponds to the mass of both electrodes (positive and negative electrodes).

$$E_{\text{sp}} = \frac{\left(\int_{t_0}^t Udt \cdot I \right)}{M} \quad (3)$$

$$P_{\text{sp}} = \frac{E_{\text{sp}}}{t - t_0} \quad (4)$$

Results and discussion

Niobium carbide/carbon hybrid nanofibers

We briefly outline the important aspects of NbC/C hybrid nanofiber synthesis, which can be found in more detail in our previous work.⁴⁰ Using NbBO as the sol-gel precursor and PVP as the carrier polymer, we have established a facile synthesis route for hybrid nanofibers with an average fiber diameter of 69 ± 30 nm. This approach employs electrospinning to obtain free-standing fiber mats, and thermal treatment yielding NbC/C hybrid nanofibers *via* carbothermal reduction. The fibers synthesized at 1700 °C (NbC-1700) presented a higher crystallinity when compared to the fibers synthesized at 1500 °C (NbC-1500), with an NbC average domain size (*i.e.*, XRD coherence length) of 65 nm compared to 38 nm, respectively.⁴⁰ Also, at a higher pyrolysis temperature, carbon presented a higher degree of graphitization (see ESI, Fig. S1†). NbC/C fibers were later evaluated as a versatile precursor to derive (1) NbC-CDC nanofibers and (2) Nb₂O₅/C hybrid nanofibers. To promote the carbide-to-carbon conversion, a lower degree of carbon ordering is preferred.²² The graphitic carbon engulfing the metal carbide crystals affects the reaction kinetics between Cl₂ and the NbC; therefore, longer Cl₂ treatment durations or higher synthesis temperatures will be needed for complete etching. To promote the carbide-to-oxide conversion without a complete loss of carbon, a higher degree of carbon ordering is desirable due to the higher stability in oxidizing atmospheres.²² Therefore, NbC-1500 was chosen as the precursor for NbC-CDC, and NbC-1700 was preferable as the precursor for Nb₂O₅/C hybrid nanofibers.

Niobium carbide-derived carbon nanofibers

Material characterization. NbC-1500 fibers were treated with chlorine gas at different temperatures and holding times. After Cl₂ treatment, a mass loss between 72 and 79 mass% was obtained, leaving behind mainly carbon. According to the EDX results (see ESI, Table S1†), the starting precursor (NbC-1500) contained about 74 mass% of niobium, which, after Cl₂ treatment, was almost completely removed (<1 mass%). The remaining niobium may be present as NbCl₅ trapped in the carbon structure or as very small residual NbC domains (*ca.* 2 nm), as shown by TEM micrographs at a few positions throughout the samples (see ESI, Fig. S2A†).

No influence on the morphology is observed as a function of the heat treatment parameters. The SEM micrographs of fibers treated for 3 h (Fig. 1) and 1 h (see ESI, Fig. S3†) show a mean fiber diameter of around 61 ± 22 nm (see ESI, Fig. S2B†). The conformal etching process during the CDC transformation is not expected to modify the macroscopic structure of the material, but rather the nanoporosity of the material (Fig. 1, inset).¹⁶ The TEM micrograph of the sample after 3 h holding time at 400 °C shows mesopores, which at higher temperatures become more organized, leading to a more densified fiber structure.

A better understanding of the influence of the treatment conditions on the carbon structure is achieved by the analysis of the Raman spectra and XRD patterns (Fig. 2). The data of samples treated for 1 h are presented in the ESI (see Fig. S4†).



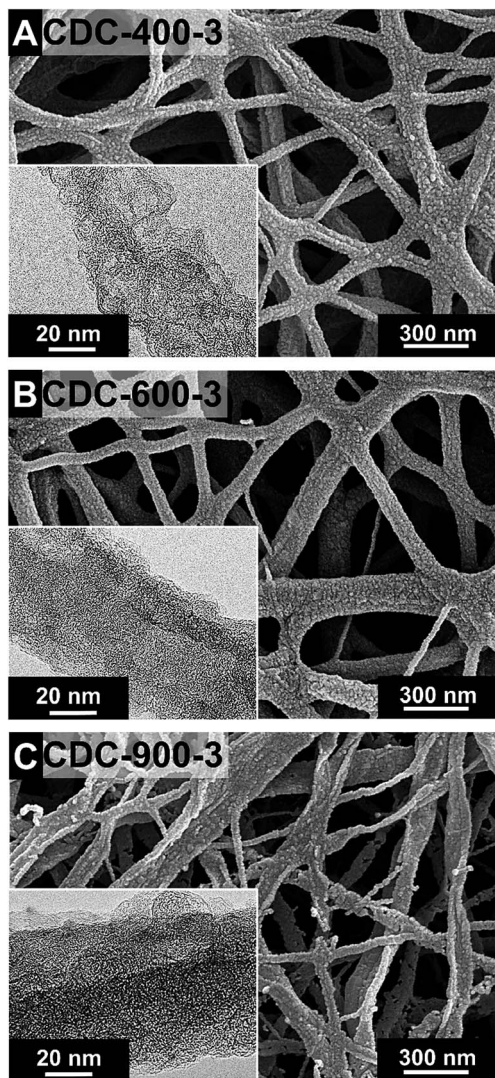


Fig. 1 SEM and TEM micrographs (inset) of NbC–CDC fibers synthesized by chlorine gas treatment for 3 h at (A) 400 °C, (B) 600 °C, and (C) 900 °C.

To understand these data, we have to consider the presence of two different carbon species: (1) carbon formed during pyrolysis at 1500 °C and present in NbC/C hybrid nanofibers and (2) carbide-derived carbon formed between 400 and 900 °C *via* chlorine gas treatment of NbC nanocrystals. The latter co-exists in NbC–CDC nanofibers in addition to the carbon formed at 1500 °C, because the CDC synthesis process does not remove initially formed carbon.⁴⁶ All Raman spectra (Fig. 2A) present two characteristic peaks for sp^2 -hybridized carbon, the D- and G-modes at around 1340 and 1600 cm^{-1} related to sp^2 -hybridized carbon atoms in rings and the presence of defects in this structure.⁴⁶ Additionally, we see the corresponding combination and overtone modes between 2500 and 3500 cm^{-1} . The position of the G-mode is shifted from 1603 to 1597 cm^{-1} when increasing the synthesis temperature from 400 °C to 900 °C, due to the successive transformation from nanocrystalline into larger graphitic structures.⁴⁶ This graphitization correlates well

with the decrease in the intensity of the amorphous carbon phase (1500–1550 cm^{-1}) with increasing temperature.^{46,47}

For the analysis of the different carbon phases, a four Voigt peak deconvolution was applied to the Raman data (see ESI, Fig. S5†). At 400 °C the I_D/I_G ratio (*i.e.*, the intensity ratio of the D- and G-mode peaks) is similar to that of the precursor (see ESI, Table S2†). At this temperature graphitic carbon, preserved from NbC-1500, co-exists with new partially amorphous/nanocrystalline CDC. At 600 °C, the grain size of nanocrystalline CDC increases proportionally to the defect concentration in hexagonal carbon rings (higher I_D/I_G ratio).⁴⁶ By treatment at 900 °C, the domains exceed a specific size (around 2 nm),⁴⁶ leading to graphitic carbon with less defects (lower I_D/I_G ratio). The successive transformation from amorphous into graphitic carbon is further supported by the sharpening of the D-mode FWHM from 96.2 ± 0.8 cm^{-1} to 82.8 ± 3.6 cm^{-1} when increasing the synthesis temperature from 400 to 900 °C.

XRD data (Fig. 2B) corroborate the transformation of $Fm\bar{3}m$ niobium carbide after chlorine gas treatment into amorphous carbon at 400 °C. While all crystalline niobium carbide peaks vanish, we observed a sharp (002)-graphite reflection ($P6_3mc$) at around $26.5^\circ 2\theta$ at 400 °C corresponding to the graphitic carbon present in the precursor. When increasing the temperature, two broad peaks are observed at around 26.5 and $44^\circ 2\theta$ related to the (002) and (110)-graphite reflections,⁴⁸ related to the transformation of the formed amorphous or nanocrystalline phase into graphitic carbon.

The pore structure of the material was analyzed before and after Cl_2 treatment by nitrogen gas sorption analysis (Fig. 2C and D). NbC-1500 presents a type I(b) isotherm,⁴⁹ with mainly micropores with an average size of 1.2 nm. With non-porous NbC nanocrystals, this porosity is completely accomplished by microporous carbon in the hybrid nanofibers. After Cl_2 treatment, the surface area is drastically increased from 120 $m^2 g^{-1}$ to maximum 1370 $m^2 g^{-1}$ (DFT SSA) and the pore volume from 0.06 $cm^3 g^{-1}$ to 1.0 $cm^3 g^{-1}$ (Table 1). The removal of Nb from the NbC crystal lattice at 400 °C for 1 h led to the formation of micro- and meso-pores (below 3 nm; see ESI, Fig. S4D†), with a mean pore size of 1.8 nm. At 600 °C for 1 h, more micropores are formed (below 2 nm), related to a higher amount of Nb etching compared to that at 400 °C, and a mean pore size of 1.1 nm was obtained. At a higher temperature (900 °C for 1 h) the redistribution of carbon slightly increases the mean pore size (1.2 nm). The isotherms after treatment for 1 h correspond to a type I(b) isotherm, with mainly micropores (see ESI, Fig. S4C†).⁴⁹ When increasing the time to 3 h, all the isotherms become type II because of pore growth, while maintaining a type I(b) shape at low pressures. The change to the type II isotherm comes with an H4 hysteresis loop related to capillary condensation⁴⁹ and a broader distribution of mesopores. The increase in the pore size when increasing the synthesis time leads to a decrease in the surface area and an increase in the pore volume (Table 1).

Electrochemical performance. For electrochemical evaluation of CDC nanofibers (treated for 3 h), a half-cell setup was initially used. For comparison, the electrochemical performance of samples treated for 1 h is presented in the ESI (Fig. S6†). The measured cyclic voltammograms (Fig. 3A) show the overall



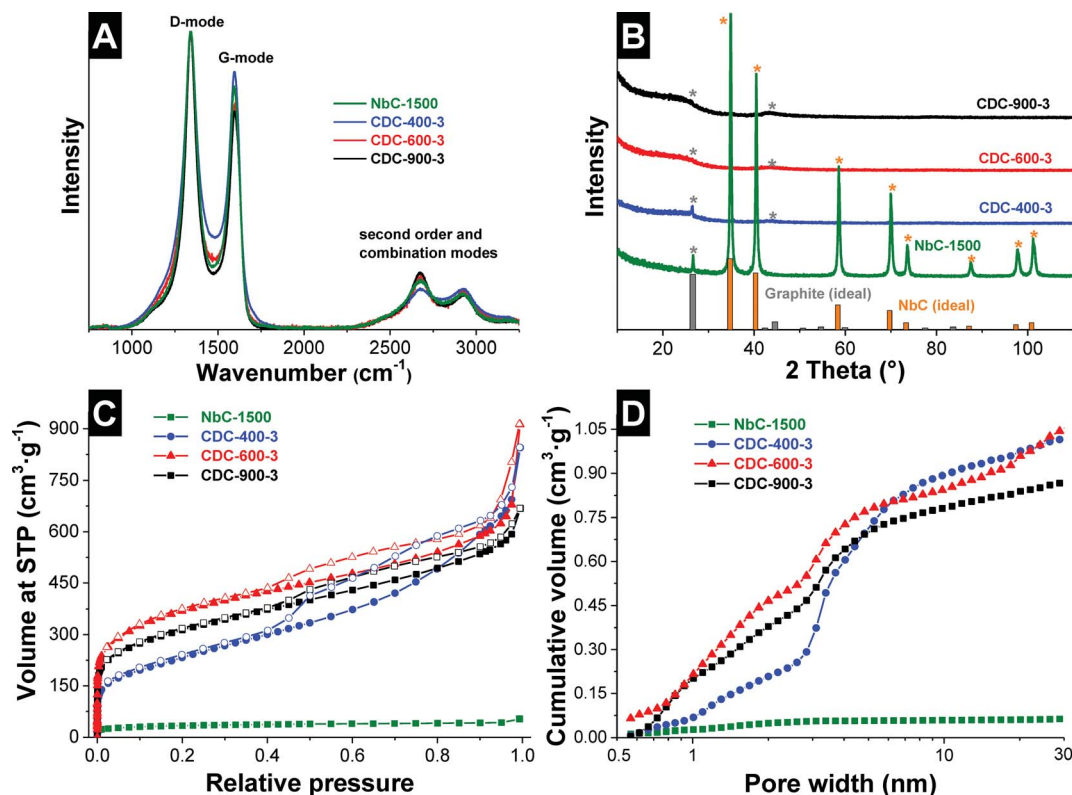


Fig. 2 Structural characterization of NbC-1500 fibers before and after chlorine treatment for 3 h. (A) Raman spectra, (B) XRD diffractograms and literature values of the diffraction peak positions of NbC (PDF: 38-1364) and graphite (PDF: 89-8487), (C) isotherms from nitrogen gas sorption at $-196\text{ }^{\circ}\text{C}$ (STP: standard temperature pressure), and (D) cumulative pore volume as a function of the pore width from QSDFT deconvolution.

rectangular shape, which is characteristic of electric double-layer capacitance.⁵ We also see an increase of the capacitance when the voltage is increased. This well-known effect is related to electrochemical doping.⁵⁰ The data presented in Fig. 3B depict the difference in specific capacitance at positive or negative polarization, that is, anion or cation electrosorption. For example, it is observed that for CDC-600-1 the capacitance at negative and positive polarization corresponds to 87 and 108 F g^{-1} , respectively (see ESI, Fig. S6B[†]). By treatment at 600 $^{\circ}\text{C}$ for 3 h, capacitance values of 102 and 115 F g^{-1} were achieved at negative and positive polarization. The lower capacitance values at negative voltage relate to the larger size of TEA^{+} compared to BF_4^{-} .^{51,52}

Full-cell performance was evaluated by cyclic voltammetry and galvanostatic cycling. The CVs (Fig. 3C) present a typical rectangular shape, with a typical increase in the capacitance

when increasing the applied voltage. At 2.7 V, maximum values are achieved between 90 and 125 F g^{-1} . Rate handling for full-cells was characterized by galvanostatic cycling to 2.5 V cell voltage. At a specific current of 0.02 A g^{-1} , capacitance values between 64 and 83 F g^{-1} were obtained for the samples with the lowest SSA (CDC-400-3 and CDC-900-3) (Table 2). The highest capacitance was achieved for the samples synthesized at 600 $^{\circ}\text{C}$ (101–108 F g^{-1} for 1–3 h of chlorine gas treatment; see Fig. 3D and Table 2). When increasing the specific current to 0.1 A g^{-1} , most of the samples present a decrease in capacitance between 10 and 20%. CDC-900-3, which presents a larger mean pore size (2.6 nm), maintained at 0.1 A g^{-1} 97% of the capacitance at 0.02 A g^{-1} . At a very high specific current of 40 A g^{-1} , all samples retained still between 44 and 56% of the initial capacitance. Compared to other CDC materials, the

Table 1 Results from the gas sorption analysis using nitrogen at $-196\text{ }^{\circ}\text{C}$

Sample	DFT SSA ($\text{m}^2\text{ g}^{-1}$)	BET SSA ($\text{m}^2\text{ g}^{-1}$)	Pore volume ($\text{cm}^3\text{ g}^{-1}$)	Mean pore size (nm)
NbC-1500	122	121	0.06	1.2
CDC-400-1	1065	1141	0.78	1.8
CDC-400-3	744	750	1.00	3.5
CDC-600-1	1369	1508	0.80	1.1
CDC-600-3	1207	1326	0.96	2.4
CDC-900-1	1092	1123	0.63	1.2
CDC-900-3	980	1122	0.87	2.6



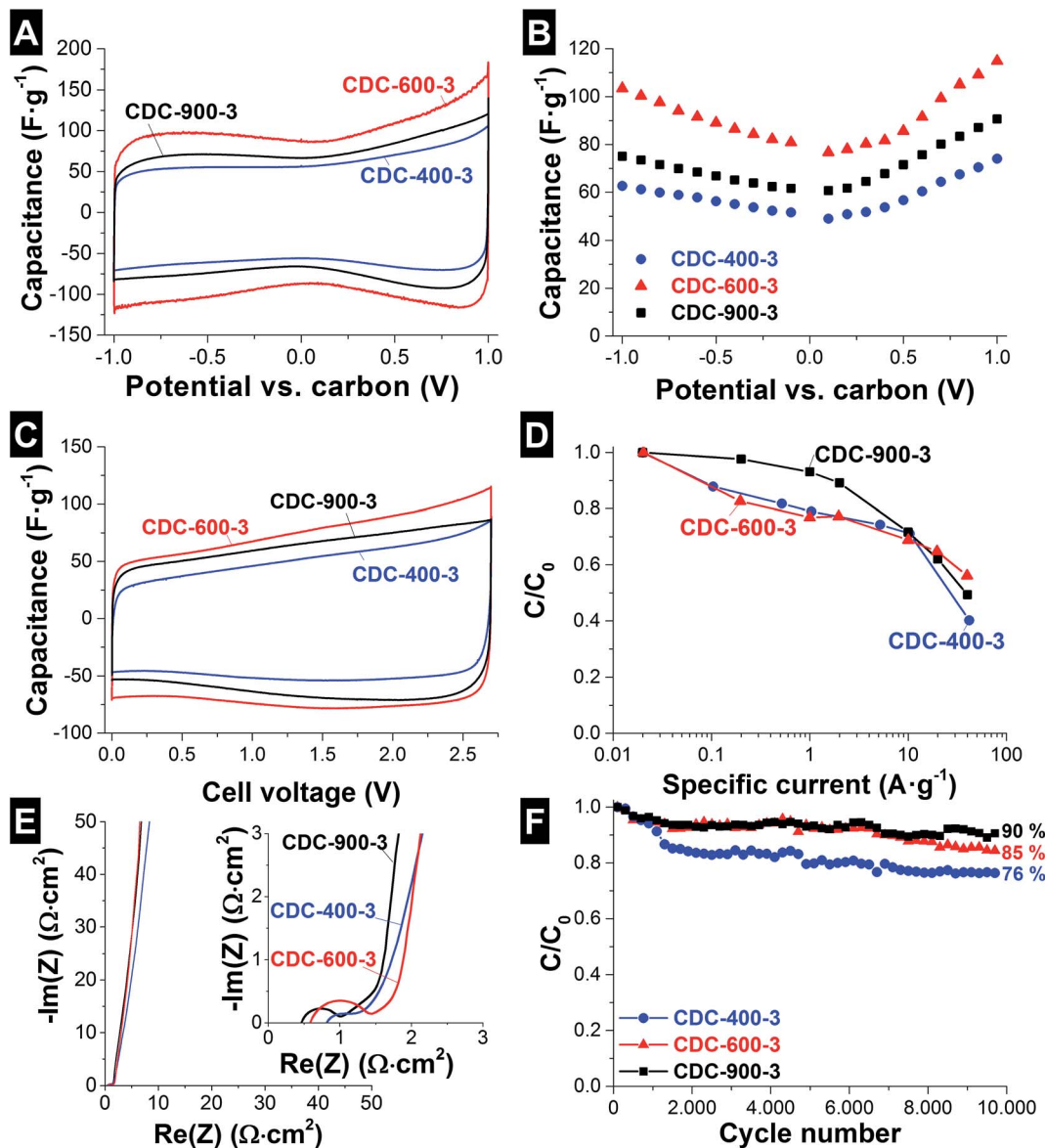


Fig. 3 Electrochemical analysis of CDC nanofiber mats in 1 M TEA-BF₄ in acetonitrile. Half-cell measurements with (A) cyclic voltammetry at 10 mV s⁻¹ and (B) GCPL profiles at 2 A g⁻¹. Full-cell measurements using (C) cyclic voltammetry at 10 mV s⁻¹, (D) GCPL power handling between 0.02 and 40 A g⁻¹ (d), (E) electrochemical impedance spectra, and (F) galvanostatic cycling stability up to 2.5 V cell voltage at 1 A g⁻¹.

electrochemical performance and energy storage capacity of NbC-CDC-600 in an organic electrolyte are good, as seen from Table 3. Compared to commercial electrodes (AC + 5% PTFE), NbC-CDC-600 presents similar capacitance values (104 F g⁻¹), but a superior capacitance retention above 10 A g⁻¹ related to the excellent charge propagation in the continuous fiber network.

To further characterize the electrochemical behavior, impedance spectroscopy (EIS) was carried out for full-cells (Fig. 3E). As seen from the inset in Fig. 3E, the evolving semi-circle correlates with a high contact resistance between the fibers and the current collector. Compared to free-standing polymer-bound carbon electrodes, fiber electrodes are less smooth at the interface with the current collector, which is why

an additional contact impedance arises.^{18,53} At very low frequencies, the constant phase element (CPE) is close to 1 with values from 0.89 to 0.97 indicative of a near-ideal capacitive behavior (Table 2).⁵³ Furthermore a direct correlation between the degree of carbon ordering, the pore structure, and the rate handling performance (Table 2) is observed. The samples with the highest degree of carbon ordering lead to the lowest equivalent serial resistance (ESR), namely the samples CL₂ treated at higher temperatures and times, CDC-600-3, CDC-900-1 and CDC-900-3 (43–53 Ω cm²).

The stability of the system was benchmarked by galvanostatic cycling (Table 2). Most of the samples retain more than 80% of the initial capacitance after 10 000 charge/discharge cycles. The only exception is CDC-400-3 with a capacitance loss



Table 2 Electrochemical performance of NbC-CDC fibers

Sample	ESR ($\Omega \text{ cm}^2$)	EDR ($\Omega \text{ cm}^2$)	CPE exponent	C (F g^{-1}) at 0.02 A g^{-1}	C loss (%) at 40 A g^{-1}	C/C_0 (%) after 10 000 cycles
CDC-400-1	0.89	0.16	0.95	97	68	85
CDC-400-3	0.73	0.28	0.89	64	60	76
CDC-600-1	0.78	0.18	0.93	101	80	91
CDC-600-3	0.53	0.45	0.94	108	44	85
CDC-900-1	0.47	0.21	0.96	85	56	92
CDC-900-3	0.43	0.49	0.97	83	50	90

of 24%. The highest capacitance retention was found for CDC-600-1 (91%) and CDC-900-1 or CDC-900-3 (90–92%). This enhanced stability may be related to the lower content of oxygen containing functional groups (Table S1†).

Niobium pentoxide–carbon hybrid nanofibers

Material characterization. For the synthesis of $\text{Nb}_2\text{O}_5/\text{C}$ hybrid nanofibers, starting from NbC-1700, first suitable synthesis conditions (atmosphere, temperature, and time) were surveyed by TGA and *in situ* Raman spectroscopy (see ESI, Fig. S7A and B†). Thermodynamic calculations (see ESI, Fig. S7C and D†) indicate that Nb_2O_5 is the stable metal oxide phase within the entire studied temperature range (*i.e.*, up to 1000 °C) in either CO_2 or O_2 atmospheres. Depending on the degree of ordering, we expect for nanoporous carbon an onset of oxidation at around 400–650 °C.²² From the literature, we would expect an initial onset of NbC oxidation at around 450 °C in O_2 .⁵⁴ Thus, the challenge is to find suitable conditions at which NbC is effectively oxidized to Nb_2O_5 without completely oxidizing solid carbon.

To identify the most suitable processing parameters, we employed thermogravimetric analysis. In CO_2 at 5 °C min^{-1} , we see an onset of mass increase at 720 °C, reaching a maximum at 950 °C (+12%). Further temperature increase resulted in a progressing mass loss associated with the burn-off of carbon. In this range of temperatures, T- Nb_2O_5 formation is expected^{36,55} as the only crystalline phase in co-existence with carbon. Therefore, 850 °C was selected as the preferred temperature for treatment under CO_2 to produce the hybrid material.

Using synthetic air, the volatilization of carbon occurs at lower temperatures, at around 500 °C (see ESI, Fig. S7A†), and at

similar temperatures to that of the carbide oxidation, at around 450 °C. At 410 °C, the mass of the system increases related to oxidation of the NbC, reaching a maximum at 460 °C (+20%). At higher temperatures, carbon burning takes place (TGA derivate peak, 590 °C) leading to mass decrease. In alignment with these data and the literature, the only expected crystalline phase in this temperature range is TT- Nb_2O_5 .^{36,55} For a better identification of an optimum temperature for the treatment in air, we carried out *in situ* Raman measurements (see ESI, Fig. S7B†). *In situ* Raman spectra show the emergence of niobia-related signals (646 to 670 cm^{-1})⁵⁶ for temperatures above 600 °C and the decrease in carbon signal intensities for the D- and G-mode peaks at 1323 and 1575 cm^{-1} , respectively. To avoid the enhanced loss of carbon, lower synthesis temperatures in air were chosen, namely 450 °C and 500 °C.

After treatment under CO_2 (850 °C) or air (450 and 500 °C), the sample mass increased between 7 and 38% (Table 4). Yet, the nanofiber morphology was fully maintained, as seen from the SEM micrographs in Fig. 4. Image analysis documents an increase in the average fiber diameter by 55% ($87 \pm 25 \text{ nm}$; see ESI, Fig. S8†), related to the difference in density between NbC and Nb_2O_5 (7.8 and 4.6 g cm^{-3} , respectively).⁵⁷ In the TEM micrographs (Fig. 4A, inset), only highly amorphous material was identified for the samples synthesized in air at 450 °C. The corresponding SAED pattern confirms the highly disordered nature of the material at 450 °C. Nanocrystalline TT- Nb_2O_5 domains emerge when using a higher synthesis temperature (500 °C) while the majority of the diffraction signal is still indicative of a highly amorphous material. Higher temperatures are required to obtain a well-developed TT- Nb_2O_5 crystal structure. However, at 500 °C, already a strong oxidation of

Table 3 Comparison among different reported carbide-derived carbon materials and commercial powder electrodes, characterized for electrical double-layer capacitors

Sample	BET-SSA ($\text{m}^2 \text{ g}^{-1}$)	Pore volume ($\text{cm}^3 \text{ g}^{-1}$)	C (F g^{-1})	Capacitance retention	Reference
NbC–CDC fibers	1508	0.80	101	20% at 40 A g^{-1}	This work, 1 M TEA-BF ₄ in ACN
NbC–CDC fibers	1326	0.96	108	56% at 40 A g^{-1}	This work, 1 M TEA-BF ₄ in ACN
SiC–CDC particles	2430	1.50	125	85% at 20 A g^{-1}	Ref. 19, 1 M TEA-BF ₄ in ACN
SiC–CDC particles	2250	1.40	160	81% at 20 A g^{-1}	Ref. 19, 1 M TEA-BF ₄ in ACN
SiOC–CDC fibers	3089	1.78	135	63% at 50 A g^{-1}	Ref. 18, 1 M TEA-BF ₄ in ACN
SiOC–CDC particles	2480	1.29	110	83% at 30 A g^{-1}	Ref. 61, 1 M TEA-BF ₄ in ACN
TiC–CDC fibers	1390	1.50	102	50% at 5 V s^{-1}	Ref. 12, 1.5 M TEA-BF ₄ in ACN
AC + 5% PTFE	1481	0.8	104	68% at 10 A g^{-1}	Ref. 62, 1.0 M TEA-BF ₄ in ACN



Table 4 EDX results of Nb₂O₅/C hybrid nanofibers, and mass change measured after thermal treatment in air or CO₂

Sample	Mass change	C (mass%)	O (mass%)	Nb (mass%)
NbC-1700	—	27.6 ± 0.5	2.0 ± 0.1	70.3 ± 1.1
Nb ₂ O ₅ -450	+16%	11.8 ± 0.7	27.8 ± 1.3	60.4 ± 1.2
Nb ₂ O ₅ -500	+7%	8.9 ± 0.6	28.8 ± 1.9	62.4 ± 1.9
Nb ₂ O ₅ -850	+38%	18.6 ± 0.8	25.0 ± 1.2	56.4 ± 1.0

carbon takes place as observed from the change in the carbon content according to the EDX data (Table 4). Therefore, a less oxidative environment was chosen in alignment with theoretical calculation, namely thermal treatment in CO₂ (see ESI, Fig. S7A†). At 850 °C, TEM micrographs show Nb₂O₅ nanocrystals engulfed in graphitic carbon (Fig. 4C). The corresponding SAED pattern is characteristic of a highly crystalline material, with diffraction patterns falling into almost continuous rings related to T-Nb₂O₅.

For a more detailed characterization of the crystal structure of the synthesized materials, XRD patterns and Raman spectra were recorded (Fig. 5). All Raman spectra indicate the presence of partially graphitic carbon in all samples. Yet, the carbon signal was very high for NbC-1700 and almost identical to that of Nb₂O₅-850. The apparent absence of clear signals from crystalline niobia in Nb₂O₅-850 is related to the very high sensitivity of Raman spectroscopy to detect sp²-hybridized carbon species.⁵⁸ In contrast, the TT-Nb₂O₅ signal and the fluorescence-related background were stronger after oxidation in air. Yet, there are differences also related to the carbon signal as seen after peak deconvolution (see ESI, Table S3†). For Nb₂O₅-450, we found broader D- and G-peaks compared to the precursor and an overall increase in the amount of amorphous carbon (see ESI, Fig. S9†) as a result of on-setting carbon oxidation. The high fluorescence background for Nb₂O₅-500 made peak deconvolution unreliable, but there was still a redshift of the G-mode peak from 1599 to 1584 cm⁻¹ due to the co-existing amorphous phase. According to the mass change during the process and EDX results (Table 4), the carbon content drastically decreased for this sample.

According to the XRD pattern (Fig. 5B), NbC is transformed after treatment in an oxidative atmosphere into a highly amorphous material for Nb₂O₅-450 and into nanocrystalline niobium pentoxide for Nb₂O₅-500 and Nb₂O₅-850. By applying the Scherrer equation,⁴¹ in air at 500 °C, TT-Nb₂O₅ is formed with an average domain size of *ca.* 20 nm and lattice parameters, *a* = 0.36 nm, *b* = 0.31 nm, and *c* = 0.39 nm. By treatment in CO₂ at 850 °C, orthorhombic T-Nb₂O₅ is formed with an average domain size of *ca.* 35 nm and lattice parameters, *a* = 0.62 nm, *b* = 2.93 nm, and *c* = 0.39 nm.

Electrochemical performance. Nb₂O₅/C hybrid nanofibers were evaluated for Li⁺ ion intercalation. It has been already reported that anodic and cathodic peaks related to Li⁺ ion intercalation–deintercalation are located between 1.0 and 2.0 V *vs.* Li/Li⁺ (between -2.4 and -1.4 V *vs.* carbon),³⁶ and in this potential window LiClO₄ in EC/DMC presents a high coulombic efficiency and stability,³⁷ and therefore this electrolyte was

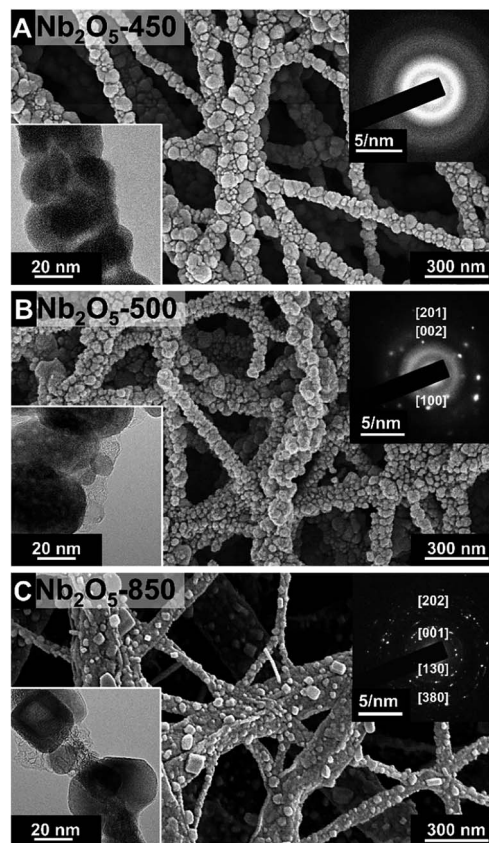


Fig. 4 SEM micrographs, TEM micrographs (inset, lower left corner), and selected area electron diffraction pattern (inset, upper right corner) of Nb₂O₅/C hybrid nanofibers synthesized at (A) 450 °C in air, (B) 500 °C in air, and (C) 850 °C in CO₂.

selected. Electrochemical testing for half-cells was performed by CV at 1 mV s⁻¹ to first confirm the potential at which the Li⁺ ion intercalation takes place. From the CV shapes (Fig. 6A), a minor electric double-layer contribution to the energy storage is observed for all samples, since the fibers present a low SSA (around 82 m² g⁻¹ DFT SSA). Nb₂O₅-450 does not present visible redox intercalation peaks due to the amorphous character of Nb₂O₅. Nb₂O₅-500 presents a broad increase in anodic current below -0.8 V *vs.* carbon, related to the slow diffusion and intercalation process. A high specific cathodic current below -0.5 V *vs.* carbon is related to the slow deintercalation of the Li⁺ ions. This indicates that Li⁺ intercalation and deintercalation take place within a broad potential window due to kinetic effects and the co-existence of amorphous and low-order domains of TT-Nb₂O₅. In the case of Nb₂O₅-850, Li⁺ deintercalation takes place at -1.2 V, and the more pronounced peak is related to the enhanced intercalation kinetics of the T-Nb₂O₅ crystal structure. These results are also confirmed by the voltage plateau observed by GCPL (see ESI, Fig. S10A†). Li⁺ intercalation takes place in two steps, as shown by the anodic peaks at -1.3 and -1.5 V *vs.* carbon. At these potentials, peak currents are higher for T-Nb₂O₅ than for TT-Nb₂O₅, suggesting a higher lithium intercalation capacity for this crystal phase.



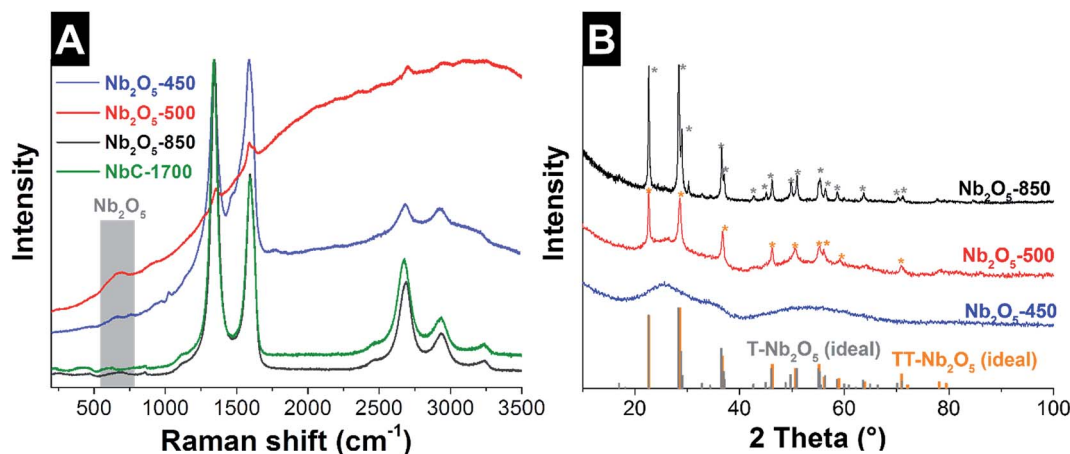


Fig. 5 (A) Raman spectra of Nb₂O₅/C hybrid nanofibers and the precursor (NbC-1700). (B) XRD diffractograms of Nb₂O₅/C hybrid nanofibers and literature values of diffraction peak positions of T-Nb₂O₅ (PDF: 27-1003) and TT-Nb₂O₅ (PDF: 07-0061).

The observed peaks are related to the electron transfer resulting from lithium intercalation according to the reaction in eqn (5), for redox couples Nb^{5+/4+} and Nb^{4+/3+}.³⁶



By GCPL to -2.0 V vs. carbon, the rate handling was evaluated for half-cells (Fig. 6B). The specific capacities of the third discharge cycle at 0.1 A g⁻¹ for Nb₂O₅-450, Nb₂O₅-500 and Nb₂O₅-850 (1 C-rate), were 6, 101, and 156 mA h g⁻¹, respectively. When normalizing the results to the mass of niobium pentoxide, as commonly done for battery systems, we obtained capacities of 111 mA h g⁻¹ and 191 mA h g⁻¹ for Nb₂O₅-500 and Nb₂O₅-850, respectively. At 0.1 A g⁻¹ the coulombic efficiency of Nb₂O₅-500 and Nb₂O₅-850 corresponds to 91 and 92%, respectively. As presented in Table 5, these values are comparable to those reported in the literature for TT-Nb₂O₅ (150 mA h g⁻¹) and T-Nb₂O₅ (between 142 and 190 mA h g⁻¹). At 20 A g⁻¹, 5% and 23% of the capacity were retained for Nb₂O₅-500 and Nb₂O₅-850, respectively. The higher rate handling performance of Nb₂O₅-850 is related not just to the graphitic carbon engulfing the T-Nb₂O₅ crystals, but also to the short diffusion length in the nanofibers and the faster ionic transport characteristic of T-Nb₂O₅. The latter was explained by Augustyn *et al.* by the almost empty octahedral sites between (001) planes presenting low energy barriers for Li⁺ ion transport throughout the *a-b* plane.⁸

In order to benchmark Nb₂O₅/C hybrid nanofibers as a cathode (electrode at negative potentials) in a device, asymmetric full-cell tests were performed (Fig. 6C and D). As an anode (electrode at positive potentials), a charge balanced AC electrode was used. This set-up has demonstrated to improve the performance of the full-cell, by limiting the polarization resistance.^{31,59} For the CVs at 1 mV s⁻¹, shown in Fig. 6C, a maximum applied cell voltage of 3.6 V was used, which was expected to lead to an appropriate operating potential range for positive and negative electrodes. For asymmetric full-cells, the

different charge-voltage-behavior of the two electrodes led to asymmetric voltage development at the anode and cathode. Therefore, the voltage in each electrode was recorded by using an activated carbon spectator reference electrode (see ESI, Fig. S10B and C†). According to the CV (Fig. 6C) of Nb₂O₅-500, a cathodic peak can be observed at 2.5 V cell voltage and broad anodic peaks are detected at 1.8 and 2.8 V cell voltages. A strong increase in current close to 3.6 V cell voltage is related to fast voltage development at the positive electrode, above the potential limit for the stability of the electrolyte, and therefore the system is not stable. The voltage at the negative electrode reaches -2.2 V vs. carbon, while for the positive electrode a voltage maximum of 1.4 V vs. carbon was obtained (see ESI, Fig. S10B†). For Nb₂O₅-850, at low voltage, a capacitive behavior was observed, related to the higher mass of AC present as the positive electrode, compared to Nb₂O₅-500. When increasing the cell voltage, Li⁺ intercalation/deintercalation takes place in the Nb₂O₅ electrode, as indicated by broad anodic peaks between 2.2 and 1.8 V cell voltages, and cathodic peaks at 1.9 and 2.6 V cell voltages. At high cell voltage, the system is more stable than Nb₂O₅-500, and no strong increase in current is observed (see ESI, Fig. S10B†).

The performance of full-cells was further characterized by GCPL to 3.6 V at 0.1 A g⁻¹ (Fig. 6D). No significant charge storage in the cell is observed below 1.2 V and 1.6 V for Nb₂O₅-850 and Nb₂O₅-500, respectively, indicating no significant faradic charge transfer to the Nb₂O₅ electrode. Above this potential, a voltage plateau is observed for both samples, indicating a transfer of charge to the electrode when Li⁺ ion intercalation takes place. From the voltage plateau during discharging and the difference in potential development for each electrode (see ESI, Fig. S10B†), it can be concluded that both samples present a high difference in charge transfer efficiency. The coulombic efficiency of Nb₂O₅-500 and Nb₂O₅-850 corresponds to 40 and 80% respectively, for asymmetric full-cells.



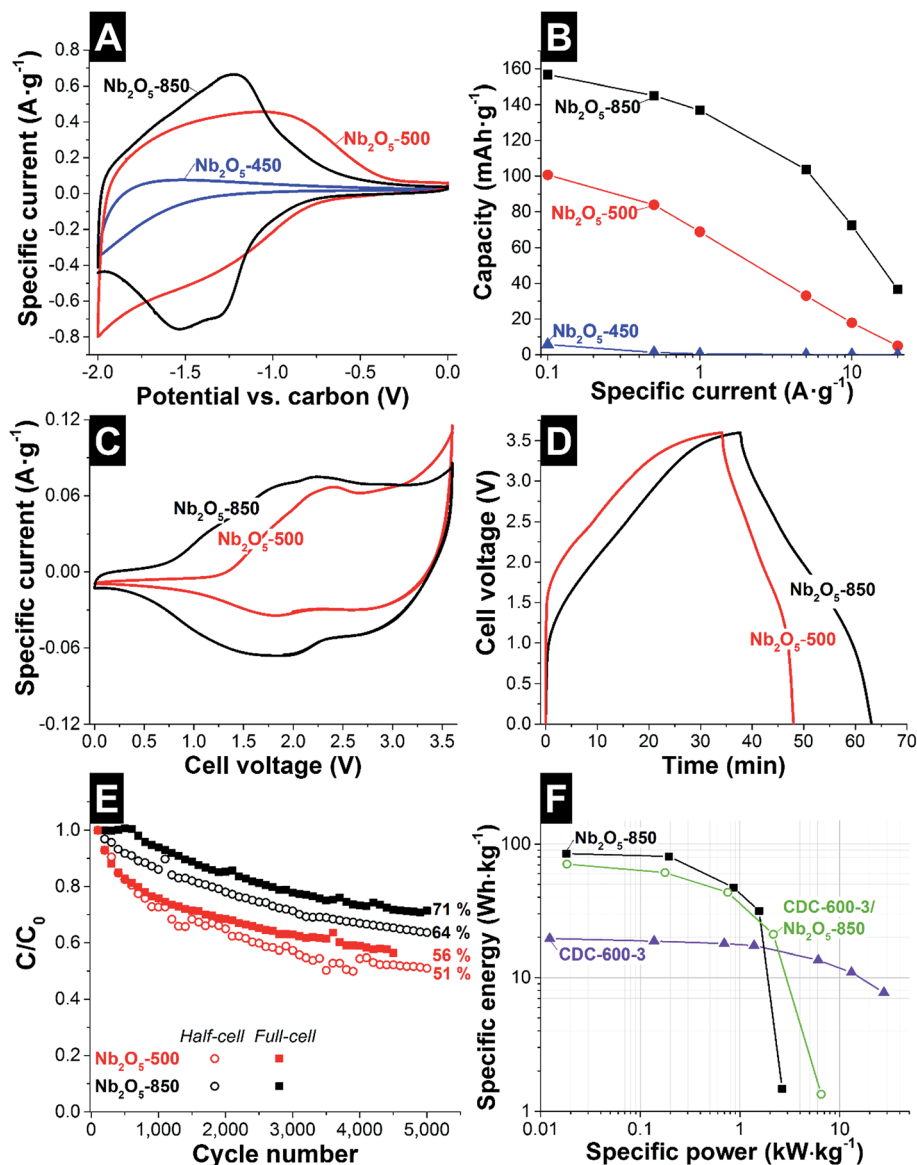


Fig. 6 Electrochemical characterization in the half-cell configuration of Nb₂O₅/C hybrid nanofibers in 1 M LiClO₄ in EC/DMC using (A) cyclic voltammetry at 1 mV s⁻¹ and (B) galvanostatic charge/discharge rate handling to -2 V vs. carbon. Electrochemical characterization in the full-cell configuration using (C) cyclic voltammetry up to 3.6 V cell voltage at 1 mV s⁻¹ and (D) GCPL charge/discharge profile at 0.1 A g⁻¹. (E) Capacity retention during galvanostatic charge/discharge cycling to 3.0 V cell voltage for full-cells or from 0 to -2 V vs. carbon for the half-cell configuration. (F) Ragone plot of full-cells.

Cycling stability tests were performed in half- and full-cell configurations (Fig. 6E). After 5000 cycles, Nb₂O₅-850 retained 64% and 71% of the capacity, in half- and full-cell setups, respectively. For Nb₂O₅-500, the lower stability of half-cells is related to the higher voltage (-2.0 V for half-cells; 3.0 V for full-cells) and the high stability of the positive material, AC. For Nb₂O₅-500, 51% of the capacity was retained for the half-cell, while for the full-cell, 56% was maintained. The lower stability is related to the low order of crystallinity of the TT-Nb₂O₅.

The materials with the best electrochemical performance for electrical double-layer capacitors and battery-like systems are plotted in the Ragone plot (Fig. 6F). CDC-600-3 presents high power handling, maintaining a specific energy of 7.6 W h kg⁻¹

at 30 kW kg⁻¹ and a maximum specific energy of 19.5 W h kg⁻¹ at 0.01 kW kg⁻¹. For Nb₂O₅-850 asymmetric full-cells, a specific energy of 86 W h kg⁻¹ at 0.02 kW kg⁻¹ was exhibited. At 1.5 kW kg⁻¹, the specific energy corresponds to 32 W h kg⁻¹. For comparison, a hybrid full-cell was also evaluated using as positive and negative electrodes CDC-600-3 and Nb₂O₅-850 respectively. Due to the lower capacitance of the CDC fibers compared to the AC (YP80 + 5% PTFE; 112 F g⁻¹),⁶⁰ a maximum specific energy of 71 W h kg⁻¹ was obtained. Above 1 kW kg⁻¹, the hybrid electrode system presents a better electrochemical performance maintaining 21 W h kg⁻¹ at 2.2 kW kg⁻¹. Cyclic voltammetry and GCPL of this full-cell are presented in the ESI (see Fig. S11†).



Table 5 Comparison among different Nb₂O₅ containing electrodes characterized as battery-like and redox-hybrid systems. For electrode preparation, most of the samples reported were admixed with carbon as a conductive additive (CA) or drop-casted in the current collector. The capacity values (mAh g⁻¹) are normalized by the electrode mass and by the active mass (am), that is, just niobia

Sample	Electrode	Capacity (mA h g ⁻¹)	Capacity retention	Reference
Nb ₂ O ₅ /C electrospun fibers	Free standing	TT-Nb ₂ O ₅ : 101 (am: 111)	TT-Nb ₂ O ₅ : 18% at 10 A g ⁻¹ (100 C-rate)	This work, 1 M LiClO ₄ in EC/DMC
		T-Nb ₂ O ₅ : 156 (am: 191)	T-Nb ₂ O ₅ : 46% at 10 A g ⁻¹ (64 C-rate); 23% at 20 A g ⁻¹ (128 C-rate)	
Nb ₂ O ₅ electrospun fibers	Mixture with CA and PTFE	TT-Nb ₂ O ₅ : 99 (am: 152) T-Nb ₂ O ₅ : 123 (am: 189)	—	Ref. 36
Nb ₂ O ₅ nano-particles	Drop cast mixture with CA	T-Nb ₂ O ₅ : 71 (am: 142)	T-Nb ₂ O ₅ : 31% at 1000 C-rate	Ref. 8, 1 M LiClO ₄ in PC
Nb ₂ O ₅ nanosheets	Mixture with CA and PVdF	T-Nb ₂ O ₅ : 117 (am: 147)	T-Nb ₂ O ₅ : 77% at 1 A g ⁻¹ (5 C-rate)	Ref. 38, 1 M LiPF ₆ in EC/DMC/DEC
Nb ₂ O ₅ mesoporous films	Free-standing thin film	T-Nb ₂ O ₅ : 190	—	Ref. 39, 1 M LiClO ₄ in PC

Conclusions

We demonstrated the suitability of NbC/C hybrid nanofibers as a versatile precursor for synthesizing electrode materials for both EDLCs and battery-like systems. Optimized EDLC electrodes were fabricated by chlorine treatment of NbC/C nanofibers at 600 °C in order to obtain a maximum pore volume of 1 cm³ g⁻¹ and a DFT-SSA of 1369 m² g⁻¹. According to the electrochemical performance, due to the highly accessible pore structure, an efficient use of the surface leads to a maximum specific energy of 19.5 W h kg⁻¹ and 7.6 W h kg⁻¹ for a maximum specific power of 30 kW kg⁻¹ in a full-cell configuration. The high specific power was accomplished due to the continuous path for electron propagation and the high graphitization of the carbon structure.

By the treatment of NbC/C nanofibers in oxidative atmospheres, TT-Nb₂O₅ and T-Nb₂O₅/C hybrid nanofibers were synthesized at 500 °C and 850 °C, respectively. The synthesis in air (500 °C) does not allow for obtaining a highly crystalline TT-Nb₂O₅ phase without oxidizing the carbon phase. By employing CO₂ (850 °C), highly crystalline T-Nb₂O₅ engulfed in graphitic carbon was obtained. The higher faradic transfer of charge led to a maximum capacity of 156 mA h g⁻¹ with respect to the full electrode mass. This value is higher than the values reported in the literature for electrode capacity, since no polymer binder or conductive additive was added to the system. The rapid ion transport characteristic of the T-Nb₂O₅ and the co-existence of a continuous graphitic carbon phase led to an outstanding capacity retention of 50% at a high rate of 10 A g⁻¹ (64 C-rate) in the battery-like system. The electrochemical performance is further highlighted by the superior stability over 5000 discharge cycles (64% retention). The combination of Nb₂O₅/C and AC in an asymmetric full-cell setup led to a specific energy of 86 W h kg⁻¹, which is among the best values reported for a hybrid full-cell.

Further optimization steps of this promising system will involve enhanced engineering of the synthesis setup. For example, by use of the same furnace for pyrolysis and either chlorine gas treatment or CO₂ annealing, the synthesis process

can be simplified. Further adaptations of our work may also involve the use of niobium carbide nanopowder instead of electrospun mats. While this may come at the expense of lowered power handling due to the loss of the free-standing and binder-free feature of our electrospun mats, we see possibilities for cost reduction by the use of powder materials.

Acknowledgements

We acknowledge funding from the German Federal Ministry for Research and Education (BMBF) in support of the nanoEES^{3D} project (award number 03EK3013) as part of the strategic funding initiative energy storage framework. This work was supported by the CREATE-Network Project, Horizon 2020 of the European Commission (RISE Project No. 644013). We thank Prof. Eduard Arzt (INM) for his continuing support, and Juhan Lee and Anna Schreiber (all at INM) for useful discussions and technical support.

References

- Z. Yang, J. Zhang, M. C. W. Kintner-Meyer, X. Lu, D. Choi, J. P. Lemmon and J. Liu, *Chem. Rev.*, 2011, **111**, 3577–3613.
- P. Simon, Y. Gogotsi and B. Dunn, *Science*, 2014, **343**, 1210–1211.
- P. R. Bandaru, H. Yamada, R. Narayanan and M. Hofer, *Mater. Sci. Eng., R*, 2015, **96**, 1–69.
- M. Salanne, B. Rotenberg, K. Naoi, K. Kaneko, P. L. Taberna, C. P. Grey, B. Dunn and P. Simon, *Nature Energy*, 2016, **1**, 16070.
- F. Béguin, V. Presser, A. Balducci and E. Frackowiak, *Adv. Mater.*, 2014, **26**, 2219–2251.
- B. Scrosati and J. Garche, *J. Power Sources*, 2010, **195**, 2419–2430.
- M. Schroeder, M. Winter, S. Passerini and A. Balducci, *J. Power Sources*, 2013, **238**, 388–394.
- V. Augustyn, J. Come, M. A. Lowe, J. W. Kim, P.-L. Taberna, S. H. Tolbert, H. D. Abruña, P. Simon and B. Dunn, *Nat. Mater.*, 2013, **12**, 518–522.



- 9 J. Lee, B. Krüner, A. Tolosa, S. Sathyamoorthi, D. Kim, S. Choudhury, K.-H. Seo and V. Presser, *Energy Environ. Sci.*, 2016, DOI: 10.1039/c6ee00712k.
- 10 B. Krüner, J. Lee, N. Jäckel, A. Tolosa and V. Presser, *ACS Appl. Mater. Interfaces*, 2016, **8**, 9104–9115.
- 11 B. Zhang, F. Kang, J.-M. Tarascon and J.-K. Kim, *Prog. Mater. Sci.*, 2016, **76**, 319–380.
- 12 V. Presser, L. F. Zhang, J. J. Niu, J. McDonough, C. Perez, H. Fong and Y. Gogotsi, *Adv. Energy Mater.*, 2011, **1**, 423–430.
- 13 L. F. Zhang, A. Aboagye, A. Kelkar, C. L. Lai and H. Fong, *J. Mater. Sci.*, 2014, **49**, 463–480.
- 14 N. C. Abeykoon, J. S. Bonso and J. P. Ferraris, *RSC Adv.*, 2015, **5**, 19865–19873.
- 15 M. Rose, E. Kockrick, I. Senkovska and S. Kaskel, *Carbon*, 2010, **48**, 403–407.
- 16 V. Presser, M. Heon and Y. Gogotsi, *Adv. Funct. Mater.*, 2011, **21**, 810–833.
- 17 J. R. Martin, L. Borchardt, M. Oschatz, G. Mondin and S. Kaskel, *Chem. Ing. Tech.*, 2013, **85**, 1742–1748.
- 18 A. Tolosa, B. Krüner, N. Jäckel, M. Aslan, C. Vakifahmetoglu and V. Presser, *J. Power Sources*, 2016, **313**, 178–188.
- 19 Y. Korenblit, M. Rose, E. Kockrick, L. Borchardt, A. Kvit, S. Kaskel and G. Yushin, *ACS Nano*, 2010, **4**, 1337–1344.
- 20 J. Xu, R. Zhang, P. Chen, D. Shen, X. Ye and S. Ge, *Carbon*, 2013, **64**, 444–455.
- 21 R. Dash, J. Chmiola, G. Yushin, Y. Gogotsi, G. Laudisio, J. Singer, J. Fischer and S. Kucheyev, *Carbon*, 2006, **44**, 2489–2497.
- 22 C. R. Pérez, S.-H. Yeon, J. Ségalini, V. Presser, P.-L. Taberna, P. Simon and Y. Gogotsi, *Adv. Funct. Mater.*, 2013, **23**, 1081–1089.
- 23 R. K. Dash, A. Nikitin and Y. Gogotsi, *Microporous Mesoporous Mater.*, 2004, **72**, 203–208.
- 24 M. Xianwen, T. A. Hatton and C. R. Gregory, *Curr. Org. Chem.*, 2013, **17**, 1390–1401.
- 25 S. Cavaliere, S. Subianto, I. Savych, D. J. Jones and J. Roziere, *Energy Environ. Sci.*, 2011, **4**, 4761–4785.
- 26 M. Zeiger, D. Weingarth and V. Presser, *ChemElectroChem*, 2015, **2**, 1117–1127.
- 27 M. Zhi, A. Manivannan, F. Meng and N. Wu, *J. Power Sources*, 2012, **208**, 345–353.
- 28 J.-G. Wang, Y. Yang, Z.-H. Huang and F. Kang, *Electrochim. Acta*, 2011, **56**, 9240–9247.
- 29 Y.-W. Ju, G.-R. Choi, H.-R. Jung, C. Kim, K.-S. Yang and W.-J. Lee, *J. Electrochem. Soc.*, 2007, **154**, A192–A197.
- 30 Y. Wu, R. Balakrishna, M. V. Reddy, A. S. Nair, B. V. R. Chowdari and S. Ramakrishna, *J. Alloys Compd.*, 2012, **517**, 69–74.
- 31 J. Come, V. Augustyn, J. W. Kim, P. Rozier, P.-L. Taberna, P. Gogotsi, J. W. Long, B. Dunn and P. Simon, *J. Electrochem. Soc.*, 2014, **161**, A718–A725.
- 32 J. W. Kim, V. Augustyn and B. Dunn, *Adv. Energy Mater.*, 2012, **2**, 141–148.
- 33 R. A. Rani, A. S. Zoolfakar, A. P. O'Mullane, M. W. Austin and K. Kalantar-Zadeh, *J. Mater. Chem. A*, 2014, **2**, 15683–15703.
- 34 B. Reichman and A. J. Bard, *J. Electrochem. Soc.*, 1980, **127**, 241–242.
- 35 R. Kodama, Y. Terada, I. Nakai, S. Komaba and N. Kumagai, *J. Electrochem. Soc.*, 2006, **153**, A583–A588.
- 36 A. L. Viet, M. V. Reddy, R. Jose, B. V. R. Chowdari and S. Ramakrishna, *J. Phys. Chem. C*, 2010, **114**, 664–671.
- 37 C. Zhang, R. Maloney, M. R. Lukatskaya, M. Beidaghi, B. Dyatkin, E. Perre, D. Long, W. Qiao, B. Dunn and Y. Gogotsi, *J. Power Sources*, 2015, **274**, 121–129.
- 38 M. Liu, C. Yan and Y. Zhang, *Sci. Rep.*, 2015, **5**, 8326.
- 39 K. Brezesinski, J. Wang, J. Haetge, C. Reitz, S. O. Steinmueller, S. H. Tolbert, B. M. Smarsly, B. Dunn and T. Brezesinski, *J. Am. Chem. Soc.*, 2010, **132**, 6982–6990.
- 40 J. S. Atchison, M. Zeiger, A. Tolosa, L. M. Funke, N. Jackel and V. Presser, *RSC Adv.*, 2015, **5**, 35683–35692.
- 41 P. Scherrer, *Nachr. Ges. Wiss. Goettingen, Math.-Phys. Kl.*, 1918, 98–100.
- 42 S. Brunauer, P. H. Emmett and E. Teller, *J. Am. Chem. Soc.*, 1938, **60**, 309–319.
- 43 G. Y. Gor, M. Thommes, K. A. Cychoz and A. V. Neimark, *Carbon*, 2012, **50**, 1583–1590.
- 44 P. W. Ruch, D. Cericola, M. Hahn, R. Kötz and A. Wokaun, *J. Electroanal. Chem.*, 2009, **636**, 128–131.
- 45 R. Kötz and M. Carlen, *Electrochim. Acta*, 2000, **45**, 2483–2498.
- 46 A. C. Ferrari, *Solid State Commun.*, 2007, **143**, 47–57.
- 47 A. C. Ferrari and D. M. Basko, *Nat. Nanotechnol.*, 2013, **8**, 235–246.
- 48 K. Faber, F. Badaczewski, M. Oschatz, G. Mondin, W. Nickel, S. Kaskel and B. M. Smarsly, *J. Phys. Chem. C*, 2014, **118**, 15705–15715.
- 49 M. Thommes, K. Kaneko, A. V. Neimark, J. P. Olivier, F. Rodriguez-Reinoso, J. Rouquerol and K. S. W. Sing, *Physisorption of Gases, with Special Reference to the Evaluation of Surface Area and Pore Size Distribution (IUPAC Technical Report)*, 2015.
- 50 D. Weingarth, M. Zeiger, N. Jäckel, M. Aslan, G. Feng and V. Presser, *Adv. Energy Mater.*, 2014, **4**, 1400316.
- 51 J. Chmiola, C. Largeot, P.-L. Taberna, P. Simon and Y. Gogotsi, *Angew. Chem., Int. Ed.*, 2008, **47**, 3392–3395.
- 52 J. Segalini, E. Iwama, P.-L. Taberna, Y. Gogotsi and P. Simon, *Electrochem. Commun.*, 2012, **15**, 63–65.
- 53 R. Kötz, M. Hahn and R. Gallay, *J. Power Sources*, 2006, **154**, 550–555.
- 54 L. Shi, Y. Gu, L. Chen, Z. Yang, J. Ma and Y. Qian, *Solid State Ionics*, 2005, **176**, 841–843.
- 55 M. V. Reddy, R. Jose, A. Le Viet, K. I. Ozoemena, B. V. R. Chowdari and S. Ramakrishna, *Electrochim. Acta*, 2014, **128**, 198–202.
- 56 T. Ikeya and M. Senna, *J. Non-Cryst. Solids*, 1988, **105**, 243–250.
- 57 V. L. S. Teixeira da Silva, M. Schmal and S. T. Oyama, *J. Solid State Chem.*, 1996, **123**, 168–182.
- 58 M. S. Dresselhaus, G. Dresselhaus, R. Saito and A. Jorio, *Phys. Rep.*, 2005, **409**, 47–99.
- 59 S. Fleischmann, N. Jäckel, M. Zeiger, B. Krüner, I. Grobelsek, P. Formanek, S. Choudhury, D. Weingarth and V. Presser, *Chem. Mater.*, 2016, **28**, 2802–2813.



- 60 N. Jäckel, D. Weingarh, A. Schreiber, B. Krüner, M. Zeiger, A. Tolosa, M. Aslan and V. Presser, *Electrochim. Acta*, 2016, **191**, 284–298.
- 61 A. Meier, M. Weinberger, K. Pinkert, M. Oschatz, S. Paasch, L. Giebeler, H. Althues, E. Brunner, J. Eckert and S. Kaskel, *Microporous Mesoporous Mater.*, 2014, **188**, 140–148.
- 62 N. Jäckel, D. Weingarh, A. Schreiber, B. Krüner, M. Zeiger, A. Tolosa, M. Aslan and V. Presser, *Electrochim. Acta*, 2016, **191**, 284–298.



3.3 Binder-free hybrid titanium-niobium oxide/carbon nanofiber mats for lithium-ion battery electrodes

Aura Tolosa,^{a,b} Simon Fleischmann,^{a,b} Ingrid Grobelsek,^a Antje Quade,^c
Eunho Lim,^a and Volker Presser^{a,b}

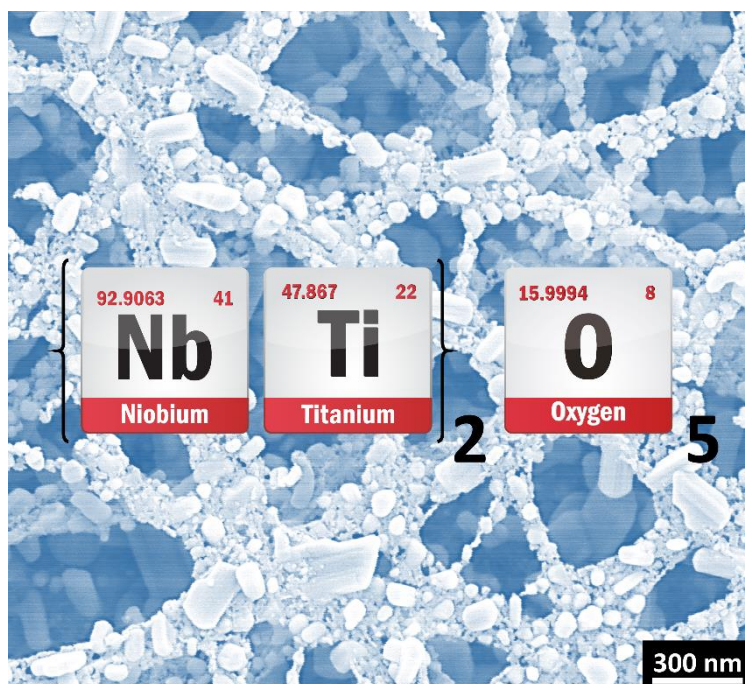
^a INM - Leibniz Institute for New Materials, 66123 Saarbrücken, Germany

^b Department of Materials Science and Engineering, Saarland University, 66123 Saarbrücken, Germany

^c Leibniz Institute for Plasma Science and Technology, 17489 Greifswald, Germany

Published in: ChemSusChem, 11 (2018), 159-170

DOI: 10.1002/cssc.201701927



Own contribution: Project management; paper writing; material synthesis; data analysis; measurements: TEM, EDX, FT-IR, Raman spectroscopy, electrochemical characterization

Binder-Free Hybrid Titanium–Niobium Oxide/Carbon Nanofiber Mats for Lithium-Ion Battery Electrodes

Aura Tolosa,^[a, b] Simon Fleischmann,^[a, b] Ingrid Grobelsek,^[a] Antje Quade,^[c] Eunho Lim,^[a] and Volker Presser^{*[a, b]}

Free-standing, binder-free, titanium–niobium oxide/carbon hybrid nanofibers are prepared for Li-ion battery applications. A one-pot synthesis offers a significant reduction of processing steps and avoids the use of environmentally unfriendly binder materials, making the approach highly sustainable. Tetragonal Nb₂O₅/C and monoclinic Ti₂Nb₁₀O₂₉/C hybrid nanofibers synthesized at 1000 °C displayed the highest electrochemical performance, with capacity values of 243 and 267 mAh g⁻¹, respectively, normalized to the electrode mass. At 5 A g⁻¹, the

Nb₂O₅/C and Ti₂Nb₁₀O₂₉/C hybrid fibers maintained 78% and 53% of the initial capacity, respectively. The higher rate performance and stability of tetragonal Nb₂O₅ compared to that of monoclinic Ti₂Nb₁₀O₂₉ is related to the low energy barriers for Li⁺ transport in its crystal structure, with no phase transformation. The improved rate performance resulted from the excellent charge propagation in the continuous nanofiber network.

Introduction

To meet the ever-growing demand for efficient and compact energy storage, Li-ion batteries have emerged as the main choice for small portable power sources.^[1] Li-ion batteries display a high specific energy ($\approx 150 \text{ Wh kg}^{-1}$) but a low specific power ($< 1 \text{ kW kg}^{-1}$) and low cycle stability compared to supercapacitors.^[2] To overcome these limitations, the development of new electrode materials has been continuously explored.^[3] Several key aspects of current research involve the use of redox couples with higher Li-ion intercalation capacity,^[4] an improved contact between the redox-active phase and the conductive phase,^[5] and the design of nanomaterials with shorter diffusion distances^[6] and low structural degradation during cycling.^[7] In this context, hybrid nanomaterials containing redox-active compounds surrounded by a conductive phase are expected to deliver an improved electrochemical performance.^[8]

Compared to conventional anode materials such as graphite, Li₄Ti₅O₁₂, or TiO₂, niobium pentoxide (Nb₂O₅) displays several advantages. The intercalation of Li⁺ in its layered structure only causes small volume expansion, it is not kinetically limited by solid-state diffusion,^[9] and occurs at a safe voltage ($\approx 1.6 \text{ V}$

vs. Li/Li⁺), leading to a high rate performance, higher stability, and no safety issues compared to graphite (the operating voltage of Nb₂O₅ is above the lowest unoccupied molecular orbital of carbonate-based electrolytes). Although Li₄Ti₅O₁₂ and TiO₂ (anatase or rutile) also display higher rate capability and structural stability than graphite, they are limited by their lower theoretical capacity (175 and 168 mAh g⁻¹, respectively).^[10]

Nb₂O₅ displays several polymorphs based on octahedrally coordinated niobium atoms: h-Nb₂O₅ (pseudo-hexagonal), o-Nb₂O₅ (orthorhombic), t-Nb₂O₅ (tetragonal), and m-Nb₂O₅ (monoclinic).^[11] For lithium intercalation, the t-Nb₂O₅ and m-Nb₂O₅ crystal phases display the highest capacity values of 200–240 mAh g⁻¹.^[12] Although it has a higher capacity,^[12a] m-Nb₂O₅ has a much higher electrical resistivity than the other polymorphs ($3 \times 10^4 \Omega \text{ cm}$).^[13] The latter can be decreased by reducing the metal oxide through a niobium-metal gettering technique; the introduction of oxygen deficiencies is accommodated in the structure by a crystallographic shear, causing a transformation to Nb₁₂O₂₉ ($4 \times 10^{-3} \Omega \text{ cm}$).^[13b] The o-Nb₂O₅ phase displays a lower capacity (160–190 mAh g⁻¹),^[12b, 14] but an improved rate handling performance comparable with that of t-Nb₂O₅.^[15] In o-Nb₂O₅, the (001)-planes form energetically favorable pathways for facile Li⁺ transport into the structure,^[16] leading to a pseudocapacitive behavior during lithiation and delithiation (i.e., absence of clearly distinguishable redox peaks and a capacitor-like electrical response),^[17] but only when the material is employed as nanoparticles.^[11] Both t-Nb₂O₅ and o-Nb₂O₅ do not undergo a phase transformation and little structural change during intercalation.^[9, 14]

Further promising materials to replace conventional anode materials are found in the mixed Ti–Nb oxide system.^[18] Depending on the stoichiometric content of the metals, different crystal structures are formed. Doping of titanium oxide

[a] A. Tolosa, S. Fleischmann, Dr. I. Grobelsek, Dr. E. Lim, Prof. Dr. V. Presser
INM—Leibniz Institute for New Materials
66123 Saarbrücken (Germany)
E-mail: volker.presser@leibniz-inm.de

[b] A. Tolosa, S. Fleischmann, Prof. Dr. V. Presser
Department of Materials Science and Engineering
Saarland University
66123 Saarbrücken (Germany)

[c] Dr. A. Quade
Leibniz Institute for Plasma Science and Technology
17489 Greifswald (Germany)

Supporting Information and the ORCID identification number(s) for the author(s) of this article can be found under <https://doi.org/10.1002/cssc.201701927>.

with a donor-like Nb modifies the Fermi level and thereby increases the electrical conductivity of TiO_2 .^[19] To compensate for the difference in oxidation states, some oxygen atoms are doubly shared (corner sharing) instead of triply shared (edge sharing) between the octahedra, compared to rutile, in which only edge sharing exists.^[19] As reported by Eror, the limit for doping is approximately 8 at% Nb.^[19] Above this limit, different phases evolve such as TiNb_2O_7 , $\text{Ti}_2\text{Nb}_{10}\text{O}_{29}$, and $\text{TiNb}_6\text{O}_{17}$. Roth and Coughanour confirmed that these mixtures correspond to different compounds and not to a solid solution of Nb_2O_5 and TiO_2 .^[20] They form a monoclinic structure different to that of monoclinic Nb_2O_5 , called Wadsley–Roth shear structure,^[21] which is formed by Ti and Nb atoms coordinated in octahedra with oxygen atoms^[21] and provide a 2D interstitial space for Li^+ insertion.^[22] The theoretical capacity of TiNb_2O_7 , $\text{Ti}_2\text{Nb}_{10}\text{O}_{29}$, and $\text{TiNb}_6\text{O}_{17}$ is 388, 396, and 397 mAh g^{-1} , respectively,^[10a] and is related to the multiple redox couples $\text{Ti}^{3+}/\text{Ti}^{4+}$, $\text{Nb}^{3+}/\text{Nb}^{4+}$, and $\text{Nb}^{4+}/\text{Nb}^{5+}$.^[23] The high average voltage for operation (1.66 V vs. Li/Li^+) avoids the formation of Li dendrites and allows for safe operation.^[10a]

Tested as anodes for Li-ion batteries, polymer-bound electrodes containing Ti–Nb oxide particles and conductive additives (15–25 wt%) have been reported.^[18] Macroporous TiNb_2O_7 and $\text{TiNb}_6\text{O}_{17}$ particles have been synthesized by sol–gel synthesis and ball milling followed by calcination between 900–1200 °C.^[24] Using sol–gel synthesis and electrospinning, TiNb_2O_7 and $\text{Ti}_2\text{Nb}_{10}\text{O}_{29}$ noncontinuous fibers have been produced by annealing between 900–1000 °C under air.^[10a,25] Despite the large theoretical capacities, TiNb_2O_7 and $\text{Ti}_2\text{Nb}_{10}\text{O}_{29}$ suffer from low intrinsic conductivity.^[26] Different strategies to increase the conductivity are based on introducing oxygen vacancies^[19] or the synthesis of Ti–Nb oxide/carbon hybrid particles by a hydrothermal synthesis.^[23]

For an improved electrical conductivity, metal oxide/carbon hybrid fiber mats can be synthesized by electrospinning for direct use as electrodes. As we have shown in a previous study, electrospun free-standing fiber mats offer several advantages: the complete electrode can be synthesized from a one-pot synthesis, there is no need for polymer binder or conductive additives, and an improved electrical conductivity is obtained.^[12b] However, these advantages can only be capitalized on if continuous fiber mats are employed and are largely lost when reconsolidated, crushed fiber electrodes are used.^[27] Surprisingly, electrodes that are reported in the literature almost exclusively contain a polymer binder to reconsolidate crushed fiber mats and a carbon conductive additive. By carefully designing the synthesis protocol, we can preserve free-standing electrode mats and nanoengineer the fibers in such a way that carbon is already in-built to serve as a facile conductive additive.

In this work, we introduce, for the first time, mixed Ti–Nb oxide/carbon hybrid continuous fiber mats ($\text{Ti}_2\text{Nb}_{10}\text{O}_{29}/\text{C}$) and explore the influence of TiO_2 compared to pristine Nb_2O_5 ($\text{t-Nb}_2\text{O}_5/\text{C}$) in a hybrid system. The continuous fibers were directly used as free-standing anodes for Li-ion batteries, free of conductive additives and polymer binder. Using a one-pot in situ synthesis, we also reveal a strategy to avoid carbon

burn-off during annealing at 1000 °C while forming monoclinic $\text{Ti}_2\text{Nb}_{10}\text{O}_{29}$ and $\text{t-Nb}_2\text{O}_5$. These metal-oxide phases can only be formed by treatment at high temperatures. Through a combination of electrochemical benchmarking and rigorous material characterization, this complex system provides important insights into the intricate structure–property relationship of hybrid metal oxide/carbon fibers. The proposed synthesis route not only yields attractive electrochemical properties but, from a practical point of view, it also offers a significant reduction of processing steps and thus a reduced environmental impact.

Experimental Section

Materials synthesis

Synthesis of metal carbide/carbon nanofibers

The synthesis of niobium carbide/carbon fibers was reported in our previous study.^[28] Niobium *n*-butoxide (NbBO ; 99% metal basis) was purchased from Alfa Aesar. Titanium(IV) butoxide (TiBO ; reagent grade, 97%), acetic anhydride (Ac_2O ; $\geq 99\%$ purity), anhydrous *N,N*-dimethylformamide (DMF; 99.8% purity), and polyvinylpyrrolidone (PVP; $M_w \approx 1\,300\,000 \text{ g mol}^{-1}$) were purchased from Sigma–Aldrich. All reagents were used as received and stored in a nitrogen-filled glove box.

To prepare the spinning dope under a N_2 atmosphere, 1.235 mL (2.94 mmol) of NbBO was stirred with 0.275 mL of Ac_2O for 2 min in a nitrogen-filled glove box. Then, 12.5 mL of DMF and 1.5 g of PVP were added. The system was stirred for 48 h until a transparent solution was obtained. For the fibers containing Ti, the same procedure was applied, maintaining the total amount of metal alkoxide moles constant. Titanium was added with two different molar ratios: ($\text{Ti}/\text{Nb} = 1:6$ and $1:2$). Both TiBO and NbBO were mixed and stirred for 2 min before adding the remaining components.

Electrospinning was performed using a nanofiber system from MECC. The humidity and temperature during the process was maintained at 15–20% and 20–30 °C, respectively. The spinning dope was transferred to two 5 mL syringes and pumped through two spinnerets (inner diameter: 400 μm) at 0.5 mL h^{-1} for each spinneret. The spinnerets were separated by 30 mm. The solution was inductively charged at 23 kV, and the fibers were collected on a static collector (aluminum foil) located 165 mm below the spinnerets.

The collected fiber mats were kept in an oven (HP110, Memmert) with controlled humidity and temperature (40%, 20 °C) for 72 h to promote further hydrolysis and condensation reactions. For the thermal annealing under 99.5% argon, a graphite-heated Thermal Technology furnace was used. The fibers were heated at $5 \text{ }^\circ\text{C min}^{-1}$ to 400 °C (for Nb fibers) or 325 °C (for Ti–Nb fibers) for 3 h, and further thermally treated at 1700 °C for 4 h to form metal carbide/carbon fibers.

Synthesis of metal oxide/carbon nanofibers

After pyrolysis, the fibers were treated under two different oxidizing atmospheres for metal oxide/carbon conversion. The fiber mats were annealed in a Xerion XROTATE tube furnace, either at 850 °C or 1000 °C for 1 h. The fibers treated at 850 °C were oxidized in flowing CO_2 ($50 \text{ cm}^3 \text{ min}^{-1}$), and the fibers treated at 1000 °C were treated under a mixture of Ar and CO_2 (400 and $40 \text{ cm}^3 \text{ min}^{-1}$,

respectively). During heating ($5^{\circ}\text{Cmin}^{-1}$) and cooling ($20^{\circ}\text{Cmin}^{-1}$), the fibers were exposed to an argon atmosphere flowing at a rate of $20\text{ cm}^3\text{ min}^{-1}$. A schematic representation of the synthesis steps is presented in Figure S1 in the Supporting Information.

Materials characterization

Structural and chemical characterization

The morphology of the fibers was examined by scanning electron microscopy (SEM) using a JEOL JSM 7500F at 3 kV and $10\ \mu\text{A}$. The samples were fixed on steel sample holders using carbon tape. Before imaging, the as-spun fibers were coated with platinum in a JEOL Autofine Coater for 100 s at 30 mA. From the SEM images, the diameters of at least 100 fibers were measured by ImageJ software.^[29] High-resolution transmission electron microscopy (TEM) was performed using a JEOL JEM-2100F system operated at 200 kV. The sample was dispersed in ethanol through sonication for 5 min and drop cast onto a copper grid with a lacy carbon film.

Energy-dispersive X-ray spectroscopy (EDX) was performed using a X-Max-150 detector (Oxford Instruments) attached to the SEM chamber. The spectra of at least ten fibers were measured using an acceleration voltage of 10 kV and an emission current of $10\ \mu\text{A}$. Fourier-transform infrared spectroscopy (FTIR) with attenuated total reflection (ATR) was performed using a diamond crystal attached to a Bruker Tensor 27 system. The spectra were integrated over 28 scans. Raman spectroscopy was performed using a Renishaw inVia Raman system. We employed a Nd-YAG laser with an excitation wavelength of 532 nm (0.5 mW at the focal point). A grating with $2400\text{ lines mm}^{-1}$ and a $50\times$ lens (numeric aperture: 0.9) was used, yielding a spectral resolution of 1.2 cm^{-1} . Peak fitting was accomplished assuming two Voigt peaks, one for the D-mode and one for the G-mode.

The titanium and niobium binding energies in the metal oxide/carbon fibers were measured by an X-ray photoelectron spectrometer (XPS) Axis Ultra (Kratos Analytical). For the excitation of the photoelectron spectra, monochromatic AlK_{α} was employed. Charge neutralization was achieved by low-energy electrons injected into the magnetic field of the lens. Wide and elemental scans were acquired using X-ray radiation at 150 W power and a pass energy of 160 and 80 eV, respectively. High-resolution measurements of the C 1s, Ti 2p, and Nb 3d lines with a pass energy of 10 eV at 225 W power were performed. Four spots at different positions on each sample were analyzed and averaged. Data acquisition and processing were performed using CasaXPS (Casa Software Ltd.).

X-ray diffraction (XRD) was conducted in a D8 Advance diffractometer (Bruker AXS) with a copper X-ray source (CuK_{α} , 40 kV, 40 mA) and a Goebel mirror in point focus (0.5 mm). We used a VANTEC-500 (Bruker AXS) 2D detector positioned at 20° , 40° , 60° , and 80° 2θ with a measurement time of 16.7 min per step. The system was calibrated with a corundum standard. The samples were crushed in a pestle and mortar and placed on a sapphire crystal for the measurement. Rietveld analysis was applied to determinate the average coherence length (roughly corresponding with the domain size) using TOPAS software from Bruker. Thermogravimetric analysis (TGA) with a TG 209 F1 Libra system (Netzsch) was employed to characterize the oxidation process of the metal carbide/carbon fibers and to determinate the carbon content in the final hybrid metal oxide/carbon fibers. TGA of the metal carbide/carbon fibers was performed either in CO_2 ($20\text{ cm}^3\text{ min}^{-1}$) or in mixtures of Ar ($19\text{ cm}^3\text{ min}^{-1}$) and CO_2 ($1\text{ cm}^3\text{ min}^{-1}$) with a heating rate of $5^{\circ}\text{Cmin}^{-1}$. TGA of the metal oxide/carbon fibers was performed in flowing synthetic air ($20\text{ cm}^3\text{ min}^{-1}$) at $5^{\circ}\text{Cmin}^{-1}$.

Electrochemical measurements

Electrochemical measurements were performed with a potentiostat/galvanostat (VSP300 from Bio-Logic), using cyclic voltammetry (CV) and galvanostatic cycling with potential limitation (GCPL). The working electrode (WE) corresponded to a 8 mm disc ($1.5\text{--}3\text{ mg}$, $70\text{--}100\ \mu\text{m}$ thickness) punched from the free-standing fiber mats (polymer-binder- and conductive-additive-free). The electrodes were tested in a three-electrode setup in a custom-built polyether ether ketone (PEEK) cells with spring loaded titanium pistons.^[30] As a counter electrode (CE), we used a 11 mm lithium disc, which was separated from the WE using a 13 mm diameter glass-fiber separator (GF/D from Whatman). The WE and CE were placed between two copper foil discs of 12 mm (0.025 mm , 99.8%, Alfa Aesar) as current collectors, and a lithium wire was inserted from the side as a reference electrode (RE), separated with a glass-fiber separator. After assembly without lithium (i.e., without CE and RE), the cells were dried at 2 kPa and 120°C for 12 h. Subsequently, the cells were placed in an argon-filled glove box (MBraun Labmaster 130, O_2 and $\text{H}_2\text{O} < 1\text{ ppm}$) and the lithium electrodes were added. The cells were subsequently filled with $60\ \mu\text{L}$ of 1 M lithium hexafluorophosphate (LiPF_6) in electrochemical grade ethylene carbonate and dimethyl carbonate (EC/DMC; BASF) 1:1 by volume electrolyte.

For rate capability measurements, the cells were subjected to GCPL between 0.8 and 3.0 V versus Li/Li^+ at different current rates from 0.025 Ag^{-1} (0.1C) for 20 cycles, and for the next 40 cycles at 0.5 (2C), 1.25 (5C), 2.5 (10C), and 5 Ag^{-1} (20C) for 10 cycles each. Further GCPL at 0.025 Ag^{-1} for 40 cycles was performed to complete 100 cycles. To evaluate the electrochemical performance at high rates, the cells were initially tested by CV within the potential range between 0.8 and 3.0 V versus Li/Li^+ at a scan rate of 0.1 mVs^{-1} for 5 cycles and later charged and discharged by GCPL at a constant rate at 2.5 Ag^{-1} (10C) for 500 cycles. From the GCPL data, the specific capacity (C_{sp}) was calculated according to Equation (1), by integrating the current during the delithiation step between starting (t_0) and end time (t), normalized to the total hybrid electrode mass (m) because neither polymer binder nor conductive additive was admixed.

$$C_{\text{sp}} = \frac{\left(\int_{t_0}^t Idt\right)}{m} \quad (1)$$

The sheet resistance of the fiber mats was measured with a custom-built spring-loaded four-point probe with blunt gold contacts (tip diameter: 1.5 mm, tip distance: 3 mm). Polymer-bound electrodes were prepared for comparison. The fiber mats were ground with an agate mortar in ethanol until a homogeneous slurry was obtained, to which 5 wt% polytetrafluoroethylene (PTFE, 60 wt% solution in water, Sigma-Aldrich) and 5 wt% carbon black (Super C65, Imerys Graphite & Carbon) were added. The obtained paste was rolled until $105 \pm 5\ \mu\text{m}$ thick electrodes were obtained (MTI HR01 rolling machine, MTI).

Electrochemical in situ XRD was conducted with a commercial in situ cell with a beryllium window from Bruker AXS. The cell contained a lithium chip as CE and RE, which was separated from the WE by a glass fiber separator. Electrochemical testing of the cell was performed with a Gamry Reference 600 potentiostat. The cell was operated chronoamperometrically with 1 h holding times at each new potential step. The same XRD setup was used as described above, with the 2D detector positioned at 30° 2θ and a measurement time of 25 min.

Results and Discussion

Metal alkoxide fibers

During the preparation of the spinning dope, Ac_2O forms a bidentate ligand with the metal alkoxides, moderating their high reactivity^[31] and stabilizing the sol growth until electrospinning has been accomplished. During electrospinning, DMF and free Ac_2O eventually evaporate, leaving behind solid fibers composed of PVP and a metal alkoxide sol. Smooth and uniform metal alkoxide fibers were obtained with an average size of approximately 160 nm, in agreement with our previous work.^[28] According to the Ti/Nb molar ratio used for the preparation of the spinning dope (0:1, 1:6, and 1:2), the as-spun samples were named as-spun Nb, TiNb_6 , and TiNb_2 , respectively. The morphology of the as-spun fibers is shown in Figure 1A–C.

We recorded the FTIR spectra of the as-spun fibers to better understand the sol–gel reaction. When the as-spun fibers were exposed to the environment, hydrolysis and condensation of the alkoxide sol continued for 72 h. As shown by the FTIR spectra in Figure 1D, the metal alkoxide network signals related to the aliphatic groups $-\text{CH}_2$ and $-\text{CH}_3$ in *n*-butoxide were indicated by the stretch modes of the bands between 2900–2827 cm^{-1} and the C–H bending modes at 1461 and 1373 cm^{-1} .^[32] The band at 1169 cm^{-1} corresponded to the stretching vibrations ($\text{Nb}-\text{O}-\text{C}_4\text{H}_9$) of different butoxy ligands bound to Nb.^[33] The absorption bands between 1150–900 cm^{-1} were assigned to the C–O terminal vibration arising from $\text{Ti}-\text{O}-\text{C}_4\text{H}_9$.^[28] Although some butoxy groups were bonded to the alkoxide network, some underwent nucleophilic substitution by acetates to produce butanol. This was con-

firmed by the (O–H) and (C–O) stretching vibrations bands at 3400 and 930 cm^{-1} .^[33] The formation of the acetate ligands was confirmed by the signals at 1494 and 1437 cm^{-1} resulting from the antisymmetric and symmetric stretching mode of COO^- .^[34]

Several bands were observed below 1000 cm^{-1} , which were related to the formation of M–O (oxo ligands). According to Sui et al., peaks below 800 cm^{-1} are related to Ti–O–Ti.^[35] All measured spectra of the samples (i.e., with and without Ti) displayed similar peaks between 900 and 640 cm^{-1} . The bands at 500–600 cm^{-1} were attributed to the Nb–O stretching vibrations, typical for oligomeric alkoxides.^[33] The peak position and shape in this region varied for each sample. The as-spun Nb sample showed a peak at 569 cm^{-1} , which was observed as two broad peaks at 562 and 571 cm^{-1} for TiNb_6 . Sharper peaks were observed at 555 and 569 cm^{-1} for the TiNb_2 sample. As reported in our previous work, TiBO sol displayed a peak resulting from the Ti–O–Ti stretching bond at 554 cm^{-1} , which explains the separation of the initial peak (569 cm^{-1}) into two peaks (555 and 569 cm^{-1}).^[28]

Metal oxide/carbon fibers

The metal alkoxide fibers were thermally annealed under argon. The fiber shape was maintained and hybrid fibers containing metal carbide crystals surrounded by highly graphitic carbon were formed. The material characterization of these fibers is presented in the Supporting Information.

To transform the metal carbide/carbon fibers to metal oxide/carbon fibers, we first conducted a TGA analysis in different oxidizing atmospheres (Figure S3). As demonstrated in our past work, heat treatment of NbC/C fiber mats under air or CO_2

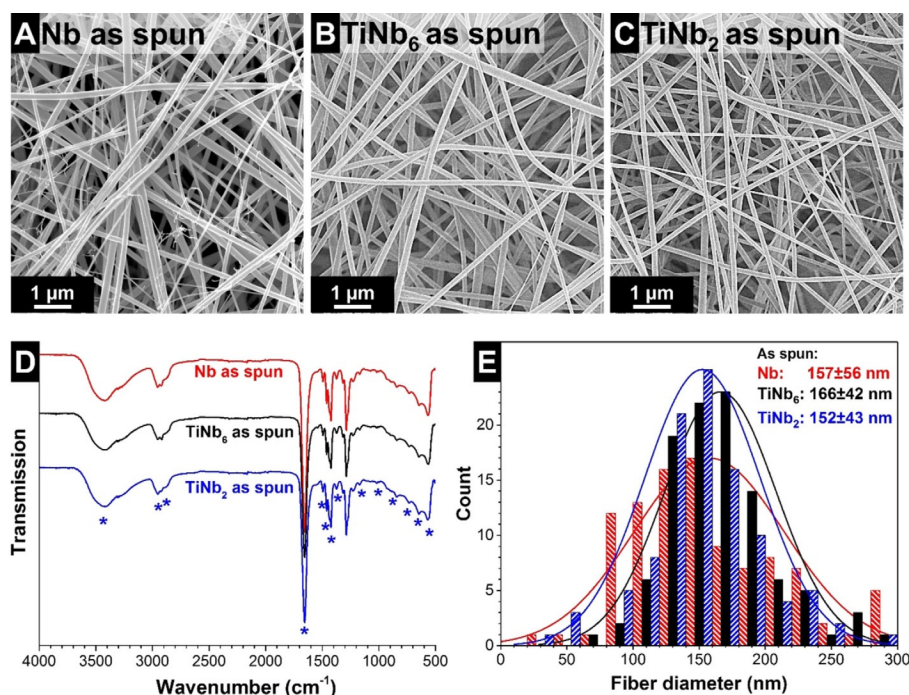


Figure 1. SEM images of Nb (A), TiNb_6 (B), and TiNb_2 (C) as-spun fibers. FTIR spectra (D) and fiber diameter distribution of the as-spun fibers (E).

leads to h- or o-Nb₂O₅/C fiber mats.^[12b] Also, the synthesis of hybrid particles containing o-Nb₂O₅ with carbon or niobium carbide has been reported by treatment of the materials under CO₂ between 800–850 °C.^[36] However, there are no reports of hybrid Nb₂O₅/C particles synthesized above 850 °C. The crystalline structure of Nb₂O₅ depends on the limited range of compatible heat-treatment conditions (atmosphere and temperature) at which carbon and Nb₂O₅ coexist. These limits correspond to 450 and 850 °C for air and CO₂ atmospheres, respectively.^[12b] As shown by Kim et al.,^[37] the thermal treatment of Nb₂O₅/C systems above 900 °C in inert atmospheres transforms Nb₂O₅ to niobium suboxide (NbO₂) and leads to the partial removal of carbon (the Supporting Information, Figure S3A). Because the standard free energy of carbon oxidation is higher than NbC oxidation, a low partial pressure of the oxidizing agent allows the oxidation of NbC above 900 °C without (complete) carbon oxidation.^[38] As corroborated for metal carbide/carbon fibers, under a CO₂ atmosphere, the oxidation of the metal carbide and carbon takes place at 816 and 968 °C, respectively, and in an Ar/CO₂ atmosphere at 1020 and above 1100 °C, respectively, as shown by the TGA analysis (the Supporting Information, Figure S3B). Therefore, we can tailor the crystalline structure of the metal oxide in the hybrid system by controlling the annealing temperature and partial pressure of CO₂. According to our data, two conditions were chosen: (1) treatment at 850 °C under a CO₂ atmosphere (CO₂ partial pressure=1; at standard temperature and pressure) and (2) treatment at 1000 °C under an Ar/CO₂ mixed atmosphere (CO₂ partial pressure=0.1; at standard temperature and pressure) for 1 h. After thermal treatment, the fibers were named according to the Ti/Nb molar ratio used (NbO_x, TiNb₆O_x, or TiNb₂O_x), and the temperature of the thermal treatment (-850 or -1000).

Structural and chemical characterization

According to the TGA results (Figure 2D), the metal oxide/carbon fibers contained approximately 12 wt% of free carbon (Table 1). The calculations of the free carbon content are presented in the Supporting Information. After thermal treatment under oxidizing atmospheres, the fiber shape was maintained,

Table 1. Elemental analysis by EDX and results of the free carbon content calculated from TGA for samples treated at 1000 °C. Data below the detection limit are marked as non-detectable (n.d.).

Material	EDX results [wt%]				TGA C _{free} [wt%]
	Ti	Nb	C	O	
NbO _x -1000	n.d.	50.2 ± 3.0	26.4 ± 1.5	23.4 ± 3.0	12.4
TiNb ₆ O _x -1000	4.4 ± 0.5	50.7 ± 5.5	22.2 ± 3.7	22.7 ± 4.1	12
TiNb ₂ O _x -1000	13.2 ± 2.0	43.7 ± 3.0	20.6 ± 1.8	22.5 ± 4.5	11.8

and we determined an average fiber diameter of 90 ± 46 nm (Figure 2A–C) through image analysis of the TEM images. The emerging metal oxides could be already identified in the SEM images. Transmission electron micrographs (Figure 2A–C, inset) show the presence of a hybrid system with metal oxide (MeO_x) crystals surrounded by graphitic carbon. To characterize the metal oxide and carbon phases, XRD patterns and Raman spectra of the samples treated at 1000 °C were recorded (Figure 3A and B). The data of the samples treated at 850 °C are shown in the Supporting Information, Figures S4 and S5.

The Raman spectra of the metal oxide/carbon fibers (Figure 3A) were similar to the spectra of the as-carbonized samples (Figure S2), with the D- and G-mode peaks and the corresponding overtones characteristic of incompletely graphitized carbon.^[39] For the characterization of the D- and G-mode, two

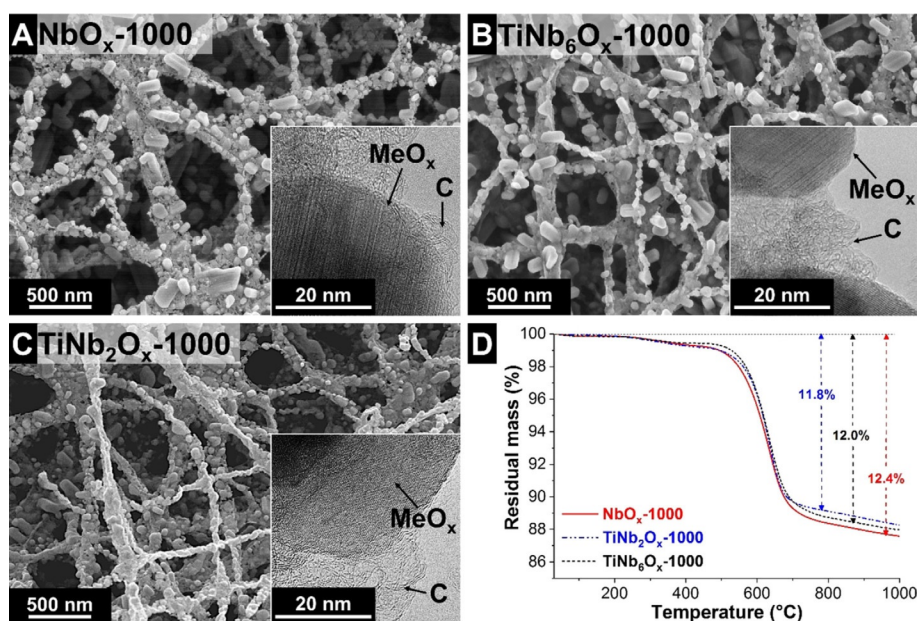


Figure 2. SEM and TEM images (inset) of metal oxide/carbon fibers synthesized at 1000 °C containing different Ti/Nb molar ratios, 0:1 (A), 1:6 (B), and 1:2 (C). Thermogravimetric analysis of the hybrid fiber under air for characterization of the carbon content (D).

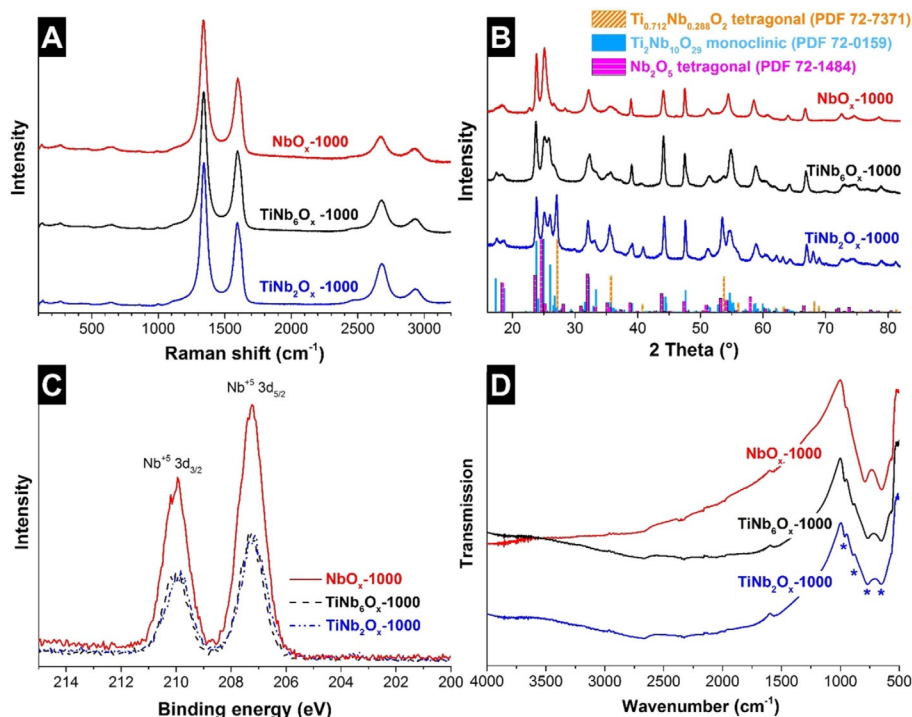


Figure 3. Chemical and structural characterization of the metal oxide/carbon fibers synthesized at 1000 °C under Ar/CO₂. Raman spectra (A), X-ray diffraction pattern and literature values for diffraction peak positions (B), high resolution X-ray photoelectron spectra of Nb 3d (C), and FTIR spectra (D).

Voigt-profile peaks were fitted in the range of 500–2000 cm⁻¹ and the calculated data are presented in Table 2. The position of the D- and G-mode, the integral I_D/I_G intensity ratio, and the full-width at half-maximum (FWHM) of these peaks contain information about the structural changes of the carbon ordering

Sample	D mode [cm ⁻¹]		G mode [cm ⁻¹]		I_D/I_G -ratio
	position	FWHM	position	FWHM	
NbO _x -850	1345	62	1596	70	1.7
NbO _x -1000	1340	64	1597	68	2
TiNb ₆ O _x -850	1339	58	1595	69	1.8
TiNb ₆ O _x -1000	1344	54	1597	68	2
TiNb ₂ O _x -850	1341	62	1595	72	1.7
TiNb ₂ O _x -1000	1343	58	1596	69	1.8

during heat treatment. Compared to the carbon present before treatment under oxidizing atmospheres, the increase in the I_D/I_G ratio suggested an increase in the defect concentration in hexagonal carbon rings.^[40] The higher presence of defects was also corroborated by a 5–15% increase in the FWHM of the D-mode peak after oxidation. This effect was related to the on-setting carbon oxidation, during which some graphitic carbon is transformed into amorphous carbon; however, the highly graphitic nature of the carbon was almost completely preserved. The formation of this co-existing amorphous carbon phase during oxidation was also observed from the red shift of the G-peak for all samples. The on setting in carbon oxidation

was also corroborated by the increase in the C–C sp³ hybridization by treatment at a higher temperature (1000 °C), and the higher presence of OH/R groups at the carbon surface (the Supporting Information, Figure S6A–C). However, approximately 85% of the carbon was present in all cases in C–C sp²-hybridization (the Supporting Information, Figure S6D). The higher sensitivity of carbon to Raman scattering results in a lower intensity of the signals from metal oxide domains. Therefore, XRD was used to characterize the metal oxide domains.

The XRD patterns of the samples after thermal treatment at 1000 °C are displayed in Figure 3B and for the samples treated at 850 °C in Figure S5B in the Supporting Information. Rietveld analysis was performed, and the data obtained are presented in Table 3. In the sample NbO_x-850, we confirmed orthorhombic *Pbam* Nb_{16.8}O₄₂ (Nb₂O₅) with an average domain size of approximately 30 nm. At higher temperatures (NbO_x-1000) mainly a tetragonal *I4/mmm* Nb₂O₅ structure was formed with a low domain size (16 nm), also containing 11 wt% of monoclinic *A2/m* Nb₁₂O₂₉ crystals and 5 wt% of orthorhombic *Pbam* Nb_{16.8}O₄₂ (40–50 nm). At 1000 °C, the formed phase has been reported by Komoda et al. as a metastable intermediate phase during the transformation between o-Nb₂O₅ and m-Nb₂O₅ and it consist mainly of t-Nb₂O₅ with some m-Nb₂O₅ crystals.^[14] Therefore, we related the lower domain size of t-Nb₂O₅ in the fibers with its metastable nature. In our work, the formed monoclinic structure Nb₁₂O₂₉ (6-Nb₂O_{4.83}) displayed oxygen vacancies, which was related to the low partial pressure of CO₂.^[13b]

For the sample TiNb₆O_x-850, broad peaks of monoclinic *A2/m* Ti₃Nb₁₀O₂₉ (TiO₂·2.5Nb₂O₅) were observed together with peaks of a titanium-rich phase, tetragonal *P42/mnm*

Table 3. Rietveld analysis of the XRD pattern for the metal oxide/carbon fibers.

Sample	Crystal phase	Lattice parameter	Crystallite size [nm]	Content [wt%]
NbO _x -1000	Nb ₂ O ₅ tetragonal <i>I4/mmm</i> (PDF-72-1484)	<i>a</i> = 2.044 nm, <i>c</i> = 0.383 nm	16	84
	Nb ₁₂ O ₂₉ monoclinic <i>A2/m</i> (PDF-73-1610)	<i>a</i> = 1.569 nm, <i>b</i> = 0.383 nm, <i>c</i> = 2.067 nm	40	11
	Nb _{16.8} O ₄₂ orthorhombic <i>Pbam</i> (PDF-27-1003)	<i>a</i> = 0.617 nm, <i>b</i> = 2.933 nm, <i>c</i> = 0.393 nm	50	5
TiNb ₆ O _x -1000	Ti ₂ Nb ₁₀ O ₂₉ monoclinic <i>A2/m</i> (PDF-72-0159)	<i>a</i> = 1.557 nm, <i>b</i> = 0.381 nm, <i>c</i> = 2.054 nm	27	96
	Ti _{0.712} Nb _{0.288} O ₂ tetragonal <i>P42/mnm</i> (PDF-72-7371)	<i>a</i> = 0.464 nm, <i>c</i> = 0.299 nm	41	4
TiNb ₂ O _x -1000	Ti ₂ Nb ₁₀ O ₂₉ monoclinic <i>A2/m</i> (PDF-72-0159)	<i>a</i> = 1.557 nm, <i>b</i> = 0.381 nm, <i>c</i> = 2.054 nm	27	79
	Ti _{0.712} Nb _{0.288} O ₂ tetragonal <i>P42/mnm</i> (PDF-72-7371)	<i>a</i> = 0.464 nm, <i>c</i> = 0.299 nm	38	21

Ti_{0.712}Nb_{0.288}O₂. At high temperature (TiNb₂O_x-1000), the same peak position was observed with a lower FWHM; the latter results from increased crystallite size from 27 to 39 nm for the monoclinic and tetragonal phase, respectively. The sample TiNb₆O_x-850 displayed mixed peaks of the crystal phases present in the samples NbO_x-850 and TiNb₂O_x-850, orthorhombic Nb₂O₅ and monoclinic Ti₂Nb₁₀O₂₉. The sample TiNb₆O_x-1000 mainly contained monoclinic Ti₂Nb₁₀O₂₉ with approximately 4 wt% of rutile and had a higher average coherence length of around 27 and 41 nm for the monoclinic and tetragonal phase, respectively. The formation of monoclinic Ti₂Nb₁₀O₂₉ occurred above 800 °C,^[10a] which was lower than the minimum temperature needed for the formation of t-Nb₂O₅ (1000 °C).^[14] This explains the larger domain size of monoclinic Ti₂Nb₁₀O₂₉ compared to t-Nb₂O₅ for samples synthesized at 1000 °C.

To better understand the chemical and electronic state of the elements present, XPS and FTIR were performed. The FTIR spectra (Figure 3D) displayed strong bands between 1000 and 500 cm⁻¹. Within this range, the peak at 966 cm⁻¹ for TiNb₂O_x-1000 shifted to 954 cm⁻¹ for NbO_x-1000. This peak has been observed in m-Nb₂O₅ and is related to the existence of crystallographic shear plane.^[41] For the samples containing Ti, an additional peak was observed at 893 cm⁻¹, arising from stretching vibrations in the TiO₆ units.^[24] The peak at approximately 650 cm⁻¹ is attributable to Nb–O–Nb bridging bond, and the peak at 793 cm⁻¹ is related to the Nb–O–Nb co-linear bonding formed by the array of NbO₆ units.^[41] The latter peak was shifted to lower wavelengths for the samples containing Ti (770 cm⁻¹), which is related to the stretching vibration of Ti–O–Ti typically at a lower wavelength (700–780 cm⁻¹).^[24,42] Based on the FTIR results, we can confirm the formation of shared octahedra with either Ti or Nb.

The XPS results allowed us to evaluate the change in niobium and titanium binding energy when both elements were incorporated in a hybrid system. High-resolution measurements of Nb 3d of the samples synthesized at 850 °C (the Supporting information, Figure S5C) showed that the binding energy of the main component 3d_{5/2} was located at 206.8 ± 0.1 eV, which is similar to the binding energy of Nb⁵⁺ in m-Nb₂O₅ and Ti₂Nb₁₀O₂₉ samples.^[10a,15a] A second component with a binding energy of 203.6 ± 0.1 eV corresponding to Nb²⁺ was present in low concentrations of 1, 5, and 9 at% for NbO_x-850, TiNb₂O_x-850, and TiNb₆O_x-850, respectively. This component was attrib-

uted to low amounts of incompletely oxidized NbC or NbO. High-resolution measurements of Nb 3d of the samples synthesized at 1000 °C (Figure 3C) show that the main component 3d_{5/2} was located at 207.2 ± 0.1 eV, corresponding to Nb⁵⁺ (207.2 eV).^[43] A second component at approximately 203.6 ± 0.1 eV (corresponding to Nb²⁺) was only present in the samples TiNb₂O_x-1000 and TiNb₆O_x-1000 with 2 and 1 at% of the total Nb species, respectively. High-resolution measurements of Ti 2p (the Supporting Information, Figure S6) of the samples displayed a low intensity Ti signal with a binding energy of approximately 458.7 eV, indicating that Ti existed as Ti⁴⁺. We observed no effect on the oxidation state of the Nb by incorporation of Ti and we confirmed that all samples displayed octahedra of Ti⁴⁺ and Nb⁵⁺.

Electrochemical characterization

Depending on the crystal phase present and crystal coherence length, differences in the electrochemical performance were observed. Comparing the CVs of the samples calcined at 850 and 1000 °C after five cycles at 0.1 mVs⁻¹ (Figure 4A and B), the samples synthesized at higher temperatures displayed sharper current peaks, indicating that Li⁺ intercalation and deintercalation occurred within a narrower potential window. NbO_x-850 displayed a broad cathodic peak at 1.65 V and an anodic peak at 1.88 V (peak separation ΔE_p = 0.23 V) from the valence variation of Nb⁵⁺/Nb⁴⁺.^[12b] For the samples containing Ti, similar cyclic voltammograms were observed, indicating that either Li⁺ intercalation–deintercalation takes place either as a one-step process or as two steps with overlapping energies, Nb⁵⁺/Nb⁴⁺ and Ti⁴⁺/Ti³⁺.

For all samples during the first cycle, a reduction peak was observed below 1 V versus Li/Li⁺ related to the reduction of the ethyl/methyl carbonate-based electrolyte (see the Supporting Information, Figure S7A–C),^[44] forming a stable solid–electrolyte–interface layer, as seen from the next cycles. For the sample NbO_x-1000, in the first cycle during the lithiation step, a first reduction peak was observed at 1.68 V versus Li/Li⁺, which was attributed to the Nb⁵⁺/Nb⁴⁺ redox couple, which increases and displaces to lower voltages during the subsequent cycles (see the Supporting Information, Figure S7A).^[15a,45] Further cathodic peaks were observed at approximately 1.21 V, which were attributed to the Nb⁴⁺/Nb³⁺ re-

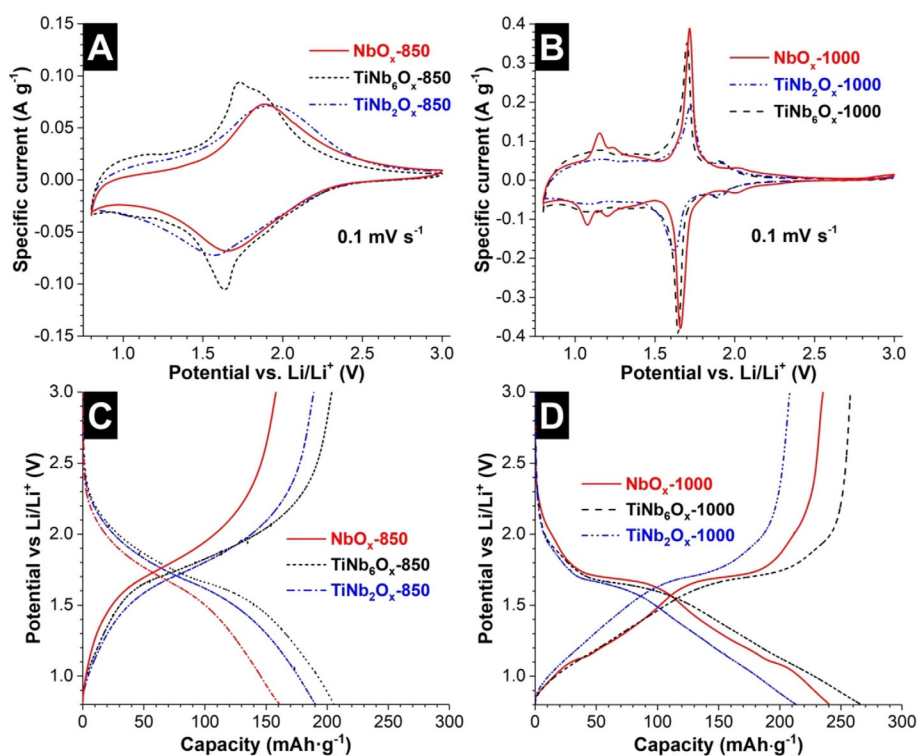
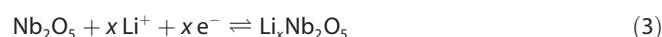
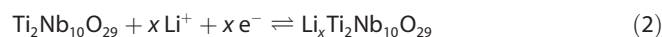


Figure 4. Electrochemical characterization after five cycles in half-cell configuration of metal oxide/carbon hybrid nanofibers synthesized at 850 (A,C) and 1000 °C (B,D) by cyclic voltammetry at 0.1 mV s⁻¹ (A,B) and galvanostatic charge/discharge (C,D) at 0.025 A g⁻¹ from 3.0–0.8 V vs. Li/Li⁺.

duction reaction.^[15a,45] During delithiation, the corresponding anodic peaks were observed, and the peaks were shifted to lower voltages with the subsequent cycles because of the polarization effect of the electrolyte during the first cycle.^[10a] This sample also had cathodic and anodic peaks at 2.0 V versus Li/Li⁺. These peaks had only been observed in t-Nb₂O₅ and m-Nb₂O₅ compared to different Nb₂O₅ polymorphs^[15a] and are related to Li⁺ insertion in the crystal structure. For the Ti-containing samples during the lithiation step, an initial cathodic peak was observed at 1.9 V, which was attributed to the Ti⁴⁺/Ti³⁺ redox couples,^[10a] followed by a sharp anodic peak at 1.63 V and broad peaks between 0.9 and 1.5 V versus Li/Li⁺. As reported by Pham-Cong et al., the peak at 1.63 V corresponded to the voltage platforms in which Li⁺ intercalates into Ti₂Nb₁₀O₂₉.^[10a] The CV of the TiNb₂O_x-1000 sample displayed a similar shape as the CV of TiNb₆O_x-1000, but with a higher transport limitation, as observed from the higher ΔE_p and the lower amplitude of the anodic and cathodic peaks (Figure 4B), which is related to the larger amount of large tetragonal Ti_{0.712}Nb_{0.288}O₂ crystals in the TiNb₂O_x-1000 sample.

The capacity during lithiation and delithiation was determined from the GCPL voltage profiles after five cycles at 0.025 A g⁻¹ (Figure 4C–D). The capacity values during delithiation (reversible capacity) of 161, 190, and 205 mAh g⁻¹ were obtained for NbO_x-850, TiNb₂O_x-850, and TiNb₆O_x-850, respectively. Correlating these values with the crystal phases present, we observed higher values for the samples containing Ti because of the formation of monoclinic Ti₂Nb₁₀O₂₉. These crystals, already formed at low temperatures, displayed a higher capaci-

ty than orthorhombic Nb_{16.8}O₄₂.^[10a,15a] At higher temperatures (NbO_x-1000), o-Nb₂O₅ transformed to t-Nb₂O₅ and m-Nb₂O₅, with an initial reversible capacity of 243 mAh g⁻¹ (normalized to metal oxide content: 277 mAh g⁻¹). The samples TiNb₆O_x-1000 and TiNb₂O_x-1000 displayed initial capacity values of 267 and 216 mAh g⁻¹, respectively, during the delithiation step; when normalized to the metal-oxide content, the values were 303 and 245 mAh g⁻¹, respectively. The different capacities were related to the crystal phases present in the system. Ti–Nb–O compounds have different theoretical capacities depending on the composition. The TiNb₆O_x-1000 sample contains mainly monoclinic Ti₂Nb₁₀O₂₉ crystals. By increasing the Ti content (TiNb₂O_x-1000), TiNb₂O₇ was not formed but the titanium excess precipitated in a tetragonal TiO₂ phase with a lower capacity. All samples displayed a voltage plateau in the region of 1.8–1.6 V versus Li/Li⁺ and an almost linear increase of the potential with the capacity below 1.5 V versus Li/Li⁺, which was in agreement with the measured CVs. The overall Li⁺-insertion/extraction reaction mechanism can be described by Equation (2) from Ref. [9] and Equation (3) from Ref. [10a]:



The rate behavior was characterized by GCPL between 0.025 (0.1C) and 5 A g⁻¹ (20C), and the data are shown in Figure 5A and B. The C rates were calculated based on a maximum capacity of 250 mAh g⁻¹. Comparing the samples synthesized at

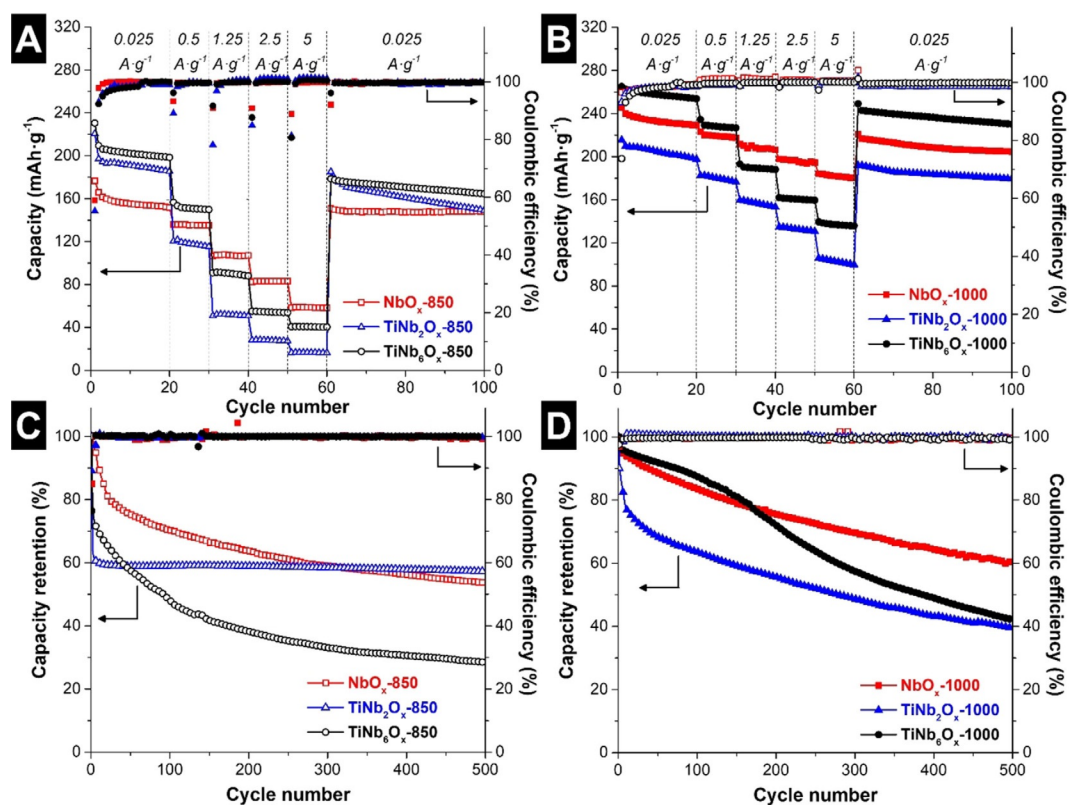


Figure 5. Rate handling performance of metal oxide/carbon hybrid nanofibers synthesized at 850 (A) and 1000 °C (B). Capacity retention during galvanostatic charge/discharge cycling at 2.5 A g⁻¹ (10C) from 0.8 to 3 V vs. Li/Li⁺ for half-cell configuration for nanofibers synthesized at 850 °C (C) and 1000 °C (D).

low and high temperatures, the lower Li-ion diffusion for the Ti-containing samples treated at 850 °C may be attributed to the incomplete phase transformations of TiO₂ and Nb₂O₅. For the samples synthesized at 850 °C, the more amorphous structure had a direct effect on the rate performance of the system. Although the *o*-Nb₂O₅ crystals with a higher coherence length maintained 40% of the initial capacity at 5 A g⁻¹, the systems containing Ti displayed a higher delithiation capacity but a lower capacity retention, 21% and 10% for TiNb₆O_x-850 and TiNb₂O_x-850, respectively. After 100 cycles at a low charge/discharge rate (Figure 5A), the sample displaying the higher capacity retention was NbO_x-850 (84%) followed by TiNb₆O_x-850 (71%) and TiNb₂O_x-850 (67%). As evidenced by the XRD pattern (see the Supporting Information, Figure S5B), NbO_x and TiNb₆O_x-850 contained orthorhombic Nb₂O₅, which is known to have a high rate handling capability and rapid ionic transport.^[9] The almost empty octahedral sites generate pathways with low energy barriers for Li-ion transport but without significant changes to the crystal lattice, explaining the improved rate performance and the performance stability.^[16]

For the samples treated at higher temperatures, an overall increase of the initial capacity was observed. This was related to the higher intercalation capacity of the newly formed *t*-Nb₂O₅ phase and the further crystallization of the Ti₂Nb₁₀O₂₉ phase. The most severe capacity fading (Figure 5B) was displayed by the two samples containing Ti, maintaining 50% and 53% of the capacity at 5 A g⁻¹, whereas the sample NbO_x-1000 maintained 78% of the capacity. After 100 cycles at a low

charge/discharge rate of 0.1C, all samples maintained more than 83% of their initial capacity. The big difference between these samples was related to the smaller crystal size of the *t*-Nb₂O₅ in NbO_x-1000 (16 nm), compared to the Ti₂Nb₁₀O₂₉ crystals present in the Ti-containing samples (27 nm). The smaller crystal size leads to shorter diffusion paths and improved Li⁺ diffusion kinetics. Furthermore, *t*-Nb₂O₅ is known to have excellent rate handling and cycling performance.^[14,15b] In this structure, owing to the planar arrangement of the Nb atoms parallel to the *b*-axis, the insertion of Li⁺ expands the spacing along the *c*- and *a*-axis.^[14] For the samples containing Ti, the higher capacity fading is related to the higher domain size of Ti₂Nb₁₀O₂₉ and the co-existence of tetragonal crystals (40 nm). The more packed tetragonal structure, with a higher edge sharing of oxygen, displayed a higher change in cell volume during Li⁺ intercalation.^[46]

The stability of the electrodes at high rates (10C) is presented in Figure 5C and D after 500 cycles. The samples synthesized at higher temperatures also displayed a higher stability at a high rate, maintaining between 40–60% of the initial charge capacity. For the Ti-containing samples synthesized at low temperatures, the capacity fading was proportional to the capacity of the material at a high rate, namely, 71% and 42% for TiNb₆O_x-850 and TiNb₂O_x-850, respectively. The sample NbO_x-850 displayed a moderate capacity fading (46%) although it had a higher capacity at high rates.

The differences observed in the electrochemical performance at high rates are related to the mechanism for Li⁺ in-

tercalation in monoclinic $\text{Ti}_2\text{Nb}_{10}\text{O}_{29}$ and $\text{t-Nb}_2\text{O}_5$ crystal phases. Monoclinic $\text{Ti}_2\text{Nb}_{10}\text{O}_{29}$ displayed a monoclinic shear ReO_3 structure (Figure 6A),^[10a] in which the octahedra of NbO_6 and TiO_6 form 2D layers with tunnel-like interstitial space for Li^+ insertion.^[10a,18] Theoretically, up to 22Li^+ can intercalate into

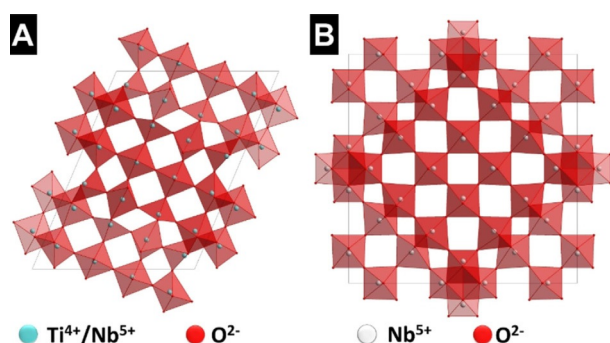


Figure 6. Crystal structures of $\text{Ti}_2\text{Nb}_{10}\text{O}_{29}$ monoclinic $A2/m$, parallel projection view along the b -axis (A), and Nb_2O_5 tetragonal $I4/mmm$, parallel projection view along the c -axis (B).

$\text{Ti}_2\text{Nb}_{10}\text{O}_{29}$ according to Equation (2). During the lithiation step of $\text{Ti}_2\text{Nb}_{10}\text{O}_{29}$, initially a solid-solution reaction takes place, followed by a two-phase coexistence and further solid-solution reaction.^[10a,47] The phase $\text{t-Nb}_2\text{O}_5$ was also formed by 2D layers of NbO_6 octahedra (Figure 6B).^[14] Compared to monoclinic $\text{Ti}_2\text{Nb}_{10}\text{O}_{29}$, more oxygen atoms were corner-shared instead of edge-shared in $\text{t-Nb}_2\text{O}_5$ owing to the difference in oxidation state (Ti^{4+} vs. Nb^{5+}).^[48] As reported by Kodama et al., between 3–1.2 V versus Li/Li^+ , Li^+ insertion in the $\text{t-Nb}_2\text{O}_5$ structure occurs between the 2D layers, which maintains the original crystal structure without the appearance of any new phase.^[14] In situ XRD measurements of $\text{t-Nb}_2\text{O}_5$ (the Supporting Information, Figure S8) indicated that from 3–1.2 V lithium insertion takes place without the formation of any new phase, and up to $x=2.09$ in $\text{Li}_x\text{Nb}_2\text{O}_5$ at 1.15 V. Lithium insertion into $\text{t-Nb}_2\text{O}_5$ was observed with a shift in peak positions to lower angles and a decrease in peak intensities. In the region between 1.2–0.8 V, we can report for the first time that further lithium ion insertion occurred into the structure, reaching a maximum

value of $x=2.73$ while maintaining the original crystal structure and without any appearance of a new phase.

Comparing the obtained results to the literature (Table 4), our capacity values are higher, not just based on the metal oxide mass but especially when normalized to the full electrode mass. For a better comparison, the operating voltage has been added to Table 4 because a significant contribution to the capacity occurs between 1–0.8 V versus Li/Li^+ . All electrodes reported so far have been composite electrodes containing between 25–30 wt% of additives, whereas our electrodes contain no additives and only 12 wt% of carbon maintained within the continuous free-standing fiber electrodes. The rate handling of our samples is comparable to reported values; however, we achieved this performance with significantly higher mass loading and much thicker electrodes. Most of the electrodes were produced by performing the doctor-blade technique directly on copper as the current collector, having a low thickness and mass loading (15–20 μm and 0.7–1.7 mg cm^{-2} , respectively) compared to our electrodes (100 μm and 4.6 mg cm^{-2} , respectively), which are free of polymer binder and conductive additives.

Comparing the energy demand and synthesis efforts to produce our electrodes with those of the literature (Table 4), the synthesis of our hybrid fiber mats offers several advantages:

1) Facile synthesis. Two heat treatments are involved: first, synthesis under argon at 1700 °C, and second, heat treatment under oxidizing atmosphere at 850–1000 °C. For the characterization of the intermediate products, these two steps were separated in our work. However, these two treatment steps can occur in one synthesis, in the same oven using two atmospheres, with the second step directly conducted during the cooling phase of the first step.

2) No need for conductive additives or binder. In the literature, the active materials are mainly produced using only the oxidation step, the electrode preparation employs between 25–30 wt% of conductive additives and polymer binder. Conductive additives, such as carbon black, are synthesized in a separate production step at temperatures between 1600–2000 °C; in addition, there is no need to employ binders, which often contain fluorine-based polymers.

Table 4. Comparison of the different Ti–Nb oxide-containing electrodes for battery-like systems. The electrode thickness or mass loading are reported in parentheses in the column for electrode preparation.

Sample	Electrode preparation ^[a]	Capacity ^[b] [mAh g ⁻¹]	Capacity retention ^[c] [V vs. Li/Li^+]	Reference
$\text{t-Nb}_2\text{O}_5/\text{C}$ nanofibers	binder free (70–100 $\mu\text{m}/4.6 \text{ mg cm}^{-2}$)	243 (mo: 277)	78% at 5 A g^{-1} (0.8–3.0 V)	this work; 1 M LiPF_6 in EC/DMC
$\text{t-Nb}_2\text{O}_5$ particles	CA and PTFE (n.r.)	161 (mo: 230)	n.r. (1.2–3.0 V)	Ref. [14]; 1 M LiPF_6 in EC/DMC
$\text{m-Nb}_2\text{O}_5$ ultrafine fibers	CA and PVdF (20 μm)	157 (mo: 242)	n.r. (1.0–2.6 V)	Ref. [15a]; 1 M LiPF_6 in EC/DMC
$\text{Ti}_2\text{Nb}_{10}\text{O}_{29}/\text{C}$ nanofibers	binder free (70–100 $\mu\text{m}/4.1 \text{ mg cm}^{-2}$)	267 (mo: 303)	53% at 5 A g^{-1} (0.8–3.0 V)	this work; 1 M LiPF_6 in EC/DMC
$\text{Ti}_2\text{Nb}_{10}\text{O}_{29}$ macroporous particles	CA and PVdF (1.1 mg cm^{-2})	147 (mo: 210)	64% at 7.7 A g^{-1} (1.0–3.0 V)	Ref. [24]; 1 M LiPF_6 in EC/DMC
$\text{Ti}_2\text{Nb}_{10}\text{O}_{29}$ nanofibers	CA and CMC (0.7 mg cm^{-2})	220 (mo: 315)	60% at 5 A g^{-1} (1.0–3.0 V)	Ref. [10a]; 1 M LiPF_6 in EC/DMC
TiNb_2O_7 nanoporous particles	CA and PVdF (1.7 mg cm^{-2})	211 (mo: 281)	69% at 7.7 A g^{-1} (1.0–3.0 V)	Ref. [47]; 1 M LiPF_6 in EC/DMC/DEC ^[d]

[a] For conventional electrode preparation, conductive additives (CA) and a polymer binder are added to the metal oxide particles. Commonly used polymer binders are polyvinylidene fluoride (PVdF), polytetrafluorethylene (PTFE), and carboxymethyl cellulose (CMC). [b] The reversible capacity values are normalized to the total electrode mass and to the metal oxide mass (mo). [c] Non-reported values are also indicated as n.r. [d] DEC: diethyl carbonate.

3) Superior conductivity of the fiber mats compared to polymer bound electrodes with a similar thickness ($\approx 100 \mu\text{m}$). The samples NbO_x -1000 and TiNb_6O_x -1000 displayed a very low resistivity 0.07 ± 0.01 and $0.11 \pm 0.02 \Omega\cdot\text{cm}$, respectively, when used as fiber mats. When the fibers were crushed and mixed with a conductive additive (carbon black, 5 wt%) and a polymer binder (PTFE, 5 wt%) to reconsolidate the powders, a higher resistivity was measured for NbO_x -1000 and TiNb_6O_x -1000 polymer-bound electrodes, 0.46 ± 0.06 and $0.62 \pm 0.10 \Omega\cdot\text{cm}$, respectively. Although the polymer-bound electrodes displayed a higher amount of conductive carbon, 12 wt% of in situ-synthesized carbon and an additional 5 wt% of conductive additive, only a superior conductivity was observed when the continuous fiber structure was maintained.

Conclusions

The synthesis and electrochemical behavior of free-standing titanium–niobium oxide/carbon hybrid fibers was investigated. The novelty of our work is based on: (1) synthesis for continuous metal oxide/carbon hybrid fibers as free-standing electrodes, (2) first work on one-pot synthesis for tetragonal Nb_2O_5 (t- Nb_2O_5)/C and monoclinic $\text{Ti}_2\text{Nb}_{10}\text{O}_{29}$ /C hybrid materials, and (3) analysis of the effect of Ti addition to the material and the electrochemical properties compared to pristine Nb_2O_5 .

Our one-pot synthesis for the electrode preparation free of polymer binders and conductive additives offers a more sustainable approach compared to traditional electrode preparation techniques. A significant amount of energy and cost can be avoided by using only one synthesis process for the free-standing electrode preparation. In our one-pot synthesis process, we demonstrated a strategy to tailor the crystalline structure of the metal oxide formed at high temperatures (850–1000 °C) while maintaining the highly graphitic nature of the carbon phase and maintaining the continuous fiber morphology.

When only Nb was present at low temperatures, orthorhombic Nb_2O_5 (o- Nb_2O_5) formed, whereas at high temperatures t- Nb_2O_5 was preferred. In the presence of Ti, monoclinic $\text{Ti}_2\text{Nb}_{10}\text{O}_{29}$ was formed already at low temperatures, and the stoichiometric excess precipitated in either Nb- or Ti-rich phases. Depending on the crystal phase present and crystal coherence length, differences in the electrochemical performance was observed. The samples synthesized at higher temperatures displayed sharper current peaks in cyclic voltammograms, indicating that Li^+ intercalation and deintercalation occurred within a narrow potential window owing to faster kinetics of these systems. Reduction reactions related to $\text{Nb}^{5+}/\text{Nb}^{4+}$, $\text{Nb}^{4+}/\text{Nb}^{3+}$, and $\text{Ti}^{4+}/\text{Ti}^{3+}$ redox couples led to high capacity values for NbO_x -1000, TiNb_6O_x -1000, and TiNb_2O_x -1000 prepared at 1000 °C, corresponding to 243, 267, and 216 mAh g^{-1} , respectively; when normalized to the metal-oxide content, these values corresponded to 277, 303, and 245 mAh g^{-1} , respectively.

Samples synthesized at 850 °C showed a lower crystallinity, which reduced the rate performance of the system. For the samples treated at higher temperatures, the highest capacity

fading was displayed by the two samples containing Ti, maintaining 50% and 53% of the capacity at 5 Ag^{-1} , whereas the sample NbO_x -1000 maintained 78% of the capacity. After 100 cycles at a low charge/discharge rate of 0.1C, all samples maintained more than 83% of the initial capacity. The big difference between these samples is related to the smaller crystal size of t- Nb_2O_5 in NbO_x -1000 (16 nm) compared to the $\text{Ti}_2\text{Nb}_{10}\text{O}_{29}$ crystals present in the Ti-containing samples (27 nm) and the Li^+ intercalation kinetics in the crystal phase. The highest capacity was obtained for the sample with the highest content of monoclinic $\text{Ti}_2\text{Nb}_{10}\text{O}_{29}$, whereas the highest rate performance and stability was obtained for the samples containing either o- or t- Nb_2O_5 . In these crystal phases, the almost empty sites between the layers formed by NbO_6 octahedra generate pathways with low energy barriers for Li-ion transport and no phase transformation occurs.

Comparing the obtained results to the literature, the capacity values obtained in this work are higher, based on the metal-oxide mass and electrode mass, because no polymers or conductive additives were added. Although the overall rate handling was comparable to reported values, we achieved this performance by using free-standing fiber mats with much higher thickness and much larger mass loading (between 3–6 times higher). The improved high rate performance of the hybrid fibers resulted from the excellent charge propagation in the continuous nanofiber network compared to conventional polymer-bound powder electrodes.

Acknowledgements

This work was part of the Carbon Metal Oxide Nanohybrid project (CarMON) supported by the by the Leibniz Association (SAW-2017). We also acknowledge funding from the German Federal Ministry for Economic Affairs and Energy (BMWi) in support of the HyBaCap project (award number 03ET6113C). The authors thank Prof. Eduard Arzt (INM) for his continuing support, and Soumyadip Choudhury and Anna Schreiber (all at INM) for useful discussions and technical support.

Conflict of interest

The authors declare no conflict of interest.

Keywords: electrochemical energy storage • nanostructures • niobium pentoxide • organic-inorganic hybrid composites • titanium-niobium oxide

- [1] M. Broussely, G. Archdale, *J. Power Sources* **2004**, *136*, 386–394.
- [2] P. Simon, Y. Gogotsi, *Nat. Mater.* **2008**, *7*, 845–854.
- [3] a) B. Scrosati, J. Hassoun, Y.-K. Sun, *Energy Environ. Sci.* **2011**, *4*, 3287–3295; b) M. Armand, J. M. Tarascon, *Nature* **2008**, *451*, 652–657.
- [4] a) D. Zhao, J. Qin, L. Zheng, M. Cao, *Chem. Mater.* **2016**, *28*, 4180–4190; b) S. Fleischmann, A. Tolosa, M. Zeiger, B. Krüner, N. J. Peter, I. Grobelsek, A. Quade, A. Kruth, V. Presser, *J. Mater. Chem. A* **2017**, *5*, 2792–2801.
- [5] a) S. Fleischmann, M. Zeiger, N. Jäckel, B. Krüner, V. Lemkova, M. Widmayer, V. Presser, *J. Mater. Chem. A* **2017**, *5*, 13039–13051; b) E. Lim, C. Jo,

- H. Kim, M.-H. Kim, Y. Mun, J. Chun, Y. Ye, J. Hwang, K.-S. Ha, K. C. Roh, K. Kang, S. Yoon, J. Lee, *ACS Nano* **2015**, *9*, 7497–7505.
- [6] V. Augustyn, P. Simon, B. Dunn, *Energy Environ. Sci.* **2014**, *7*, 1597–1614.
- [7] A. S. Aricò, P. Bruce, B. Scrosati, J.-M. Tarascon, W. Van Schalkwijk, *Nat. Mater.* **2005**, *4*, 366–377.
- [8] a) M. R. Lukatskaya, B. Dunn, Y. Gogotsi, *Nat. Commun.* **2016**, *7*, 12647; b) M. Zeiger, T. Ariyanto, B. Krüner, N. J. Peter, S. Fleischmann, B. J. M. Etzold, V. Presser, *J. Mater. Chem. A* **2016**, *4*, 18899–18909.
- [9] V. Augustyn, J. Come, M. A. Lowe, J. W. Kim, P.-L. Taberna, S. H. Tolbert, H. D. Abruña, P. Simon, B. Dunn, *Nat. Mater.* **2013**, *12*, 518–522.
- [10] a) D. Pham-Cong, J. Kim, V. T. Tran, S. J. Kim, S.-Y. Jeong, J.-H. Choi, C. R. Cho, *Electrochim. Acta* **2017**, *236*, 451–459; b) M. Xie, X. Sun, C. Zhou, A. S. Cavanagh, H. Sun, T. Hu, G. Wang, J. Lian, S. M. George, *J. Electrochem. Soc.* **2015**, *162*, A974–A981.
- [11] R. A. Rani, A. S. Zoofakar, A. P. O'Mullane, M. W. Austin, K. Kalantar-Zadeh, *J. Mater. Chem. A* **2014**, *2*, 15683–15703.
- [12] a) M. V. Reddy, R. Jose, A. Le Viet, K. I. Ozoemena, B. V. R. Chowdari, S. Ramakrishna, *Electrochim. Acta* **2014**, *128*, 198–202; b) A. Tolosa, B. Krüner, S. Fleischmann, N. Jäckel, M. Zeiger, M. Aslan, I. Grobelsek, V. Presser, *J. Mater. Chem. A* **2016**, *4*, 16003–16016.
- [13] a) J. W. Kim, V. Augustyn, B. Dunn, *Adv. Energy Mater.* **2012**, *2*, 141–148; b) R. J. Cava, B. Batlogg, J. J. Krajewski, H. F. Poulsen, P. Gammel, W. F. Peck, L. W. Rupp, *Phys. Rev. B* **1991**, *44*, 6973–6981.
- [14] R. Kodama, Y. Terada, I. Nakai, S. Komaba, N. Kumagai, *J. Electrochem. Soc.* **2006**, *153*, A583–A588.
- [15] a) A. L. Viet, M. V. Reddy, R. Jose, B. V. R. Chowdari, S. Ramakrishna, *J. Phys. Chem. C* **2010**, *114*, 664–671; b) L. Kong, X. Cao, J. Wang, W. Qiao, L. Ling, D. Long, *J. Power Sources* **2016**, *309*, 42–49.
- [16] J. Come, V. Augustyn, J. W. Kim, P. Rozier, P.-L. Taberna, P. Gogotsi, J. W. Long, B. Dunn, P. Simon, *J. Electrochem. Soc.* **2014**, *161*, A718–A725.
- [17] T. Brousse, D. Bélanger, J. W. Long, *J. Electrochem. Soc.* **2015**, *162*, A5185–A5189.
- [18] L. Yan, X. Rui, G. Chen, W. Xu, G. Zou, H. Luo, *Nanoscale* **2016**, *8*, 8443–8465.
- [19] N. G. Eror, *J. Solid State Chem.* **1981**, *38*, 281–287.
- [20] R. S. Roth, W. Coughanour, *J. Res. Natl. Bur. Stand.* **1955**, *55*, 209–214.
- [21] A. Wadsley, *Acta Crystallogr.* **1961**, *14*, 660–664.
- [22] J.-T. Han, J. B. Goodenough, *Chem. Mater.* **2011**, *23*, 3404–3407.
- [23] J.-T. Han, Y.-H. Huang, J. B. Goodenough, *Chem. Mater.* **2011**, *23*, 2027–2029.
- [24] S. Lou, X. Cheng, Y. Zhao, A. Lushington, J. Gao, Q. Li, P. Zuo, B. Wang, Y. Gao, Y. Ma, C. Du, G. Yin, X. Sun, *Nano Energy* **2017**, *34*, 15–25.
- [25] S. Jayaraman, V. Aravindan, P. Suresh Kumar, W. Chui Ling, S. Ramakrishna, S. Madhavi, *ACS Appl. Mater. Interfaces* **2014**, *6*, 8660–8666.
- [26] C. Lin, G. Wang, S. Lin, J. Li, L. Lu, *Chem. Commun.* **2015**, *51*, 8970–8973.
- [27] A. Tolosa, B. Krüner, N. Jäckel, M. Aslan, C. Vakifahmetoglu, V. Presser, *J. Power Sources* **2016**, *313*, 178–188.
- [28] J. S. Atchison, M. Zeiger, A. Tolosa, L. M. Funke, N. Jäckel, V. Presser, *RSC Adv.* **2015**, *5*, 35683–35692.
- [29] C. A. Schneider, W. S. Rasband, K. W. Eliceiri, *Nat. Methods* **2012**, *9*, 671–675.
- [30] D. Weingarh, M. Zeiger, N. Jäckel, M. Aslan, G. Feng, V. Presser, *Adv. Energy Mater.* **2014**, *4*, 1400316.
- [31] B. S. Buyuktas, *Transition Met. Chem.* **2006**, *31*, 786–791.
- [32] Z. Jiang, W. E. Rhine, *Chem. Mater.* **1991**, *3*, 1132–1137.
- [33] P. Griesmar, G. Papin, C. Sanchez, J. Livage, *Chem. Mater.* **1991**, *3*, 335–339.
- [34] S. Doeuff, M. Henry, C. Sanchez, J. Livage, *J. Non-Cryst. Solids* **1987**, *89*, 206–216.
- [35] R. H. Sui, A. S. Rizkalla, P. A. Charpentier, *J. Phys. Chem. B* **2006**, *110*, 16212–16218.
- [36] a) C. Zhang, S. J. Kim, M. Ghidui, M.-Q. Zhao, M. W. Barsoum, V. Nicolosi, Y. Gogotsi, *Adv. Funct. Mater.* **2016**, *26*, 4143–4151; b) C. Zhang, M. Beidaghi, M. Naguib, M. R. Lukatskaya, M.-Q. Zhao, B. Dyatkin, K. M. Cook, S. J. Kim, B. Eng, X. Xiao, D. Long, W. Qiao, B. Dunn, Y. Gogotsi, *Chem. Mater.* **2016**, *28*, 3937–3943; c) C. Zhang, R. Maloney, M. R. Lukatskaya, M. Beidaghi, B. Dyatkin, E. Perre, D. Long, W. Qiao, B. Dunn, Y. Gogotsi, *J. Power Sources* **2015**, *274*, 121–129.
- [37] K. Kim, S.-G. Woo, Y. N. Jo, J. Lee, J.-H. Kim, *Electrochim. Acta* **2017**, *240*, 316–322.
- [38] H. J. T. Ellingham, *J. Soc. Chem. Ind.* **1944**, *10*, 125–133.
- [39] A. C. Ferrari, D. M. Basko, *Nat. Nanotechnol.* **2013**, *8*, 235–246.
- [40] A. C. Ferrari, *Solid State Commun.* **2007**, *143*, 47–57.
- [41] T. Ikeya, M. Senna, *J. Non-Cryst. Solids* **1988**, *105*, 243–250.
- [42] E. D. Costa, C. O. Avellaneda, A. Pawlicka, *J. Mater. Sci.* **2001**, *36*, 1407–1410.
- [43] N. Özer, M. D. Rubin, C. M. Lampert, *Solar Energy Mater. Solar Cells* **1996**, *40*, 285–296.
- [44] D. Pham-Cong, J. H. Choi, J. Yun, A. S. Bandarenka, J. Kim, P. V. Braun, S. Y. Jeong, C. R. Cho, *ACS Nano* **2017**, *11*, 1026–1033.
- [45] M. Wei, K. Wei, M. Ichihara, H. Zhou, *Electrochem. Commun.* **2008**, *10*, 980–983.
- [46] J. Wang, J. Polleux, J. Lim, B. Dunn, *J. Phys. Chem. C* **2007**, *111*, 14925–14931.
- [47] B. Guo, X. Yu, X.-G. Sun, M. Chi, Z.-A. Qiao, J. Liu, Y.-S. Hu, X.-Q. Yang, J. B. Goodenough, S. Dai, *Energy Environ. Sci.* **2014**, *7*, 2220–2226.
- [48] M. Fehse, S. Cavaliere, P. E. Lippens, I. Savych, A. Iadecola, L. Monconduit, D. J. Jones, J. Rozière, F. Fischer, C. Tessier, L. Stievano, *J. Phys. Chem. C* **2013**, *117*, 13827–13835.

Manuscript received: October 10, 2017

Revised manuscript received: October 30, 2017

Accepted manuscript online: November 3, 2017

Version of record online: December 20, 2017

3.4 Continuous silicon oxycarbide fiber mats with tin nanoparticles as high capacity anode for lithium-ion batteries

Aura Tolosa,^{a, b} Mathias Widmaier,^{b, c} Benjamin Krüner,^{a, b}
John M. Griffin,^d and Volker Presser^{a, b}

^a INM - Leibniz Institute for New Materials, 66123 Saarbrücken, Germany

^b Department of Materials Science and Engineering, Saarland University, 66123 Saarbrücken, Germany

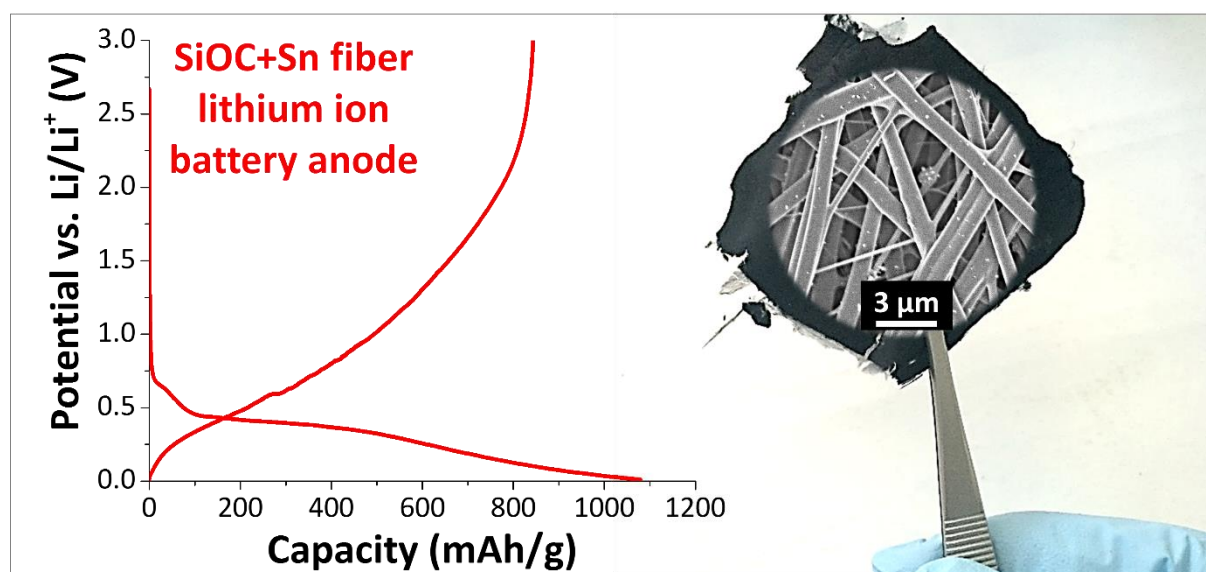
^c Robert Bosch GmbH, Robert-Bosch-Campus 1, 71272 Renningen, Germany

^d Department of Chemistry, Lancaster University, Lancaster, LA1 4YB, United Kingdom

Published in: Sustainable Energy Fuels, 2 (2018), 215-228

DOI: 10.1039/c7se00431a

Reproduced by permission of The Royal Society of Chemistry



Own contribution: Project management; paper writing; material synthesis; data analysis; measurements: SEM, TEM, EDX, FT-IR, Raman spectroscopy, electrochemical characterization



Cite this: *Sustainable Energy Fuels*,
2018, 2, 215

Continuous silicon oxycarbide fiber mats with tin nanoparticles as a high capacity anode for lithium-ion batteries†

Aura Tolosa,^a Mathias Widmaier,^{b,c} Benjamin Krüner,^a John M. Griffin^d
and Volker Presser^a

Continuous fiber mats are attractive electrodes for lithium-ion batteries, because they allow operation at high charge/discharge rates in addition to being free of polymer binders and conductive additives. In this work, we synthesize and characterize continuous Sn/SiOC fibers (diameter ca. 0.95 μm), as a Li-ion battery anode. Our synthesis employs electrospinning of a low-cost silicone resin, using tin acetate in a dual role both as a polymer crosslinker and as a tin precursor (6–22 mass%). The hybrid electrodes present very high initial reversible capacities (840–994 mA h g^{-1}) at 35 mA g^{-1} , and retain 280–310 mA h g^{-1} at 350 mA g^{-1} . After 100 cycles at 70 mA g^{-1} , the hybrid fibers maintained 400–509 mA h g^{-1} . Adding low amounts of Sn is beneficial not just for the crosslinking of the polymer precursor, but also to decrease the presence of electrochemically inactive silicon carbide domains within the SiOC fibers. Also, the metallic tin clusters contribute to a higher Li^+ insertion in the first cycles. However, high amounts of Sn decrease the electrochemical performance stability. In SiOC fibers synthesized at high temperatures (1200 $^{\circ}\text{C}$), the C_{free} phase has a significant influence on the stability of the system, by compensating for the volume expansion from the alloying systems (Sn and SiO_2), and improving the conductivity of the hybrid system. Therefore, a high amount of carbon and a high graphitization degree are crucial for a high conductivity and a stable electrochemical performance.

Received 5th September 2017
Accepted 20th October 2017

DOI: 10.1039/c7se00431a

rsc.li/sustainable-energy

1. Introduction

To meet the growing requirements for mobile electrochemical energy storage,¹ it is important to advance present-day electrode materials both in regard to charge/discharge rates (power) and storage capacity (energy).² Li-ion batteries (LIBs) present high energy density, being today the main choice for consumer electronics and electrical or hybrid vehicles.³ To further improve the capacity of LIBs, significant efforts have been dedicated to replacing graphite anodes (theoretical capacity $\approx 372 \text{ mA h g}^{-1}$) with other elements from group IV (Si, Sn, and Ge; cf. ref. 4) which undergo alloying reactions with lithium leading to high capacity values (4200, 1627, and 993 mA h g^{-1} theoretical capacity of Si, Ge, and Sn, respectively).⁵ Such high capacities are accomplished not without complications; for example, in the case of silicon, a complete lithiation ($\text{Li}_{22}\text{Si}_5$ alloy)

corresponds to a volumetric expansion of about 400%,⁶ leading to poor cycling and huge capacity fading. To improve the specific capacity and cycle life of anode materials, nanoparticles of Si, Sn, or Ge, have been synthesized in a carbon matrix^{5,6} to compensate for the volumetric changes (volume expansion of graphite $\approx 10\%$)⁵ and to improve the electrical conductivity of the system. These Si/C composite materials present a maximum theoretical capacity of 712 mA h g^{-1} , corresponding to 11.7 mass% Si, at which the volumetric expansion of Si can be compensated for by the presence of pores, without decreasing the volumetric capacity.⁶

Since the early work of Wilson and Dahn,⁷ polymer-derived SiOC materials have been investigated as an alternative to Si/C composites due to the lower cost of synthesis, high capacity values (between 500 and 900 mA h g^{-1}), and reduced capacity fading.^{6,8} Polymer-derived SiOC synthesized at 1000–1800 $^{\circ}\text{C}$ is predominately amorphous and consists of Si–O–C nano-domains engulfed by carbon.⁹ The latter is called free carbon (C_{free}), that is carbon beyond the stoichiometric amount necessary to saturate all the Si valences.⁹ The Si–O–C nano-domains consist of amorphous silica, and $\text{SiC}_x\text{O}_{4-x}$ tetrahedral units (with $1 \leq x \leq 4$).^{9,10} The microstructure and composition of SiOC depend on the precursor material and the pyrolysis temperature. Above 1000 $^{\circ}\text{C}$, carbon segregates and forms turbostratic graphite which encapsulates silica domains with local

^aINM – Leibniz Institute for New Materials, Campus D2 2, 66123 Saarbrücken, Germany. E-mail: volker.presser@leibniz-inm.de

^bDepartment of Materials Science and Engineering, Saarland University, Campus D2 2, 66123 Saarbrücken, Germany

^cRobert Bosch GmbH, Robert-Bosch-Campus 1, 71272 Renningen, Germany

^dDepartment of Chemistry, Lancaster University, Lancaster, LA1 4YB, UK

† Electronic supplementary information (ESI) available. See DOI: 10.1039/c7se00431a

precipitation of SiC by local carbothermal reduction.⁹ Riedel *et al.* have demonstrated the effect of the composition and microstructure of SiOC powder electrodes on the electrochemical performance as anodes for LIBs.^{11–13} Using a polysiloxane as a precursor (polyamic RD-684a), samples pyrolyzed at 900 °C presented the highest initial reversible capacity (738 mA h g⁻¹), but suffered from strong capacity fading.¹³ At higher synthesis temperature, the stability of the system is improved, with an optimum for samples pyrolyzed at 1100 °C for 3 h with a lower initial reversible capacity (532 mA h g⁻¹).¹³ Adding divinylbenzene to the polysiloxane precursor leads to an increase in the carbon content of the SiOC.⁸ It was found that SiOC behaves as a hybrid material, consisting of disordered Si–O–C nanodomains having a high first Li⁺ insertion capacity of 1300° mA h g⁻¹, and C_{free} having an estimated capacity of 350° mA h g⁻¹ (ref. 8). Among them, the material with the highest reversible capacity and best cyclability contained 51 mass% Si–O–C nanodomains and 49 mass% C_{free}.⁸

The incorporation of commercially available or *in situ* synthesized Si nanoparticles into SiOC has also been investigated,^{14,15} finding that the SiOC network helps to improve the conductivity of the system and buffers the volume change.¹⁵ Compared to pure SiOC synthesized at 1100 °C, incorporating amorphous or crystalline Si leads to higher initial capacities, namely 704 mA h g⁻¹ or 905 mA h g⁻¹, respectively.¹⁴ After 30 cycles, the capacity of crystalline Si/SiOC fades below the capacity of pure SiOC, while the amorphous Si/SiOC maintained 85% of the capacity.¹⁴ Sn nanoparticles have also been incorporated into low- and high-content carbon SiOC by mixing polysilsesquioxanes with tin(II) acetate, followed by pyrolysis at 1000 °C.¹⁶ Adding 25 mass% of Sn increases the initial reversible capacity compared to the high- and low-carbon SiOC samples, by 9% and 140%, respectively.¹⁶ The increase in capacity is related to the formation of Li₂₂Sn₅ and Li₇Sn₂, and the increase in rate capability and stability is attributed to the electrically conductive C_{free} phase.¹⁶ All these studies on polymer-derived SiOC have employed polymer-bound powder electrodes.

Continuous fiber electrodes, being free-standing and polymer binder free, are attractive because the continuous path for electron transport enables operation at much higher charge/discharge rates.¹⁷ Also, for hybrid fibers containing carbon and redox-active materials, no additional conductive additives are needed.¹⁸ The absence of inactive components (conductive additives and polymer binders) increases the overall gravimetric energy density of the electrode. So far, only continuous fibers have been fabricated by Zhang *et al.* using nanoparticles dispersed in a polyacrylonitrile (PAN) derived carbon matrix to obtain free-standing electrodes.^{19–21} The dispersed nanoparticles have been commercially available Si,^{19–21} Ge,¹⁹ and Sn,^{19,22} or synthesized SiOC and SiO₂ particles.^{21,23} The main issue of this synthesis process is that inorganic nanoparticles show a very high surface energy and tend to agglomerate in an organic medium.²⁴ Therefore, the resulting material is inhomogeneous, affecting the material properties. To obtain homogeneous materials without the need for surface active agents, it is better to employ approaches leading to the *in situ* formation of nanodomains.²⁴

In our past work, we have demonstrated electrospinning of SiOC electrospun fibers obtained from low-cost silicone resins.¹⁷ For this synthesis, one always needs a crosslinker, such as zirconium acetylacetonate or zinc acetylacetonate.^{17,25} However, parts of these crosslinkers remain in the system forming (undesired/unnecessary) metal compounds.²⁶ We now have explored the direct use of a Sn-containing crosslinker to enable enhanced electrochemical performance of the resulting SiOC–Sn-compound. According to the Ellingham diagrams,²⁷ the Gibbs free energy of SiO₂ between 900 and 1300 °C is lower than SnO₂; therefore, SiO₂ acts as a reducing agent for SnO₂, leading to the formation of metallic Sn domains. In this study, we evaluate for the first time polymer-derived SiOC–Sn fibers as anode materials for LIBs. The process variables correspond to the pyrolysis temperature (1000–1200 °C) and Sn-containing crosslinker amount (5–20 mass%). The effect of the process variables on the material properties and electrochemical performance is evaluated.

2. Experimental description

2.1. Materials synthesis

The solvents trichloromethane (TCM, stabilized, GPR Rectapur) and *N,N*-dimethylformamide (DMF; anhydrous, 99.8%) were purchased from VWR Chemicals and Sigma Aldrich, respectively. The polymers, silicone resin namely H44 (polymethylphenyl-silsesquioxane) and polyvinylpyrrolidone (PVP, *M*_w ≈ 1 300 000 g mol⁻¹), were purchased from Wacker Chemie and Sigma Aldrich, respectively. Moisture sensitive tin(II) acetate (SnAc) was purchased from Sigma Aldrich and stored in a moisture free nitrogen atmosphere in a glovebox (H₂O, O₂ < 0.1 ppm). All chemicals were used as-received.

The synthesis of SiOC fibers is based on the approach followed in past studies,¹⁷ but modified using PVP to improve rheological behavior for electrospinning.²⁵ 30 mass% polymer (75 : 25 mass ratio of H44 : PVP) solutions were prepared in a 1 : 1 volumetric ratio of TCM : DMF. After the polymers were completely dissolved, the SnAc was added and stirred for 1 h before electrospinning. SnAc was added in different amounts: 2.5, 4.5, and 9.0 mass%. These amounts correspond to stoichiometric ratios of 0.05, 0.1, and 0.2 mol of Sn per 1 mol of Si.

Electrospinning was carried out with a MECC Co. NF-103V nanofiber system. The spinning dope (5 mL) was pumped at 1 mL h⁻¹ through a spinneret (inner diameter: 510 μm) which was inductively charged at 28 kV. The fibers were collected on a stationary grounded target at 21 cm from the spinneret. The spinneret head moved parallel to the collector with a travel distance of 10 cm at a travel velocity of 2 cm s⁻¹. The collected material was then heated at 100 °C for 24 h to stabilize the fiber shape. The pyrolysis of the crosslinked silicone resin was achieved by heating the material at 5 °C min⁻¹ to 200 °C for 2 h and later to 1000 °C or 1200° under argon in a graphite heater (Thermal Technologies, Model 1100C) for 2 h. After the heat treatment, non-woven SiOC fiber mats were cooled to room temperature at a rate of 20 °C min⁻¹. The Sn/SiOC fiber mats were named according to the added Sn content (0.05 Sn, 0.1 Sn, or 0.2 Sn) and the pyrolysis temperature (–1000 or –1200).

SiOC was also produced without a Sn precursor, as a monolith using the same procedure and thermal treatment used for the spinning dope preparation, but without the addition of SnAc. Also, a monolith containing 0.05 Sn was prepared for comparison of the electrochemical performance. These monoliths with and without Sn were named M-0.05 Sn and M-SiOC, respectively, and according to the pyrolysis temperature (−1000 or −1200).

2.2. Materials characterization

2.2.1. Structural and chemical characterization. The morphology of the fibers was examined by scanning electron microscopy using a JEOL JSM 7500F field emission scanning electron microscope (FE-SEM). For imaging, the fiber mats were fixed to a steel sample holder with sticky carbon tape. The as-spun fibers were coated with a thin layer of platinum in a JEOL Autofine Coater. The fiber diameter corresponds to the average diameter of at least 100 fibers, measured from the SEM images by using ImageJ software.²⁸ The elemental composition of the fibers was analyzed by EDX using an X-Max 150 detector from Oxford Instruments attached to the SEM chamber. Under 10 kV acceleration voltage and 10 μ A emission current, the spectra of at least ten fibers were acquired and average values were calculated.

Transmission electron microscopy (TEM) was done with a JEOL JEM-2100F system operating at 200 kV in vacuum. Ground fiber mats were dispersed and sonicated in ethanol, and drop cast onto a copper grid with a carbon film. Energy dispersive X-ray spectroscopy (EDX) point analysis was performed using a Thermo Scientific MC100021 detector attached to the TEM chamber. The spectra were acquired at 200 kV and 2 min for point measurements.

To characterize the chemical composition of the system, Fourier-transform infrared spectroscopy (FT-IR), and nuclear magnetic resonance spectroscopy (NMR) were used. FT-IR was performed with a diamond total attenuated reflectance crystal (ATR) using a Bruker Tensor 27 system. Raman spectra were measured using a Renishaw InVia Raman system, and a green laser (532 nm excitation wavelength) with 0.5 mW power on the sample, using a spectral resolution of *ca.* 1.2 cm^{-1} and a 50 \times objective (numerical aperture: 0.9). X-ray diffraction (XRD) was conducted employing a D8 Advance diffractometer (Bruker AXS) with a copper X-ray source (Cu-K α , 40 kV, 40 mA) in point focus (0.5 mm) and a Goebel mirror. A VANTEC-500 (Bruker AXS) 2D detector ($\sim 25^\circ$ per step; measurement time, 1000 s per step) was employed. The samples were ground and placed on a Si wafer. Solid-state magic-angle spinning (MAS) NMR measurements were performed on Bruker Avance III spectrometers operating at magnetic field strengths of 9.4 T (^{13}C) and 16.4 T (^{29}Si). The MAS frequency for all experiments was 12.5 kHz. All experiments were performed with direct polarization using a 90 $^\circ$ -acquire pulse sequence. A recycle interval of 15 s was used for all experiments. Chemical shifts were referenced to the CH $_3$ resonance of L-alanine at 20.5 ppm for ^{13}C and kaolinite (Al $_2$ Si $_2$ O $_5$ (OH) $_4$) at −91.2 ppm for ^{29}Si .

Thermogravimetric measurements combined with a mass spectrometer (TGA-MS) were performed for the as-spun

samples, using a STA 449 F3 Jupiter and QMS 403C Aëolos from Netzsch. The samples were heated to 1200 $^\circ\text{C}$ at 5 $^\circ\text{C min}^{-1}$ under N $_2$. Analysis of the tin content was performed by inductively coupled plasma atomic emission spectroscopy (ICP-AES). The samples (30 mg) were placed in microwave vessels, and mixed with 6 mL of HNO $_3$, 4 mL of H $_2$ SO $_4$, and 3 mL of HF. The vessels were maintained at 150 $^\circ\text{C}$ with a pressure of 300 kPa for several days until a homogenous liquid solution was observed. After cooling, the samples were placed in 50 mL polyethylene flasks and filled to the calibration mark for inductively coupled plasma atomic emission spectroscopy (ICP-AES) using a Horiba Jobin Yvon Ultima 2 system.

2.2.2. Electrochemical measurements. SiOC fiber mats were tested as anodes for Li-ion batteries. The measurements were performed in custom-built polyether ether ketone (PEEK) cells with spring loaded titanium pistons as a three-electrode system.²⁹ The SiOC electrodes were punched into 8 mm diameter discs (≈ 3.5 mg, 150 μm thickness), and tested *versus* a lithium disc (11 mm diameter) as the counter electrode. Working and counter electrodes were separated by a glass fiber separator (13 mm diameter; GF/D from Whatman) and we used 12 mm copper foil discs as current collector (0.025 mm thickness, 99.8%, Alfa Aesar). After assembling (without the lithium disc), the cells were dried at 2 kPa, 120 $^\circ\text{C}$ for 12 h. After cooling, the cells were placed in an argon-filled glovebox (MBraun Labmaster 130, O $_2$ and H $_2$ O < 1 ppm), and the lithium disc was placed at the corresponding position. After closing the cell, a piece of glass fiber (GF/D from Whatman) followed by a lithium wire (reference electrode) was inserted from the side in the electrolyte reservoir. The cell was filled with 60 μL of 1 M lithium hexafluorophosphate (LiPF $_6$) in electrochemical grade ethylene carbonate and dimethylcarbonate (1 : 1 by mass (EC/DMC)) from BASF as the electrolyte.

The sheet resistance of the fiber mats was measured with a custom-built spring-loaded four-point probe with blunt gold contacts (tip diameter: 1.5 mm, tip distance: 3 mm). Cyclic voltammetry (CV) was performed using a VSP300 potentiostat/galvanostat (Bio-Logic) and for galvanostatic cycling with potential limitation (GCPL) an Astrol BatSmall battery analyzer was used. For rate capability measurements, the cells were subjected to GCPL between +0.01 V and +3.0 V *vs.* Li/Li $^+$ at different current rates. Based on a material capacity of 700 mA h g^{-1} , different specific currents were applied, starting at 35 mA g^{-1} (0.05C) for 5 cycles, followed by GCPL at 70 mA g^{-1} (0.1C) for 20 cycles, and 140 mA g^{-1} (0.2C), 350 mA g^{-1} (0.5C), 700 mA g^{-1} (1C) and 1400 mA g^{-1} (2C), for 10 cycles each. Further GCPL was performed at 70 mA g^{-1} for 40 cycles to complete 100 cycles. To evaluate the electrochemical performance in the first 5 cycles, the cells were tested by CV in the potential range between +0.01 V and +3.0 V *vs.* Li/Li $^+$ at a scan rate of 0.1 mV s^{-1} . From the GCPL data, the specific capacity (C_{sp}) was calculated according to eqn (1), by integrating the current between the starting time (t_0) and end time (t) of the delithiation step, normalized to the total electrode mass (m). The electrode mass corresponds to the mass of the Sn/SiOC fiber mats, which are free of any polymer binder or any conductive additives.

$$C_{\text{sp}} = \frac{\left(\int_{t_0}^t Idt \right)}{m} \quad (1)$$

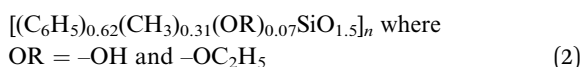
Polymer-bound electrodes were prepared for comparison. The produced monoliths (M-SiOC and M-0.05 Sn) were ground with an agate mortar in ethanol until obtaining a homogeneous slurry, to which 10 mass% polytetrafluoroethylene (PTFE, 60 mass% solution in water, Sigma Aldrich) and 5 mass% carbon black Super C65 (Imerys Graphite & Carbon) were added. The obtained paste was rolled until $126 \pm 7 \mu\text{m}$ thick electrodes were obtained (MTI HR01 rolling machine, MTI).

3. Results and discussion

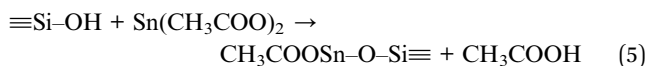
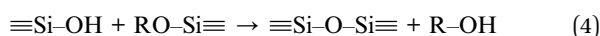
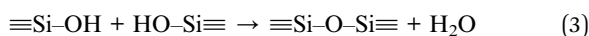
3.1. Polysilsesquioxane modified fibers

To electrospin SiOC fibers derived from polysilsesquioxanes, one must employ a crosslinker to maintain the fiber shape during pyrolysis. In our previous work on electrospun SiOC fiber mats for electrochemical applications, we had used zinc acetylacetonate as a crosslinker.¹⁷ After pyrolysis, low amounts (5–10 mass%) of zinc are present in the fibers. For this reason, we have replaced zinc acetylacetonate with a Sn-containing crosslinker (SnAc) to not only benefit from the crosslinker activity during synthesis, but also to form electroactive Sn after pyrolysis to enhance the energy storage performance.

H44 is a commercially available polysilsesquioxane with the chemical formula described in eqn (2), where –OR corresponds to the functional groups where further crosslinking takes place.



In the absence of metal alkoxides as crosslinkers or polymer modifiers, the condensation reactions described in eqn (3) and (4) take place. In the presence of transition metal alkoxides, the metal alkoxide reacts following the reaction described in eqn (5), exemplified for SnAc.¹⁶



Based on the reaction described in eqn (5) and the number of crosslinking groups of the polymer, the minimum amount of Sn added was fixed to occupy most of the crosslinking positions, which was 0.05 mol of Sn per 1 mol of Si. Based on this proportion, an excess of Sn was added (0.1 mol and 0.2 mol of Sn per 1 mol of Si). After electrospinning, the samples are named according to the Sn amount (0.05 Sn, 0.1 Sn, or 0.2 Sn), and after pyrolysis according to the tin content and the pyrolysis temperature (for example: 0.05 Sn-1200).

The as-prepared spinning dopes were electrospun and ultrafine fibers with a smooth and uniform morphology were

obtained, as confirmed by scanning electron micrographs (Fig. 1A and B). The as-spun fibers had an average diameter of $1.64 \pm 0.30 \mu\text{m}$ (Fig. 1C). During electrospinning, the solvent evaporates, leaving behind the solid fibers containing H44, PVP and SnAc.

The reactions in the as-spun fibers during heating at $100 \text{ }^\circ\text{C}$ were characterized by FT-IR (Fig. 1D). The infrared spectra show absorption bands of the H44 polymer: the Si–O stretching vibration of the Si–O–Si ladder-type structure appeared between 1040 and 1027 cm^{-1} (ref. 17), the band at 1128 cm^{-1} is related to phenolic groups,³⁰ and the band at 1428 cm^{-1} comes from the C–H vibration modes of the methyl groups.³⁰ The absorbance of the bridging bond Si–C in the Si–CH₃ was observed at 733 cm^{-1} (ref. 31). The absorption bands corresponding to acetate ligands are either very weak or not observed. This can be related to the complete reaction of Sn in the Si–O–Sn and Sn–O–Sn networks, forming volatile acetic acid. Absorption bands at 695 cm^{-1} and 928 cm^{-1} correspond to the stretching modes of Sn–O and Si–O–Si, respectively.¹⁶ Also, several signals of the PVP can be observed: the small peak at 1017 cm^{-1} corresponds to the C–C polymer backbone and the band at 930 cm^{-1} is the breathing mode of the ring.²⁶ The bands at 1270 – 1288 cm^{-1} emerge from the C–N bonds in the polymer.³² Comparing the infrared spectra, no significant differences are observed when increasing the SnAc content. All spectra are similar and confirm the formation of Sn–O bonds, either as a part of the Si–O–Si network, or forming separated Sn–O–Sn domains.

3.2. Sn/SiOC fibers

After the fibers were completely crosslinked, the fibers were treated under Ar at either $1000 \text{ }^\circ\text{C}$ or $1200 \text{ }^\circ\text{C}$ to form SiOC/Sn fibers. To understand the effect of the crosslinker during thermal treatment, thermogravimetric analysis coupled with mass spectrometry (TGA-MS) was carried out in an inert atmosphere (Fig. 1E and F). At $250 \text{ }^\circ\text{C}$, a mass loss of 4% is observed as water is being desorbed. At 300 – $600 \text{ }^\circ\text{C}$, we see a drastic mass decrease due to redistribution reactions and the decomposition of the polysilsesquioxane. In this temperature range, the initial exchange reactions between the bonds present in the crosslinked resin take place, forming volatile organosilicon species.³³ Later, the decomposition of the network occurs by bond-cleavage³⁴ and methyl and phenyl groups diffuse through the bulk material. During the diffusion of the aliphatic and aromatic groups, some condense to form aromatic clusters which will later be seeds for carbon domains, while other leave as volatile compounds. Above $600 \text{ }^\circ\text{C}$, hydrogen gas is produced by the aromatic/turbostratic carbon domains, leading to a continuous mass loss of 5%.³⁴ After pyrolysis is completed, a total mass loss of 45% was obtained compared to the initial mass. The Sn–O–Sn domains initially form SnO, which above $600 \text{ }^\circ\text{C}$ is not favored in the presence of C and Si according to the Ellingham diagrams.²⁷ SnO is reduced to metallic tin, together with the release of hydrogen and CO upon ceramization, and it does not form either silicides or carbides.³⁵

After pyrolysis, the fibers present a smooth surface with some beads present on the fiber surface and between the

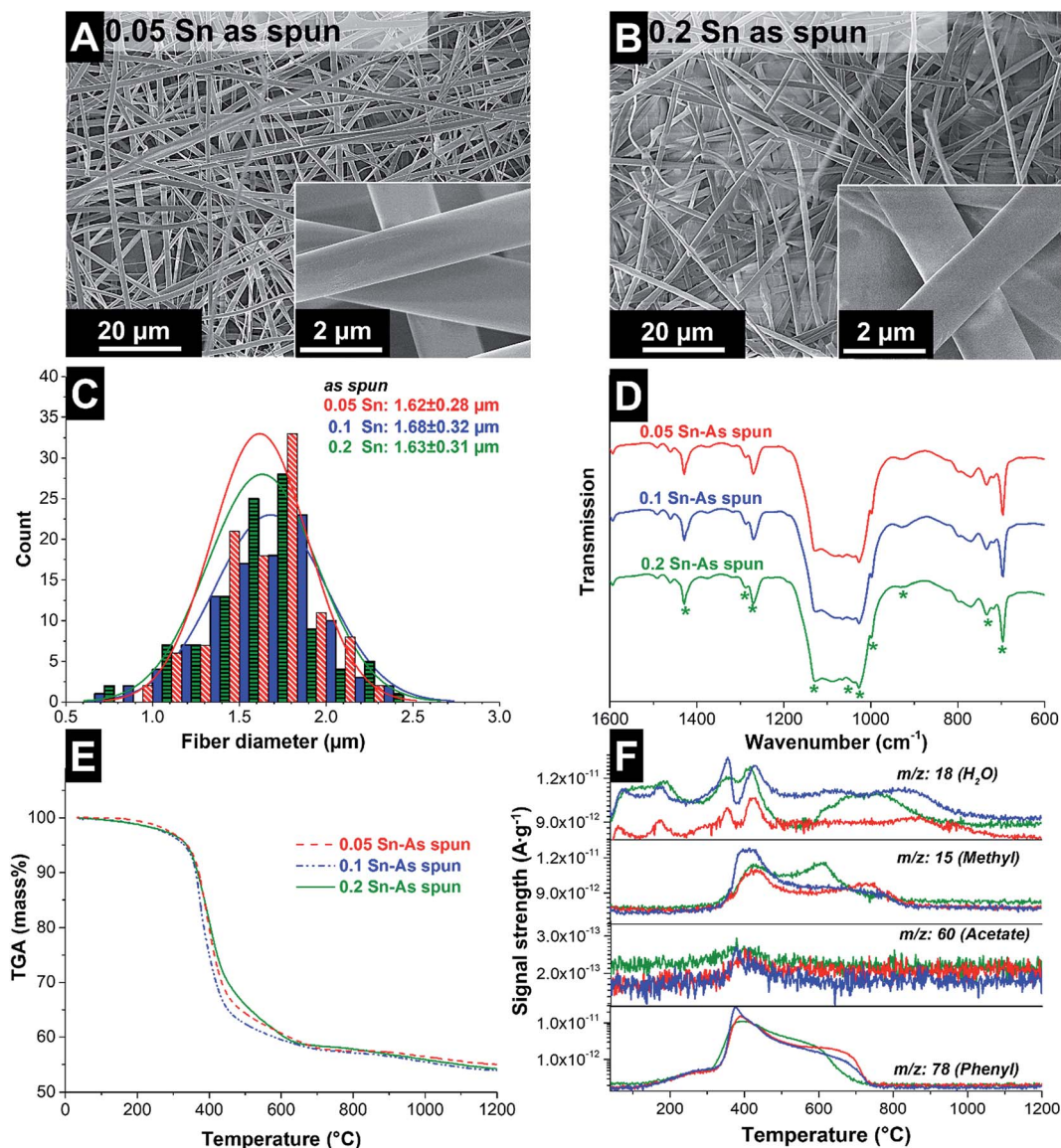


Fig. 1 SEM micrographs of the as-spun silicon resin fibers containing 0.05 Sn (A) and 0.2 Sn (B). Fiber diameter distribution (C) and Fourier transform infrared spectra (D) of the as-spun fibers. Thermogravimetric analysis (E) and mass spectra of the most important moieties (F), during heat treatment under an inert atmosphere of the as-spun fibers.

fibers as observed from the scanning electron micrographs (Fig. 2). The material characterization data for the samples treated at 1000 °C are presented in the ESI (Fig. S1 and S3†). The amorphous fibers present an average diameter of $0.96 \pm 0.25 \mu\text{m}$ after pyrolysis (Fig. 3A). There are also some crystalline domains inside the fibers, as observed from the transmission electron micrographs (Fig. 2). Also, the beads located outside the fibers present a crystalline structure engulfed by an amorphous matrix. EDX analysis was carried during TEM analysis (ESI, Fig. S2 and Table S1†), and we determined that the clusters inside and outside the fibers correspond to Sn covered by a SiOC shell. The size and distribution of Sn beads depend on the pyrolysis temperature and the used amount of SnAc, reaching a diameter size up to 0.8–1.0 μm for the sample 0.2 Sn-1000, as observed from the scanning electron

micrographs (ESI, Fig. S1†). Fibers synthesized at 1200 °C show a smaller number of beads (Fig. 2) and a larger number of Sn clusters inside the fibers; also, the beads present are smaller ($\leq 200 \text{ nm}$) compared to the samples synthesized at 1000 °C.

During pyrolysis and above 600 °C, metallic tin melts³⁶ and the liquid tin forms droplets due to surface tension.³⁶ This diffusion limited process takes place mainly during the holding time at 1000–1200 °C. Therefore, the process of tin droplet formation depends on the diffusion kinetics of tin in the formed SiOC. The lower diffusion kinetics of metallic tin in the denser structure of SiOC synthesized at high temperature restrict the formation of droplets with large sizes.

The chemical composition was characterized by EDX, confirming the presence of mainly SiOC (Table 1). The tin content

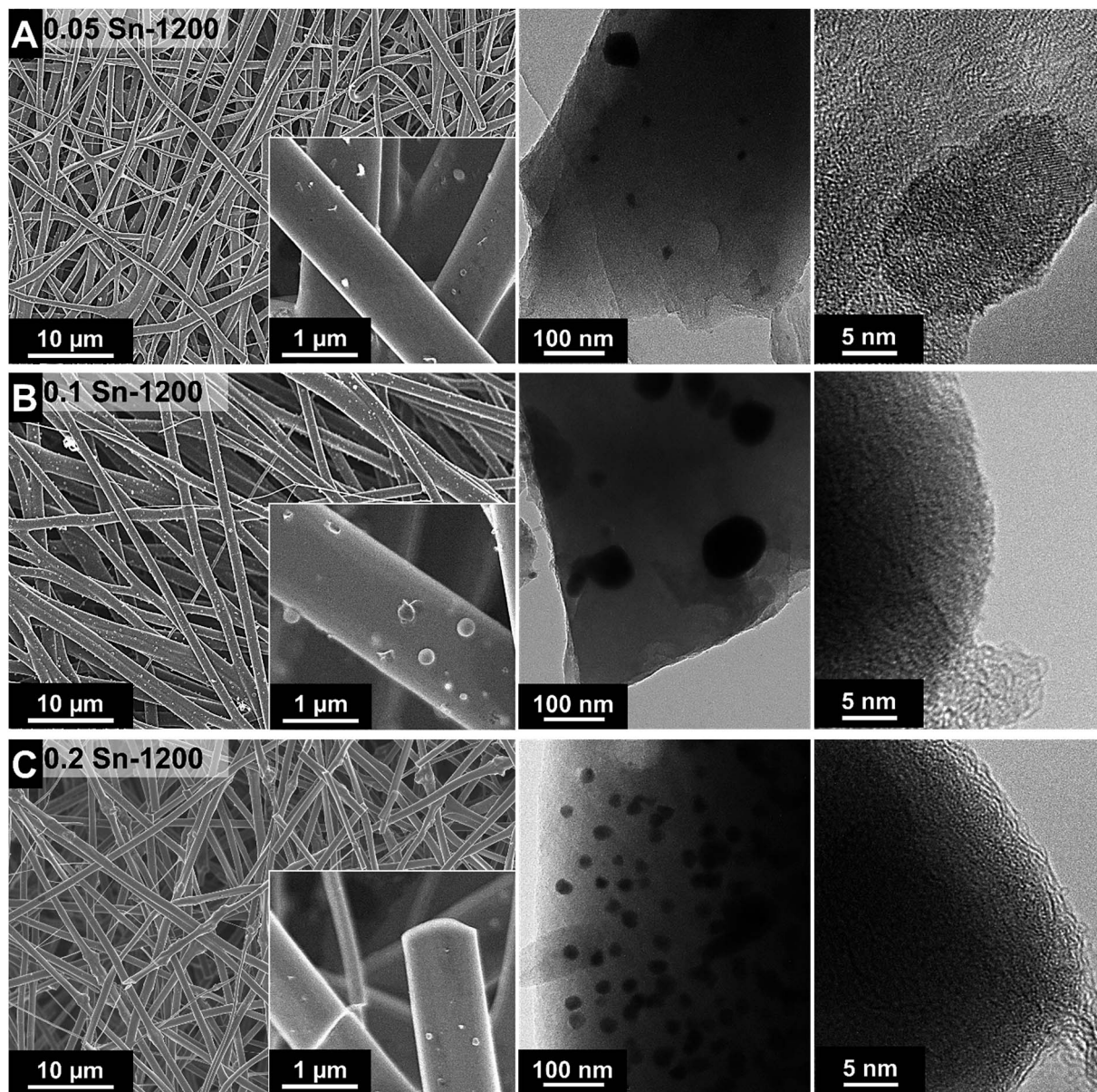


Fig. 2 SEM and TEM micrographs (inset) of the SiOC fibers synthesized at 1200 °C, containing different amounts of Sn: 0.05 (A), 0.1 (B), and 0.2 (C).

measured by EDX is not equal to the initially added amount and presents a high standard deviation due to the segregation of Sn as beads. The tin content, determined with ICP-AES (Table 1), varied in the range of 6–24 mass% and is not statistically different for samples pyrolyzed at different temperatures. Based on the EDX and ICP-AES results, an estimate of the molar ratio Sn/Si was calculated (Table 1). The values confirm that the molar ratio remains unchanged compared to the initial state, meaning that although Sn droplets are formed the initial tin content is maintained. From the EDX results, an estimate of the SiOC composition (C_{free} and the Si–O–C domains) can be obtained. The molar amount of O is for every sample at least 2 times the amount of Si, implying a composition of SiO_2 as the most likely compound to be formed. For a more accurate

characterization of the Si–O–C domains, results from ^{29}Si MAS NMR are presented later. It can be observed that the C_{free} content significantly decreases with increasing the tin content: from 3.5–3.7 mol C_{free} to 2.0–2.4 mol C_{free} per 1 mol of Si for the 0.05 Sn and 0.2 Sn samples, respectively.

The C_{free} phase in the fibers was characterized by Raman spectroscopy (Fig. 3C). All fibers present characteristic peaks for partially graphitized carbon, with corresponding D- and G-modes at $1333\text{--}1350\text{ cm}^{-1}$ and $1602\text{--}1609\text{ cm}^{-1}$, respectively, and higher order and combination modes at $2500\text{--}3000\text{ cm}^{-1}$. The D-mode is related to the breathing modes of six-atom rings and is activated when a defect is present.³⁷ The G-mode is associated with the bond stretching of pairs of sp^2 -hybridized carbon atoms in rings and chains.³⁸ The position of the G-mode

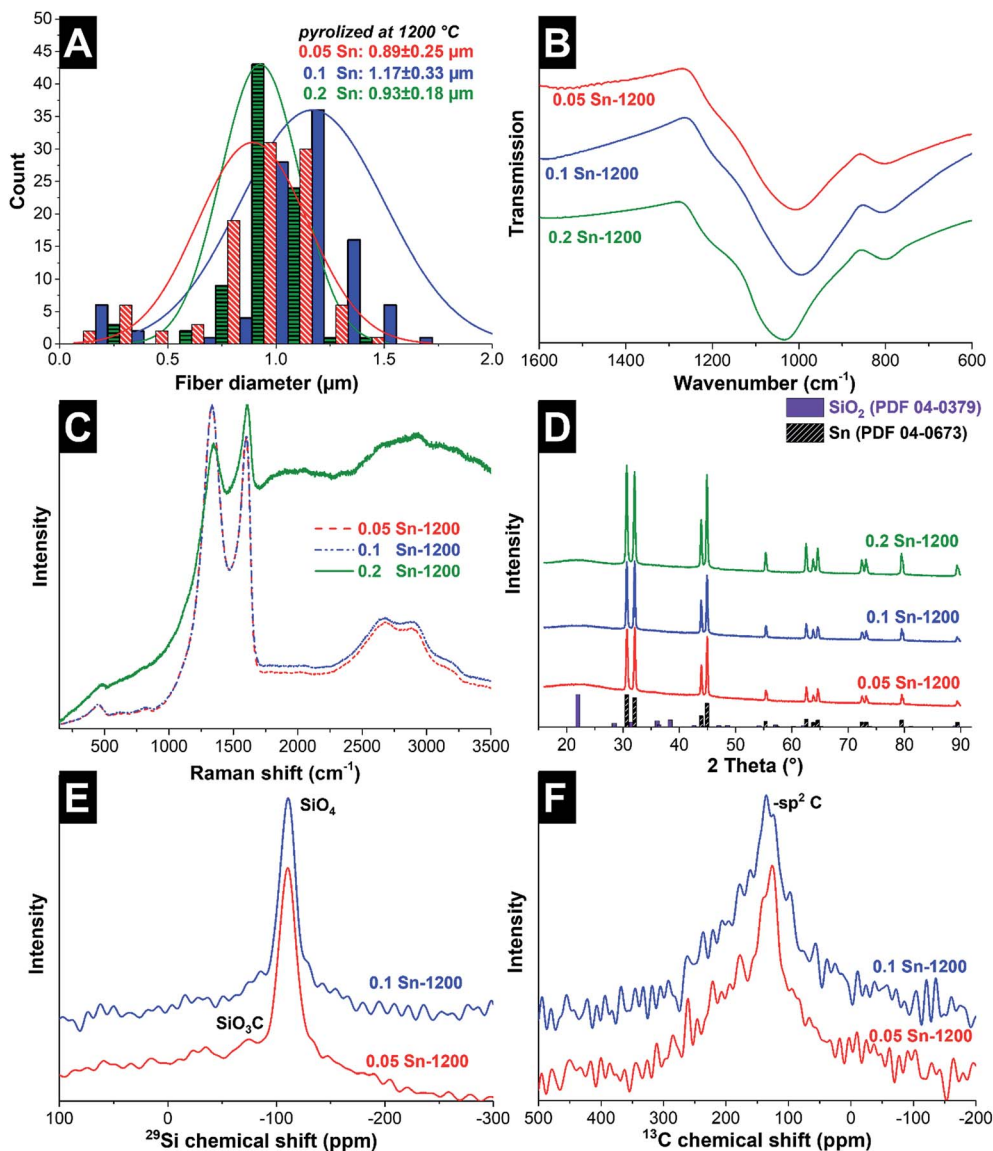


Fig. 3 Material characterization of fibers synthesized at 1200 °C. Fiber diameter distribution (A), Fourier transform infrared spectra (B), Raman spectra (C), X-ray diffraction pattern and literature values for diffraction peak positions (D), solid-state ^{29}Si NMR (E), and ^{13}C NMR (F).

Table 1 Results from the EDX and ICP-AES of the fiber mats (Sn/SiOC) and monoliths (SiOC). Calculated composition of SiOC based on the EDX results, and calculated values of the Sn/Si molar ratio based on EDX and ICP-AES results

Sample	SiOC composition	Sn/Si molar ratio	EDX results (mass%)				ICP-AES Sn mass%
			C	O	Si	Sn	
M-SiOC-1000	4.6 C_{free} + SiO_2	—	47 ± 2	28 ± 1	24 ± 3	—	—
0.05 Sn-1000	3.5 C_{free} + SiO_2	0.06	36 ± 2	28 ± 2	24 ± 3	11 ± 4	6.2 ± 0.1
0.1 Sn-1000	3.0 C_{free} + SiO_2	0.10	32 ± 1	33 ± 2	25 ± 2	9 ± 2	10.4 ± 0.2
0.2 Sn-1000	2.4 C_{free} + SiO_2	0.24	24 ± 2	38 ± 2	24 ± 3	14 ± 6	22.1 ± 0.1
M-SiOC-1200	4.1 C_{free} + $\text{SiO}_{1.35}\text{C}_{0.32}$	—	52 ± 8	21 ± 5	26 ± 2	—	—
0.05 Sn-1200	3.7 C_{free} + SiO_2	0.06	41 ± 1	32 ± 2	26 ± 2	1 ± 1	6.4 ± 0.1
0.1 Sn-1200	3.2 C_{free} + SiO_2	0.10	36 ± 1	32 ± 1	26 ± 1	5 ± 1	10.7 ± 0.1
0.2 Sn-1200	2.0 C_{free} + SiO_2	0.22	23 ± 3	37 ± 4	27 ± 5	13 ± 10	21.9 ± 0.1

(1602–1609 cm^{-1}) correlates with the coexistence of amorphous carbon (1550 cm^{-1}) and sp^2 -hybridized carbon chains, which for pure graphite is located at 1581 cm^{-1} (ref. 38). For further

analysis, peak deconvolution was performed by using three Voigt profile peaks in the range of 500–2000 cm^{-1} (ESI, Fig. S4†). The data of the peak position, integral I_D/I_G ratio, and full-width

at half-maximum (FWHM) are presented in Table 2. Samples treated at 1000 °C present different spectra according to their tin content. Both the D- and G-modes shift to higher wavelengths when increasing the tin content, indicative of a higher presence of amorphous carbon and *trans*-polyacetylene (between 1200 cm⁻¹ and 1260 cm⁻¹). Also, by increasing the tin content, the I_D/I_G ratio reduces, which for graphite domains smaller than 2 nm implies that less hexagonal carbon rings (also, defects from the hexagonal carbon rings) are present.³⁸ For the samples synthesized at high temperatures, no effect on the carbon structure is observed as a function of the tin content. All samples present similar Raman spectra, which compared to the samples synthesized at lower temperatures present a sharper G-mode peak and a lower amorphous signal, meaning a higher graphitization degree. The FT-IR spectra of the pyrolyzed samples (Fig. 3B) present mainly one peak centered between 994 and 1033 cm⁻¹, corresponding to the vibration mode of the bond Si–O–Si, and one smaller peak between 801 and 809 cm⁻¹, corresponding to Si–C.³¹ No bands related to Sn–O–Sn bonds are observed, aligning with the absence of SnO₂.

For additional analysis of the crystal structure, XRD patterns of the samples were recorded (Fig. 3D). In all samples, broad signals coming from tetragonal SiO₂ *P4₁2₁2* (PDF 04-0379; lattice parameters: $a = 0.497$ nm and $c = 0.693$ nm) are detected together with sharp peaks corresponding to tetragonal Sn *I41/amd* (PDF 04-0673; lattice parameters: $a = 0.583$ nm and $c = 3.182$ nm). By applying the Scherrer equation, the average coherence length of the metallic Sn in the fibers is about 101–138 nm (Table 2).

To understand the effect of Sn and the pyrolysis temperature on the resulting SiOC network, ²⁹Si MAS and ¹³C MAS NMR spectra were collected (Fig. 3E and F). The ²⁹Si MAS NMR spectra indicate that in the synthesized samples, the increase in the tin content leads to a decrease in the presence of SiC_xO_{4-x} tetrahedral units (with 1 ≤ x ≤ 4); consequently, mainly SiO₄ units are obtained. This effect is also observed for higher thermal treatment temperatures. For all samples, the ²⁹Si MAS NMR spectra exhibit an intense peak in the range of –105 ppm to –110 ppm which corresponds to SiO₄ units. For 0.05 Sn-1000, a second peak is observed at –71 ppm, corresponding to SiO₃C units (ESI, Fig. S3E†).³⁹ The intensity of this peak decreases with increasing the heat treatment temperature and is barely visible for the sample 0.05 Sn-1200 in Fig. 3E. We did not observe any peaks corresponding to SiO₂C₂ (–34 ppm), SiOC₃ (7 ppm), or SiC₄ (–11 ppm) in any sample. ¹³C MAS NMR presents mainly

a broad peak around 130 ppm for all samples, which is consistent with sp²-hybridized carbon. The broad character of the peak is related to large anisotropic susceptibility effects which are not fully averaged by MAS.³⁹ As reported by Widgeon *et al.* for high- and low-carbon SiOC synthesized at 1100 °C, low-carbon SiOC ($C_{\text{free}} = 5.7$ mass%) presents more SiO₄ units (44% of the Si units), while the high-carbon SiOC ($C_{\text{free}} = 41.3$ mass%) presented fewer SiO₄ units (32% of the Si units) and a larger number of SiC₄ units (17% of the Si units).^{16,39} The larger number of SiO₄ units (above 70%) and the absence of SiC₄ units in our system are explained by the reduction of SnO by C and Si, leading to an oxidation of C and Si. The oxidation of carbon to volatile species is supported by the decrease in the carbon content when increasing the tin content, as supported by the EDX results (Table 1), while the silicon content remains constant. For comparison, the elemental composition of monoliths without Sn (M-SiOC) is presented in Table 1, corroborating that the presence of Sn modifies the composition of the SiOC material.

We can conclude that our SiOC material consists of a cellular network of low order graphitic sp²-hybridized carbon, where nanodomains of mainly SiO₄ units are sequestered within cells created by the graphitic sheets, and this SiOC material is engulfing larger domains of metallic Sn.

3.3. Electrochemical performance

The fabrication of this hybrid fiber material was motivated by enabling several electrochemical advantages: (i) multiple sites for Li⁺ insertion in both systems SiOC ($C_{\text{free}} + \text{Si–O–C}$ nanodomains) and metallic Sn, (ii) benefit from the elastic properties of SiOC to mitigate the volume changes of Sn,¹⁶ (iii) interfiber space is beneficial to buffer the large volume expansion of the material, and (iv) high conductivity due to the continuous carbon phase in the SiOC fibers. The fiber mats were tested as free-standing electrodes without the addition of any polymer binder or any type of conductive additive. The electrochemical performance was evaluated in 1 M LiPF₆ in EC/DMC, between 3 and 0.01 V vs. Li/Li⁺. Cyclic voltammograms (CVs) were recorded at 0.1 mV s⁻¹, and are presented in Fig. 4 and ESI, Fig. S5.† During the first cycle, all samples showed a cathodic peak below 1 V vs. Li/Li⁺ from the reductive decomposition of the electrolyte and the formation of a solid electrolyte interphase (SEI). Therefore, initially the system was cycled at low rates (C/20) to promote SEI formation. The latter is a dynamic

Table 2 Results of the average coherence length of tetragonal Sn from XRD analysis and results from the peak deconvolution of Raman spectra

Sample	Coherence length (nm)	D-mode (cm ⁻¹)	G-mode (cm ⁻¹)	I_D/I_G	FWHM (cm ⁻¹)	
					D-mode	G-mode
0.05 Sn-1000	132	1335	1602	2.01	200.0 ± 0.6	71.4 ± 1.0
0.1 Sn-1000	105	1340	1603	2.03	206.6 ± 0.7	72.1 ± 0.8
0.2 Sn-1000	101	1350	1607	1.73	203.1 ± 1.0	71.9 ± 2.0
0.05 Sn-1200	122	1335	1603	1.58	180.9 ± 0.5	65.4 ± 1.0
0.1 Sn-1200	102	1333	1604	1.67	178.3 ± 0.5	63.2 ± 0.8
0.2 Sn-1200	138	1339	1609	1.56	178.1 ± 0.8	65.8 ± 1.4

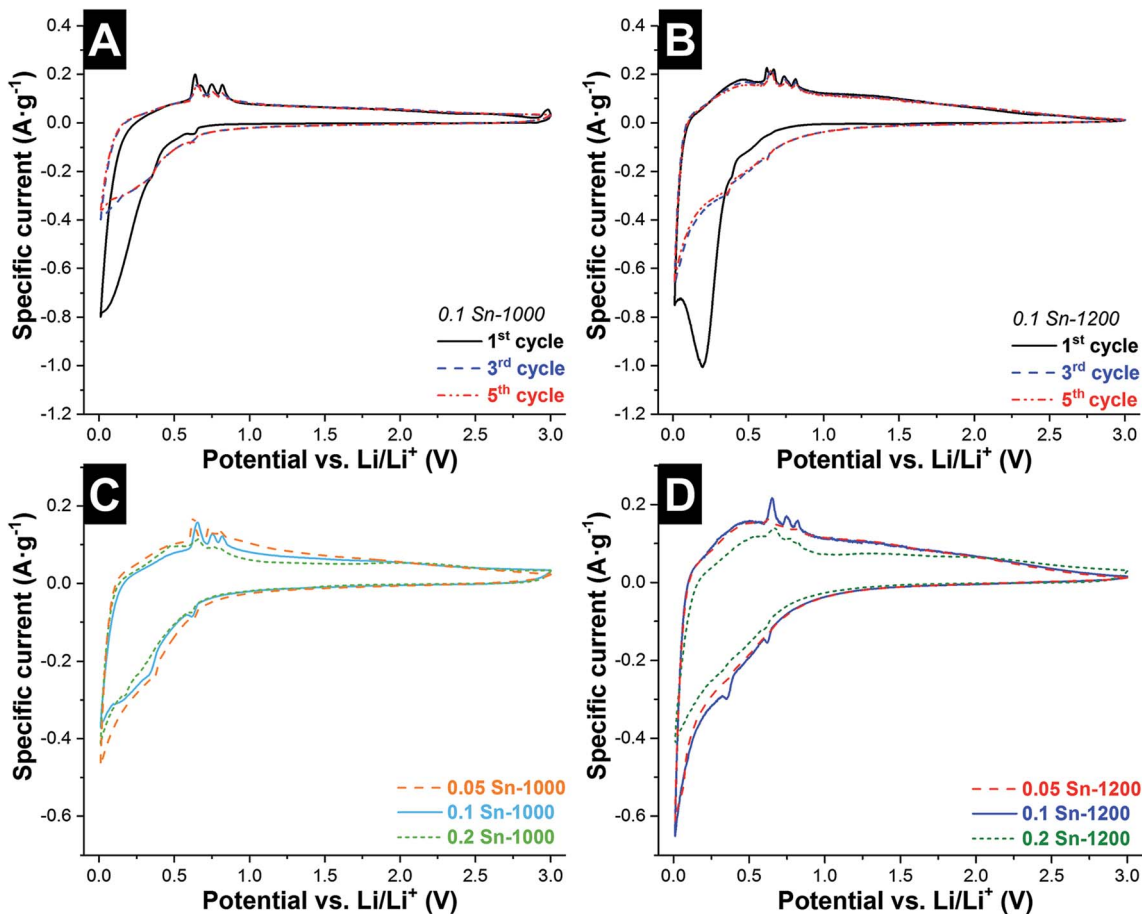


Fig. 4 Electrochemical characterization in a half-cell configuration of SiOC/Sn hybrid fibers by cyclic voltammetry at 0.1 mV s^{-1} . First 5 cycles for the samples containing 0.1 Sn synthesized at $1000 \text{ }^\circ\text{C}$ (A) and $1200 \text{ }^\circ\text{C}$ (B). 5th cycle of the samples synthesized at $1000 \text{ }^\circ\text{C}$ (C) and $1200 \text{ }^\circ\text{C}$ (D).

process in alloy anodes, breaking and reforming in each cycle due to the high volume changes of the electrode.⁴⁰

During the first cycle of the 0.1 Sn-1000 sample, further cathodic peaks at $+0.62 \text{ V}$ and $+0.34 \text{ V vs. Li/Li}^+$ are observed, corresponding to LiSn and $\text{Li}_{22}\text{Sn}_5$, respectively, followed by a broad and large peak at lower voltages, related to the Li^+ insertion in the SiOC matrix. All these peaks are blurred by SEI formation reactions during the first cycle, but become clearer in the subsequent cycles. During oxidation, several anodic peaks between $+0.63 \text{ V}$ and $+0.82 \text{ V vs. Li/Li}^+$ are observed. During the first cycle, 4 peaks are identified ($+0.64$, $+0.67$, $+0.75$, and $+0.82 \text{ V vs. Li/Li}^+$), while only 3 peaks occur in the subsequent cycles ($+0.65$, $+0.75$ and $+0.82 \text{ V vs. Li/Li}^+$). The numerous peaks indicate that dealloying in Sn occurs *via* multiple reactions and stages (Li_7Sn_2 , $\text{Li}_{13}\text{Sn}_5$, Li_5Sn_2 , Li_7Sn_3 , Li_2Sn_5 , and LiSn),⁴¹ and not as the reverse path described by the cathodic peaks during Li^+ insertion. The broad peak observed during the oxidation is related to the Li^+ extraction of carbon,³⁶ and SiO_2 nanodomains. Further anodic peaks are only observed during the first cycle at almost $+3 \text{ V vs. Li/Li}^+$, which could be related to the reabsorption of hydrogen formed during the reduction step.

Comparing the first cycle of the samples pyrolyzed at $1000 \text{ }^\circ\text{C}$, the amplitude of the anodic peaks (between $+0.63 \text{ V}$

and $+0.82 \text{ V vs. Li/Li}^+$) increases proportionally to the tin content (ESI, Fig. S5A and B[†]). The intensity of these peaks in the next cycles decreases proportionally to the tin content. In the 5th cycle (Fig. 4C), all CVs present similar shapes, but some differences in the peak position and intensity are observed. During lithiation, the first cathodic peak is shifted from $+0.63 \text{ V}$ to $+0.61 \text{ V vs. Li/Li}^+$, while the intensity of a second peak at $+0.36 \text{ V vs. Li/Li}^+$ decreases when increasing the tin content. During Li^+ extraction, the peaks located at $+0.63 \text{ V}$, $+0.73 \text{ V}$, and $+0.80 \text{ V vs. Li/Li}^+$ shift to higher voltages for the sample 0.05 Sn-1000. The increase of the voltage difference, for reduction and oxidation, together with the decrease in the intensity of the peaks, indicates increasing overpotential due to electron transport limitations. As observed for hybrid Sn/C particles, during the first cycles a high capacity fading is observed related to the partial particle pulverization of the Sn particles.³⁶ The large size of the Sn particles in our system and the segregation of some of them due to Sn melting during pyrolysis contribute to a large capacity fading in the first cycles.

Compared to samples synthesized at higher temperatures (Fig. 4B and D), two main differences are observed. For the samples synthesized at $1200 \text{ }^\circ\text{C}$, the peaks related to tin redox-reactions are less intense, but are observed at similar voltages,

and the CVs present a higher area, which indicates a generally higher capacity. Also, after the 5th cycle, these samples present similar shapes (Fig. 4D). There exist mainly two differences between the materials synthesized at 1000 °C and 1200 °C: the degree of carbon ordering and the particle size of the Sn beads. An increase in the conductivity of the SiOC matrix leads to a higher Li⁺ insertion into the Si–O–C tetrahedral units and a more homogenous current and voltage distribution throughout the electrode during charging. The effect of the pyrolysis temperature on the conductivity is corroborated by the sheet resistance values, 0.71–0.98 Ω cm and 0.28–0.32 Ω cm for samples synthesized at 1000 °C and 1200 °C, respectively (Table 3). The decrease in the intensity of the Sn alloy peaks is related to the lower formation of long-range ordered structures.⁴¹ For the samples synthesized at 1000 °C, lithium is intercalated into Sn in two different mechanisms, the well dispersed nanoparticles in the SiOC fibers and the large segregated Sn sub-micrometer-sized particles outside the fibers. For the samples synthesized at 1200 °C, Sn is mainly present as nanoparticles well dispersed inside the SiOC fibers, which explains the lower but more stable intensity of the Sn alloy peaks.

For a quantitative characterization of Li⁺ insertion in the hybrid material, the capacity during lithiation and delithiation was characterized by galvanostatic cycling between 3 and 0.01 V vs. Li/Li⁺. The voltage profile for the first cycle (35 mA g⁻¹, 0.05C) is presented in Fig. 5A and B and key data are reported in Table 3. During the discharging step, we see a rapid decrease in the voltage before achieving +1 V vs. Li/Li⁺, at which reduction reactions start to take place, leading later to a voltage plateau at 0.5–0.01 V vs. Li/Li⁺. The initial insertion capacity was similar for all samples, namely 1075–1178 mA h g⁻¹. The SEI formation and the irreversible Li⁺ insertion into the nanocomponents⁴² lead to a low coulombic efficiency of 0.75 and 0.82 for the samples treated at 1000 °C and 1200 °C, respectively. This could be influenced by the carbon ordering, since ordered carbons are characterized by a higher initial charge efficiency.⁴³ It was observed that the coulombic efficiency for the first cycle increases with increasing the tin content and the pyrolysis temperature. However the coulombic efficiency stabilizes faster achieving values close to 1, for low tin content, and also the capacity fading is lower for low tin content, which is related to the partial particle pulverization of the large Sn particles.³⁶ In the case of the samples treated at high temperatures, the initial

lithiation/delithiation capacity is proportional to the tin content, while for the sample at 1000 °C, the highest capacity was obtained for the sample 0.1 Sn-1000. A fast decay in the reversible capacity is observed in the next 5 cycles, but with a decrease of the irreversible capacity. After 5 cycles, the samples synthesized at high temperatures maintain a higher delithiation capacity between 842 and 791 mA h g⁻¹.

At higher rates (140 mA g⁻¹), the samples treated at 1200 °C maintain similar capacity values around 550 mA h g⁻¹. For samples synthesized at lower temperatures, larger differences are observed. The sample 0.1 Sn-1000 presented a higher capacity (525 mA h g⁻¹) while the other samples retained 380–430 mA h g⁻¹. At higher rates, the capacity values for all samples tend to be similar; only the sample 0.05 Sn-1000 presented consistently a lower capacity. For the samples treated at low temperature, after the fast decay in the first cycles, the sample which presents a more stable rate capability performance was 0.2 Sn-1000, which after 100 cycles also maintained the highest capacity of 277 mA h g⁻¹. Samples with a lower amount of Sn presented a higher capacity fading. For the samples synthesized at higher temperatures, higher capacity retention is observed, maintaining between 400 and 509 mA h g⁻¹ after 100 cycles. In this case, the samples present a more similar rate capability behavior and stability.

To explain the effect of the heat treatment and tin content on the observed electrochemical performance, we must consider the theoretical Li⁺ insertion capacity of the present phases and how the Li-storage takes place in silicon oxycarbides. The theoretical capacity of graphite, SiO₂, and Sn corresponds to 372, 1784, and 993 mA h g⁻¹, respectively.^{5,40} Therefore, our samples have a maximum theoretical capacity of 1150–1300 mA h g⁻¹ when applying a simplified model for the SiOC composition (ESI, Table S2†). There is still an open debate in the literature on the active sites for the Li storage in silicon oxycarbides; however, there are some features which are often reported: SiC is not electrochemically active and both Si–O–C nanodomains and the C_{free} phase contribute to the Li⁺ insertion.⁸ The proposed sites for reversible lithium storage in SiOC include the Si–O–C tetrahedral units, micropores, and the free carbon phase.⁸ Without free carbon, lithium storage in the Si–O–C domains cannot occur since a certain amount of carbon is needed to ensure sufficient electronic conductivity.⁴⁴ Additionally, the electronic conductivity of the free carbon phase can homogenize the voltage and current distribution throughout

Table 3 Results from electrochemical testing by galvanostatic cycling and sheet resistance of the electrodes

Sample	Capacity at 35 mA g ⁻¹ (mA h g ⁻¹)				Reversible capacity after 100 cycles (mA h g ⁻¹)	Sheet resistance (Ω cm)
	1 st lithiation	1 st delithiation	5 th lithiation	5 th delithiation		
0.05 Sn-1000	1097	789	725	607	221	0.71 ± 0.10
0.1 Sn-1000	1143	881	750	744	281	0.90 ± 0.15
0.2 Sn-1000	1093	821	632	613	277	0.98 ± 0.13
0.05 Sn-1200	1075	840	804	801	509	0.28 ± 0.05
0.1 Sn-1200	1145	939	854	842	457	0.31 ± 0.05
0.2 Sn-1200	1178	994	806	791	400	0.32 ± 0.03

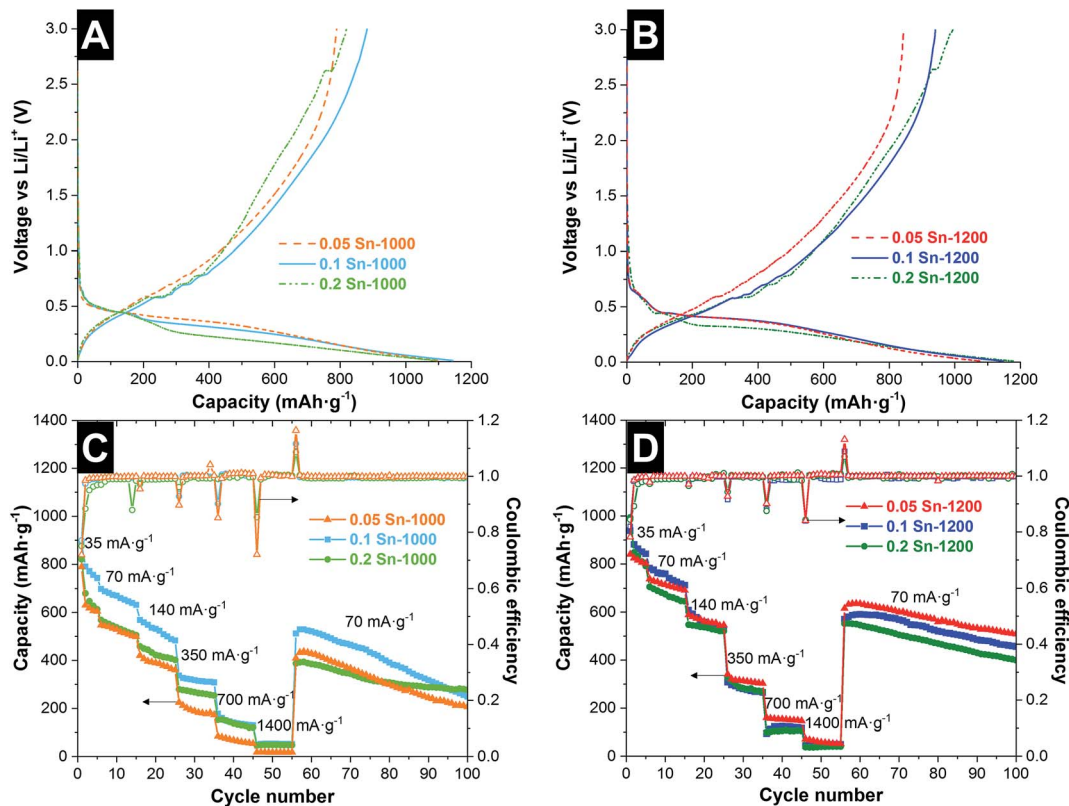


Fig. 5 First cycle of galvanostatic lithiation/delithiation at 35 mA g^{-1} from 3.0 to 0.01 V vs. Li/Li^+ , for SiOC/Sn hybrid fibers synthesized at 1000°C (A) and 1200°C (B). Rate capability performance of samples synthesized at 1000°C (C) and 1200°C (D).

the electrode in order to avoid local electrode degradation spots.⁴⁵ While in some aspects, the presence of C_{free} is beneficial, there are some aspects in which it is not. The C_{free} phase facilitates the formation of Li-O bonds, leading to irreversible lithium uptake in the presence of carbon in the SiOC .^{16,44} Also, while a higher graphitization degree of carbon is beneficial for a higher conductivity, higher ordered carbons can host less Li^+ than less ordered carbons.¹³

In our system, all three phases contribute to the overall Li^+ insertion/extraction. A graphical representation of the phases is presented in the ESI, Fig. S6A.† A higher tin content yields a higher initial reversible capacity; however, this is accompanied by a fast capacity fading after the first 5 cycles. Also, this increase in the reversible capacity with the tin content was only observed for the samples synthesized at 1200°C , with a more conductive C_{free} phase (Table 3). The C_{free} phase presents the lowest volumetric expansion ($\approx 10\%$; ref. 5) and demonstrates to have a crucial role in the stability and rate capability of the system. Therefore, we found that a high and stable performance depends on the electrical conductivity and the volumetric expansion during Li^+ insertion/extraction. During Li^+ insertion/extraction, the large particle size and the high volumetric expansion of the metallic tin ($\approx 260\%$)⁴⁰ may pulverize the particles; therefore, the contribution of the metallic tin to the electrochemical performance decreases during the first cycles. It has been already reported that for C-rich SiOC , the carbon phase accommodates the high volume expansion during

alloying with Li^+ , preventing electrode failure.¹⁶ Cracking and pulverization of the active particles and the surrounding matrix lead to the disconnection of some alloy particles from the conductive carbon or current collector, and this isolation of the particles leads to an incomplete delithiation reaction.⁴⁰ In our case, the fiber morphology is maintained (ESI, Fig. S6B and C†) and the electrodes continue to be free-standing after 100 cycles; possibly, the interfiber space helps to compensate for the volume expansion. However, the Sn beads have disappeared after 100 cycles, and some particles unconnected to the fiber network are observed, which could be related to the pulverization of the Sn beads. To corroborate this failure mechanism during the cyclic test, post-mortem TEM and EDX analysis was performed (ESI, Fig. S6 and S7†). The TEM images are characterized by two different regions: a dense SiOC material and a less dense region with the presence of Sn nanoparticles. The post-mortem SiOC material presents more holes compared to pristine SiOC , and some Sn nanoparticles were observed dispersed outside of the SiOC particles. According to the elemental analysis, the less dense region consists mainly of C, O, F, and P engulfing the Sn nanoparticles, as observed from the TEM images. As can be seen, some of the Sn nanoparticles are seemingly separated from the SiOC matrix during cyclic testing.

The electrochemical performance of the samples 0.05 Sn-1200 and 0.2 Sn-1200 was compared with the literature and Table 4 includes data of the pyrolysis temperature and tin content. The electrochemical data presented in Table 4

Table 4 Comparison of different SiOC and Sn/SiOC electrodes for battery-like systems. For electrode preparation, conductive additives (CA) and polyvinylidene fluoride (PVdF) are added during deposition by using a doctor blade (DBD) technique to the current collector. The mass loading of the electrodes is reported here for a fair comparison. The capacity values (mA h g^{-1}) are normalized to the total electrode mass and to the active mass (am)

Sample	Electrode	1 st cycle C_{rev} (mA h g^{-1})	Capacity at high rate (V vs. Li/Li ⁺)	Reference
Sn (6 mass%)/SiOC-1200 °C fibers	Free standing (8.6 mg cm^{-2})	840 (am: 840)	303 (am: 303) at 350 mA g^{-1}	This work; 1 M LiPF ₆ in EC/DM
Sn (22 mass%)/SiOC-1200 °C fibers	Free standing (8.3 mg cm^{-2})	994 (am: 994)	268 (am: 268) at 350 mA g^{-1}	This work; 1 M LiPF ₆ in EC/DM
SiOC-1100 °C microsized particles	DBD with CA and PVdF (3.3 mg cm^{-2})	452 (am: 532)	274 (am: 323) at 372 mA g^{-1}	Ref. 13; 1 M LiPF ₆ in EC/DMC
Sn (25 mass%)/SiOC-1000 °C microsized particles	DBD with CA and PVdF (4.5 mg cm^{-2})	553 (am: 651)	230 (am: 270) at 372 mA g^{-1}	Ref. 16; 1 M LiPF ₆ in EC/DMC
SiOC-1000 °C microsized particles	DBD with CA and PVdF ($3\text{--}5 \text{ mg cm}^{-2}$)	483 (am: 568)	246 (am: 290) at 372 mA g^{-1}	Ref. 8; 1 M LiPF ₆ in EC/DMC
SiOC-1300 °C microsized particles	DBD with CA and PVdF ($3\text{--}5 \text{ mg cm}^{-2}$)	250 (am: 293)	68 (am: 80) at 372 mA g^{-1}	Ref. 8; 1 M LiPF ₆ in EC/DMC
(Low carbon) SiOC-1300 °C microsized particles	DBD with CA and PVdF ($3\text{--}5 \text{ mg cm}^{-2}$)	619 (am: 728)	43 (am: 50) at 372 mA g^{-1}	Ref. 8; 1 M LiPF ₆ in EC/DMC

correspond mostly to high-carbon SiOC materials for a fair comparison, since low-carbon SiOC is well known for presenting a lower electrochemical performance.⁸ Our materials present a higher first cycle reversible capacity. This is attributed to several factors: the complete electrode mass contributes to the lithium insertion (no polymer-binder or additional conductive additive), the presence of metallic tin, and the high conductivity of the continuous fiber network. The improved conductivity is indicated by the higher capacity retention at higher rates, despite the higher mass loading of our electrodes. Also, compared to the literature, the effect of pyrolysis on the electrochemical performance of SiOC systems differs. It has been reported that a lower pyrolysis temperature (900 °C) leads to higher capacity values.¹³ For high-carbon SiOC, a higher pyrolysis temperature leads to an increase in SiC₄ units, which are not electrochemically active,⁸ decreasing the capacity of the system. In our systems, the presence of Sn promoted the increase of SiO₄ units and avoided the formation of C containing units, and therefore a heat treatment at higher temperatures helped to obtain a more conductive material, leading to higher capacity values and a higher stability.

3.4. Comparison to Sn-free SiOC

The chemical characterization results in Section 3.2 have demonstrated that Sn modifies the composition of SiOC. To corroborate the effect of Sn on the electrochemical performance, SiOC monoliths with (M-0.05 Sn) and without Sn (M-SiOC) were prepared and tested. The monoliths were tested as polymer-bound electrodes by admixing carbon black (C65) as the conductive additive. The results are presented in the ESI, Fig. S8.†

Comparing the polymer-bound electrodes and the fiber electrodes, a drastic difference is observed in the rate capability performance which is related to the much higher sheet resistivity of the polymer-bound electrodes compared to the fiber

mat electrodes (ESI, Table S3†). Comparing the monoliths, when adding 0.05 Sn the first reversible capacity increases from 635 to 681 mA h g^{-1} , and from 677 to 741 mA h g^{-1} for the samples synthesized at 1000 and 1200 °C, respectively. The monoliths produced at higher temperature present a more stable performance, but in all cases lower than the fiber mat electrodes. The lower stability of the polymer-bound electrodes is related to the higher particle size (5–10 μm) and lower conductivity of the non-continuous network, compared to the fiber mats.

4. Conclusions

We synthesized continuous SiOC fiber mat electrodes free of polymer binders and conductive additives, for the use as an anode material for Li-ion batteries. The synthesis is based on the electrospinning of a low-cost silicone resin, using tin acetate as a polymer crosslinker. We found that adding a low amount of tin acetate (0.05 mol Sn per 1 mol Si) is necessary for a complete crosslinking, maintaining the fiber shape during thermal treatment. After crosslinking and during pyrolysis between 1000 and 1200 °C, a hybrid material is formed, containing a carbon-rich SiOC matrix and metallic tin clusters. During pyrolysis, SnO is reduced to metallic tin, causing the oxidation of carbon and silicon, promoting a higher presence of SiO₄ units in the SiOC matrix and reducing the carbon content. This effect depends on the amount of added tin, with low amounts of tin (0.05 mol Sn per 1 mol Si) avoiding the formation of electrochemically inactive SiC₄ units. Higher tin amounts decrease the conductivity of the fibers by removing the conductive carbon phase. Since the presence of Sn promotes the existence of SiO₄ units, pyrolysis can be performed at higher temperatures (1200 °C) without forming inactive SiC₄ and benefiting the formation of a more graphitic and conductive C_{free} phase. It was also found that pyrolysis at 1000 °C and high amounts of tin (0.1–0.2 mol per 1 mol Si) lead to a higher segregation of tin into beads

outside the fiber shape. This single precursor approach has several advantages for producing continuous Sn/SiOC composite fibers: (i) by an *in situ* synthesis a uniform distribution of Sn particles in the SiOC matrix is obtained, (ii) the continuous matrix ensures the conductivity of the system and helps to constrain the volume expansion, and (iii) the material properties can be tailored according to the desired electrochemical properties.

The hybrid materials synthesized at 1200 °C present very high initial reversible capacities (840–994 mA h g⁻¹) at 35 mA g⁻¹, and retain 280–310 mA h g⁻¹ at 350 mA g⁻¹ specific current. After 100 cycles at 70 mA g⁻¹, the hybrid fibers maintained between 400 and 509 mA h g⁻¹. This capacity values are related to tin alloying and Li⁺ insertion reactions into the Si–O–C tetrahedral units, the presence of micropores, and the C_{free} phase. Without tin segregation outside the fibers and uniform distribution of tin in the SiOC fiber matrix (pyrolysis 1200 °C), a higher amount of Sn is beneficial for a higher reversible capacity in the first cycles. However, the higher volumetric expansion during lithiation of metallic tin possibly explains a higher capacity fading and a lower performance stability. At high rates, all systems have similar capacity values, meaning that tin is not significantly contributing to the Li⁺ insertion capacity, but mainly the C-rich SiOC. The C_{free} phase has a significant influence on the stability of the system. The C_{free} phase is present mainly as sp²-hybridized layers, and according to the electrochemical performance of the different samples, it was found that a higher amount of carbon and a higher graphitization degree are crucial for a higher conductivity and a stable electrochemical performance. Adding low amounts of Sn is beneficial not just for the crosslinking of the polymer precursor, but also to decrease the presence of SiC₄ electrochemically inactive species in the SiOC, and form metallic tin clusters which contribute to a higher Li⁺ insertion in the first cycles.

Conflicts of interest

There are no conflicts to declare.

Acknowledgements

We acknowledge funding from the German Federal Ministry for Economic Affairs and Energy (BMWi) in support of the HyBaCap project (award number 03ET6113C). The authors thank Prof. Eduard Arzt for his continuing support, Robert Drumm for his support in TGA-MS measurements and Andrea Jung for her support with ICP-AES measurements (all at INM). We also thank Dr Soumyadip Choudhury, Nicolas Jäckel, Juhan Lee, and Dr Eunho Lim for discussions and brainstorming (all at INM).

References

- B. Dunn, H. Kamath and J.-M. Tarascon, *Science*, 2011, **334**, 928–935.
- H. Li, Z. Wang, L. Chen and X. Huang, *Adv. Mater.*, 2009, **21**, 4593–4607.
- B. Scrosati and J. Garche, *J. Power Sources*, 2010, **195**, 2419–2430.
- B. Scrosati, J. Hassoun and Y.-K. Sun, *Energy Environ. Sci.*, 2011, **4**, 3287–3295.
- S. Goriparti, E. Miele, F. De Angelis, E. Di Fabrizio, R. Proietti Zaccaria and C. Capiglia, *J. Power Sources*, 2014, **257**, 421–443.
- R. Dash and S. Pannala, *Sci. Rep.*, 2016, **6**, 27449.
- A. M. Wilson and J. R. Dahn, *J. Electrochem. Soc.*, 1995, **142**, 326–332.
- V. S. Pradeep, M. Graczyk-Zajac, R. Riedel and G. D. Soraru, *Electrochim. Acta*, 2014, **119**, 78–85.
- P. Colombo, G. Mera, R. Riedel and G. D. Soraru, *J. Am. Ceram. Soc.*, 2010, **93**, 1805–1837.
- G. Mera, A. Navrotsky, S. Sen, H.-J. Kleebe and R. Riedel, *J. Mater. Chem. A*, 2013, **1**, 3826–3836.
- M. Graczyk-Zajac, L. Toma, C. Fasel and R. Riedel, *Solid State Ionics*, 2012, **225**, 522–526.
- P. Dibandjo, M. Graczyk-Zajac, R. Riedel, V. S. Pradeep and G. D. Soraru, *J. Eur. Ceram. Soc.*, 2012, **32**, 2495–2503.
- J. Kaspar, M. Graczyk-Zajac and R. Riedel, *J. Power Sources*, 2013, **244**, 450–455.
- J. Kaspar, M. Graczyk-Zajac, S. Lauterbach, H.-J. Kleebe and R. Riedel, *J. Power Sources*, 2014, **269**, 164–172.
- M. Zhu, J. Yang, Z. Yu, H. Chen and F. Pan, *J. Mater. Chem. A*, 2017, **5**, 7026–7034.
- J. Kaspar, C. Terzioglu, E. Ionescu, M. Graczyk-Zajac, S. Hapis, H.-J. Kleebe and R. Riedel, *Adv. Funct. Mater.*, 2014, **24**, 4097–4104.
- A. Tolosa, B. Krüner, N. Jäckel, M. Aslan, C. Vakifahmetoglu and V. Presser, *J. Power Sources*, 2016, **313**, 178–188.
- A. Tolosa, B. Krüner, S. Fleischmann, N. Jäckel, M. Zeiger, M. Aslan, I. Grobelsek and V. Presser, *J. Mater. Chem. A*, 2016, **4**, 16003–16016.
- S. Li, C. Chen, K. Fu, L. Xue, C. Zhao, S. Zhang, Y. Hu, L. Zhou and X. Zhang, *Solid State Ionics*, 2014, **254**, 17–26.
- Y. Li, B. Guo, L. Ji, Z. Lin, G. Xu, Y. Liang, S. Zhang, O. Toprakci, Y. Hu, M. Alcoutlabi and X. Zhang, *Carbon*, 2013, **51**, 185–194.
- Y. Li, Y. Hu, Y. Lu, S. Zhang, G. Xu, K. Fu, S. Li, C. Chen, L. Zhou, X. Xia and X. Zhang, *J. Power Sources*, 2014, **254**, 33–38.
- X. Xia, X. Wang, H. Zhou, X. Niu, L. Xue, X. Zhang and Q. Wei, *Electrochim. Acta*, 2014, **121**, 345–351.
- M. Dirican, O. Yildiz, Y. Lu, X. Fang, H. Jiang, H. Kizil and X. Zhang, *Electrochim. Acta*, 2015, **169**, 52–60.
- G. Kickelbick, in *Hybrid Materials*, Wiley-VCH Verlag GmbH & Co. KGaA, 2007, pp. 1–48, DOI: 10.1002/9783527610495.ch1.
- A. Guo, M. Roso, M. Modesti, J. Liu and P. Colombo, *J. Appl. Polym. Sci.*, 2014, **131**, 39836.
- J. S. Atchison, M. Zeiger, A. Tolosa, L. M. Funke, N. Jäckel and V. Presser, *RSC Adv.*, 2015, **5**, 35683–35692.
- H. J. T. Ellingham, *J. Soc. Chem. Ind., London, Trans. Commun.*, 1944, **63**, 125–133.
- C. A. Schneider, W. S. Rasband and K. W. Eliceiri, *Nat. Methods*, 2012, **9**, 671–675.

- 29 D. Weingarth, M. Zeiger, N. Jäckel, M. Aslan, G. Feng and V. Presser, *Adv. Energy Mater.*, 2014, **4**, 1400316.
- 30 G. Socrates, *Infrared and Raman Characteristic Group Frequencies: Tables and Charts*, Wiley, 2004.
- 31 T. Oh and C. Choi, *J. Korean Phys. Soc.*, 2010, **56**(4), 1150–1155.
- 32 D. L. Pavia, G. M. Lampman, G. S. Kriz and J. A. Vyvyan, *Introduction to Spectroscopy*, Cengage Learning, 2008.
- 33 V. Belot, R. J. P. Corriu, D. Leclercq, P. H. Mutin and A. Vioux, *J. Polym. Sci., Part A: Polym. Chem.*, 1992, **30**, 613–623.
- 34 J. Cordelair and P. Greil, *J. Eur. Ceram. Soc.*, 2000, **20**, 1947–1957.
- 35 E. Ionescu, C. Terzioglu, C. Linck, J. Kaspar, A. Navrotsky and R. Riedel, *J. Am. Ceram. Soc.*, 2013, **96**, 1899–1903.
- 36 W.-M. Zhang, J.-S. Hu, Y.-G. Guo, S.-F. Zheng, L.-S. Zhong, W.-G. Song and L.-J. Wan, *Adv. Mater.*, 2008, **20**, 1160–1165.
- 37 A. C. Ferrari and D. M. Basko, *Nat. Nanotechnol.*, 2013, **8**, 235–246.
- 38 A. C. Ferrari, *Solid State Commun.*, 2007, **143**, 47–57.
- 39 S. J. Widgeon, S. Sen, G. Mera, E. Ionescu, R. Riedel and A. Navrotsky, *Chem. Mater.*, 2010, **22**, 6221–6228.
- 40 W.-J. Zhang, *J. Power Sources*, 2011, **196**, 13–24.
- 41 M. Winter and J. O. Besenhard, *Electrochim. Acta*, 1999, **45**, 31–50.
- 42 Y.-S. Hu, R. Demir-Cakan, M.-M. Titirici, J.-O. Müller, R. Schlögl, M. Antonietti and J. Maier, *Angew. Chem., Int. Ed.*, 2008, **47**, 1645–1649.
- 43 Y. Nishi, *Electrochem. Soc. Interface*, 2016, **25**, 71–74.
- 44 M. Graczyk-Zajac, L. Reinold, J. Kaspar, P. Sasikumar, G.-D. Soraru and R. Riedel, *Nanomaterials*, 2015, **5**, 233.
- 45 M. Widmaier, N. Jäckel, M. Zeiger, M. Abuzarli, C. Engel, L. Bommer and V. Presser, *Electrochim. Acta*, 2017, **247**, 1006–1018.

3.5 Electrospun hybrid vanadium oxide/carbon fiber mats for lithium and sodium-ion battery electrodes

Aura Tolosa,^{a, b} Simon Fleischmann,^{a, b} Ingrid Grobelsek,^a and Volker Presser ^{a, b}

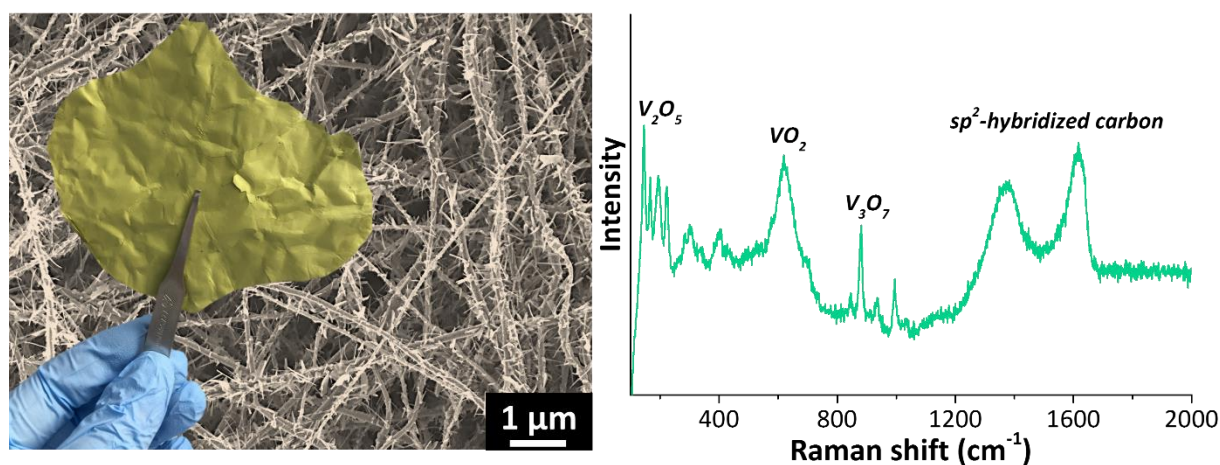
^a INM - Leibniz Institute for New Materials, 66123 Saarbrücken, Germany

^b Department of Materials Science and Engineering, Saarland University, 66123 Saarbrücken, Germany

Reprinted with permission from: ACS Applied Energy Materials, 1(2018), 3790-3801

DOI: 10.1021/acsaem.8b00572

Copyright (2018) American Chemical Society



Own contribution: Project management; paper writing; material synthesis; data analysis; measurements: rheometry, TEM, FT-IR, Raman spectroscopy, electrochemical characterization

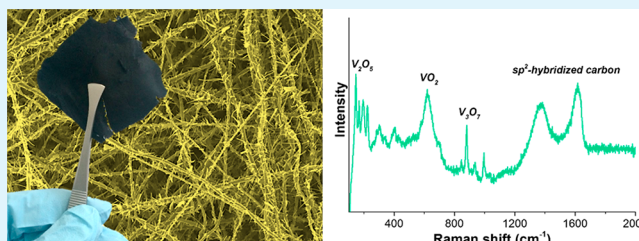
Electrospun Hybrid Vanadium Oxide/Carbon Fiber Mats for Lithium- and Sodium-Ion Battery Electrodes

Aura Tolosa,^{†,‡} Simon Fleischmann,^{†,‡} Ingrid Grobelsek,[†] and Volker Presser^{*,†,‡,§}[†]INM—Leibniz Institute for New Materials, 66123 Saarbrücken, Germany[‡]Department of Materials Science and Engineering, Saarland University, 66123 Saarbrücken, Germany

S Supporting Information

ABSTRACT: Vanadium oxide nanostructures are constantly being researched and developed for cathodes in lithium- and sodium-ion batteries. To improve the internal resistance and the discharge capacity, this study explores the synthesis and characterization of continuous one-dimensional hybrid nanostructures. Starting from a sol–gel synthesis, followed by electrospinning and controlled thermal treatment, we obtained hybrid fibers consisting of metal oxide crystals (orthorhombic V_2O_5 and monoclinic VO_2) engulfed in conductive carbon. For use as Li-ion battery cathode, a higher amount of carbon yields a more stable performance and an improved capacity. Monoclinic VO_2/C fibers present a specific capacity of $269 \text{ mAh}\cdot\text{g}_{VO_x}^{-1}$ and maintain 66% of the initial capacity at a rate of $0.5 \text{ A}\cdot\text{g}^{-1}$. Orthorhombic V_2O_5/C presents a higher specific capacity of $316 \text{ mAh}\cdot\text{g}_{VO_x}^{-1}$, but a more limited lithium diffusion, leading to a less favorable rate handling. Tested as cathodes for Na-ion batteries, we confirmed the importance of a conductive carbon network and nanostructures for improved electrochemical performance. Orthorhombic V_2O_5/C hybrid fibers presented very low specific capacity while monoclinic VO_2/C fibers presented an improved specific capacity and rate performance with a capacity of $126 \text{ mAh}\cdot\text{g}_{VO_x}^{-1}$.

KEYWORDS: hybrid material, vanadium oxide, electrospinning, nanofibers, lithium-ion battery, sodium-ion battery

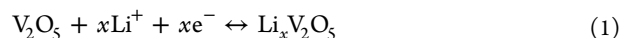


1. INTRODUCTION

The development of new and more efficient devices for electrochemical energy storage (EES) is key for the energy transition to sustainable technologies.^{1–3} Li-ion batteries (LIBs) are used for mobile and stationary energy storage applications due to high specific energy ($\approx 150 \text{ Wh}\cdot\text{kg}^{-1}$).⁴ The limited availability of lithium and some other LIBs components have led to the development of alternative ion systems, such as Na-ion batteries (NIBs).⁵ Although presenting very attractive energy density values, both systems present a low specific power ($< 1 \text{ kW}\cdot\text{kg}^{-1}$) and cycle stability compared to supercapacitors.⁶

Layered transition metal oxides are one of the most important battery electrode materials since they can offer an open framework for cation insertion.⁷ These oxides can efficiently store charge via intercalation of ions with improved diffusion and reaction kinetics, leading to an improved electrochemical performance.^{7–9} Vanadium pentoxide (orthorhombic V_2O_5) presents layers of VO_5 square pyramids sharing edges and corners along the c -axis, which serve as host for reversible lithium insertion and extraction.⁸ The reversible transformation from $\alpha\text{-Li}_{0.3}V_2O_5 \rightarrow \epsilon\text{-Li}_{0.5}V_2O_5$, $\epsilon\text{-Li}_{0.5}V_2O_5 \rightarrow \delta\text{-Li}V_2O_5$, and $\delta\text{-Li}V_2O_5 \rightarrow \gamma\text{-Li}_2V_2O_5$ leads to a maximum theoretical capacity of $294 \text{ mAh}\cdot\text{g}^{-1}$ according to eq 1, for a voltage range higher than 1.9 V vs Li/Li⁺.⁸ Further lithiation leads to the formation of an irreversible ω -phase with a rock-

salt structure up to $x = 3$, with a theoretical capacity of $442 \text{ mAh}\cdot\text{g}^{-1}$.⁸



For tetragonal $\omega\text{-Li}_xV_2O_5$, the highest possible reversible lithium insertion occurs in the limits of $0.4 \leq x \leq 2.65$.¹⁰ Upon lithium insertion, the lithium diffusion coefficient decreases from $3.3 \times 10^{-9} \text{ cm}^2\cdot\text{s}^{-1}$ for $0.4 \leq x \leq 0.7$ to $10^{-10} \text{ cm}^2\cdot\text{s}^{-1}$ for $x = 2.0$, reaching $10^{-12} \text{ cm}^2\cdot\text{s}^{-1}$ at $x = 3$.^{8,10} Therefore, the practical application of V_2O_5 is hindered by its limited ionic diffusion and moderate electrical conductivity ($10^{-2}\text{--}10^{-3} \text{ S}\cdot\text{cm}^{-1}$), leading to inferior battery performance with a low initial capacity, rapid capacity fading, and poor rate capability.¹¹ For NIBs, V_2O_5 exhibits a very high theoretic capacity of $236 \text{ mAh}\cdot\text{g}^{-1}$ (assuming two Na^+ per formula unit at 3.8–1.5 V vs Na/Na⁺).¹² Also, metal phosphates, such as $Na_3V_2(PO_4)_3$, have been studied as cathodes for NIBs.¹³ The insertion of Na^+ induces higher volumetric changes compared to Li^+ insertion due to the larger ionic size of 1.02 \AA compared to 0.59 \AA of Li^+ .¹⁴ To further improve the poor rate capability and decrease the capacity fading, layered V_2O_5 is often used as nanosized

Received: April 10, 2018

Accepted: July 17, 2018

Published: July 17, 2018

particles,¹⁵ as hybrid systems with carbon,^{16–18} or as materials with a continuous path for electron transport.^{19–22}

Several works have reported the synthesis of V₂O₅ materials and investigated the electrochemical performance as Li-ion battery electrodes, either as nanostructures or hybrid nanoparticles containing V₂O₅ and carbon.^{23,24} Among the hybrid nanoparticles, bottom-up approaches based on the coating of carbon substrates have employed hydrothermal synthesis^{17,25} and atomic layer deposition (ALD).^{9,18,26} Along these works, different substrates have been investigated, such as mesoporous carbon,^{18,25} microporous carbon,²⁶ carbon onions,^{9,17,26} carbon fibers,²⁷ and carbon nanotubes.^{28–30} By top-down methods, Zeiger et al. reported the synthesis of a hybrid core–shell V₂O₅/C system starting from vanadium carbide particles, by chlorine treatment of the particle shell and selective oxidation of the particle core.³¹ In the case of NIBs, due to the high structure deterioration and low Na⁺ diffusion, it has been shown that nanostructuring is beneficial to enhance the Na⁺ storage kinetics.³² Hybrid nanoparticles have been produced by hydrolysis deposition of vanadium oxide in nonporous carbon¹⁵ or by ALD deposition onto mesoporous carbon.¹⁸ Coating approaches bring along the need for nanoscale control of the layer thickness to keep diffusional pathlengths short and to avoid electrical insulation of the carbon substrate. Also, inhomogeneous deposition of V₂O₅ on the carbon framework will lead to a capacity loss.²⁵ Therefore, it is necessary to optimize the distribution of deposited V₂O₅ in the conductive substrate when preparing hybrid composites.

Compared to hydrothermal or emulsion synthesis, electrospinning can be used to obtain metal oxide nanostructures while avoiding segregation of the nanoparticles.³³ Electrospinning further allows for the production of sub-micrometer- and nanometer-sized one-dimensional structures, including short rods or continuous fibers.³⁴ In earlier work, V₂O₅ rods have been produced by electrospinning and mechanically mixed with conductive carbon and polymer binders for electrode preparation.^{11,33} The additives content was 30–40 mass % of the electrode, which translates to a much lower capacity normalized to the complete electrode. In polymer-bound composite electrodes, the electron transfer occurs at the points of contact between the metal oxide particles and the carbon additives, resulting in high resistivity.¹⁶ In contrast to such composite systems, electrospinning allows for the production of continuous nanofiber mats with continuous paths for electron transport. The fibers provide an open-percolated network with short diffusion distance into the nanofibers and an improved rate handling performance when being maintained as continuous electrodes.³⁵ In past studies, we have demonstrated a different strategy for electrode preparation based on the in situ formation of hybrid materials by a one-pot approach, leading to freestanding and additive-free continuous fibers.³⁶ We also demonstrated that continuous fibers present an improved specific power when compared to polymer-bound electrodes.³⁵ Together with this, we have also shown the use of freestanding and highly conductive fiber electrodes by the synthesis of hybrid fibers where metal oxide crystals are engulfed in conductive carbon.^{19,36}

In this work, we introduce for the first time vanadium oxide/carbon hybrid electrodes with continuous fiber architecture. The novelty of this work is based on the use of electrospinning to obtain freestanding vanadium oxide/carbon hybrid fiber mats, without polymer binder and conductive additives. This

approach differentiates from literature, because we maintain the continuous fiber morphology during the complete process, and both phases, vanadium oxide and carbon, are produced by a one-pot in situ synthesis. The in situ synthesis of both phases presents several challenges which are addressed in this work. For the synthesis of the hybrid materials, rigorous evaluation and optimization of the heat treatment conditions were applied to obtain metal oxide crystals (orthorhombic V₂O₅ and monoclinic VO₂) engulfed in conductive carbon. The continuous fibers were directly used as freestanding electrodes for Li- and Na-ion batteries. Through combination of material characterization and rigorous electrochemical benchmarking, we gain important insights into the effect of the material properties on the electrochemical performance, mainly the effect of carbon content, fiber diameter, and vanadium oxide crystal phase. The proposed synthesis route yields attractive electrochemical properties and offers a significant reduction of processing steps; thereby, the environmental impact is reduced.

2. EXPERIMENTAL DESCRIPTION

2.1. Materials Synthesis. **2.1.1. Synthesis of Metal Oxide/Carbon Fibers.** Hybrid vanadium oxide/carbon fibers were synthesized by a sol–gel approach and electrospinning. Vanadium(V) oxytripropoxide (VITP, 98% metal basis), acetic anhydride (Ac₂O, ≥98% purity), and ethanol (EtOH, analytical standard) were purchased from Sigma-Aldrich. Poly(vinyl acetate) (PVAc, $M_w = 86,000 \text{ g}\cdot\text{mol}^{-1}$) was purchased from Synthomer. Graphitic carbon nanohorn powder (trademark name, Graphene Nano-Stars, NS) were purchased from Graphene Laboratories. The term nanohorn follows the initial report of this material by Iijima et al.,³⁷ while the material would be called nanocone following the nomenclature recommendations of Suarez-Martinez et al.³⁸ All reactants were stored in a nitrogen-filled glovebox and used as received.

Electrospinning was performed following the synthesis proposed by Viswanamurthi et al.³⁹ A 1.93 mL aliquot of VITP was stirred with 2.53 mL of EtOH for 5 min, followed by the addition of 0.72 g of PVAc. The mixture was further stirred for 18 h until a transparent solution was obtained. In the case of the electrospun fibers with NS, prior to electrospinning 0.80 mL of Ac₂O was added to the VITP solution and stirred for 5 min, followed by addition of 4.03 g of a 2 mass % NS solution in EtOH. Electrospinning was carried out in an NF-103 V MECC nanofiber system, maintaining the humidity and temperature at 20% and 30 °C inside of the spinning chamber. The spinning dope was inductively charged at 28 kV and pumped through a spinneret at 0.5 mL·h⁻¹ (inner diameter, 400 μm). The spinneret head moved parallel to the current collector with a velocity of 2 cm·s⁻¹ and a travel distance of 8 cm. The spun fibers were collected on an aluminum current collector located horizontally at 20 cm from the spinneret.

After electrospinning, the collected fibers were stored in an oven HP110 (Mettmert) at 20 °C and 40% humidity for 48 h to promote cross-linking reactions of the metal alkoxide. Later, thermal annealing was performed under argon (99.5%) in a graphite heated Thermal Technology furnace. The fiber mats were heated to 700 °C at 5 °C·min⁻¹, held at this temperature for 3 h, and cooled to room temperature at a rate of 20 °C·min⁻¹. Later, the fibers were treated under Ar/synthetic air mixed atmospheres in a GP-CVD VG Scienta tube furnace for 0.5–3 h. The samples were annealed at either 300 or 350 °C under a mix of argon and synthetic air with a flow rate ratio of either 50:50 (cm³·min⁻¹) or 500:50 (cm³·min⁻¹).

2.2. Material Characterization. **2.2.1. Structural and Chemical Characterization.** The viscosity of the spinning dopes was measured using a modular compact rheometer from Paar Physica with a cone–plate geometry, 49.94 mm in diameter and an angle of 0.99°. The sample chamber was left open to ambient humidity, and viscosities were measured for 300 s at a constant shear rate of 200 s⁻¹.

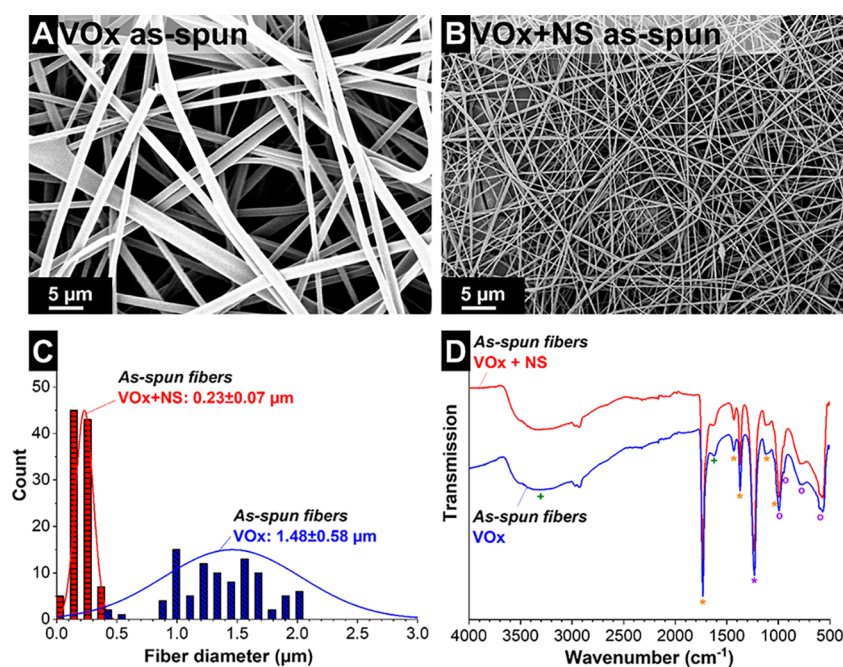


Figure 1. Scanning electron micrographs of the as-spun fibers without (A) and with graphitic carbon nanohorns (NS) (B). Fiber diameter distribution (C). Fourier transform infrared spectra (D).

The morphology of the electrospun fibers was characterized by scanning electron microscopy (SEM) using a JEOL JSM 7500F at an acceleration voltage of 3 kV and an emission current of 10 μ A. The fiber mats were placed on a carbon tape fixed to a aluminum sample holder. To quantify the fiber diameter from scanning electron micrographs, the size of 100 fibers was measured by the software ImageJ.⁴⁰ High-resolution micrographs were recorded by transmission electron microscopy (TEM) using a JEOL JEM-2100F system at 200 kV. For sample imaging, the fiber mats were dispersed in isopropanol via sonication for 2 min and drop-cast on a copper grid with carbon film.

The chemical composition and structure of the fibers was studied by spectroscopy. Fourier transform infrared spectroscopy (FTIR) was performed with attenuated transmission reflectance (ATR) using a diamond crystal on a Bruker Tensor 27 system. Raman spectroscopy was performed in a Renishaw inVia Raman system using an Nd:YAG laser (excitation wavelength, 532 nm). The spectral resolution was about 1.2 cm^{-1} using an objective with a numeric aperture of 0.75, and a power of 0.1 mW was present at the focal point. For peak fitting, four Voigt peaks were used for the D- and G-modes and sp^3 amorphous carbon. Energy dispersive X-ray spectroscopy (EDX) was performed using an X-Max^N detector from Oxford Instruments attached to the SEM chamber. The spectrum of at least 30 different fibers was recorded using an acceleration voltage of 14 kV and 3 nA probe current. The carbon content was quantified by CHNS analyzer (system vario Micro Cube, from Elementar). The combustion tube temperature was 1150 $^{\circ}\text{C}$ and the reduction temperature 850 $^{\circ}\text{C}$.

X-ray diffraction (XRD) was performed in a D8 Discover diffractometer (Bruker AXS) with a copper X-ray source (Cu $K\alpha$, 40 kV, 40 mA), using line focus and an LYNXEYE detector. The system was calibrated with a corundum standard. The fiber mats were stacked and placed on a sapphire single crystal for the measurement. Rietveld analysis was applied to determine the average coherence length (roughly corresponding with the domain size) using TOPAS software from Bruker. For thermogravimetric analysis (TGA), we used a TG 209 F1 Libra system (Netzsch). The thermograms were recorded using synthetic air and a heating rate of 5 $^{\circ}\text{C}\cdot\text{min}^{-1}$. To identify the onset of the oxidation reactions, the derivate of the gravimetric curve (DTG) was calculated.

2.2.2. Electrochemical Measurements. A potentiostat/galvanostat (VSP300 from Bio-Logic) was employed for cyclic voltammetry (CV)

and galvanostatic cycling with potential limitation (GCPL). The fiber mats were tested using a three-electrode setup with polyether ether ketone (PEEK) cells with spring-loaded titanium pistons.⁴¹ The working electrode (WE) was punched from the fiber mats as 8 mm disc (1.5 mg, 100 μm thickness). For lithium-ion batteries, a lithium metal disc of 11 mm was used as the counter electrode (CE), and a lithium wire was inserted from the side as reference electrode (RE), separated by a glass-fiber separator. The current collector for the CE side was a copper foil disc of 12 mm (25 μm thickness, 99.8%, Alfa Aesar) and for the WE side was carbon-coated aluminum foil of 12 mm (Zflo 2653, Exopack Technologies). The WE and CE were separated using a 13 mm diameter glass-fiber separator (GF/D from Whatman). For sodium-ion batteries, a sodium metal disc of 11 mm was used as the counter electrode, and a sodium wire was inserted from the side as reference electrode, separated by a glass-fiber separator. The CE and WE were placed between two aluminum foil discs of 12 mm (12 μm thickness, Exopack) and separated using a 13 mm diameter glass-fiber separator (Whatman GF/D).

After partial cell assembly without lithium and sodium metal, the cells were dried at 120 $^{\circ}\text{C}$ and 2 kPa for 12 h. Later, cell assembly was completed in an argon-filled glovebox (MBraun Labmaster 130, O_2 and $\text{H}_2\text{O} < 1$ ppm), where either lithium or sodium metal electrodes were placed. For LIBs, the cells were filled with 60 μL of 1 M lithium hexafluorophosphate (LiPF_6) in ethylene carbonate and dimethyl carbonate 1:1 by volume (EC/DMC) from BASF, electrochemical grade. For NIBs, the electrolyte was prepared using the chemicals as received from Sigma-Aldrich. The cells were filled with 60 μL of 1 M sodium hexafluorophosphate (NaPF_6) in propylene carbonate (PC).

The cells were initially tested by CV at a scan rate of 0.1 $\text{mV}\cdot\text{s}^{-1}$ for five cycles, within the potential range between 4.0 and 1.7 V vs Li/Li^+ for LIBs and between 3.8 and 1.5 V vs Na/Na^+ for NIBs. For rate capability measurements the cells were subjected to GCPL using the same voltage range as that for CV. GCPL was measured at different current rates from 0.025 to 10 $\text{A}\cdot\text{g}^{-1}$. From the GCPL data, the specific capacity (C_{sp}) was calculated according to eq 2 by integrating the current during the delithiation step between starting (t_0) and end times (t), normalized to the total hybrid electrode mass (m), since neither polymer binder nor conductive additive was added.

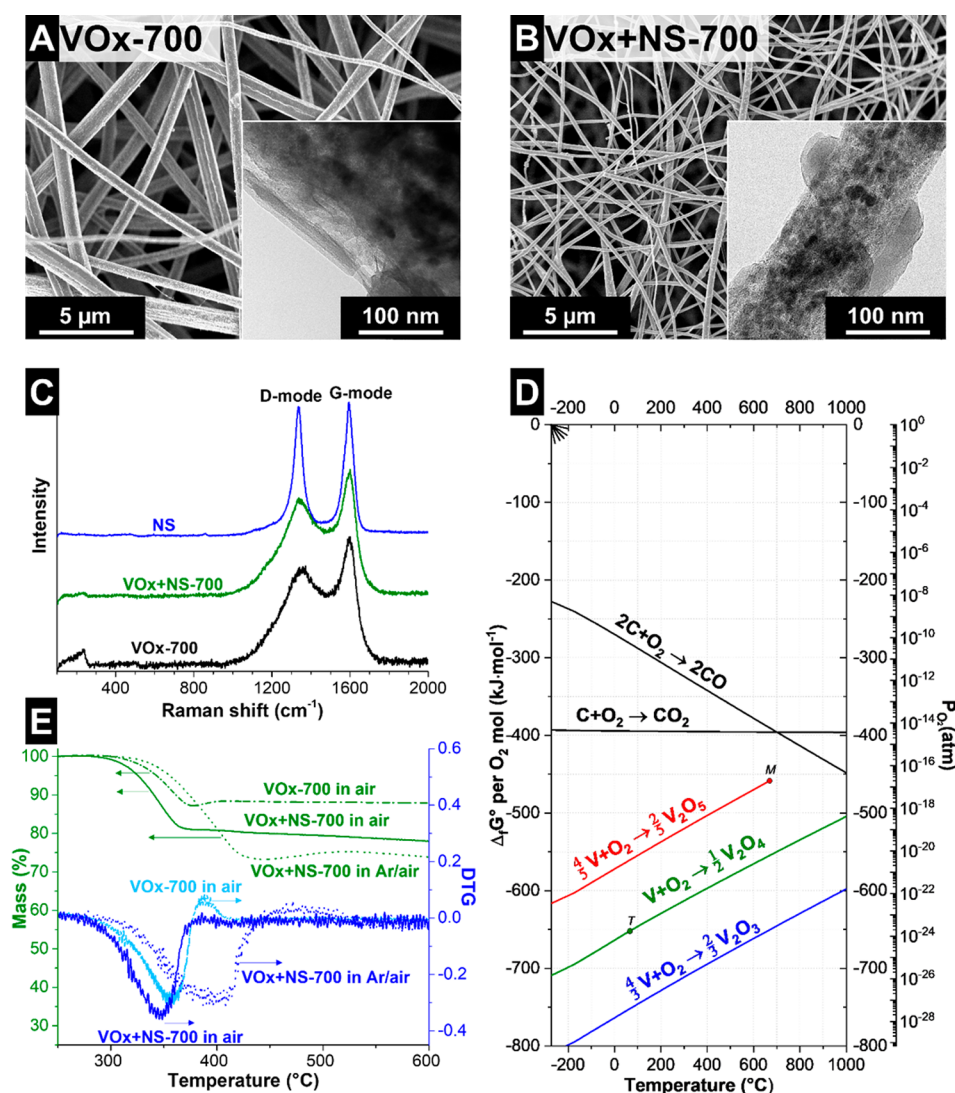


Figure 2. Scanning and transmission electron micrographs (inset) of the fibers without (A) and with NS (B) after pyrolysis at 700 °C. Raman spectra of the pyrolyzed fibers and NS (C). Ellingham diagram of the components present in the fibers (D). Data were obtained from NIST-JANAF Thermochemical Tables.⁶⁵ Thermogravimetric analysis of the pyrolyzed fibers under oxidizing atmospheres (E).

$$C_{\text{sp}} = \frac{\left(\int_{t_0}^t I dt \right)}{m} \quad (2)$$

Electrical impedance spectra were recorded in half-cells vs sodium discs, from 100 kHz to 10 MHz at 3.8 V vs Na/Na⁺ with 10 points per decade and averaged over five measurements. Polymer-bound electrodes were prepared by grounding the fiber mats with an agate mortar in isopropanol until obtaining a homogeneous slurry, to which 10 mass % polytetrafluoroethylene (PTFE, 60 mass % solution in water, Sigma-Aldrich) and 20 mass % of conductive additive BP2000 (CA, Cabot) were added. The obtained paste was rolled until 101 ± 20 μm thick electrodes were obtained (MTI HR01 rolling machine, MTI).

For postmortem analysis, the fiber mats were first completely delithiated/desodiated. The cells were disassembled in an argon-filled glovebox, and the electrodes were placed in a glass container with polycarbonate to remove the excess of ions, before exposure to the environment.

3. RESULTS AND DISCUSSION

3.1. Metal Alkoxide Fibers. The synthesis of the hybrid vanadium oxide/carbon fibers was performed either by having

an organic source for carbon or by addition of commercially available graphitic carbon nanohorns. The purpose of it was to compare the advantages and disadvantages of the different carbon sources and to modify the carbon content in the final hybrid fiber. The metal oxide and carbon precursors were added directly into the spinning dope.

To prepare the spinning dope with NS, a separate experiment was performed to determine the optimum amount of NS, Ac₂O, and EtOH. It was observed that the presence of Ac₂O is crucial to control the kinetics of the sol-gel reaction and to have a stable solution for electrospinning. Under the presence of NS with oxygen-containing groups and a large surface area,⁴² the rate of the hydrolysis and condensation reactions increases. Ac₂O strongly chelates and forms bidentate ligands to the metal alkoxide controlling the reaction rate.^{43,44} Scanning and transmission electron micrographs, and the FTIR spectrum of the NS are presented in the Supporting Information, Figure S1. The presence of oxygen-containing groups was confirmed by FTIR, and EDX yields a composition of 96.6 mass % C and 3.4 mass % O.

Adding NS to the spinning dope affects the spinning dope properties, especially the viscosity and the solution conductivity. The viscosity of the spinning dope with and without NS was 23 ± 3 and 45 ± 7 mPa·s⁻¹, respectively. After electrospinning, the addition of NS led to a much higher difference in the fiber diameter (Figure 1A–C). The VOx as-spun fibers show an average diameter of 1.48 ± 0.58 μm , while for the VOx + NS as-spun fibers the value was 0.23 ± 0.07 μm . The higher conductivity of the VOx + NS spinning dope causes the lower fiber diameter. PVAc has a low intrinsic conductivity and benefits from adding graphitic carbon nanohorns to the spinning dope. The increase in the charge carriers leads to a higher acceleration of the solution jet and therefore a decrease in the fiber diameter.^{45,46} A similar effect was observed by Ceretti et al., where the average fiber diameter decreased from 1.7 μm to about 0.5 μm after adding 2 mass % graphene to the spinning dope with polycaprolactone.⁴⁵

After electrospinning, the as-spun fibers were exposed to 40% humidity at 20 °C and for 48 h. During this time, gelation is completed causing some V⁵⁺-to-V⁴⁺ reduction (red/yellow-to-blue), and the initially yellow fibers change their color to green. The effect of the NS and Ac₂O in the as-spun fibers was also investigated with FTIR (Figure 1D). After complete hydrolysis and condensation of the metal alkoxides, volatile products such as propanol and acetic acid are expected to evaporate. This process will leave behind mainly the V–O–V domains and the PVAc. The as-spun fibers with and without NS present very similar spectra. For PVAc, the absorbance band of the carboxylate ester (C=O) is observed at 1731 cm⁻¹, together with other characteristic peaks for PVAc at 1432, 1371, 1232, and 1014 cm⁻¹.⁴⁷ The small bands appearing at 1090–1124 cm⁻¹ correspond to the atactic and isotactic structure of the polymer.⁴⁸ Absorption bands due to water molecules are observed at 3300 and 1622 cm⁻¹.⁴⁹ The vanadium–oxygen bonds are indicated by the strong absorption band for vanadyl (V=O) double bonds at 993 and 947 cm⁻¹,⁵⁰ and the broad bands from V–O–V are observed at lower frequencies.^{39,49} For V–O–V, the asymmetric stretching mode is observed at 792–763 cm⁻¹ and the symmetric and in-plane bending between 650 and 550 cm⁻¹.⁵¹ These findings show that the initially added NS and Ac₂O do not affect or constrain the gelation reactions of the vanadium alkoxide after exposure at 20 °C and 40% humidity for 48 h.

After complete gelation of the metal alkoxide, pyrolysis of the fibers was carried out in argon. Through an optimization experiment, it was found that 700 °C for 3 h was the optimum condition to form turbostratic carbon with V₂O₃/VO₂. Treatment at higher temperatures leads to a carbothermal reduction, which results in the formation of vanadium carbide and the loss of free carbon in the sample (see Supporting Information, Figure S2). After pyrolysis, the fiber morphology is maintained (Figure 2A,B), and the fibers present an amorphous structure according to the TEM micrographs. VOx-700 refers to the fibers without NS and VOx + NS-700 to the fibers with NS after pyrolysis.

The phase structure of the fibers was characterized by Raman spectroscopy. The spectra present clear signals of incompletely graphitized carbon, namely, the D-mode peak at 1337–1348 cm⁻¹ and a G-mode peak at 1599–1601 cm⁻¹ (Figure 2C). The D-mode relates to the breathing modes of sp²-hybridized carbon atoms in rings which is active when a defect is present, while the G-mode represents bond stretching

of all pairs of sp²-hybridized carbon atoms.^{52,53} The high degree of carbon ordering is reflected by sharp and well-distinct D- and G-modes for NS. In the case of the fibers, signals are also observed at 1196 and 1528 cm⁻¹ which relate to amorphous carbon and *trans*-polyacetylene, respectively.⁵³ Deconvolution of the Raman spectra by fitting four Voigt peaks is presented in the Supporting Information (Figure S3), and the results of the integral I_D/I_G ratio and full width at half-maximum are found in Table 1. The pyrolyzed fibers with and

Table 1. Peak Analysis of Raman Spectra by Fitting Four Voigt Peaks

sample	D-mode (cm ⁻¹)		G-mode (cm ⁻¹)		I _D /I _G ratio
	position	fwhm	position	fwhm	
NS	1337	59	1600	58	1.19
VOx-700	1348	177	1601	75	1.88
300 °C-3h	1366	145	1616	59	2.45
350 °C-0.5h	1367	140	1614	59	2.83
350 °C-1h	1359	127	1618	49	2.30
VOx + NS-700	1341	157	1599	70	1.97
NS 300 °C-3h	1363	119	1614	56	2.29
NS 350 °C-0.5h	1370	140	1617	60	2.56
NS 350 °C-1h	1353	64	1621	54	1.38

without NS present very similar results, with a much lower degree of carbon ordering seen compared to the graphitic carbon nanohorns. A broad peak at 236 cm⁻¹ is observed, which is in the range of signals attributed to V₂O₃ (160 and 264 cm⁻¹); see the Supporting Information, Figure S2. In this work, this broad signal is attributed to locally reduced vanadium (V³⁺ and V²⁺) at the interface with the carbon domains, which aligns with the V:O molar ratio of 1:1.42 according to the EDX results (Table 2). Preiss et al. confirmed that the carbothermal reduction of V₂O₅ starts with the formation of V₂O₃ followed by the formation of a vanadium oxycarbide, and finally VC is formed at 1170 °C.⁵⁴ Based on the CHNS results (Table 2), the amount of carbon in the samples corresponds to 19.0 and 27.0 mass % for the fibers without and with NS, respectively.

3.2. Metal Oxide/Carbon Fibers. **3.2.1. Energetic Considerations for the Synthesis Conditions.** To successfully synthesize V₂O₅/C hybrid fibers, one must carefully identify suitable conditions for the formation of crystalline V₂O₅ without completely oxidizing the free carbon. According to the standard Gibbs energy of formation represented in an Ellingham diagram (Figure 2D),⁵⁵ the formation of crystalline V₂O₅ is preferred over carbon oxide evolution. However, under standard conditions ($T = 25$ °C, and $P_{\text{O}_2} = 0.21$ atm), the formation of both carbon and vanadium oxides is thermodynamically more stable. According to the thermodynamic data, a higher oxidation state of vanadium makes it a weaker reduction agent, reaching similar $\Delta_f G^\circ$ to carbon dioxide. This implies a higher difficulty to form V₂O₅ without carbon dioxide formation. Kinetically, the oxidation at room temperature is limited to the surface of the material. The kinetics of the reaction at higher temperatures was studied by thermogravimetric analysis under mixed atmospheres of air and argon. Since the $\Delta_f G^\circ$ of carbon dioxide is higher than that for vanadium oxide, we varied the temperature and the partial pressure of O₂ to achieve a selective oxidation. Thermogravimetric analysis (Figure 2E) was performed under synthetic air

Table 2. Elemental Composition Analysis by EDX and C/V Mass Ratio Calculated from the EDX Results (Carbon Content Measured by Elemental CHNS Analysis)

sample	EDX data (mass %)			mass ratio C/V	carbon content (mass %)
	V	C	O		
VOx-700	51.2 ± 6.0	25.0 ± 2.3	23.7 ± 4.0	0.5	19.0 ± 1.7
300 °C-3h	57.9 ± 8.2	10.1 ± 5.9	32.0 ± 6.9	0.2	5.8 ± 0.8
350 °C-0.5h	62.8 ± 7.1	6.4 ± 1.5	30.8 ± 6.9	0.1	10.1 ± 0.8
350 °C-1h	55.9 ± 9.0	7.2 ± 4.3	36.9 ± 8.0	0.1	1.1 ± 0.1
VOx + NS-700	42.9 ± 3.0	37.8 ± 2.8	19.3 ± 1.3	0.9	27.0 ± 0.6
NS 300 °C-3h	59.7 ± 8.1	10.3 ± 4.1	30.1 ± 5.3	0.2	4.2 ± 1.3
NS 350 °C-0.5h	52.1 ± 7.9	23.7 ± 7.3	24.2 ± 4.1	0.5	15.4 ± 0.5
NS 350 °C-1h	57.7 ± 9.2	6.8 ± 9.9	35.6 ± 5.2	0.1	2.0 ± 0.1

and argon mixed atmospheres. Under synthetic air, the onset of carbon oxidation occurs at 350–360 °C, being slightly lower for the fibers with NS due to the lower fiber diameter. By treatment under lower O₂ partial pressure (Ar/air), the onset of carbon oxidation occurs at 400 °C for the fibers with NS. Yet, in the latter case, the peaks for carbon and vanadium oxidation cannot be clearly separated. Based on these results, the fibers were treated for 0.5, 1, or 3 h, either at 300 °C (50 cm³(STP) min⁻¹ synthetic air and 50 cm³(STP) min⁻¹ Ar) or at 350 °C (50 cm³(STP) min⁻¹ synthetic air and 500 cm³(STP) min⁻¹ Ar). The samples are named according to the heat treatment conditions (temperature and time) and the addition of graphitic carbon nanohorns prior to electrospinning.

3.2.2. Structural and Chemical Characterization. After treatment in an oxidizing atmosphere, the fiber morphology was maintained for the samples with and without NS (Figure 3). Also, the formation of nanotubular structures on the fiber

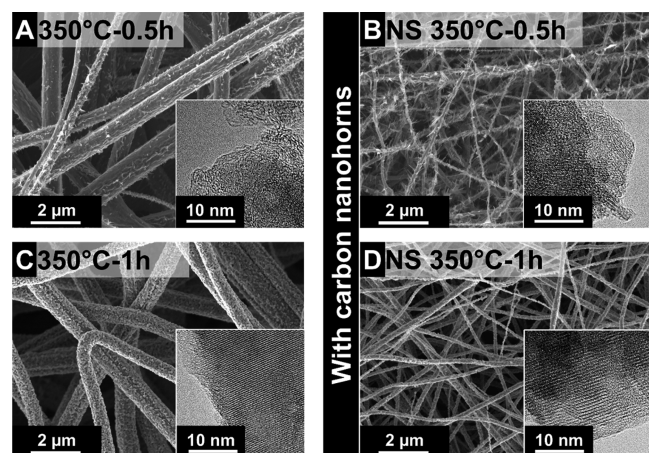


Figure 3. Scanning and transmission electron micrographs (inset) of the fibers without (A and C) and with NS (B and D) after treatment at 350 °C under an oxidizing atmosphere.

surface can be observed, being clearer for sample NS 350 °C-0.5h. The changes in the fiber structure are observed by TEM (Figure 3, inset), where higher ordered crystals are observed at higher temperature and time, engulfed in amorphous carbon. Raman spectroscopy and X-ray diffraction were performed on the fibers without NS to help identify conditions which lead to the formation of graphitic carbon and vanadium pentoxide. The Raman spectra of the samples treated at 350 °C are presented in Figure 4A and for the samples treated at 300 °C in the Supporting Information (Figure S5A). During treatment

at 350 °C after 0.5 h, D- and G-mode peaks are present in the Raman spectra indicating the presence of sp²-hybridized carbon together with VO₂ signals at 194, 223, and 621 cm⁻¹.⁵⁶ In the case of samples treated for 1 h, we observed peaks at 146, 198, 285, 304, 404, 484, 527, 702, and 995 cm⁻¹ which correspond to the vibrational modes of orthorhombic V₂O₅.^{56,57} Other peaks with a lower intensity are observed at 167, 846, 881, and 937 cm⁻¹. In past studies, these signals were assigned to V₆O₁₃ (V₂O_{4.33}),⁵⁶ but in our samples, no V₆O₁₃ is present as demonstrated later by XRD. These signals in our work were present in samples containing V₃O₇ (V₂O_{4.66}) and V₄O₉ (V₂O_{4.5}). Other works have reported that these Raman peaks are characteristic of curved opal structures of V₂O₅,⁵⁷ vanadium oxide nanotubes,⁵⁸ or a phase seen in vanadium oxide nanotubes before thermal decomposition and rearrangement to form V₂O₅.⁵⁹ These findings correlate with the presence of nanotubes as observed by SEM and TEM (see Supporting Information, Figure S4). The presence of these nanostructures strongly depends on the valency of the vanadium, where a decreased ratio of V⁺⁵ to V⁺⁴ allows curved structures to form.⁵⁹ Under the presence of V⁺⁴, a distortion of the vanadyl group takes place to compensate the charge of the oxo-anions.⁵⁹

Also, after treatment for 1–3 h at 350 °C, we observed a drastic decrease in carbon signals according to the Raman spectra. This decrease in the carbon aligns with the decrease of elemental carbon according to the CHNS and EDX results (Table 2), the broadening of the D- and G-modes of the Raman spectra (Table 1), and variations in the I_D/I_G ratio. The measured I_D/I_G ratio correlates with the transformation of graphite to nanocrystalline graphite leading to an increase of the ratio, followed by the transformation of nanocrystalline graphite to amorphous carbon observed by a decrease in the I_D/I_G ratio.⁵²

We further used XRD to gain more insights about the crystal structure of the vanadium oxides (Figure 4B). For phase analysis, Rietveld refinement was performed and the most important data are shown in Figure 4C. The diffractograms of the samples treated at 300 °C and the complete refined data after Rietveld analysis are presented in the Supporting Information (Figure S5B and Table S1). After treatment at 300 °C for 3 h, we obtained monoclinic V₃O₇ (32 nm) and orthorhombic V₂O₅ (65 nm). By treatment at 350 °C, initially V₂O₃ and VO₂ are formed. After 1 h at 350 °C, we obtained orthorhombic V₂O₅ and monoclinic V₃O₇ with average domain sizes of 82 and 115 nm, respectively. Longer treatment at 350 °C converts 98% of V₃O₇ to V₂O₅ with a domain size of the latter of 79 nm.

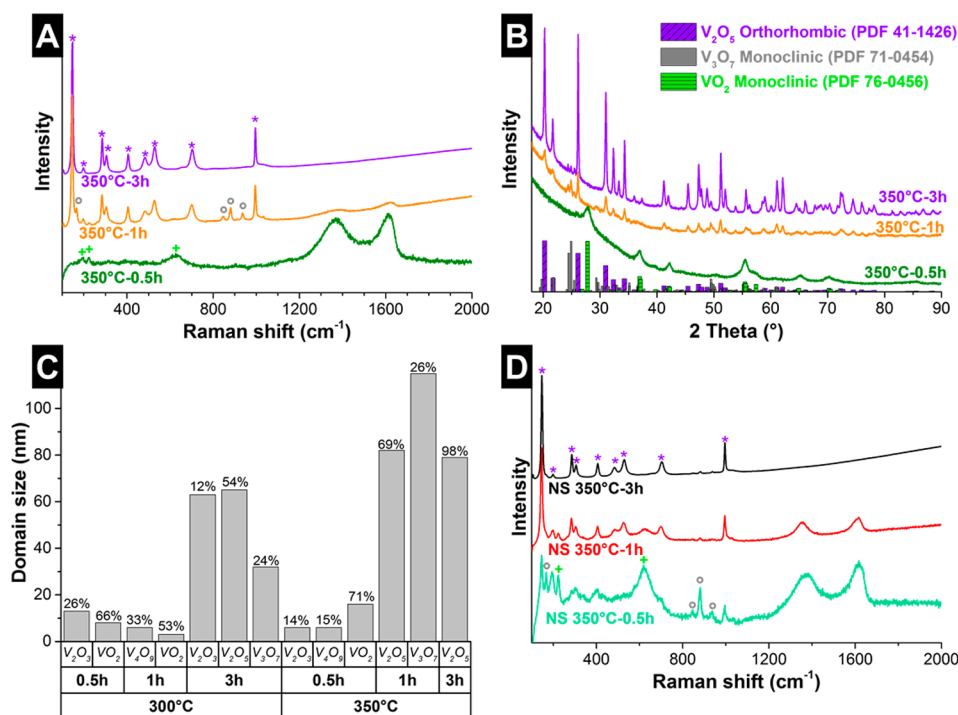


Figure 4. Raman spectra (A) and X-ray diffractograms (B) of fibers without NS synthesized under oxidizing atmospheres at 350 °C. (C) Results from the Rietveld refinement, for average coherence length of the different phases and mass %. (D) Raman spectra of fibers with NS synthesized under oxidizing atmospheres.

Based on the Raman and XRD results, we see that the only conditions where a more developed crystalline vanadium oxide and graphitic carbon are presented were 300 °C for 3 h, 350 °C for 0.5 h, and 350 °C for 1 h. Only these samples were selected for electrochemical characterization, due to the synergic effect of the electrochemical activity of crystalline vanadium oxide (VO₂ and V₂O₅) and the conductivity of carbon. For comparison, the pyrolyzed fibers with NS were treated under the same conditions for electrochemical characterization.

The Raman spectra of the fibers with NS differ from the fibers without NS (Figure 4D) mainly due to the differences in fiber diameter and initial carbon amount. Due to the shorter fiber diameter, the reaction rate of carbon and vanadium oxidation increases. The fibers with NS presented a higher amount of carbon after pyrolysis. However, the carbon burnoff occurs drastically leading to much lower carbon amount than the initial one (Table 2). The Raman spectra of the sample NS 350 °C-0.5h differs from the sample without NS, where sharper peaks of VO₂, V₄O₉, and V₂O₅ are observed together with carbon signals. The shorter fiber diameter leads to higher vanadium oxidation already after 0.5 h of heat treatment. The strong signals at 167, 846, 881, and 937 cm⁻¹ are attributed to V₄O₉-V₃O₇ with nanotubular morphology, as seen in scanning electron micrographs (Figure 3B). The peak at 167 cm⁻¹ has been associated with VO_x nanotubular structures, while the peaks at 846 and 937 cm⁻¹ have been assigned to VO₂.⁶⁰

3.2.3. Electrochemical Characterization as a Cathode for Lithium-Ion Batteries. We further evaluated the freestanding fiber mats as cathodes for LIBs. We observed a very similar electrochemical behavior for the samples treated at 300 °C for 3 h and 350 °C for 1 h; therefore, we focus on the discussion of the electrochemical results for the samples treated at 350 °C

for 0.5 and 1 h. The results of the samples treated at 300 °C for 3 h are presented in the Supporting Information, Figure S6.

As seen from cyclic voltammetry (Figure 5A), the samples without NS showed a very different behavior depending on the vanadium oxide crystal phase present in the fiber and the carbon content. The sample with more orthorhombic V₂O₅ (350 °C-1h) present in the cathodic scan broad peaks at 3.36, 3.11, and 2.02 V vs Li/Li⁺, which are similar to the peaks reported during the transformation of α -Li_{0.3}V₂O₅ → γ -Li₂V₂O₅ (3.30, 3.15, and 2.20 V vs Li/Li⁺).³¹ During the anodic scan, we see broad peaks at 2.5 and 3.6 V vs Li/Li⁺. The broad peaks in the voltammograms relate to the partial formation of the ω -phase, which occurs at around 1.8–1.5 V vs Li/Li⁺.¹¹ The electrochemical behavior of sample 350 °C-0.5h was different due to the higher presence of monoclinic VO₂; accordingly, we observed broad cathodic peaks at 2.82, 2.44, and 1.8 V vs Li/Li⁺ and broad anodic peaks at 2.1–3.0 V vs Li/Li⁺. The voltammogram had a more rectangular shape below 3.25 V vs Li/Li⁺, which is typical for a pseudocapacitive material. This sample is composed mainly of monoclinic VO₂ (space group, P12₁/c1), and the pseudocapacitive behavior of this phase was reported by Fleischmann et al.¹⁷

The fibers with NS exhibit an improved electrochemical behavior compared to the fibers without NS (Figure 5A). In all cases, we observed very similar cathodic and anodic peaks to the samples without NS, but larger current amplitudes. For a higher amount of VO₂ (NS 350 °C-0.5h), the more significant pseudocapacitive response is observed together with cathodic and anodic peaks at 2.47 and 2.66 V vs Li/Li⁺, respectively, in agreement with previous work.¹⁷ Independent of the presence or absence of NS, all samples containing mainly VO₂ showed rectangular cyclic voltammograms and a lower ΔE_p compared to samples with mainly V₂O₅.

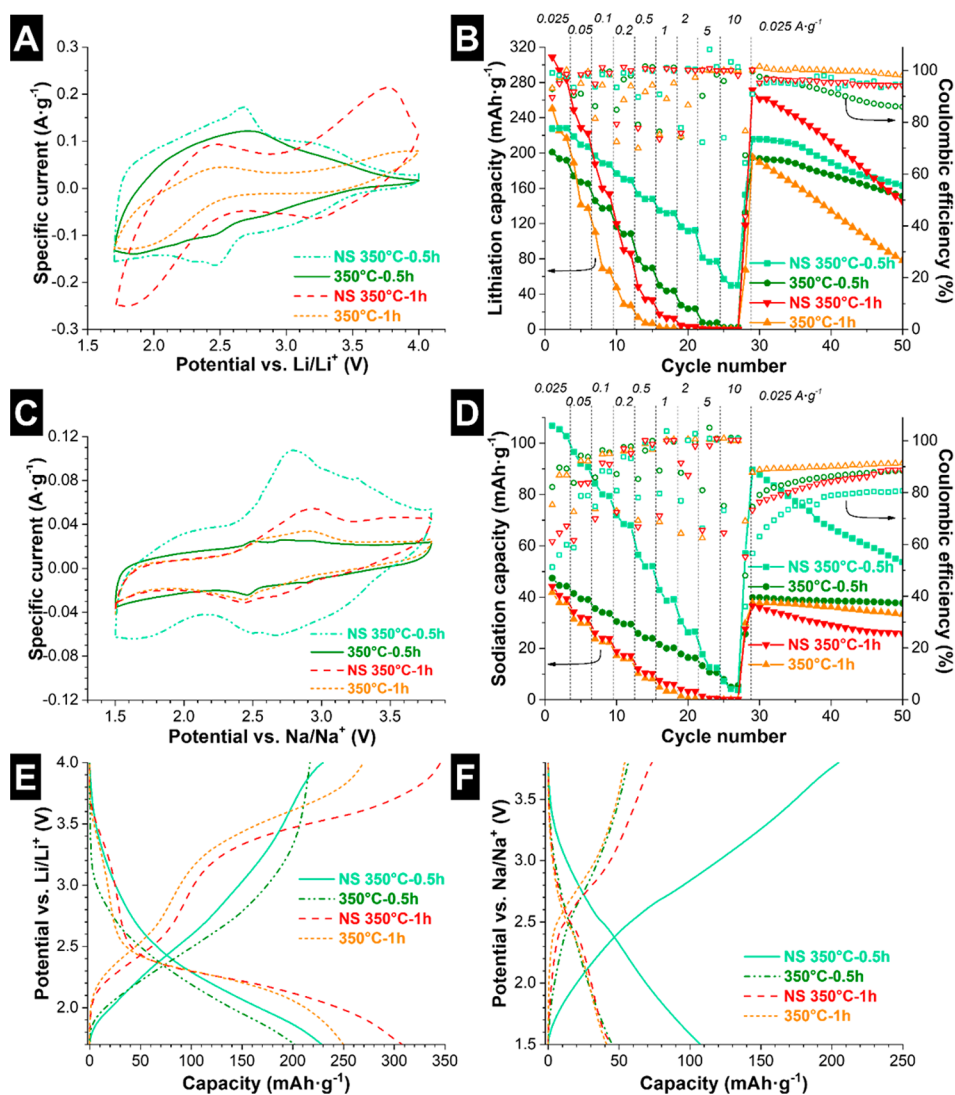


Figure 5. Cyclic voltammogram of the fifth cycle at $0.1 \text{ mV}\cdot\text{s}^{-1}$ of the fibers synthesized at $350 \text{ }^\circ\text{C}$, tested as a freestanding cathode for lithium-ion batteries (A) and sodium-ion batteries (C). Discharge capacity and Coulombic efficiency by galvanostatic cycling at rates of $0.025\text{--}10 \text{ A}\cdot\text{g}^{-1}$, tested as a cathode for lithium-ion batteries (B) and sodium-ion batteries (D). Galvanostatic curves for delithiation/lithiation (E) and desodiation/sodiation (F) for the first cycle at $0.025 \text{ A}\cdot\text{g}^{-1}$. All gravimetric values refer to the full mass of the electrode (that is, vanadium oxide and carbon).

The capacity for lithiation (discharge) and rate handling of the samples were evaluated by galvanostatic cycling (Figure 5B). For the samples without NS, the highest initial capacity at a low rate of $0.025 \text{ A}\cdot\text{g}^{-1}$ was for the sample $350 \text{ }^\circ\text{C}\text{-1h}$, with a value of $249 \text{ mAh}\cdot\text{g}^{-1}$. The latter lost 97.5% of its initial charge storage capacity at $0.5 \text{ A}\cdot\text{g}^{-1}$, and this low performance is accompanied by poor cycling stability. The high initial capacity relates to the formation of ternary $\text{Li}_x\text{V}_2\text{O}_5$ phases.⁶¹ The sample with a higher amount of VO_2 ($350 \text{ }^\circ\text{C}\text{-0.5h}$) had a lower initial capacity of $200 \text{ mAh}\cdot\text{g}^{-1}$ ($222 \text{ mAh}\cdot\text{g}_{\text{VO}_2}^{-1}$), but better stability and rate handling performance (36% of the capacity at $0.5 \text{ A}\cdot\text{g}^{-1}$). Although presenting initially the lowest capacity, the improved stability of $350 \text{ }^\circ\text{C}\text{-0.5h}$ leads to the highest capacity after 50 cycles of $153 \text{ mAh}\cdot\text{g}^{-1}$ of all studied samples. Galvanostatic charge/discharge curves of the first cycle at a low rate of $0.025 \text{ A}\cdot\text{g}^{-1}$ are presented in Figure 5E.

The samples with NS present in general a higher initial capacity, Coulombic efficiency, and rate handling than the samples without NS. This correlates to the shorter fiber diameter and a larger amount of free carbon. NS $350 \text{ }^\circ\text{C}\text{-1h}$

showed an initial value of $310 \text{ mAh}\cdot\text{g}^{-1}$ ($316 \text{ mAh}\cdot\text{g}_{\text{VO}_2}^{-1}$) which correspond to 2.2 Li^+ ions per mole of V_2O_5 , meaning that mainly V^{5+} is reduced to V^{4+} , but also partially to V^{3+} . At high rate ($0.5 \text{ A}\cdot\text{g}^{-1}$) only 13% of the initial capacity was maintained. The sample $350 \text{ }^\circ\text{C}\text{-0.5h}$ had a low initial capacity of $228 \text{ mAh}\cdot\text{g}^{-1}$ ($269 \text{ mAh}\cdot\text{g}_{\text{VO}_2}^{-1}$) but presented the highest capacity retention of 66% at $0.5 \text{ A}\cdot\text{g}^{-1}$ and 34% at $5 \text{ A}\cdot\text{g}^{-1}$. This sample had a higher amount of monoclinic VO_2 and carbon; therefore, the improved electrochemical performance comes from the pseudocapacitive behavior of monoclinic VO_2 and the improved electrical conductivity from the carbon. Lithium insertion in monoclinic VO_2 (space group $P12_1/c1$) occurs with low volumetric changes, from which the cycling performance should benefit.¹⁷ The material with the highest initial Coulombic efficiency (98%) also had the highest amount of carbon NS $350 \text{ }^\circ\text{C}\text{-0.5h}$ (Table 2). The material synthesized at $350 \text{ }^\circ\text{C}$ for 1 h had a Coulombic efficiency of 89% and 93% with and without NS, respectively. The lower Coulombic efficiency of materials synthesized by using a longer

Table 3. Comparison of Different Vanadium Oxide Containing Electrodes for Battery-like Systems^a

material	electrode preparation	initial capacity (mAh·g ⁻¹)	capacity retention (applied voltage)	ref
V ₂ O ₅ /C electrospun fibers	additive-free (100 μm/3 mg·cm ⁻²)	310 mo = 316	13% at 0.5 A·g ⁻¹ (1.7–4.0 V vs Li/Li ⁺)	this work, 1 M LiPF ₆ in EC/DMC
VO ₂ /C electrospun fibers	additive-free (100 μm/3 mg·cm ⁻²)	228 mo = 269	66% at 0.5 A·g ⁻¹ (1.7–4.0 V vs Li/Li ⁺)	this work, 1 M LiPF ₆ in EC/DMC
V ₂ O ₅ electrospun fibers	with CA and PB (n.r.)	192 mo = 320	25% at 0.35 A·g ⁻¹ (1.8–4.0 V vs Li/Li ⁺)	11, 1 M LiPF ₆ in EC/DEC
V ₂ O ₅ electrospun fibers	with CA and PB (n.r.)	273 mo = 390	(n.r.) (1.8–4.0 V vs Li/Li ⁺)	33, 1 M LiPF ₆ in EC/DMC
V ₂ O ₅ /C hybrid nanoparticles	additive-free (50 μm)	149 mo = 310	46% at 17 A·g ⁻¹ (–1.2 V to +1.0 V vs carbon)	18, 1 M LiClO ₄ in ACN
V ₂ O ₅ nanoparticles	with CA and PB (n.r.)	192 mo = 274	91% at 1 A·g ⁻¹ (2.0–4.0 V vs Li/Li ⁺)	64, 1 M LiPF ₆ in EC/DEC
V ₂ O ₅ /C electrospun fibers	additive-free (100 μm/3 mg·cm ⁻²)	62 mo = 66	32% at 0.5 A·g ⁻¹ (1.5–3.5 V vs Na/Na ⁺)	this work, 1 M NaClO ₄ in PC
VO ₂ /C electrospun fiber	additive-free (100 μm/3 mg·cm ⁻²)	107 mo = 126	53% at 0.5 A·g ⁻¹ (1.5–3.5 V vs Na/Na ⁺)	this work, 1 M NaClO ₄ in PC
V ₂ O ₅ /C hybrid nanoparticles	with CA and PB (1.3 mg·cm ⁻²)	193 mo = 276	50% at 0.6 A·g ⁻¹ (1.5–3.8 V vs Na/Na ⁺)	15, 1 M NaClO ₄ in PC
V ₂ O ₅ nanoparticles	additive-free (n.r.)	150 mo = 150	(n.r.) (1.5–3.8 V vs Na/Na ⁺)	12, 1 M NaClO ₄ in PC
V ₂ O ₅ /C hybrid nanoparticles	additive-free (50 μm)	120 mo = 250	51% at 11 A·g ⁻¹ (–1.2 V to +1.0 V vs carbon)	18, 1 M NaClO ₄ in ACN

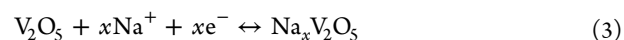
^aFor conventional electrode preparation, conductive additives (CA) and a polymer binder (PB) are added to the metal oxide particles. The electrode thickness or mass loading is reported here. The discharge capacity values (mAh·g⁻¹) are normalized to electrode mass and to metal oxide mass (mo). Non-reported values are also indicated (n.r.). EC, ethylene carbonate; DMC, dimethyl carbonate; DEC, diethyl carbonate; ACN, acetonitrile; PC, propylene carbonate.

annealing time correlates with the lower cyclic stability of these samples.

Several parameters have an influence on an efficient charge transfer and stable performance, including the uniform distribution and higher presence of a conductive phase,¹⁶ and the stability of the vanadium oxide phase in the used voltage window.^{8,10} Table 3 compares our results with literature values. A direct comparison cannot be made because previous works crushed electrospun fibers and reconsolidated them to electrodes by admixing conductive additives and a polymer binder. In comparison, we see for our materials a good capacity and rate capability, since no conductive additive and polymer binder are used.

3.2.4. Electrochemical Characterization as a Cathode for Sodium-Ion Batteries. To the best of our knowledge, there is no work on electrospun vanadium oxide as cathodes for NIBs. We evaluated the electrospun hybrid fibers as cathodes for NIBs, finding electrochemical behavior very different from that of lithium. In the case of the fibers without NS, a very poor electrochemical response was observed (Figure 5C,D), which is significantly improved for the fibers with NS. Cyclic voltammograms of the samples with NS show higher specific currents than the samples without NS (Figure 5C). The sample NS 350 °C-1h presents broad cathodic peaks at 3.16, 2.72, and 2.45 V vs Na/Na⁺, while the anodic peaks are observed at 2.58, 3.04, and 3.41 V vs Na/Na⁺. Peaks in this range have been attributed to the sequential insertion and

extraction of Na⁺, and the reduction of V⁵⁺ to V⁴⁺.¹⁵ The sample NS 350 °C-0.5h presents a different behavior with broad cathodic peaks at 3.57, 3.0, 2.68, 2.48, and 1.72 V vs Na/Na⁺. In the anodic scan, a broad peak at 2.04 V is observed followed by sharper peaks at 2.79, 3.04, and 3.28 V vs Na/Na⁺. These peaks are attributed to a multistep insertion and extraction of Na⁺ in monoclinic VO₂, leading to the reduction of V⁴⁺ to V³⁺. The processes for V₂O₅ and VO₂ follow eqs 3 and 4, where the insertion of 1 Na⁺ leads to a theoretical specific capacity of 147 and 323 mAh·g⁻¹, respectively.



For the characterization of the sodium insertion capacity and rate handling performance, galvanostatic cycling at different rates was performed. For the fibers without NS, initial capacity values are obtained of 47 and 42 mAh·g⁻¹ for the samples 350 °C-0.5h and 350 °C-1h, respectively. Galvanostatic charge/discharge curves of the first cycle at a low rate of 0.025 A·g⁻¹ are presented in (Figure 5F). The sample 350 °C-0.5h presented the highest capacity retention maintaining 37% of the capacity at 5 A·g⁻¹ and stable performance after rate handling. Under the presence of NS, the capacity values drastically increase. The sample rich in VO₂ (NS 350 °C-0.5h) had the highest initial capacity of 107 mAh·g⁻¹ (126 mAh·g_{VOx}⁻¹). In the case of orthorhombic V₂O₅, for the sample NS

350 °C-1h no significant enhancement is observed, probably related to the low amount of carbon (2.0 to 1.1 mass %). However, for the sample NS 300 °C-3h which presents also orthorhombic V_2O_5 , nanostructuring led to a significant increase in the capacity as presented in the Supporting Information Figure S6D. The capacity increased from 34 to 62 $\text{mAh}\cdot\text{g}^{-1}$ ($66 \text{ mAh}\cdot\text{g}_{\text{VOx}}^{-1}$) when NS was added, which is attributed to the higher carbon amount (5.8 to 4.2 mass %) compared to NS 350 °C-1h. The positive effect of nanostructuring is more clearly observed for the monoclinic VO_2 -rich sample.

Comparing the initial Coulombic efficiency of the same material, a lower efficiency was observed in the case of sodium compared to lithium insertion/extraction. The sample NS 350 °C-0.5h presented the lowest efficiency (51%), followed by the sample NS 350 °C-1h (61%), and the sample 350 °C-0.5h presented the highest efficiency (82%). The lower efficiency correlates with a lower cycling performance. We attribute the nanostructuring and higher carbon content to a higher sodium insertion into the material, which is however not completely reversible and highly demanding under the voltage window used in this work.

The effect of the carbon nanohorns and the heat treatment on the internal resistance of the system has been studied by electrochemical impedance spectroscopy. The Nyquist plots after five voltammetry cycles ($0.1 \text{ mV}\cdot\text{s}^{-1}$) are presented in the Supporting Information (Figure S8). The first parameter studied was the pure Ohmic resistance (r_o) of the battery, at high frequencies, where $-\text{Im}(Z) = 0$. The samples synthesized at 350 °C for 0.5 h present the lowest resistance, namely, 0.89 and $1.05 \Omega\cdot\text{cm}^2$ for the sample with and without NS, respectively. The samples synthesized for 1 h show values of $1.57\text{--}1.63 \Omega\cdot\text{cm}^2$. At the high–middle frequency region, one pronounced semicircle is observed for the samples 350 °C-0.5h and NS 350 °C-0.5h, which describes the charge transfer reaction at the electrode/electrolyte interface.⁶² This semicircle shifts to lower frequencies, and additional semicircles can be distinguished for the samples synthesized at 350 °C for 1 h. Also, these samples present a higher charge transfer resistance, observed from a higher difference between r_o and the real impedance at the local minimum of $-\text{Im}(Z)$.⁶³ We conclude that for the same heat treatment the presence of nanohorns leads to lower Ohmic and charge transfer resistance.

3.2.5. Postmortem Analysis and Comparison with Polymer-Bound Electrodes. To gain further insights into the degradation mechanism of the electrode material during electrochemical testing, postmortem scanning and transmission electron micrographs of NS 350 °C-0.5h and NS 350 °C-1h were recorded and are presented in the Supporting Information, Figure S7. Compared to the freestanding electrode before electrochemical testing (Figure 3), the fiber morphology and the crystalline nature of the materials are maintained. Locally, we also find broken fibers, but it is unclear if this has resulted from electrochemical operation of sample preparation.

To better understand the degradation process, we prepared polymer-bound electrodes using the sample NS 350 °C-0.5h. We consider that two different parameters could be contributing to the degradation of the electrode: the low carbon content and the chosen voltage operation window, which leads to the formation of irreversible vanadium oxide phases. The low carbon content could lead to a loss of electrical percolation and a nonuniform charge distribution,

which locally creates degradation spots.¹⁶ The effect of the carbon amount was analyzed by comparing the fiber mats with polymer-bound fibers with and without conductive additives (Supporting Information, Figure S8A). Comparing the fiber mats with the polymer-bound electrodes containing 20 mass % conductive additives, we observed a similar capacity loss after 50 cycles. Consequently, the low carbon content in the hybrid fibers does not seem to be the main contributor to capacity degradation. The incorporation of the conductive additives, however, increased the rate handling performance of the electrode.

We see a much larger influence on the capacity stability when comparing the polymer-bound electrodes with conductive additives at different voltages (Supporting Information, Figure S8B). For the sample containing monoclinic VO_2 (NS 350 °C-0.5h), we found higher stability when the voltage window was maintained between 3.5 and 1.7 V vs Li/Li⁺. Low stability was observed between 4.0 and 2.0 V vs Li/Li⁺, which is typically the voltage range chosen for V_2O_5 electrodes. In the case of orthorhombic V_2O_5 , nonreversible crystal phases are formed below 1.9 V vs Li/Li⁺.⁸

4. CONCLUSIONS

In this work, electrospinning was used to produce freestanding, binder-free hybrid vanadium oxide/carbon nanofibers. Starting from a sol–gel synthesis using poly(vinyl acetate) and vanadium oxytripropoxide as molecular precursors, micrometer-sized fibers were obtained. To increase the carbon amount in the fiber mat, graphitic carbon nanohorns were added into the spinning dope obtaining a reduction of 85% in the fiber diameter. The as-spun fibers were annealed in argon at 700 °C, leading to the formation of nanocrystalline carbon and V_2O_3 amorphous domains. For transformation to crystalline VO_2 and V_2O_5 , the fibers were later treated at 300–350 °C, for 0.5, 1, and 3 h under Ar/air mixed atmospheres. Hybrid fibers containing nanocrystalline carbon and crystalline vanadium oxide (orthorhombic V_2O_5 and monoclinic V_3O_7) were obtained after treatment under 300 °C for 3 h and 350 °C for 1 h. By treatment at 350 °C for 0.5 h, crystalline tetragonal VO_2 and monoclinic VO_2 are formed with higher amounts of carbon (10–15 mass %). Shorter treatment times (such as 0.5 h) are beneficial for the synthesis of hybrid vanadium oxide/carbon fibers.

Tested as a cathode for LIBs, it was found that a higher amount of carbon is crucial for more stable performance and improved capacity. The uniform distribution of carbon avoids the formation of local degradation regions via a uniform charge distribution. Comparing the electrochemical behavior of the orthorhombic V_2O_5 and monoclinic VO_2 fibers, specific capacity values obtained are 310 and $228 \text{ mAh}\cdot\text{g}^{-1}$, respectively. Monoclinic VO_2 has a superior electrochemical performance at 1.7–4.0 V vs Li/Li⁺ due to the pseudocapacitive behavior, maintaining 66% of the initial capacity at $0.5 \text{ A}\cdot\text{g}^{-1}$.

Tested as cathodes for NIBs, an improved electrochemical performance was observed for nanostructured fibers. The importance of a conductive carbon network for improved electrochemical performance was also corroborated. Orthorhombic V_2O_5 /C hybrid fibers presented very low specific capacity and capacity retention values, which are related to the low diffusion of Na^+ in orthorhombic V_2O_5 . The hybrid fibers containing monoclinic VO_2 and carbon presented an improved

specific capacity and rate performance, especially when used as nanostructures with a maximum capacity of 107 mAh·g⁻¹.

■ ASSOCIATED CONTENT

5 Supporting Information

The Supporting Information is available free of charge on the ACS Publications website at DOI: 10.1021/acsaem.8b00572.

Comprehensive material characterization of graphitic carbon nanohorn particles, Raman data (including peak deconvolution analysis), additional high-resolution transmission electron micrographs, and comprehensive data analysis (Raman, XRD, and electrochemistry) for samples synthesized at 300 °C (PDF)

■ AUTHOR INFORMATION

Corresponding Author

*E-mail: volker.presser@leibniz-inm.de.

ORCID

Volker Presser: 0000-0003-2181-0590

Notes

The authors declare no competing financial interest.

■ ACKNOWLEDGMENTS

This work was part of the Carbon Metal Oxide Nanohybrid project (CarMON) supported by the Leibniz Association (Grant SAW-2017). We thank Eduard Arzt for his continuing support, Andrea Jung for the CHNS measurements, Öznil Budak, and Anna Schreiber (all at INM) for useful discussions and technical support.

■ REFERENCES

- (1) Scrosati, B.; Hassoun, J.; Sun, Y.-K. Lithium-Ion Batteries. A Look Into the Future. *Energy Environ. Sci.* **2011**, *4* (9), 3287–3295.
- (2) Yang, Z.; Zhang, J.; Kintner-Meyer, M. C. W.; Lu, X.; Choi, D.; Lemmon, J. P.; Liu, J. Electrochemical Energy Storage for Green Grid. *Chem. Rev.* **2011**, *111* (5), 3577–3613.
- (3) Fleischmann, S.; Tolosa, A.; Presser, V. Design of Carbon/Metal Oxide Hybrids for Electrochemical Energy Storage. *Chem. - Eur. J.* **2018**, DOI: 10.1002/chem.201800772.
- (4) Broussely, M.; Archdale, G. Li-Ion Batteries and Portable Power Source Prospects for the Next 5–10 Years. *J. Power Sources* **2004**, *136* (2), 386–394.
- (5) Kim, S.-W.; Seo, D.-H.; Ma, X.; Ceder, G.; Kang, K. Electrode Materials for Rechargeable Sodium-Ion Batteries: Potential Alternatives to Current Lithium-Ion Batteries. *Adv. Energy Mater.* **2012**, *2* (7), 710–721.
- (6) Simon, P.; Gogotsi, Y. Materials for Electrochemical Capacitors. *Nat. Mater.* **2008**, *7*, 845–854.
- (7) Augustyn, V. Tuning the Interlayer of Transition Metal Oxides for Electrochemical Energy Storage. *J. Mater. Res.* **2017**, *32* (1), 2–15.
- (8) Chernova, N. A.; Roppolo, M.; Dillon, A. C.; Whittingham, M. S. Layered Vanadium and Molybdenum Oxides: Batteries and Electrochromics. *J. Mater. Chem.* **2009**, *19* (17), 2526–2552.
- (9) Fleischmann, S.; Tolosa, A.; Zeiger, M.; Krüner, B.; Peter, N. J.; Grobelsek, I.; Quade, A.; Kruth, A.; Presser, V. Vanadia-Titania Multilayer Nanodecoration of Carbon Onions Via Atomic Layer Deposition for High Performance Electrochemical Energy Storage. *J. Mater. Chem. A* **2017**, *5* (6), 2792–2801.
- (10) Leger, C.; Bach, S.; Soudan, P.; Pereira-Ramos, J.-P. Structural and Electrochemical Properties of ω Li_xV₂O₅ (0.4 ≤ x ≤ 3) as Rechargeable Cathodic Material for Lithium Batteries. *J. Electrochem. Soc.* **2005**, *152* (1), A236–A241.
- (11) Cheah, Y. L.; Gupta, N.; Pramana, S. S.; Aravindan, V.; Wee, G.; Srinivasan, M. Morphology, Structure and Electrochemical

Properties of Single Phase Electrospun Vanadium Pentoxide Nanofibers for Lithium Ion Batteries. *J. Power Sources* **2011**, *196* (15), 6465–6472.

(12) Tepavcevic, S.; Xiong, H.; Stamenkovic, V. R.; Zuo, X.; Balasubramanian, M.; Prakapenka, V. B.; Johnson, C. S.; Rajh, T. Nanostructured Bilayered Vanadium Oxide Electrodes for Rechargeable Sodium-Ion Batteries. *ACS Nano* **2012**, *6* (1), 530–538.

(13) Cao, X.; Pan, A.; Liu, S.; Zhou, J.; Li, S.; Cao, G.; Liu, J.; Liang, S. Chemical Synthesis of 3D Graphene-Like Cages for Sodium-Ion Batteries Applications. *Adv. Energy Mater.* **2017**, *7* (20), 1700797.

(14) Nayak, P. K.; Yang, L.; Brehm, W.; Adelhelm, P. From Lithium-Ion to Sodium-Ion Batteries: Advantages, Challenges, and Surprises. *Angew. Chem., Int. Ed.* **2018**, *57* (1), 102–120.

(15) Raju, V.; Rains, J.; Gates, C.; Luo, W.; Wang, X.; Stickle, W. F.; Stucky, G. D.; Ji, X. Superior Cathode of Sodium-Ion Batteries: Orthorhombic V₂O₅ Nanoparticles Generated in Nanoporous Carbon by Ambient Hydrolysis Deposition. *Nano Lett.* **2014**, *14* (7), 4119–4124.

(16) Widmaier, M.; Jäckel, N.; Zeiger, M.; Abuzarli, M.; Engel, C.; Bommer, L.; Presser, V. Influence of Carbon Distribution on the Electrochemical Performance and Stability of Lithium Titanate Based Energy Storage Devices. *Electrochim. Acta* **2017**, *247* (Suppl. C), 1006–1018.

(17) Fleischmann, S.; Zeiger, M.; Jäckel, N.; Krüner, B.; Lemkova, V.; Widmaier, M.; Presser, V. Tuning Pseudocapacitive and Battery-Like Lithium Intercalation in Vanadium Dioxide/Carbon Onion Hybrids for Asymmetric Supercapacitor Anodes. *J. Mater. Chem. A* **2017**, *5* (25), 13039–13051.

(18) Fleischmann, S.; Leistenschneider, D.; Lemkova, V.; Krüner, B.; Zeiger, M.; Borchardt, L.; Presser, V. Tailored Mesoporous Carbon/Vanadium Pentoxide Hybrid Electrodes for High Power Pseudocapacitive Lithium and Sodium Intercalation. *Chem. Mater.* **2017**, *29* (20), 8653–8662.

(19) Tolosa, A.; Krüner, B.; Fleischmann, S.; Jäckel, N.; Zeiger, M.; Aslan, M.; Grobelsek, I.; Presser, V. Niobium Carbide Nanofibers as a Versatile Precursor for High Power Supercapacitor and High Energy Battery Electrodes. *J. Mater. Chem. A* **2016**, *4* (41), 16003–16016.

(20) Kim, B.-H.; Yang, K. S.; Yang, D. J. Electrochemical Behavior of Activated Carbon Nanofiber-Vanadium Pentoxide Composites for Double-Layer Capacitors. *Electrochim. Acta* **2013**, *109* (Suppl. C), 859–865.

(21) Wu, G.-M.; Wang, A.-R.; Zhang, M.-X.; Yang, H.-Y.; Zhou, B.; Shen, J. Investigation on Properties of V₂O₅-MWCNTs Composites as Cathode Materials. *J. Sol-Gel Sci. Technol.* **2008**, *46* (1), 79–85.

(22) Tolosa, A.; Fleischmann, S.; Grobelsek, I.; Quade, A.; Lim, E.; Presser, V. Binder-Free Hybrid Titanium-Niobium Oxide/Carbon Nanofiber Mats for Lithium-Ion Battery Electrodes. *ChemSusChem* **2018**, *11* (1), 159–170.

(23) Pan, A. Q.; Wu, H. B.; Zhang, L.; Lou, X. W. Uniform V₂O₅ Nanosheet-Assembled Hollow Microflowers with Excellent Lithium Storage Properties. *Energy Environ. Sci.* **2013**, *6* (5), 1476–1479.

(24) Pan, A.; Wu, H. B.; Yu, L.; Lou, X. W. Template-Free Synthesis of VO₂ Hollow Microspheres with Various Interiors and Their Conversion into V₂O₅ for Lithium-Ion Batteries. *Angew. Chem., Int. Ed.* **2013**, *52* (8), 2226–2230.

(25) Yamada, H.; Tagawa, K.; Komatsu, M.; Moriguchi, I.; Kudo, T. High Power Battery Electrodes Using Nanoporous V₂O₅/Carbon Composites. *J. Phys. Chem. C* **2007**, *111* (23), 8397–8402.

(26) Fleischmann, S.; Jäckel, N.; Zeiger, M.; Krüner, B.; Grobelsek, I.; Formanek, P.; Choudhury, S.; Weingarh, D.; Presser, V. Enhanced Electrochemical Energy Storage by Nanoscopic Decoration of Endohedral and Exohedral Carbon with Vanadium Oxide via Atomic Layer Deposition. *Chem. Mater.* **2016**, *28* (8), 2802–2813.

(27) Perera, S. D.; Patel, B.; Bonso, J.; Grunewald, M.; Ferraris, J. P.; Balkus, K. J. Vanadium Oxide Nanotube Spherical Clusters Prepared on Carbon Fabrics for Energy Storage Applications. *ACS Appl. Mater. Interfaces* **2011**, *3* (11), 4512–4517.

(28) Perera, S. D.; Patel, B.; Nijem, N.; Roodenko, K.; Seitz, O.; Ferraris, J. P.; Chabal, Y. J.; Balkus, K. J. Vanadium Oxide Nanowire–

Carbon Nanotube Binder-Free Flexible Electrodes for Supercapacitors. *Adv. Energy Mater.* **2011**, *1* (5), 936–945.

(29) Sakamoto, J. S.; Dunn, B. Vanadium Oxide-Carbon Nanotube Composite Electrodes for Use in Secondary Lithium Batteries. *J. Electrochem. Soc.* **2002**, *149* (1), A26–A30.

(30) Seng, K. H.; Liu, J.; Guo, Z. P.; Chen, Z. X.; Jia, D.; Liu, H. K. Free-Standing V_2O_5 Electrode for Flexible Lithium Ion Batteries. *Electrochem. Commun.* **2011**, *13* (5), 383–386.

(31) Zeiger, M.; Ariyanto, T.; Krüner, B.; Peter, N. J.; Fleischmann, S.; Etzold, B. J. M.; Presser, V. Vanadium Pentoxide/Carbide-Derived Carbon Core-Shell Hybrid Particles for High Performance Electrochemical Energy Storage. *J. Mater. Chem. A* **2016**, *4* (48), 18899–18909.

(32) Chen, Z.; Augustyn, V.; Jia, X.; Xiao, Q.; Dunn, B.; Lu, Y. High-Performance Sodium-Ion Pseudocapacitors Based on Hierarchically Porous Nanowire Composites. *ACS Nano* **2012**, *6* (5), 4319–4327.

(33) Mai, L.; Xu, L.; Han, C.; Xu, X.; Luo, Y.; Zhao, S.; Zhao, Y. Electrospun Ultralong Hierarchical Vanadium Oxide Nanowires with High Performance for Lithium Ion Batteries. *Nano Lett.* **2010**, *10* (11), 4750–4755.

(34) Cavaliere, S.; Subianto, S.; Savych, I.; Jones, D. J.; Roziere, J. Electrospinning: Designed Architectures for Energy Conversion and Storage Devices. *Energy Environ. Sci.* **2011**, *4* (12), 4761–4785.

(35) Tolosa, A.; Krüner, B.; Jäckel, N.; Aslan, M.; Vakifahmetoglu, C.; Presser, V. Electrospinning and Electrospinning of Silicon Oxycarbide-Derived Nanoporous Carbon for Supercapacitor Electrodes. *J. Power Sources* **2016**, *313*, 178–188.

(36) Tolosa, A.; Widmaier, M.; Krüner, B.; Griffin, J.; Presser, V. Continuous Silicon Oxycarbide Fiber Mats with Tin Nanoparticles as High Capacity Anode for Lithium-Ion Batteries. *Sustainable Energy Fuels* **2018**, *2*, 215–228.

(37) Iijima, S.; Yudasaka, M.; Yamada, R.; Bandow, S.; Suenaga, K.; Kokai, F.; Takahashi, K. Nano-Aggregates of Single-Walled Graphitic Carbon Nano-Horns. *Chem. Phys. Lett.* **1999**, *309* (3), 165–170.

(38) Suarez-Martinez, I.; Grobert, N.; Ewels, C. P. Nomenclature of sp^2 Carbon Nanoforms. *Carbon* **2012**, *50* (3), 741–747.

(39) Viswanathamurthi, P.; Bhattarai, N.; Kim, H. Y.; Lee, D. R. Vanadium Pentoxide Nanofibers by Electrospinning. *Scr. Mater.* **2003**, *49* (6), 577–581.

(40) Schneider, C. A.; Rasband, W. S.; Eliceiri, K. W. NIH Image to ImageJ: 25 years of Image Analysis. *Nat. Methods* **2012**, *9*, 671.

(41) Weingarh, D.; Zeiger, M.; Jäckel, N.; Aslan, M.; Feng, G.; Presser, V. Graphitization as a Universal Tool to Tailor the Potential-Dependent Capacitance of Carbon Supercapacitors. *Adv. Energy Mater.* **2014**, *4* (13), 1400316.

(42) Jäckel, N.; Weingarh, D.; Schreiber, A.; Krüner, B.; Zeiger, M.; Tolosa, A.; Aslan, M.; Presser, V. Performance Evaluation of Conductive Additives for Activated Carbon Supercapacitors in Organic Electrolyte. *Electrochim. Acta* **2016**, *191*, 284–298.

(43) Vioux, A. Nonhydrolytic Sol–Gel Routes to Oxides. *Chem. Mater.* **1997**, *9* (11), 2292–2299.

(44) Sanchez, C.; Livage, J. Sol-Gel Chemistry from Metal Alkoxide Precursors. *New J. Chem.* **1990**, *14* (6–7), 513–521.

(45) Ceretti, E.; Ginestra, P. S.; Ghazinejad, M.; Fiorentino, A.; Madou, M. Electrospinning and Characterization of Polymer–Graphene Powder Scaffolds. *CIRP Ann.* **2017**, *66* (1), 233–236.

(46) Li, Z.; Wang, C. Effects of Working Parameters on Electrospinning. *One-Dimensional Nanostructures*; Springer: Berlin, Heidelberg, 2013; Chapter 2, pp 15–28, DOI: 10.1007/978-3-642-36427-3_2.

(47) D'Amelia, R. P.; Gentile, S.; Nirode, W. F.; Huang, L. Quantitative Analysis of Copolymers and Blends of Polyvinyl Acetate (PVAc) Using Fourier Transform Infrared Spectroscopy (FTIR) and Elemental Analysis (EA). *World J. Chem. Educ.* **2016**, *4* (2), 25–31.

(48) Fujii, K. Tacticity and Infrared Spectra of Poly(Vinyl Acetate). *J. Polym. Sci., Part B: Polym. Lett.* **1967**, *5* (7), 551–556.

(49) Chaput, F.; Dunn, B.; Fuqua, P.; Salloux, K. Synthesis and Characterization of Vanadium Oxide Aerogels. *J. Non-Cryst. Solids* **1995**, *188* (1), 11–18.

(50) Roppolo, M.; Jacobs, C. B.; Upreti, S.; Chernova, N. A.; Whittingham, M. S. Synthesis and Characterization of Layered and Scrolled Amine-Templated Vanadium Oxides. *J. Mater. Sci.* **2008**, *43* (14), 4742–4748.

(51) Menezes, W. G.; Reis, D. M.; Benedetti, T. M.; Oliveira, M. M.; Soares, J. F.; Torresi, R. M.; Zabin, A. J. G. V_2O_5 Nanoparticles Obtained From a Synthetic Bariandite-Like Vanadium Oxide: Synthesis, Characterization and Electrochemical Behavior in an Ionic Liquid. *J. Colloid Interface Sci.* **2009**, *337* (2), 586–593.

(52) Ferrari, A. C. Raman Spectroscopy of Graphene and Graphite: Disorder, Electron–Phonon Coupling, Doping and Nonadiabatic Effects. *Solid State Commun.* **2007**, *143* (1–2), 47–57.

(53) Ferrari, A. C.; Robertson, J. Raman Spectroscopy of Amorphous, Nanostructured, Diamond-Like Carbon, and Nanodiamond. *Philos. Trans. R. Soc., A* **2004**, *362* (1824), 2477–2512.

(54) Preiss, H.; Schultze, D.; Szulzewsky, K. Carbothermal Synthesis of Vanadium and Chromium Carbides from Solution-Derived Precursors. *J. Eur. Ceram. Soc.* **1999**, *19* (2), 187–194.

(55) Dannatt, C. W.; Ellingham, H. J. T. Roasting and Reduction Processes. Roasting and Reduction Processes - a General Survey. *Discuss. Faraday Soc.* **1948**, *4* (0), 126–139.

(56) Zhang, C.; Yang, Q.; Koughia, C.; Ye, F.; Sanayei, M.; Wen, S.-J.; Kasap, S. Characterization of Vanadium Oxide Thin Films with Different Stoichiometry Using Raman Spectroscopy. *Thin Solid Films* **2016**, *620* (Suppl. C), 64–69.

(57) Armstrong, E.; Osiak, M.; Geaney, H.; Glynn, C.; O'Dwyer, C. 2D and 3D Vanadium Oxide Inverse Opals and Hollow Sphere Arrays. *CrystEngComm* **2014**, *16* (47), 10804–10815.

(58) Huotari, J.; Lappalainen, J.; Puustinen, J.; Lloyd Spetz, A. Gas Sensing Properties of Pulsed Laser Deposited Vanadium Oxide Thin Films with Various Crystal Structures. *Sens. Actuators, B* **2013**, *187*, 386–394.

(59) O'Dwyer, C.; Lavayen, V.; Newcomb, S. B.; Santa Ana, M. A.; Benavente, E.; González, G.; Sotomayor Torres, C. M. Vanadate Conformation Variations in Vanadium Pentoxide Nanostructures. *J. Electrochem. Soc.* **2007**, *154* (8), K29–K35.

(60) Armstrong, E.; Osiak, M.; Glynn, C.; O'Dwyer, C. Investigations into Structure and Chemistry of 1D, 2D and 3D Structured Vanadium Oxide Nanomaterials for Li-Ion Batteries. *ECSS Trans.* **2014**, *58* (14), 3–12.

(61) Armstrong, E.; McNulty, D.; Geaney, H.; O'Dwyer, C. Electrodeposited Structurally Stable V_2O_5 Inverse Opal Networks as High Performance Thin Film Lithium Batteries. *ACS Appl. Mater. Interfaces* **2015**, *7* (48), 27006–27015.

(62) Liang, S.; Cao, X.; Wang, Y.; Hu, Y.; Pan, A.; Cao, G. Uniform $8LiFePO_4 \cdot Li_3V_2(PO_4)_3/C$ Nanoflakes for High-Performance Li-Ion Batteries. *Nano Energy* **2016**, *22*, 48–58.

(63) Waag, W.; Käbitz, S.; Sauer, D. U. Experimental Investigation of the Lithium-Ion Battery Impedance Characteristic at Various Conditions and Aging States and Its Influence on the Application. *Appl. Energy* **2013**, *102*, 885–897.

(64) Pan, A.; Wu, H. B.; Yu, L.; Zhu, T.; Lou, X. W. Synthesis of Hierarchical Three-Dimensional Vanadium Oxide Microstructures as High-Capacity Cathode Materials for Lithium-Ion Batteries. *ACS Appl. Mater. Interfaces* **2012**, *4* (8), 3874–3879.

(65) Chase, M. W., Jr. *NIST-JANAF Thermochemical Tables*, 4th ed.; Journal of Physical and Chemical Reference Data Monograph No. 9 (Part I and Part II); National Institute of Standards and Technology: Gaithersburg, MD, USA, 1998.

3.6 Design of carbon/metal oxide hybrids for electrochemical energy storage

Simon Fleischmann,^{a,b} Aura Tolosa,^{a,b} and Volker Presser^{a,b}

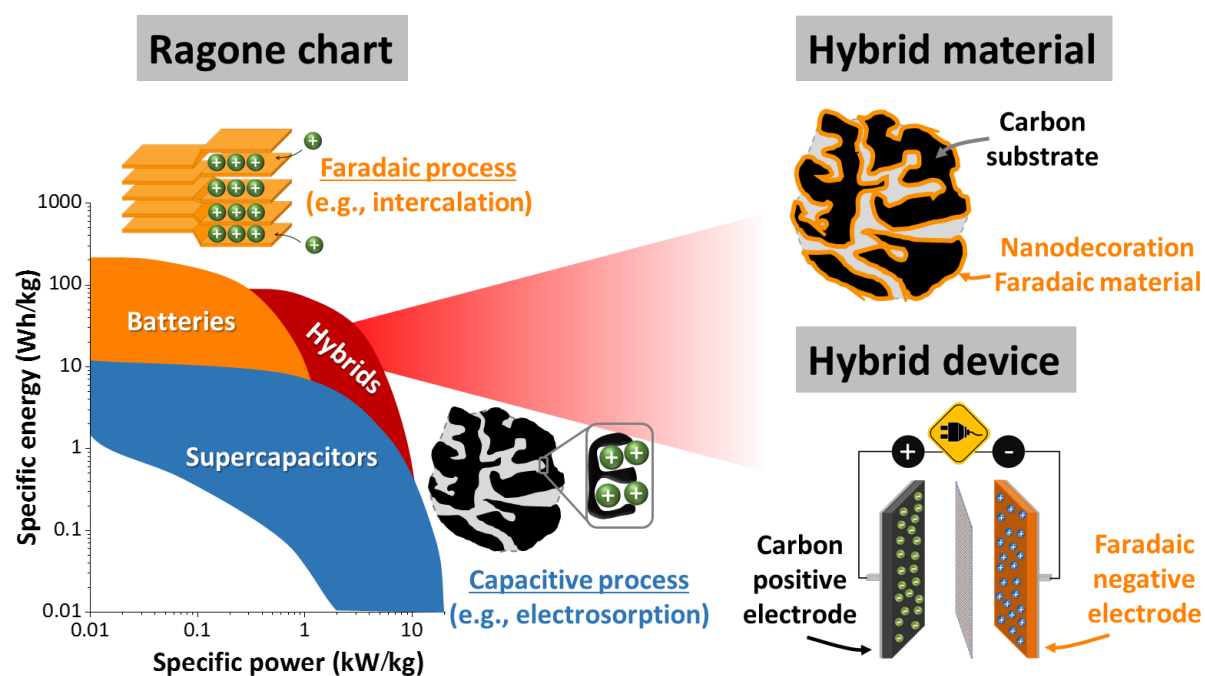
^a INM - Leibniz Institute for New Materials, 66123 Saarbrücken, Germany

^b Department of Materials Science and Engineering, Saarland University, 66123 Saarbrücken, Germany

Published in: Chemistry-A European Journal, 24 (2018), 12143-12153

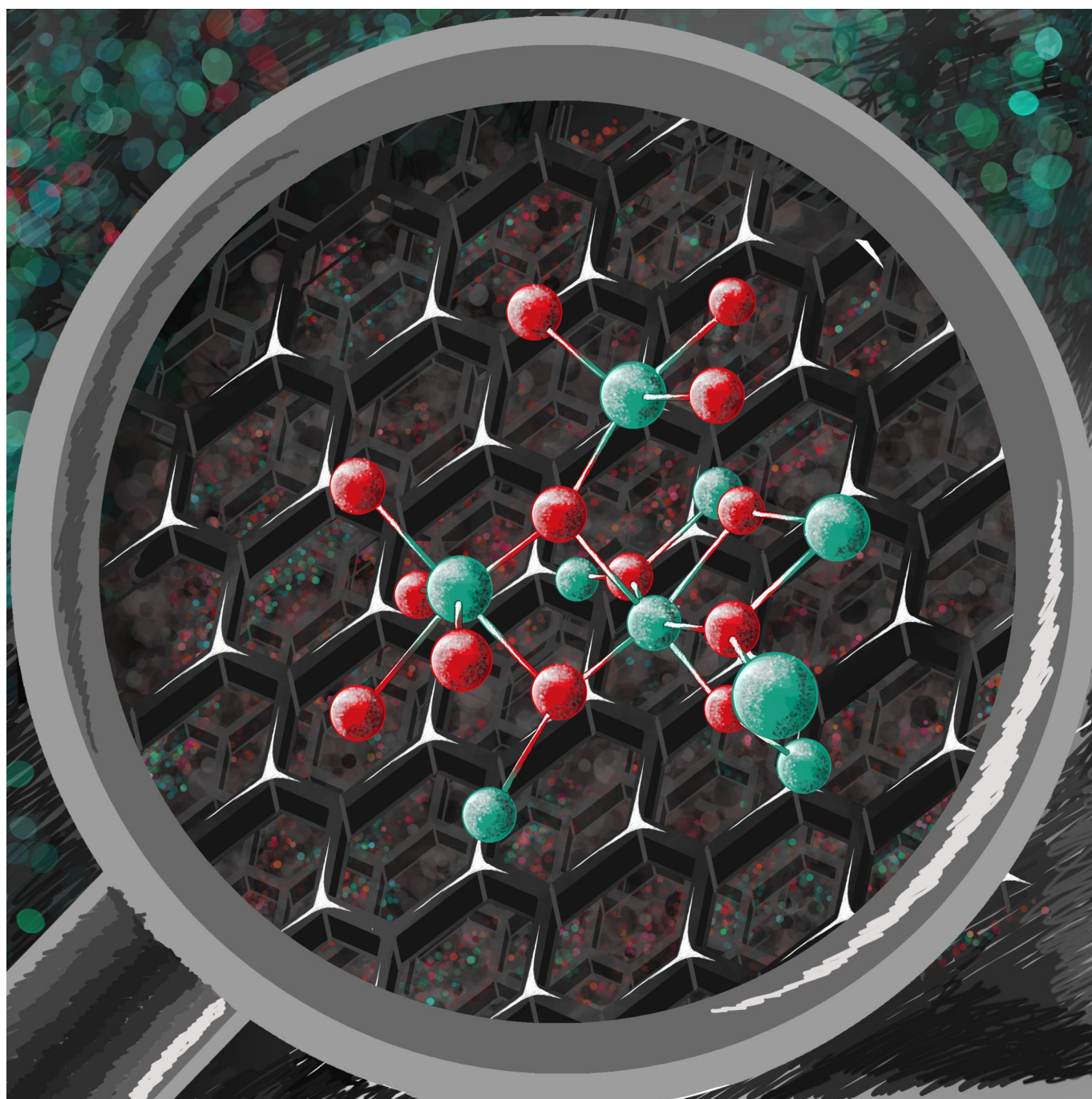
DOI: 10.1002/chem.201800772

Copyright Wiley-VCH Verlag GmbH & Co. KGaA. Reproduced with permission



Own contribution: Support by paper writing

■ Renewable Energy

YC Design of Carbon/Metal Oxide Hybrids for Electrochemical Energy StorageSimon Fleischmann,^[a, b] Aura Tolosa,^[a, b] and Volker Presser^{*[a, b]}

Abstract: Next generation electrochemical energy storage materials that enable a combination of high specific energy, specific power, and cycling stability can be obtained by a hybridization approach. This involves electrode materials that contain carbon and metal oxide phases linked on a nanoscopic level and combine characteristics of supercapacitors and batteries. The combination of the components requires careful design to create synergistic effects for an increased electrochemical performance. Improved understanding of the role of carbon as a substrate has advanced the power handling and cycling stability of hybrid materials significantly in recent years. This Concept outlines different design strategies for the design of hybrid electrode materials: (1) the deposition of metal oxides on readily existing carbon substrates and (2) co-synthesizing both carbon and metal oxide phase during the synthesis procedure. The implications of carbon properties on the hybrid material's structure and performance will be assessed and the impact of the hybrid electrode architecture will be analyzed. The advantages and disadvantages of all approaches are highlighted and strategies to overcome the latter will be proposed.

Introduction

Electrochemical energy storage

In the face of global warming, scarcity of fossil fuels, and a steadily growing energy demand, the transition to renewable energy sources has been identified as one of the most urgent tasks to the scientific community during the next decades.^[1] The large-scale implementation of renewable energy, however, leads to a shifting paradigm for power generation, that is, from production on demand to production when available. The resulting fluctuations make the use of fast-responding electrochemical energy storage (EES) devices indispensable.^[2] Generally, EES devices can typically be divided into two groups, (1) supercapacitors, or electrical double-layer capacitors (EDLCs) that store energy by physical electroadsorption of ions at the surface of their electrodes, and (2) batteries that employ Faradaic reactions in the bulk volume of their electrodes.

EDLCs are a prominent technology for rapid and highly reversible energy storage that utilize the separation of electrical

charges at the interface of electrodes and electrolyte.^[3] When an EDLC is charged, electrolyte ions diffuse to and electroadsorb on the surface of the oppositely charged electrode, forming the electrical double-layer. Suitable electrode materials offer a high surface area for ion adsorption, as well as good electrical conductivity. These properties are well met by microporous carbons, such as activated carbons^[4] or carbide-derived carbons^[5] and nanocarbons like graphene,^[6] carbon onions,^[7] or carbon nanotubes.^[8] The electroadsorption process is distinguished by very fast charge/discharge kinetics, leading to a quick energy uptake/release of supercapacitors (over 10 kW kg⁻¹). In contrast, the specific energy remains about an order of magnitude below that of batteries.^[3b] Despite efforts to further increase the specific energy of EDLCs by extending the surface area of microporous carbons or matching their pore sizes with the electrolyte ion sizes,^[9] the capacitance (and therefore the energy) of an EDLC is intrinsically limited to about 0.1 F m⁻² because even smaller pores can no longer accommodate ions and thinner pore walls can no longer screen electrical charges.^[10]

In contrast, a battery stores energy by Faradaic processes such as intercalation, conversion, or alloying reactions between its electrolyte ions and its electrodes. The most prominent system is the lithium-ion intercalation battery, but because of the high cost and geographically limited availability of lithium,^[11] alternative ionic systems like sodium^[12] or potassium^[13] are being explored. Unlike an EDLC, lithium-ion batteries employ two different materials as anode and cathode. When charged, lithium ions are extracted from the cathode and inserted into the anode material, resulting in Faradaic charge transfer. The different electrochemical potentials of the anode and the lithium and cathode determine the cell voltage of the battery.^[14] The electrode materials need to enable the insertion (intercalation) of lithium and should show a low (anode) or a high standard reduction potential (cathode). Typical candidates for intercalation-type electrodes are graphite^[15] or metal oxides^[16] that exhibit a layered structure, in between which the lithium ions can be stored or released. During intercalation, lithium ions must diffuse through the electrode material to reach the reaction sites, which is a kinetically limited process and leads to a relatively low power output of batteries (<1 kW kg⁻¹). Furthermore, intercalation and deintercalation processes are associated with expansion and shrinking of the electrodes, which exercises substantial mechanical stresses on the host material,^[17] limiting the cycling life of a battery to typically below 1000 cycles.


Hybrid electrochemical energy storage materials

It is obvious that EDLCs and batteries offer both certain distinct advantages. Therefore, hybridization of EDLC and batteries is highly attractive. Nowadays, hybridization is becoming increasingly popular in the field of electrochemical energy storage for the creation of novel electrode materials that offer both a high specific energy and power. Yet, improved performance can only be reached when following certain design

[a] S. Fleischmann, A. Tolosa, Prof. Dr. V. Presser
INM-Leibniz Institute for New Materials
66123 Saarbrücken (Germany)
E-mail: volker.presser@leibniz-inm.de

[b] S. Fleischmann, A. Tolosa, Prof. Dr. V. Presser
Department of Materials Science and Engineering
Saarland University, 66123 Saarbrücken (Germany)

 The ORCID numbers for the authors of this article can be found under:
<https://doi.org/10.1002/chem.201800772>.

 Part of a Special Issue to commemorate young and emerging scientists. To view the complete issue, visit Issue 47.

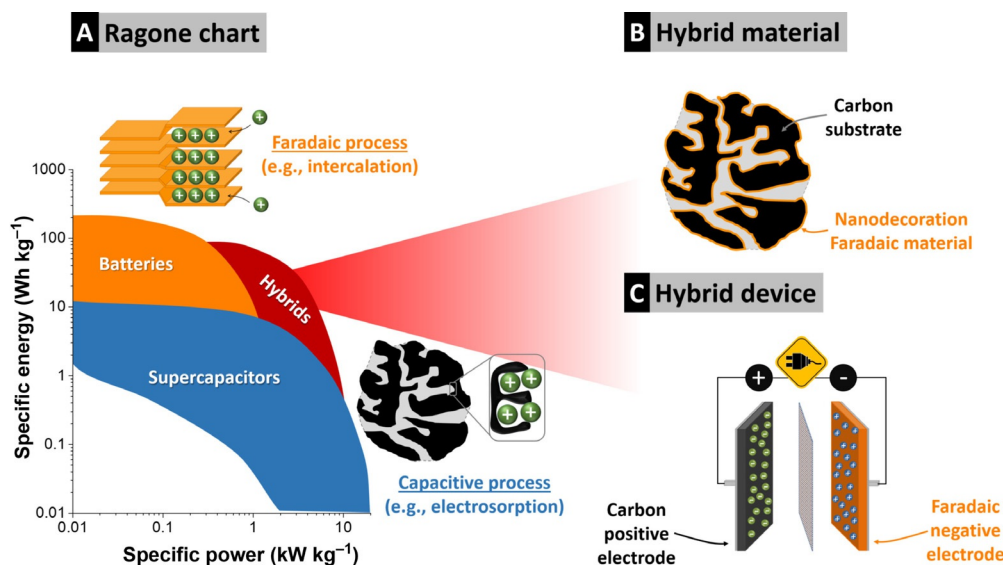


Figure 1. (A) Ragone chart displaying typical ranges of specific energy and specific power for supercapacitors, batteries, and hybrids. (B) Scheme of a hybrid material consisting of a porous carbon substrate coated with Faradaic material. (C) Scheme of a hybrid supercapacitor device using a capacitive positive electrode and a Faradaic negative electrode.

guidelines to avoid the detrimental effects intrinsic to both individual technologies.

Supercapacitors and batteries are often compared in a Ragone chart (Figure 1A), comparing energy and power performances. A synergistic combination of the two technologies can yield superior properties regarding specific energy and power handling of the resulting material or device.^[18] Yet, such hybridization can be realized in different ways. On an electrode material level, the introduction of thin layers or nanoparticles of Faradaic materials to a high surface area carbon yields a hybrid material (Figure 1B). By this way, high conductivity, high specific surface area, and redox-active surfaces are combined in one material. Common synthesis techniques to assure a homogenous mixing of both components include wet-chemical approaches^[16b, 19] and non-line-of-sight vapor deposition like atomic layer deposition^[20] or chemical vapor deposition.^[21] Yet, hybridization can also be realized from a device engineering point of view. Hybrid supercapacitors (also referred to as asymmetric supercapacitors or lithium-ion capacitors)^[22] combine two electrodes that each use a different charge storage mechanism; for example, a nanoporous carbon employing double-layer capacitance as the positive electrode and a material enabling intercalation reactions as the negative electrode (Figure 1C). The resulting devices may yield attractive performance metrics that constitute an intriguing alternative to pure supercapacitor or battery systems, if the used Faradaic electrode offers sufficient reaction kinetics.^[23] This makes hybrid materials excellent candidates for the use as the Faradaic electrode in hybrid supercapacitors. This Concept article will focus exclusively on hybridization of electrode materials. These materials will find use in advanced hybrid supercapacitor devices and enable batteries with improved power handling.

Although the surface of carbons used for EDLC electrodes is ideally chemically inert towards the ions of the electrolyte, Faradaic materials undergo redox reactions with the ions. Nano-

scale decoration of carbons with a battery material introduces Faradaic charge transfer to the system, thereby significantly enhancing the specific capacity. The nanoscopic size of the Faradaic materials incorporated in the carbon electrodes leads to a confinement of the redox reactions close to the electrode/electrolyte interface. Therefore, pathways for ions to the reaction sites are short and high rates, comparable to EDLCs, are enabled as the system is significantly less limited by solid-state diffusion in the electrode bulk.^[24] Further, maintaining a continuous carbon network throughout the hybrid electrode ensures electrical percolation and enables facile electron transport to the often electrically insulating domains of Faradaic material. This combination of Faradaic materials and carbon, which are chemically linked on a molecular scale, yields a hybrid electrode material (Figure 2). That way, synergistic effects between both phases can be created. An alternative to hybridization is the mechanical mixing of Faradaic materials with conductive additives to form composite electrodes (Figure 2). Here, usually no chemical bonding between the separate phases is created

Volker Presser obtained his Ph.D. in 2006 from the Eberhard Karls University in Tübingen, Germany. As a Humboldt Research Fellow and Research Assistant Professor, he worked between 2010 and 2012 at the A. J. Drexel Nanotechnology Institute in the team of Yury Gogotsi at Drexel University, Philadelphia, USA. Today, he is Full Professor at the Department of Materials Science and Engineering at Saarland University and Program Division Leader at the INM-Leibniz Institute for New Materials in Saarbrücken, Germany. His current work focusses on nanocarbon and hybrid nanomaterials for electrochemical applications, such as energy storage, harvesting, and water desalination.



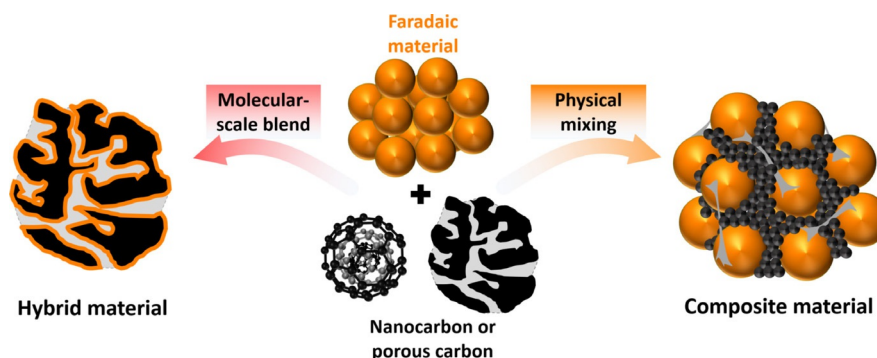


Figure 2. Schematic representation of different synthetic approaches for the combination of carbon with Faradaic material and proposed terminology. Hybridization yields a chemical connection of the two components on a nanoscale and creates synergistic interactions (left). Composite materials are obtained by a physical mixing of the two components, usually without chemical bonding between separate phases, using individual properties of both phases (right).

and the individual properties of the components (e.g., redox activity and electrical conductivity) are used.^[25] Hybridization enables a much more intimate interface between the two components, as clustering of two separate phases with often dissimilar surface chemistries is avoided, leading to enhanced charge transfer in hybrid materials.^[25,26] The proposed terminology in Figure 2 is inspired by Eder and co-workers^[25] and enables us to differentiate between these two types of electrode materials in a clear and consistent manner throughout the paper.

A variety of Faradaic materials has been employed in hybrid electrodes, most prominently metal oxides for intercalation-type hybrids (e.g., V_2O_5 ,^[16a] MnO_2 ,^[27] Nb_2O_5 ,^[28] TiO_2 ,^[29] MoO_2),^[30] but recently, also carbon/sulfur hybrids^[31] and carbon/transition-metal dichalcogenide hybrids^[32] have been introduced. The design of hybrid electrode materials requires a firm understanding for the role of both components (carbon and Faradaic material) and how a synergy between both can be created. Most studies solely focus on the optimization of the Faradaic component, for example, by modifying the crystal structure by doping with foreign atoms^[33] or the introduction of oxygen vacancies.^[34] It is often neglected that also the properties of the carbon substrate have a major impact on the electrochemical properties of the hybrid material. The choice of the type of carbon must be adjusted to the used Faradaic material, the synthesis technique, and the desired application. There is a plethora of carbon materials with vast differences in morphology, graphitization, surface area, and porosity, with the latter being considerably the most important property for many applications.

When comparing carbon materials, it is helpful to differentiate two types of pore architectures (according to ref. [35]):

- (1) Endohedral carbons exhibit a negative surface curvature and show intraparticle porosity, meaning pores are located inside the particles or fibers. Common carbons of this group are activated carbons, carbide-derived carbons, or templated carbons (Figure 3A). Typically, such carbons show high specific surface areas ($> 1500 \text{ m}^2 \text{ g}^{-1}$; inner surface) and are mainly microporous (pore sizes $< 2 \text{ nm}$). They are usually synthesized by physicochemical activation

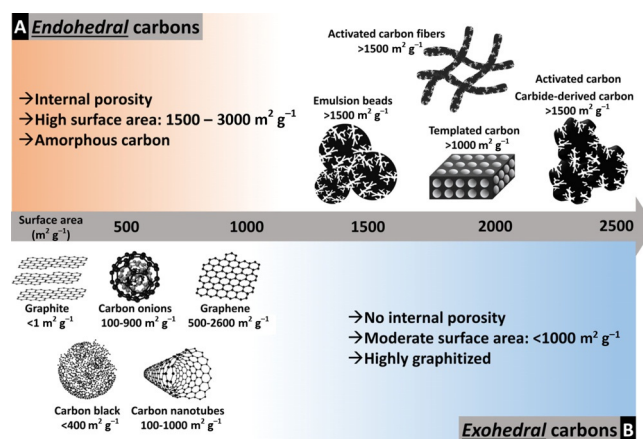


Figure 3. Classification of carbon materials according to their porosity and specific surface area. (A) Endohedral carbons that show internal porosity and typically high specific surface area. (B) Exohedral carbons without internal porosity, often nanocarbons with moderate specific surface area.

or etching processes. Such internal pores create structural disruptions, yielding a reduced graphitic order with incompletely crystalline/amorphous carbon.

- (2) Exohedral carbons with positive surface curvatures show mostly external surface area outside the bulk particle (outer surface; Figure 3B). These materials include nanocarbons such as carbon nanotubes or carbon onions with specific surface areas below $1000 \text{ m}^2 \text{ g}^{-1}$. They form predominantly meso- and macropores in between the particles or aggregates, in the interparticle volume. Exohedral carbons exhibit far less defective graphitic structures, yielding electrical conductivity that is superior to that of endohedral carbons.

In a hybrid electrode, requirements of the carbon component include a high specific surface area to maximize the electrode/electrolyte interface, a pore structure that provides easy access for electrolyte ions and allows for the incorporation of large amounts of Faradaic material, and a graphitic structure that maximizes electrical conductivity. Conventional carbons do not meet all of these properties; for example, increasing the specific surface area often comes at the cost of narrower,

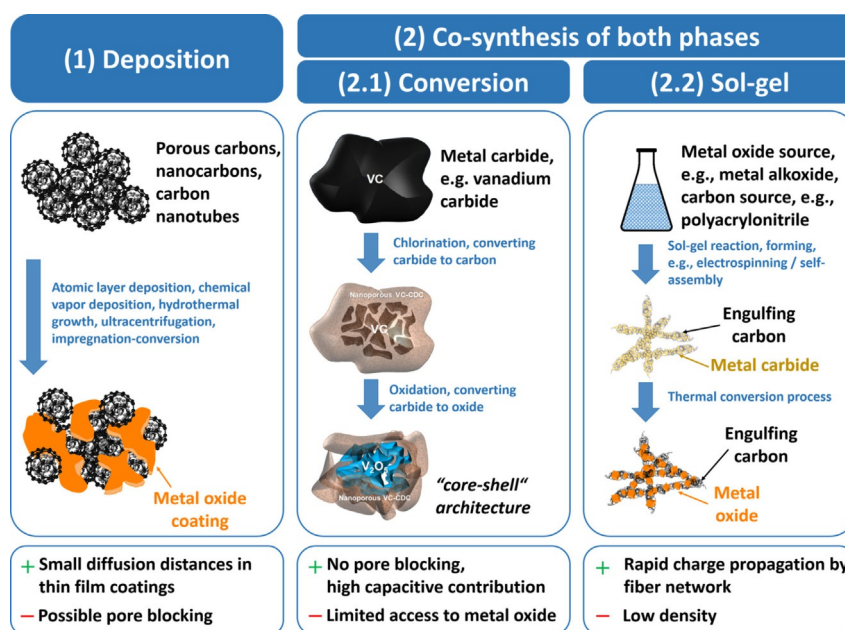


Figure 4. Illustration of discussed synthesis strategies for hybrid materials. (1) Deposition of metal oxide onto an existing carbon substrate. (2) Co-synthesizing metal oxide engulfed by a carbon phase by either (2.1) conversion of a single precursor or (2.2) controlled sol-gel synthesis.

less accessible pores. Strategies to address these issues for carbon/metal oxide hybrid materials will be discussed in the following sections. Figure 4 provides an outline of the discussed synthesis routes with distinction between two general concepts: (1) the deposition of a metal oxide onto an already existing carbon substrate, and (2) co-synthesizing both carbon and metal oxide components during the synthesis procedure.

Strategy 1: Thin Metal Oxide Coating on a Carbon Substrate

A common route to obtain hybrid electrode materials is the deposition of metal oxide on a carbon substrate. In that case, a metal oxide will be incorporated into the interparticle and/or intraparticle volume of the carbon. Consequently, the porosity of the substrate strongly influences the structure of the final hybrid material. For example, atomic layer deposition (ALD) can be employed to deposit metal oxide directly on free-standing or casted thin-film carbon electrodes. ALD allows non-line-of-sight decoration of a substrate by use of self-limiting vapor deposition through binary cycles.^[20] During each reaction cycle, ideally one atomic layer of the desired material is deposited (Figure 5A), giving precise control over the coating thickness by adjusting the number of deposition cycles.

In a recent study by our group, representatives of endohedral carbon (activated carbon) and exohedral carbon (carbon onions) were employed as substrates for atomic layer deposited vanadium oxide (Figure 5B) to give insights into the influence of porosity on the resulting hybrid electrode structure and electrochemical performance.^[36] First indications for the structural changes are given by the mass change of the electrodes during the ALD process. The mass of carbon onion-based electrodes increases linearly with the number of deposi-

tion cycles (Figure 5C), which indicates highly conformal ALD in which a constant number of adsorption sites for the precursor molecules is maintained throughout the process. Contrarily, the mass gain of activated carbon-based electrodes reaches a saturation after 100 ALD cycles (Figure 5C). This reveals that internal surface area of activated carbon becomes blocked by growing vanadium oxide layers, drastically reducing the number of available growth sites for further vanadium oxide deposition. Pore blocking, which was further verified in the study by gas sorption analysis, is unwanted for hybrid electrodes because it seals the activated carbon particles and prevents access to the inner surface area for electrolyte ions. Therefore, the high surface area advantage of activated carbon over carbon onions is negated.

Other studies came to similar conclusions. Daubert et al. described difficulties in the coating process when carbon substrate pore sizes were in the range of the ALD precursor molecule size, effectively inhibiting precursor diffusion.^[37] The latter work also determined a critical pore diameter for successful vanadium oxide deposition by modeling carbon pores as a series of connected, narrowing tubes. It was shown that pores below a diameter of 1.3 nm become completely sealed during the ALD process because of size limitations posed by the precursor dimensions.^[38] Thereby, we can formulate the following guideline for coating porous materials by ALD: Pores smaller than 2 nm are inaccessible to the precursors and become blocked by growing layers at higher mass loadings; mesopores larger than 2–3 nm, however, are well-suited for metal oxide deposition by ALD.^[36]

In a further study by our group, the benefits of mesopores were exemplified for a carbon substrate with a well-tailored pore size distribution. Hard-templating using silica nanoparticles yielded an well-defined mesoporous carbon with a con-

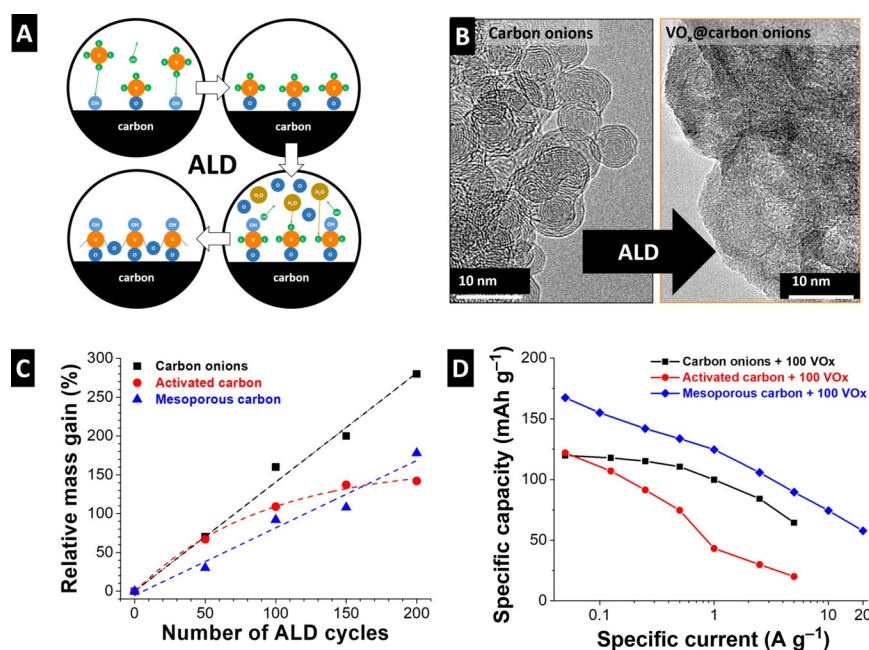


Figure 5. (A) Representation of a single atomic layer deposition (ALD) reaction cycle depositing vanadium oxide. (B) Transmission electron micrographs of carbon onions before and after deposition of 200 ALD cycles of vanadium oxide. (C) Measured mass gain of carbon onion, activated carbon, and tailored mesoporous carbon electrodes when coating with 50, 100, 150, and 200 ALD cycles of vanadium oxide. (D) Rate handling behavior of the respective hybrid materials coated with 100 ALD cycles in 1 M LiClO₄ in acetonitrile as electrolyte. Data replotted from ref. [36,39].

trollable pore structure in the size range of the used silica particles.^[39] This endohedral carbon consisted of micrometer-sized particles with internal porosity and a specific surface area of 1000 m²g⁻¹ which was mostly created by mesopores in range the of 5–20 nm. During the vanadium oxide growth by ALD, a linear mass gain relation similar to carbon onions was observed for mesoporous carbon (Figure 5C), indicating the absence of pore blocking. Hence, mesoporous carbons combine a large specific surface area, leading to a large electrode/electrolyte interface, with a pore structure that is suitable for metal oxide deposition.

The electrochemical performance of carbon onions, activated carbon, and mesoporous carbon coated with 100 ALD cycles of vanadium oxide was compared in 1 M LiClO₄ in acetonitrile organic electrolyte (Figure 5D). When cycling the electrodes at a very low current, carbon onion- and activated carbon-based hybrids show similar specific capacity of about 120 mAh g⁻¹ because the system is given enough time for solid-state diffusion. Therefore, Li ions can reach the intercalation sites in both the open, exohedral carbon onion-hybrid structure, as well as in the partially blocked, endohedral activated carbon particles. Higher charging currents, however, reveal the advantage of carbon onions as a substrate that offers better access for Li ions and a superior electrical conductivity. Mesoporous carbon as a substrate exhibited a higher initial capacity of around 170 mAh g⁻¹ and the best rate handling. The reason for the higher specific capacity is that more of the vanadium oxide coating is connected to the conductive network and able to partake in Faradaic reactions with Li ions. This is related to the well-defined, spherical mesopore structure that leads to more homogeneously distributed vanadium

oxide domains. The high specific surface area of the endohedral structure further leads to thinner coatings that are responsible for the improved rate handling, with mesoporous carbon hybrids showing the same capacity of around 65 mAh g⁻¹ at a 4-fold higher discharging current (20 A g⁻¹) when compared to the carbon onion hybrid (5 A g⁻¹).

Volumetric expansion of Faradaic material during intercalation may lead to disintegration and loss of contact from the conducting network of the electrode.^[17] Here lies a distinct advantage of substrates with endohedral porosity: The internal porosity can effectively prevent this disintegration by confining the metal oxide coating inside the limited pore space. Cycling stability measurements of mesoporous carbon-based hybrid electrodes showed a slightly increasing specific capacity after more than 2000 charge/discharge cycles in 1 M LiClO₄ in acetonitrile electrolyte, and only small capacity decay using 1 M NaClO₄ electrolyte, which represented the most stable performance of vanadium oxide-based materials for sodium intercalation.^[39]

The findings gained from hybrid materials obtained by ALD can also be transferred to other synthesis techniques. A cheap and large-scale production of hybrid material can be achieved through wet-chemical methods. Comparing the suitability of activated carbon and carbon onions as substrates for hydrothermally grown manganese oxide showed similar findings like the studies using ALD. Carbon onions provided good conditions for homogenous deposition of birnessite-type manganese oxide,^[40] whereas blocking of internal surface area was observed for activated carbon. However, considering that the hydrothermal approach is less precise compared to ALD, the minimum accessible pore size was bigger, and a sealing of the

activated carbon particles was already observed at lower mass loadings.^[16b] The study further concluded that the degree of carbon onion graphitization had a substantial impact on the electrochemical properties of the hybrid materials. Carbon onions synthesized at 1700 °C yielded higher electrical conductivity than at 1300 °C, resulting in an improved rate handling of the carbon onion/manganese oxide hybrid electrodes in 1 M Na₂SO₄ aqueous electrolyte.^[16b]

A study by Zhang et al. investigated the suitability of layered carbide-derived carbon (CDC) as a substrate for hydrothermally deposited niobia.^[41] It was found that even by the use of a guiding agent during deposition, about 80% of the surface area became blocked by introducing niobia, resulting in a limited maximum capacity of about 44 mAh g⁻¹ at 20 C. The follow-up study of Lai et al. found an intriguing concept to avoid blocking of internal surface area.^[42] By first depositing niobia on a reduced graphene oxide substrate before introducing to the CDC scaffold, niobia/graphene oxide material preferentially anchored at the edges of CDC layers due to controlled surface charges, thus avoiding blocking of internal CDC surface area. The resulting niobia/reduced graphene oxide/CDC hybrid material showed improved capacity and rate handling with about 100 mAh g⁻¹ at 1 C and 60 mAh g⁻¹ at 40 C, owing to an additional double-layer component to the overall charge storage and better accessibility for the electrolyte.^[42]

Achieving high loadings of Faradaic materials in hybrid electrodes is of particular interest for the transfer to industrial applications, because the mass proportion of electrode to other inactive device components is increased.^[43] High areal mass loadings can be reached by increasing the thickness of the hybrid electrode, which often significantly decreases the gravimetric performance compared to thin electrodes.^[43] Addressing this issue, Sun et al. used holey graphene as a substrate for niobium oxide with varying areal loadings of 1–11 mg cm⁻².^[44] The influence of graphene porosity was investigated by introducing in-plane pores by H₂O₂ activation, in which an increasing activation time led to larger average pore sizes (up to 2.7 nm) and higher specific surface area. Electrochemical impedance spectroscopy indicated a decreased ionic resistance for larger graphene pores, which led to a more than 2-fold increase in rate handling for lithiation reactions compared to non-activated graphene/niobia hybrids. When increasing the areal mass loading from 1 mg cm⁻² to 11 mg cm⁻², holey graphene/niobia hybrids with high mass loading demonstrated a capacity retention of about 110 mAh g⁻¹ at 20 C, whereas non-activated graphene/niobia exhibited a significant capacity drop at higher rates, with a retention of only about 20 mAh g⁻¹ at 20 C (Figure 6A). The porosity of the holey graphene substrates provided ion transport shortcuts, reducing diffusion limitations even in thick electrodes (Figure 6B,C).^[44] Thus, the study underlines a feasible method to exploit carbon porosity to enable the use of high areal mass loadings that are attractive for practical application.

As a further approach to grow of Faradaic material on carbon substrates, Naoi et al. introduced ultracentrifugation to create hybrid materials. By inducing high mechanical force of 65 000 N through centrifugation at 75 000 G, various metal

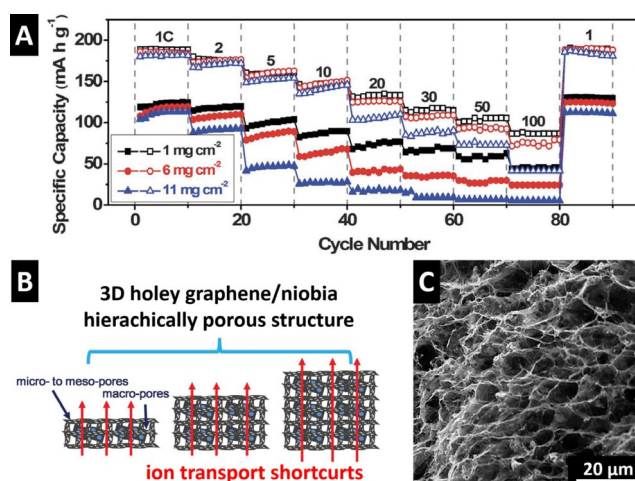


Figure 6. (A) Rate handling of holey graphene/niobia hybrids (open symbols) and graphene/niobia hybrid materials (closed symbols) at different areal loadings. (B) Schematic illustration and (C) scanning electron micrograph of holey graphene/niobia hybrid material offering ion transport shortcuts even at high thicknesses. Adapted from ref. [44]. Reprinted with permission from AAAS.

oxides are grown from in situ sol-gel reactions directly on different carbon substrates.^[45] In a study on carbon fiber/lithium titanate hybrid materials, the carbon fibers became well-distributed in the lithium titanate precursor solution by mechanical agitation, before nucleation occurred by sol-gel reaction on the carbon surface. That way, homogeneously distributed lithium titanate nanoparticles were obtained within the carbon fiber network, leading to high surface area and conductivity of the hybrid material.^[45a,d] This synthesis approach is particularly effective because carbon synergistically interacts during reaction towards an optimized hybrid material. By acting as an anchor for lithium titanate precursors, metal oxide coarsening was prevented during the crystallization reaction because lithium titanate grew following the carbon fiber shape. The influence of the carbon substrate was further underlined by replacing the carbon fibers with especially designed single-walled carbon nanotubes. Thus, the number of anchoring sites is increased, leading to even better dispersion of the lithium titanate. The resulting hybrid electrodes showed remarkable rate handling performance, with a retention of up to 60% of the maximum capacity (130 mAh g⁻¹) at an ultrahigh C-rate of 1200.^[45d]

Carbon/lithium titanate hybrid material was synthesized by a vacuum-impregnation method by Zhao et al.^[46] Using three different kinds of porous carbons with different mesopore volumes, they impregnated the particles dropwise with a liquid precursor solution and applied vacuum in several intervals for homogenous distribution. After calcination at 800 °C, nano-sized lithium titanate particles (< 4 nm) formed inside the pore volume and made up about 52 mass% of the hybrid material. It was found that the carbon particles that offered the largest mesopore volume showed the best electrochemical performance in 1 M LiPF₆ in acetonitrile electrolyte, exhibiting a high capacity retention of 105 mAh g⁻¹ at a rate of 350 C (in addition to the hybrid material, the electrode contained 15

mass6% conductive additive for comparability with previous studies). The carbon mesopores were necessary to synthesize this sample because they trapped the titanate particles to avoid coarsening during calcination at a high temperature.

In summary, we conclude that the choice of an optimized carbon substrate and a suitable synthesis protocol can significantly enhance all performance metrics of hybrid electrode materials, including specific capacity, rate behavior, and longevity. When designing an idealized carbon substrate, properties should be prioritized in this order:

- (1) Pores must be in an accessible size range for the used synthesis method to avoid pore blocking effects and diffusion limitations at high mass loadings.
- (2) The specific surface area must be maximized to obtain thinner coatings at constant mass loading.
- (3) Internal porosity offers confinement of Faradaic material to enhance the longevity by preventing disintegration and to avoid particle coarsening during heat treatment.
- (4) A higher degree of carbon ordering of the substrate leads to enhanced electrical conductivity of the hybrid electrode.

Strategy 2: Co-Synthesizing Faradaic Materials Engulfed by Carbon

Conversion of one precursor material to carbon/metal oxide hybrid

Creating hybrid electrode materials by deposition of Faradaic material onto a carbon substrate is a highly attractive approach to maximize the specific surface area of the hybrid and obtain nanoscale mixing of the two components. However,

issues may arise from possible pore blocking and several synthesis steps are necessary to obtain the final product. An alternative path towards hybrid electrode fabrication is to inverse the electrode architecture and tailor the carbon phase around the Faradaic component. Recently, we presented a promising concept of a vanadium pentoxide/carbide-derived carbon (V_2O_5/CDC) hybrid material with core-shell architecture.^[47] The goal was to employ an endohedral carbon with a large specific surface area to maximize the capacitive charge storage component of the hybrid electrode. The intriguing aspect of arranging the carbon phase around the Faradaic core is that difficulties arising from pore blocking can be completely avoided. The hybrid material is synthesized using only one precursor (e.g., vanadium carbide) that serves as carbon and vanadium source (Figure 7A). In a first step, vanadium was etched from the outside towards the inside of the vanadium carbide particles by chlorine gas treatment, until only a small vanadium carbide (VC) core remained. By selectively etching vanadium from the lattice, a high surface area ($1500\text{ m}^2\text{g}^{-1}$) microporous carbide-derived carbon shell is obtained (Figure 7B). In a second step, the remaining VC is calcinated under oxidizing atmosphere to form a V_2O_5 core (Figure 7C). The hybrid electrode composition (i.e., the V_2O_5/CDC ratio) can be precisely tuned by adjusting the degree of chlorination. The necessary high control over the chlorination step was achieved by using in situ formation of chlorine gas in which nickel chloride was homogeneously mixed with VC and served as chlorine source. Upon heating, Cl_2 was locally released from decomposing $NiCl_2$, ensuring a homogeneous chlorination of the entire synthesized batch. By variation of the $NiCl_2$ amount, the degree of chlorination and the amount of CDC is determined. This allows to finely tune the capacitive and Faradaic contributions to the overall charge storage of the hybrid electrode. However, the oxidation step

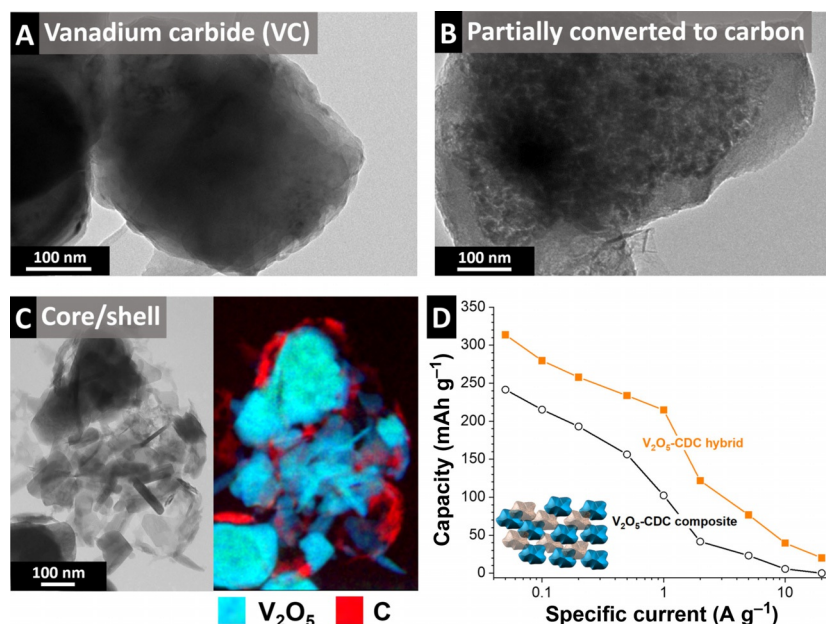


Figure 7. Transmission electron micrographs of (A) precursor vanadium carbide particles, (B) after partial chlorination to form the CDC shell, and (C) final hybrid material after oxidation to form the V_2O_5 core, including chemical mapping from electron energy loss spectroscopy. (D) Electrochemical characterization of V_2O_5 -CDC core-shell hybrid material (orange) and V_2O_5 -CDC composite by galvanostatic cycling in 1 M $LiClO_4$ in ACN electrolyte. Adapted from ref. [47] and reproduced with permission of the Royal Society of Chemistry.

must be precisely adjusted to avoid burning of the carbon phase. The method is therefore limited to Faradaic materials that crystallize at lower temperature and pressure than carbon oxidation.

To analyze the impact of the core-shell architecture on the electrochemical performance of the hybrid material, a composite material was synthesized from mechanically mixing fully chlorinated CDC particles with fully oxidized V_2O_5 particles, both derived from VC, for comparison. Electrochemical characterization in 1 M $LiClO_4$ in acetonitrile electrolyte revealed a higher maximum specific capacity of 310 mAh g^{-1} for the hybrid material, compared to the composite electrode with 240 mAh g^{-1} (Figure 7D). Also, the rate handling of the hybrid was improved, with a retention of 70% of the maximum capacity at 1 Ag^{-1} , compared to a retention of 42% for the composite material at the same rate.

We believe this core-shell architecture provides several key advantages. (1) The surrounding carbon shell can be highly porous because no pore blocking is expected, yielding a high surface area and a large capacitive contribution to the overall charge storage. (2) By encapsulating V_2O_5 with a carbon shell, large contact resistances between the insulating particles are avoided and a highly conductive electrode is obtained. (3) The domain sizes of V_2O_5 are kept very small, reducing the limitations posed by solid-state diffusion. (4) Disintegration of V_2O_5 particles is reduced by the surrounding carbon phase improving longevity of the hybrid material. Yet, the disadvantage compared to carbon substrates coated with Faradaic material lies in the accessibility for ions to the reaction sites. In core-shell materials, the carbon shell enclosing the metal oxide needs to be highly penetrable for the intercalating ions. Though sealing of internal carbon surface area is avoided by the core-shell architecture, sealing effects of metal oxide particles by dense carbon layers must be considered.

Controlled sol-gel approaches

Carbon-coated, porous metal oxide particles have also been synthesized by other approaches. For example, Lim et al. investigated a block-copolymer assisted self-assembly synthesis for mesoporous Nb_2O_5 -C hybrid material.^[48] The carbon phase was obtained by the thermal decomposition of the hydrophobic part in the block-copolymer phase during calcination and it surrounded the Nb_2O_5 phase. In a different approach, the group synthesized Li_3VO_4 -C hybrids by water-in-oil microemulsion, in which the carbon was obtained by carbonization of the emulsifier.^[49] In both studies, the advantage of the hybridization approach over pristine metal oxide particles was clearly demonstrated by comparison of their electrochemical properties. The Nb_2O_5 -C hybrid and the corresponding composite showed a similar maximum capacity of around 180 mAh g^{-1} at a rate of 0.01 Ag^{-1} , however, the hybrid retained about 60% of the maximum capacity at 5 Ag^{-1} , whereas the capacity of the composite faded almost completely.^[48] The presence of the carbonized phase drastically improved the conductivity of the electrode materials and improved the rate handling. The good rate handling enabled a successful use of both hybrid materials

when employed as anodes in lithium-ion capacitor cells, with maximum specific energies of 74 Wh kg^{-1} for the Nb_2O_5 -C hybrid device^[48] and up to 190 Wh kg^{-1} for the Li_3VO_4 -C hybrid device.^[49] However, the as-formed carbon did not exhibit notable porosity and, therefore, may be less penetrable for the electrolyte ions and it does not contribute a capacitive charge storage component to the hybrid electrode. Possibly, a subsequent activation step inducing microporosity to the carbon phase could further elevate the electrochemical performance of these intriguing systems by allowing easier ion access and adding double-layer capacitance.

Compared to these particle-based hybrid materials, fiber-shaped materials offer several advantages. Fibers can form free-standing electrodes without the need for additional binder material. They present continuous conductive networks with improved electrical conductivity without conductive additives, and nanofibers offer short diffusion distances for intercalating ions (Figure 8A). In particle-based systems with conduc-

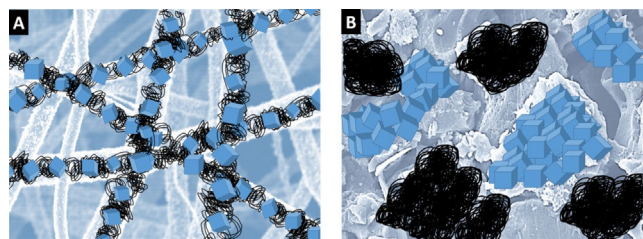


Figure 8. Comparison of fiber-based hybrid electrode material (A) and particle-based composite electrode material (B). Although in the electrospun fibers, metal oxide domains (blue) are engulfed by a continuous conductive carbon network (black), particles can experience disruptions in the conductive network due to agglomerations of metal oxide and carbon domains.

tive additives, the surface chemistry of the metal oxide particles (hydrophilic) and the carbon particles (often hydrophobic) may lead to agglomeration and inhomogeneous material distribution (Figure 8B). Electrospinning has been demonstrated as a suitable synthesis method to obtain free-standing microporous carbon electrodes for supercapacitor applications.^[50] By adjusting the synthesis protocol, our group demonstrated that it is possible to obtain niobium oxide or mixed niobium-titanium oxide/carbon hybrid fiber materials in a one-pot synthesis.^[28,51] During electrospinning, metal alkoxide fibers with thicknesses below 100 nm can be obtained, which are transformed to metal carbide/carbon fibers by annealing in argon atmosphere. By subsequently introducing an oxidizing atmosphere, a transformation to metal oxide/carbon fibers can be achieved. The oxidation process must be precisely controlled to achieve full metal carbide to metal oxide transformation, while preventing burn-off of the carbon phase and maintaining of the fiber-shape. It was demonstrated that the use of CO_2 as oxidizing atmosphere at elevated temperatures above 850°C with reduced partial pressures is a suitable method.^[28,51] In the hybrid material, nanoscopic metal oxide domains are engulfed by a highly porous, conducting carbon network. Niobium pentoxide/carbon hybrid fiber materials showed excellent electrochemical properties, with a maximum capacity of

160 mAhg⁻¹ and a retention of 70% at high rate of 5 Ag⁻¹, allowing for a successful transfer as anodes in lithium-ion capacitor cells with a maximum specific energy of up to 86 Whkg⁻¹.^[28] Advantages of the electrospinning approach include the few synthesis steps necessary to obtain the final hybrid material that works free of conductive additives and polymer binders. The microporous carbon encapsulating metal oxide domains brings additional double-layer capacitance, electrical conductivity and structural integrity to the continuous fiber network. However, the main disadvantage of fiber systems is the relatively low packing density, which significantly decreases the volumetric capacity of such materials. However, we believe that adjustments to the electrospinning protocol can in part resolve this issue. By use of a rotating disc current collector, alignment of the electrospun fibers can be achieved that exhibits much higher packing densities compared to randomly oriented fibers obtained on a static collector.^[52]

Summary and Outlook

This article introduces hybrid materials consisting of carbon and metal oxides for electrochemical energy storage, with an emphasis on the role of the carbon component towards the structure and performance of the hybrid electrode. Two general types of electrode architectures are discussed: (1) the use of an existing carbon as a substrate for the nanoscopic decoration with redox active metal oxides and (2) co-synthesis of metal oxide and an engulfing carbon component in a simultaneous manner.

When using carbon as a substrate, the porosity plays a critical role as metal oxide is mainly deposited in the carbon interparticle or intraparticle pore volume. Carbons with internal porosity yield higher specific surface area and can prevent disintegration of the metal oxide phase upon volumetric expansions during operation. Microporous carbons can only accommodate small metal oxide loadings because micropores may become sealed by metal oxide coatings, drastically reducing the hybrid electrode performance. By determining the minimum accessible pore size for the chosen coating method, ideal carbon substrates can be tailored that exhibit high internal surface area without pore blocking issues. Further research on tailored mesoporous carbon substrates towards the utilization with sodium or potassium that cause larger volumetric changes during intercalation could address issues with the longevity of these systems. Considering the recent emergence of studies on transition metal dichalcogenide electrodes storing charge by conversion reactions, the use of appropriate mesoporous carbon substrates can greatly benefit their often poor kinetical and stability properties.

Alternative architectures of using metal oxides surrounded by the carbon phase can prevent the issues arising from unwanted pore blocking effects. The striking advantage of this approach is that even microporous carbons with very high specific surface areas can be used in hybrid electrodes, increasing the capacitive component of the electrodes' charge storage behavior and minimizing contact resistances in the hybrid electrodes. Achieving this architecture requires advanced syn-

thesis protocols because the activation of the carbon phase must be carried out with the metal oxide phase present, which can lead to a change in crystal structure. Also, effective access of the electrolyte to the Faradaic metal oxide core must be ensured. With further research addressing these obstacles, this intriguing hybrid electrode architecture holds the potential to further elevate the power handling of electrochemical energy storage devices.

Acknowledgements

The work at INM was part of the Carbon Metal Oxide Nanohybrid project (CarMON) supported by the Leibniz Association (SAW-2017). We thank Eduard Arzt (INM) for his continuing support. The authors also thank Valeria Lemkova, Eunho Lim, and Marco Zeiger (all at INM) for discussions and creative graphical support.

Conflict of interest

The authors declare no conflict of interest.

Keywords: core-shell material · hybrid material · lithium-ion battery · sol-gel synthesis · supercapacitor

- [1] V. S. Arunachalam, E. L. Fleischer, *MRS Bull.* **2008**, *33*, 264–288.
- [2] a) Z. Yang, J. Zhang, M. C. Kintner-Meyer, X. Lu, D. Choi, J. P. Lemmon, J. Liu, *Chem. Rev.* **2011**, *111*, 3577–3613; b) B. Dunn, H. Kamath, J.-M. Tarascon, *Science* **2011**, *334*, 928–935.
- [3] a) P. Simon, Y. Gogotsi, *Nat. Mater.* **2008**, *7*, 845–854; b) F. Béguin, V. Presser, A. Balducci, E. Frackowiak, *Adv. Mater.* **2014**, *26*, 2219–2251.
- [4] D. Qu, H. Shi, *J. Power Sources* **1998**, *74*, 99–107.
- [5] V. Presser, M. Heon, Y. Gogotsi, *Adv. Funct. Mater.* **2011**, *21*, 810–833.
- [6] M. D. Stoller, C. W. Magnuson, Y. Zhu, S. Murali, J. W. Suk, R. Piner, R. S. Ruoff, *Energy Environ. Sci.* **2011**, *4*, 4685–4689.
- [7] a) D. Pech, M. Brunet, H. Durou, P. Huang, V. Mochalin, Y. Gogotsi, P.-L. Taberna, P. Simon, *Nat. Nanotechnol.* **2010**, *5*, 651–654; b) M. Zeiger, N. Jäckel, V. N. Mochalin, V. Presser, *J. Mater. Chem. A* **2016**, *4*, 3172–3196.
- [8] E. Frackowiak, K. Metenier, V. Bertagna, F. Béguin, *Appl. Phys. Lett.* **2000**, *77*, 2421–2423.
- [9] C. Largeot, C. Portet, J. Chmiola, P.-L. Taberna, Y. Gogotsi, P. Simon, *J. Am. Chem. Soc.* **2008**, *130*, 2730–2731.
- [10] N. Jäckel, M. Rodner, A. Schreiber, J. Jeongwook, M. Zeiger, M. Aslan, D. Weingarh, V. Presser, *J. Power Sources* **2016**, *326*, 660–671.
- [11] N. Ortiz-Vitoriano, N. E. Drewett, E. Gonzalo, T. Rojo, *Energy Environ. Sci.* **2017**, *10*, 1051–1074.
- [12] M. D. Slater, D. Kim, E. Lee, C. S. Johnson, *Adv. Funct. Mater.* **2013**, *23*, 947–958.
- [13] S. Komaba, T. Hasegawa, M. Dahbi, K. Kubota, *Electrochem. Commun.* **2015**, *60*, 172–175.
- [14] M. S. Whittingham, *Chem. Rev.* **2004**, *104*, 4271–4302.
- [15] E. Peled, C. Menachem, D. Bar-Tow, A. Melman, *J. Electrochem. Soc.* **1996**, *143*, L4–L7.
- [16] a) S. Boukhalfa, K. Evanoff, G. Yushin, *Energy Environ. Sci.* **2012**, *5*, 6872–6879; b) M. Zeiger, S. Fleischmann, B. Krüner, A. Tolosa, S. Bechtel, M. Baltes, A. Schreiber, R. Moroni, S. Vierrath, S. Thiele, V. Presser, *RSC Adv.* **2016**, *6*, 107163–107179.
- [17] N. Shpigel, M. D. Levi, S. Sigalov, O. Girshevitz, D. Aurbach, L. Daikhin, P. Pikma, M. Marandi, A. Jänes, E. Lust, N. Jäckel, V. Presser, *Nat. Mater.* **2016**, *15*, 570–575.
- [18] D. Dubal, O. Ayyad, V. Ruiz, P. Gómez-Romero, *Chem. Soc. Rev.* **2015**, *44*, 1777–1790.
- [19] E. Lim, C. Jo, J. Lee, *Nanoscale* **2016**, *8*, 7827–7833.

- [20] S. M. George, *Chem. Rev.* **2010**, *110*, 111–131.
- [21] X. Wang, G. Yushin, *Energy Environ. Sci.* **2015**, *8*, 1889–1904.
- [22] G. G. Amatucci, F. Badway, A. Du Pasquier, T. Zheng, *J. Electrochem. Soc.* **2001**, *148*, A930–A939.
- [23] M. R. Lukatskaya, B. Dunn, Y. Gogotsi, *Nat. Commun.* **2016**, *7*, 12647.
- [24] a) V. Augustyn, J. Come, M. A. Lowe, J. W. Kim, P.-L. Taberna, S. H. Tolbert, H. D. Abruña, P. Simon, B. Dunn, *Nat. Mater.* **2013**, *12*, 518–522; b) V. Augustyn, P. Simon, B. Dunn, *Energy Environ. Sci.* **2014**, *7*, 1597–1614.
- [25] J. J. Vilatela, D. Eder, *ChemSusChem* **2012**, *5*, 456–478.
- [26] a) G. Kickelbick, *Hybrid materials: synthesis, characterization, and applications*, Wiley, Hoboken, **2007**; b) S. Fleischmann, M. Zeiger, N. Jäckel, B. Krüner, V. Lemkova, M. Widmaier, V. Presser, *J. Mater. Chem. A* **2017**, *5*, 13039–13051.
- [27] Y. He, W. Chen, X. Li, Z. Zhang, J. Fu, C. Zhao, E. Xie, *ACS Nano* **2013**, *7*, 174–182.
- [28] A. Tolosa, B. Krüner, S. Fleischmann, N. Jäckel, M. Zeiger, M. Aslan, I. Grobelsek, V. Presser, *J. Mater. Chem. A* **2016**, *4*, 16003–16016.
- [29] Z. Le, F. Liu, P. Nie, X. Li, X. Liu, Z. Bian, G. Chen, H. B. Wu, Y. Lu, *ACS Nano* **2017**, *11*, 2952–2960.
- [30] H.-S. Kim, J. B. Cook, S. H. Tolbert, B. Dunn, *J. Electrochem. Soc.* **2015**, *162*, A5083–A5090.
- [31] a) S. Choudhury, P. Srimuk, K. Raju, A. Tolosa, S. Fleischmann, M. Zeiger, K. I. Ozoemena, L. Borchardt, V. Presser, *Sustainable Energy Fuels* **2018**, *2*, 133–146; b) S. Choudhury, M. Zeiger, P. Massuti-Ballester, S. Fleischmann, P. Formanek, L. Borchardt, V. Presser, *Sustainable Energy Fuels* **2017**, *1*, 84–94.
- [32] a) J. B. Cook, H. S. Kim, T. C. Lin, C. H. Lai, B. Dunn, S. H. Tolbert, *Adv. Energy Mater.* **2017**, *7*, 1601283; b) Z. Zhang, H. Zhao, Y. Teng, X. Chang, Q. Xia, Z. Li, J. Fang, Z. Du, K. Świerczek, *Adv. Energy Mater.* **2018**, *8*, 1700174.
- [33] S. Fleischmann, A. Tolosa, M. Zeiger, B. Krüner, N. J. Peter, I. Grobelsek, A. Quade, A. Kruth, V. Presser, *J. Mater. Chem. A* **2017**, *5*, 2792–2801.
- [34] H.-S. Kim, J. B. Cook, H. Lin, J. S. Ko, S. H. Tolbert, V. Ozolins, B. Dunn, *Nat. Mater.* **2017**, *16*, 454–460.
- [35] J. Huang, B. G. Sumpter, V. Meunier, *Chem. Eur. J.* **2008**, *14*, 6614–6626.
- [36] S. Fleischmann, N. Jäckel, M. Zeiger, B. Krüner, I. Grobelsek, P. Formanek, S. Choudhury, D. Weingarh, V. Presser, *Chem. Mater.* **2016**, *28*, 2802–2813.
- [37] J. S. Daubert, N. P. Lewis, H. N. Gotsch, J. Z. Mundy, D. N. Monroe, E. C. Dickey, M. D. Losego, G. N. Parsons, *Chem. Mater.* **2015**, *27*, 6524–6534.
- [38] J. S. Daubert, R. Wang, J. S. Ovental, H. F. Barton, R. Rajagopalan, V. Augustyn, G. N. Parsons, *J. Mater. Chem. A* **2017**, *5*, 13086–13097.
- [39] S. Fleischmann, D. Leistenschneider, V. Lemkova, B. Krüner, M. Zeiger, L. Borchardt, V. Presser, *Chem. Mater.* **2017**, *29*, 8653–8662.
- [40] K. Makgopa, P. M. Ejikeme, C. J. Jafta, K. Raju, M. Zeiger, V. Presser, K. I. Ozoemena, *J. Mater. Chem. A* **2015**, *3*, 3480–3490.
- [41] C. J. Zhang, R. Maloney, M. R. Lukatskaya, M. Beidaghi, B. Dyatkin, E. Perre, D. Long, W. Qiao, B. Dunn, Y. Gogotsi, *J. Power Sources* **2015**, *274*, 121–129.
- [42] C.-H. Lai, D. Ashby, M. K. Moz, Y. Gogotsi, L. Pilon, B. S. Dunn, *Langmuir* **2017**, *33*, 9407–9415.
- [43] Y. Gogotsi, P. Simon, *Science* **2011**, *334*, 917–918.
- [44] H. Sun, L. Mei, J. Liang, Z. Zhao, C. Lee, H. Fei, M. Ding, J. Lau, M. Li, C. Wang, X. Xu, G. Hao, B. Papandrea, I. Shakir, B. Dunn, Y. Huang, X. Duan, *Science* **2017**, *356*, 599–604.
- [45] a) K. Naoi, S. Ishimoto, Y. Isobe, S. Aoyagi, *J. Power Sources* **2010**, *195*, 6250–6254; b) K. Naoi, K. Kisu, E. Iwama, S. Nakashima, Y. Sakai, Y. Oriksa, P. Leone, N. Dupré, T. Brousse, P. Rozier, W. Naoi, P. Simon, *Energy Environ. Sci.* **2016**, *9*, 2143–2151; c) K. Naoi, T. Kurita, M. Abe, T. Furuhashi, Y. Abe, K. Okazaki, J. Miyamoto, E. Iwama, S. Aoyagi, W. Naoi, P. Simon, *Adv. Mater.* **2016**, *28*, 6751–6757; d) K. Naoi, W. Naoi, S. Aoyagi, J.-i. Miyamoto, T. Kamino, *Acc. Chem. Res.* **2013**, *46*, 1075–1083.
- [46] E. Zhao, C. Qin, H.-R. Jung, G. Berdichevsky, A. Nese, S. Marder, G. Yushin, *ACS Nano* **2016**, *10*, 3977–3984.
- [47] M. Zeiger, T. Ariyanto, B. Krüner, N. J. Peter, S. Fleischmann, B. J. M. Etzold, V. Presser, *J. Mater. Chem. A* **2016**, *4*, 18899–18909.
- [48] E. Lim, H. Kim, C. Jo, J. Chun, K. Ku, S. Kim, H. I. Lee, I.-S. Nam, S. Yoon, K. Kang, *ACS Nano* **2014**, *8*, 8968–8978.
- [49] E. Lim, W.-g. Lim, C. Jo, J. Chun, M.-H. Kim, K. C. Roh, J. Lee, *J. Mater. Chem. A* **2017**, *5*, 20969–20977.
- [50] a) V. Presser, L. Zhang, J. J. Niu, J. McDonough, C. Perez, H. Fong, Y. Gogotsi, *Adv. Energy Mater.* **2011**, *1*, 423–430; b) A. Tolosa, B. Krüner, N. Jäckel, M. Aslan, C. Vakifahmetoglu, V. Presser, *J. Power Sources* **2016**, *313*, 178–188.
- [51] A. Tolosa, S. Fleischmann, I. Grobelsek, A. Quade, E. Lim, V. Presser, *ChemSusChem* **2018**, *11*, 159–170.
- [52] L. E. Sperling, K. P. Reis, L. G. Pozzobon, C. S. Girardi, P. Pranke, *J. Biomed. Mater. Res. Part A* **2017**, *105*, 1333–1345.

Manuscript received: February 14, 2018

Accepted manuscript online: April 19, 2018

Version of record online: June 8, 2018

4. Conclusions and outlook

My work has explored the synthesis of carbon and hybrid electrospun non-woven fiber mats and evaluates the electrochemical performance as electrodes for energy storage devices. The components of the fibers were synthesized from molecular precursors, by a one pot in situ synthesis approach. *Chapter 3* presents the optimization of the synthesis conditions to finally obtain either highly porous carbon fiber mats for electrical double-layer capacitors or metal oxide/carbon hybrid fiber mats for LIBs batteries. The electrochemical performance was compared to conventional polymer-bound electrodes to obtain a clear overview of the advantages and disadvantages of the fiber mats. **Figure 14** presents the specific capacity at different current rates normalized to the electrode mass and volume.

For the synthesis of highly porous carbon fibers, the influence of the metal (oxy-)carbide, and the chlorine treatment parameters were evaluated. Selective extractions of metal and metalloids atoms in NbC and SiOC domains allows for a tunable porosity and carbon structure. The highly porous carbon is formed by inward growth, retaining the shape of the continuous fiber mat. In the case of SiOC-CDC, high surface areas and pore volume were obtained by treatment at 1200 °C for 3 h with a broad pore size distribution for micropores and mesopores. The micropores are formed by etching Si atoms from amorphous SiC, while pores between 1-3 nm result from the removal of Si and O atoms from the Si-O-C domains. In the case of cubic NbC-CDC, lower pore volume and surface area were obtained compared to SiOC-CDC. The chlorine treatment tends to yield a narrow pore size distribution at low temperatures (600 °C for 1 h). At higher temperature and time (up to 900 °C for 3 h) the pore size increases due to higher carbon mobility, along with self-organization and increased crystallinity of the carbon material. As a general key finding, treatment at higher temperatures leads to a larger graphitization degree of the carbon and larger average pore size. However, these parameters depend on the crystal structure of the precursor, and the onset temperature of the reaction with chlorine gas.

For lithium-ion and sodium-ion batteries, hybrid metal oxide/carbon fiber mats were synthesized and electrochemically evaluated as free-standing electrodes. For hybrid material synthesis, the reaction was thermodynamically and kinetically controlled to tune the composition of the final material. As anode material for high rate handling, the

synthesis of the hybrid niobium oxide/carbon fiber mats was demonstrated, by a one-pot synthesis followed by two-step heat treatment. Optimization of the heat treatment conditions allows tuning the crystal structure of niobium pentoxide to obtain hybrid fibers containing either pseudo-hexagonal, orthorhombic, or tetragonal niobium pentoxide engulfed by partially graphitic carbon. Heat treatment parameters were modified, such as the oxidizing atmosphere, gas partial pressure, temperature treatment and holding time. The effect of titanium in the crystalline structure of niobium oxide was studied, and for the studied Ti:Nb stoichiometric ratio, a monoclinic Ti-Nb oxide phase is obtained at lower temperatures (850 °C). As anode materials for high capacity, SiOC/Sn hybrid fibers were produced from a low-cost silicone resin and tin acetate as the polymer crosslinker. The addition of tin acetate had a high influence in the developed structure after pyrolysis at 1000-1200 °C. A key finding for this work is that adding low amounts of Sn decreases the presence of free carbon and electrochemically inactive silicon carbide domains within the SiOC fibers. During electrochemical testing, Li-Sn alloying reaction contributes to a higher initial capacity, but the material suffers from low cycle life. An inferior electrochemical performance is observed by increasing the Sn amount in the material.

The fiber mats were tested as electrodes for electrical double-layer capacitors (**Figure 14A, C**), and lithium-ion batteries (**Figure 14B, D**). The effect of the material morphology when adding a polymer binder was studied for non-continuous structures: beads and short fibers. My work demonstrates that electrospinning of molecular precursor is an attractive approach for the synthesis of carbon and hybrid fiber mats. By in situ synthesis, material properties such as phase composition, crystal structure, and phase distribution are well tuned to achieve the desired electrochemical properties. The synthesis approach offers a reduction of steps, by in situ synthesis of all electrode components, and leads to reproducible materials. However, through this work, the disadvantages and limitations of this process for electrode preparation were identified:

- In the case of sol-gel systems, a high sensibility to the environmental conditions requires a reliable and controllable environment for reproducible results.
- The material processing occurs in batch production, and the process itself has a low production yield.

- The high interfiber volume of the fiber mats leads to a lower density than for polymer-bound electrodes, which is typically between two to three times smaller, also presenting lower volumetric performance metrics.
- For the electrospinning setup that I have used, the non-woven random oriented fibers present a non-uniform thickness and higher resistivity at the electrode/current collector interphase, due to the reduced contact (**Figure 15**).

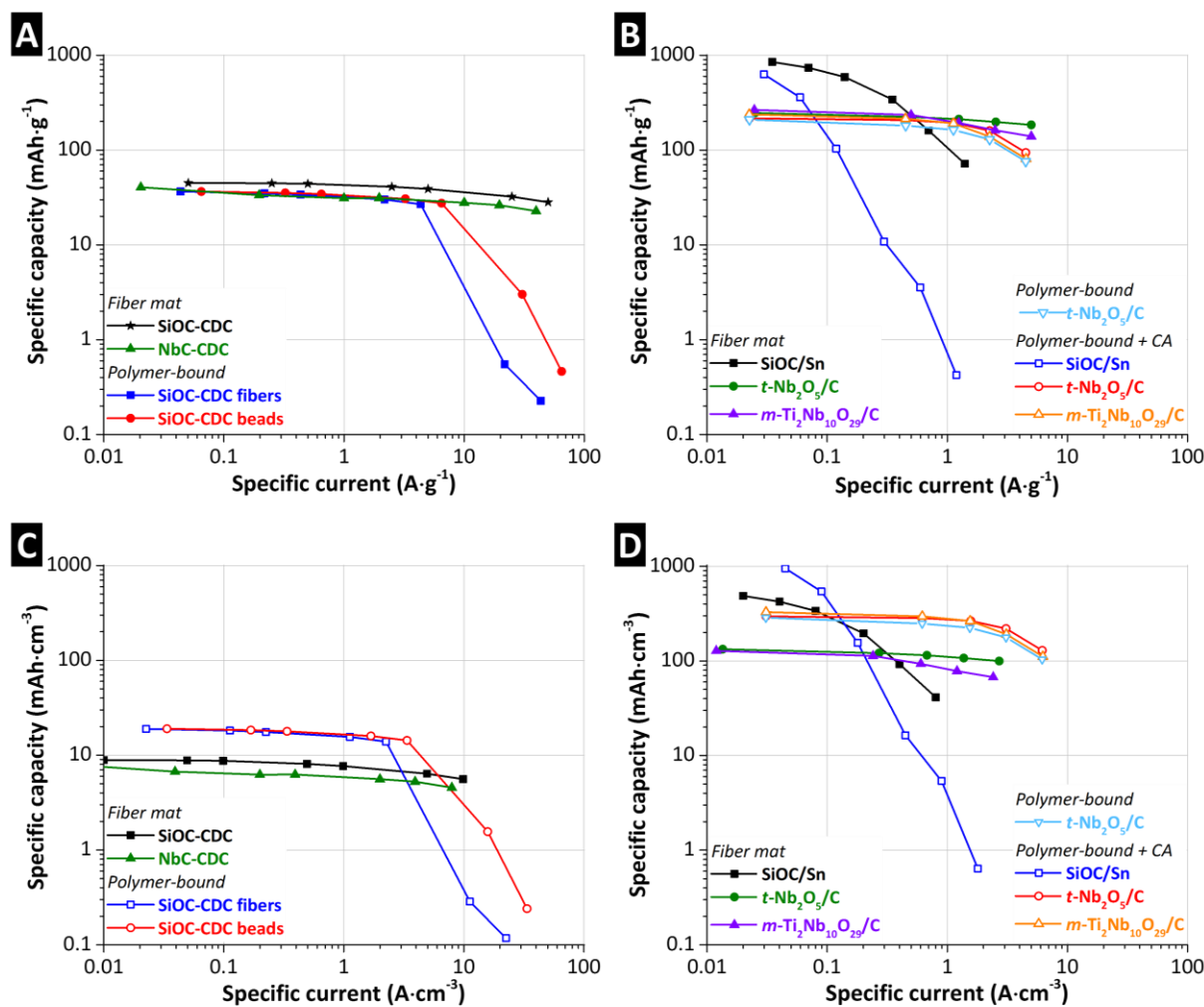


Figure 14. Specific capacity and rate handling performance of continuous fiber electrodes compared to polymer-bound electrodes, for electrical double-layer capacitors (A, C) and lithium-ion batteries (B, D). Specific values normalized to the electrode mass (A, B) and the electrode volume (C, D). Data from Ref. ¹⁶⁹⁻¹⁷².

The synthesis approach presents significant advantages compared to polymer-bound electrodes. Conventional electrode preparation involves the synthesis of the three typical constituents in separated processes: electroactive material, the conductive additive, and the polymer binder.

Comparing the energy demand and synthesis efforts to produce our electrodes with conventional electrodes, the synthesis of our hybrid fiber mats offers several advantages:

- Electrospinning allows the production of materials with nanoscale features, such as high surface area/volume aspect ratio, and short diffusion length for ions. A high electrode/electrolyte contact area increases the rate capability of the device.
- Compared to particle synthesis, electrospinning easily enables the fabrication of nanostructures and reduces/avoids sintering-related coarsening, due to the interfiber space. The coarsening of nanoparticles leads to large grain size and aggregation, losing the high surface areas and merits associated with nanostructures.
- The fiber mats present a superior gravimetric performance metrics, tested as electrodes for energy storage devices. The improved gravimetric capacity correlates with the absence of a polymer binder and conductive additives. The in situ synthesized carbon and the continuous morphology, efficiently ensure a high conductivity.
- Although presenting a lower volumetric performance, the fibers retain a higher volumetric capacity at very high rates, especially for the highly porous carbon systems. The continuous fiber mats are attractive for high current applications.
- The fiber mats present superior capacity retention at high rates. The improved rate handling is not attributed to the hybrid material but the continuous fiber network. Electron transport takes place continuously along the fiber and at the sintered points between the fibers, ensuring a high electrical percolation. For polymer-bound electrodes, the electron transport has to overcome the particle boundary, leading to a higher scattering in the electron transport. The differences between the continuous fiber mats and the polymer-bound electrodes are schematically represented in **Figure 15**.
- When the continuous network is fragmented, the addition of 5-10 mass% of conductive additives did not compensate for the loss in electrical conductivity, except for the vanadium oxide/carbon hybrid fibers. The low amount and low graphitic degree of the carbon phase in the hybrid fibers led to an improved rate handling by the production of polymer-bound electrodes containing 5 mass% of conductive additives.
- Free-standing electrodes are prepared without the presence of environmentally unfriendly polymer binders (e.g., fluorine-containing polymer), and there is no influence of the polymer binder degradation during electrochemically testing.¹⁶⁸ The

use of binder-free electrodes avoids partial pore blocking of the electrode material by the polymer binder.

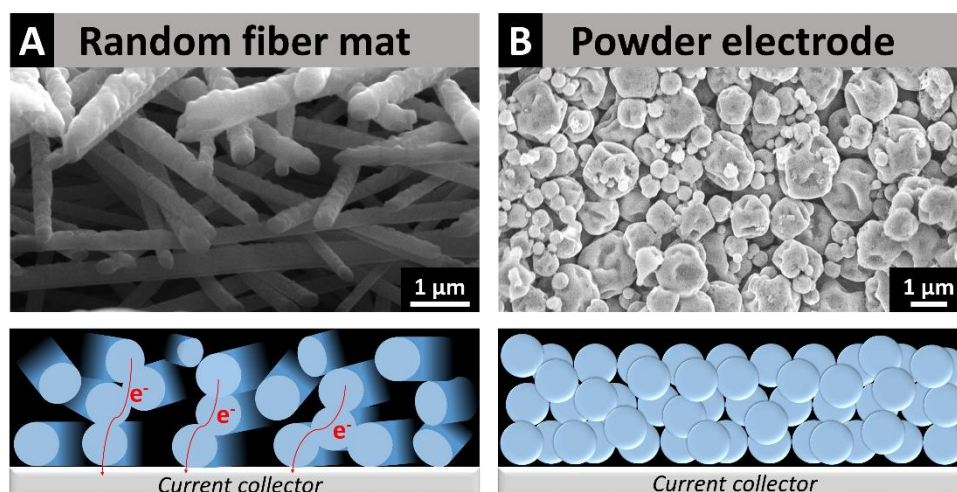


Figure 15. Scanning electron micrographs of continuous fiber (A) and powder (B) electrode. Schematic representation of the electrode material distribution at the current collector.

My work explores the advantages and limitations of electrospun fiber mats as electrodes for electrochemical energy storage devices. The mentioned disadvantages limit the employment of the fiber mats for applications where the volume of the device is a critical factor. However, there is room for improvement, and adjustments to the electrospinning protocol may (partially) resolve these issues. By use of a rotating disc current collector, the electrospun fibers are aligned and exhibit much higher packing densities compared to randomly oriented fibers obtained on a static collector.¹⁶⁴ Also, the production of woven mats could be an alternative. Woven fibers, produced by melt spinning, are commercially available and are attractive as free-standing electrodes for electrochemical energy storage and water desalination. In the same way, twisted assemblies of nanofibers could be produced, such as nanofiber-based ropes, cable, and yarns.¹⁷³⁻¹⁷⁴ Therefore, the knowledge gain in this thesis about hybrid nanofiber synthesis and electrochemical benchmarking could be applied to scale up the synthesis. The production of nanofiber yarn, compared to the random-oriented non-woven mats, leads to fiber mats with a larger production yield, better packing, higher density, and uniform thickness, due to the increased cohesive forces between the fibers.

References

1. European Commission, *Renewable Energy Progress Report. Report from the commission to the European parliament, the council, the European economic and social committee and the committee of the regions*; Brussels, 2017.
2. Fraunhofer-Institut für Solare Energiesysteme, Nettoerzeugung von Kraftwerken zur öffentlichen Stromversorgung. www.energy-charts.de (accessed 29th March 2018).
3. European Commission, *A policy framework for climate and energy in the period from 2020 to 2030. Report from the commission to the European parliament, the council, the European economic and social committee and the committee of the regions*; Brussels, 2014.
4. Dell, R. M.; Rand, D. A. J., Energy storage — a key technology for global energy sustainability. *Journal of Power Sources* **2001**, *100* (1), 2-17.
5. Kim, I.-T.; Egashira, M.; Yoshimoto, N.; Morita, M., On the electric double-layer structure at carbon electrode/organic electrolyte solution interface analyzed by ac impedance and electrochemical quartz-crystal microbalance responses. *Electrochimica Acta* **2011**, *56* (21), 7319-7326.
6. Brett, C. M. A.; Brett, A. M. O., *Electrochemistry: Principles, Methods, and Applications*. Oxford University Press: 1993.
7. Helmholtz, H., Studien über elektrische Grenzschichten. *Annalen der Physik* **1879**, *243* (7), 337-382.
8. Conway, B. E., Transition from “Supercapacitor” to “Battery” Behavior in Electrochemical Energy Storage. *Journal of The Electrochemical Society* **1991**, *138* (6), 1539-1548.
9. Béguin, F.; Presser, V.; Balducci, A.; Frackowiak, E., Carbons and Electrolytes for Advanced Supercapacitors. *Advanced Materials* **2014**, *26* (14), 2219-2251.
10. Barbieri, O.; Hahn, M.; Herzog, A.; Kötz, R., Capacitance limits of high surface area activated carbons for double layer capacitors. *Carbon* **2005**, *43* (6), 1303-1310.
11. Haas, O.; J. Cairns, E., Chapter 6. Electrochemical energy storage. *Annual Reports Section "C" (Physical Chemistry)* **1999**, *95* (0), 163-198.
12. Eftekhari, A., Energy efficiency: a critically important but neglected factor in battery research. *Sustainable Energy & Fuels* **2017**.
13. Simon, P.; Gogotsi, Y.; Dunn, B., Where Do Batteries End and Supercapacitors Begin? *Science* **2014**, *343* (6176), 1210-1211.
14. Augustyn, V.; Simon, P.; Dunn, B., Pseudocapacitive oxide materials for high-rate electrochemical energy storage. *Energy & Environmental Science* **2014**, *7* (5), 1597-1614.
15. Andreas, H. A., Self-Discharge in Electrochemical Capacitors: A Perspective Article. *Journal of The Electrochemical Society* **2015**, *162* (5), A5047-A5053.
16. Ragone, D., Review of Battery Systems for Electrically Powered Vehicles. In *Mid-Year Meeting of the Society of Automotive Engineers*, Detroit, MI, 1968.
17. Christen, T.; Carlen, M. W., Theory of Ragone plots. *Journal of Power Sources* **2000**, *91* (2), 210-216.
18. Simon, P.; Gogotsi, Y., Materials for electrochemical capacitors. *Nature Materials* **2008**, *7*, 845-854.
19. Merlet, C.; Rotenberg, B.; Madden, P. A.; Taberna, P.-L.; Simon, P.; Gogotsi, Y.; Salanne, M., On the molecular origin of supercapacitance in nanoporous carbon electrodes. *Nature Materials* **2012**, *11*, 306.
20. Kavan, L., Electrochemical Carbon. *Chemical Reviews* **1997**, *97* (8), 3061-3082.
21. Sharma, P.; Bhatti, T. S., A review on electrochemical double-layer capacitors. *Energy Conversion and Management* **2010**, *51* (12), 2901-2912.
22. Weingarh, D. Ionic liquids for electrochemical double layer capacitors. Doctoral thesis, ETH Zürich, 2013.

23. Chmiola, J.; Largeot, C.; Taberna, P.-L.; Simon, P.; Gogotsi, Y., Desolvation of Ions in Subnanometer Pores and Its Effect on Capacitance and Double-Layer Theory. *Angewandte Chemie International Edition* **2008**, *47* (18), 3392-3395.
24. Stern, O., Zur Theorie der elektrolytischen Doppelschicht. *Zeitschrift für Elektrochemie und angewandte physikalische Chemie* **1924**, *30* (21-22), 508-516.
25. Bockris, J. O. M.; Devanathan, M. A. V.; Müller, K., On the structure of charged interfaces. *Proceedings of the Royal Society of London. Series A. Mathematical and Physical Sciences* **1963**, *274* (1356), 55-79.
26. Merlet, C.; Limmer, D. T.; Salanne, M.; van Roij, R.; Madden, P. A.; Chandler, D.; Rotenberg, B., The Electric Double Layer Has a Life of Its Own. *The Journal of Physical Chemistry C* **2014**, *118* (32), 18291-18298.
27. Raymundo-Piñero, E.; Kierzek, K.; Machnikowski, J.; Béguin, F., Relationship between the nanoporous texture of activated carbons and their capacitance properties in different electrolytes. *Carbon* **2006**, *44* (12), 2498-2507.
28. Chmiola, J.; Yushin, G.; Gogotsi, Y.; Portet, C.; Simon, P.; Taberna, P. L., Anomalous Increase in Carbon Capacitance at Pore Sizes Less Than 1 Nanometer. *Science* **2006**, *313* (5794), 1760-1763.
29. Centeno, T. A.; Sereda, O.; Stoeckli, F., Capacitance in carbon pores of 0.7 to 15 nm: a regular pattern. *Physical Chemistry Chemical Physics* **2011**, *13* (27), 12403-12406.
30. Jäckel, N.; Rodner, M.; Schreiber, A.; Jeongwook, J.; Zeiger, M.; Aslan, M.; Weingarth, D.; Presser, V., Anomalous or regular capacitance? The influence of pore size dispersity on double-layer formation. *Journal of Power Sources* **2016**, *326* (15), 660-671.
31. Frackowiak, E.; Béguin, F., Carbon materials for the electrochemical storage of energy in capacitors. *Carbon* **2001**, *39* (6), 937-950.
32. Demarconnay, L.; Raymundo-Piñero, E.; Béguin, F., A symmetric carbon/carbon supercapacitor operating at 1.6V by using a neutral aqueous solution. *Electrochemistry Communications* **2010**, *12* (10), 1275-1278.
33. Fic, K.; Lota, G.; Meller, M.; Frackowiak, E., Novel insight into neutral medium as electrolyte for high-voltage supercapacitors. *Energy & Environmental Science* **2012**, *5* (2), 5842-5850.
34. Fic, K.; Meller, M.; Menzel, J.; Frackowiak, E., Around the thermodynamic limitations of supercapacitors operating in aqueous electrolytes. *Electrochimica Acta* **2016**, *206*, 496-503.
35. Qu, D.; Shi, H., Studies of activated carbons used in double-layer capacitors. *Journal of Power Sources* **1998**, *74* (1), 99-107.
36. Presser, V.; Heon, M.; Gogotsi, Y., Carbide-Derived Carbons – From Porous Networks to Nanotubes and Graphene. *Advanced Functional Materials* **2011**, *21* (5), 810-833.
37. Stoller, M. D.; Magnuson, C. W.; Zhu, Y.; Murali, S.; Suk, J. W.; Piner, R.; Ruoff, R. S., Interfacial capacitance of single layer graphene. *Energy & Environmental Science* **2011**, *4* (11), 4685-4689.
38. Jäckel, N.; Weingarth, D.; Zeiger, M.; Aslan, M.; Grobelsek, I.; Presser, V., Comparison of carbon onions and carbon blacks as conductive additives for carbon supercapacitors in organic electrolytes. *Journal of Power Sources* **2014**, *272* (0), 1122-1133.
39. Frackowiak, E.; Metenier, K.; Bertagna, V.; Béguin, F., Supercapacitor electrodes from multiwalled carbon nanotubes. *Applied Physics Letters* **2000**, *77* (15), 2421-2423.
40. Jäckel, N.; Weingarth, D.; Schreiber, A.; Krüner, B.; Zeiger, M.; Tolosa, A.; Aslan, M.; Presser, V., Performance evaluation of conductive additives for activated carbon supercapacitors in organic electrolyte. *Electrochimica Acta* **2016**, *191*, 284-298.
41. Mohun, W. A., A novel amorphous carbon. In *Proceedings of the 4th Biennial Conference on Carbon*, Symposium Publications Division, Pergamon Press: Oxford, 1959; pp 443-453.
42. Zheng, J. P.; Cygan, P. J.; Jow, T. R., Hydrous Ruthenium Oxide as an Electrode Material for Electrochemical Capacitors. *Journal of The Electrochemical Society* **1995**, *142* (8), 2699-2703.
43. Jiang, J.; Kucernak, A., Electrochemical supercapacitor material based on manganese oxide: preparation and characterization. *Electrochimica Acta* **2002**, *47* (15), 2381-2386.
44. Mendoza-Sánchez, B.; Gogotsi, Y., Synthesis of Two-Dimensional Materials for Capacitive Energy Storage. *Advanced Materials* **2016**, *28* (29), 6104-6135.

45. Srimuk, P.; Kaasik, F.; Krüner, B.; Tolosa, A.; Fleischmann, S.; Jäckel, N.; Tekeli, M. C.; Aslan, M.; Suss, M. E.; Presser, V., MXene as a novel intercalation-type pseudocapacitive cathode and anode for capacitive deionization. *Journal of Materials Chemistry A* **2016**, *4* (47), 18265-18271.
46. Djire, A.; Ishimwe, J. Y.; Choi, S.; Thompson, L. T., Enhanced performance for early transition metal nitrides via pseudocapacitance in protic ionic liquid electrolytes. *Electrochemistry Communications* **2017**, *77*, 19-23.
47. Zeiger, M.; Fleischmann, S.; Krüner, B.; Tolosa, A.; Bechtel, S.; Balthes, M.; Schreiber, A.; Moroni, R.; Vierrath, S.; Thiele, S.; Presser, V., Influence of carbon substrate on the electrochemical performance of carbon/manganese oxide hybrids in aqueous and organic electrolytes. *RSC Advances* **2016**, *6* (109), 107163-107179.
48. Ewert, J. K.; Weingarth, D.; Denner, C.; Friedrich, M.; Zeiger, M.; Schreiber, A.; Jäckel, N.; Presser, V.; Kempe, R., Enhanced Capacitance of Nitrogen-Doped Hierarchical Porous Carbide-Derived Carbon in Matched Ionic Liquids. *Journal of Materials Chemistry A* **2015**, (3), 18906-18912.
49. Oh, Y. J.; Yoo, J. J.; Kim, Y. I.; Yoon, J. K.; Yoon, H. N.; Kim, J.-H.; Park, S. B., Oxygen functional groups and electrochemical capacitive behavior of incompletely reduced graphene oxides as a thin-film electrode of supercapacitor. *Electrochimica Acta* **2014**, *116*, 118-128.
50. Trasatti, S.; Buzzanca, G., Ruthenium dioxide: a new interesting electrode material. Solid state structure and electrochemical behaviour. *Journal of Electroanalytical Chemistry and Interfacial Electrochemistry* **1971**, *29* (2), A1-A5.
51. Long, J. W.; Swider, K. E.; Merzbacher, C. I.; Rolison, D. R., Voltammetric Characterization of Ruthenium Oxide-Based Aerogels and Other RuO₂ Solids: The Nature of Capacitance in Nanostructured Materials. *Langmuir* **1999**, *15* (3), 780-785.
52. Conway, B. E., *Electrochemical Supercapacitors: Scientific Fundamentals and Technological Applications*. Springer Science & Business Media, New York, 2013.
53. Augustyn, V.; Come, J.; Lowe, M. A.; Kim, J. W.; Taberna, P.-L.; Tolbert, S. H.; Abruña, H. D.; Simon, P.; Dunn, B., High-rate electrochemical energy storage through Li⁺ intercalation pseudocapacitance. *Nat Mater* **2013**, *12* (6), 518-522.
54. Kim, K.; Woo, S.-G.; Jo, Y. N.; Lee, J.; Kim, J.-H., Niobium oxide nanoparticle core–amorphous carbon shell structure for fast reversible lithium storage. *Electrochimica Acta* **2017**, *240*, 316-322.
55. Delacourt, C.; Poizot, P.; Levasseur, S.; Masquelier, C., Size Effects on Carbon-Free LiFePO₄ Powders: The Key to Superior Energy Density. *Electrochemical and Solid-State Letters* **2006**, *9* (7), A352-A355.
56. Okubo, M.; Hosono, E.; Kim, J.; Enomoto, M.; Kojima, N.; Kudo, T.; Zhou, H.; Honma, I., Nanosize Effect on High-Rate Li-Ion Intercalation in LiCoO₂ Electrode. *Journal of the American Chemical Society* **2007**, *129* (23), 7444-7452.
57. Nayak, P. K.; Yang, L.; Brehm, W.; Adelhelm, P., From Lithium-Ion to Sodium-Ion Batteries: Advantages, Challenges, and Surprises. *Angewandte Chemie International Edition* **2018**, *57* (1), 102-120.
58. Van Noorden, R., A better battery. *Nature* **2014**, *507*, 26-28.
59. Nitta, N.; Wu, F.; Lee, J. T.; Yushin, G., Li-ion battery materials: present and future. *Materials Today* **2015**, *18* (5), 252-264.
60. Goriparti, S.; Miele, E.; De Angelis, F.; Di Fabrizio, E.; Proietti Zaccaria, R.; Capiglia, C., Review on recent progress of nanostructured anode materials for Li-ion batteries. *Journal of Power Sources* **2014**, *257*, 421-443.
61. Persson, K.; Sethuraman, V. A.; Hardwick, L. J.; Hinuma, Y.; Meng, Y. S.; van der Ven, A.; Srinivasan, V.; Kostecki, R.; Ceder, G., Lithium Diffusion in Graphitic Carbon. *The Journal of Physical Chemistry Letters* **2010**, *1* (8), 1176-1180.
62. Bieker, G.; Winter, M.; Bieker, P., Electrochemical in situ investigations of SEI and dendrite formation on the lithium metal anode. *Physical Chemistry Chemical Physics* **2015**, *17* (14), 8670-8679.
63. Bogart, T. D.; Chockla, A. M.; Korgel, B. A., High capacity lithium ion battery anodes of silicon and germanium. *Current Opinion in Chemical Engineering* **2013**, *2* (3), 286-293.
64. Dash, R.; Pannala, S., The potential of silicon anode based lithium ion batteries. *Materials Today* **2016**, *19* (9), 483-484.

65. Winter, M.; Besenhard, J. O., Electrochemical lithiation of tin and tin-based intermetallics and composites. *Electrochimica Acta* **1999**, *45* (1), 31-50.
66. Li, X.; Chen, Y.; Zhou, L.; Mai, Y.-W.; Huang, H., Exceptional electrochemical performance of porous TiO₂-carbon nanofibers for lithium ion battery anodes. *Journal of Materials Chemistry A* **2014**, *2* (11), 3875-3880.
67. Widmaier, M.; Jäckel, N.; Zeiger, M.; Abuzarli, M.; Engel, C.; Bommer, L.; Presser, V., Influence of carbon distribution on the electrochemical performance and stability of lithium titanate based energy storage devices. *Electrochimica Acta* **2017**, *247* (Supplement C), 1006-1018.
68. Kumagai, N.; Koishikawa, Y.; Komaba, S.; Koshiba, N., Thermodynamics and Kinetics of Lithium Intercalation into Nb₂O₅ Electrodes for a 2 V Rechargeable Lithium Battery. *Journal of The Electrochemical Society* **1999**, *146* (9), 3203-3210.
69. Aso, K.; Hayashi, A.; Tatsumisago, M., Synthesis of NiS-carbon fiber composites in high-boiling solvent to improve electrochemical performance in all-solid-state lithium secondary batteries. *Electrochimica Acta* **2012**, *83*, 448-453.
70. Paolella, A.; George, C.; Povia, M.; Zhang, Y.; Krahne, R.; Gich, M.; Genovese, A.; Falqui, A.; Longobardi, M.; Guardia, P.; Pellegrino, T.; Manna, L., Charge Transport and Electrochemical Properties of Colloidal Greigite (Fe₃S₄) Nanoplatelets. *Chemistry of Materials* **2011**, *23* (16), 3762-3768.
71. Pereira, N.; Dupont, L.; Tarascon, J. M.; Klein, L. C.; Amatucci, G. G., Electrochemistry of Cu₃N with Lithium: A Complex System with Parallel Processes. *Journal of The Electrochemical Society* **2003**, *150* (9), A1273-A1280.
72. Das, B.; Reddy, M. V.; Malar, P.; Osipowicz, T.; Subba Rao, G. V.; Chowdari, B. V. R., Nanoflake CoN as a high capacity anode for Li-ion batteries. *Solid State Ionics* **2009**, *180* (17), 1061-1068.
73. Wadia, C.; Albertus, P.; Srinivasan, V., Resource constraints on the battery energy storage potential for grid and transportation applications. *Journal of Power Sources* **2011**, *196* (3), 1593-1598.
74. Ohzuku, T.; Ueda, A.; Nagayama, M.; Iwakoshi, Y.; Komori, H., Comparative study of LiCoO₂, LiNi₁₂Co₁₂O₂ and LiNiO₂ for 4 volt secondary lithium cells. *Electrochimica Acta* **1993**, *38* (9), 1159-1167.
75. Thackeray, M. M.; Kang, S.-H.; Johnson, C. S.; Vaughey, J. T.; Benedek, R.; Hackney, S. A., Li₂MnO₃-stabilized LiMO₂ (M = Mn, Ni, Co) electrodes for lithium-ion batteries. *Journal of Materials Chemistry* **2007**, *17* (30), 3112-3125.
76. Setiawati, E.; Hayashi, M.; Tsuda, M.; Hayashi, K.; Kobayashi, R., Electrochemical properties of carbon-composite NASICON-type iron sulfate Fe₂(SO₄)₃ as a cathode for lithium secondary batteries. *Journal of Power Sources* **2013**, *244*, 207-213.
77. Higuchi, M.; Katayama, K.; Azuma, Y.; Yukawa, M.; Suhara, M., Synthesis of LiFePO₄ cathode material by microwave processing. *Journal of Power Sources* **2003**, *119-121*, 258-261.
78. Whittingham, M. S., Ultimate Limits to Intercalation Reactions for Lithium Batteries. *Chemical Reviews* **2014**, *114* (23), 11414-11443.
79. Huggins, R., *Advanced Batteries: Materials Science Aspects*. Springer US: New York, 2008.
80. Fok, E. C. W.; Madden, J. D., Measurement of the Diffusion Coefficient of Lithium in Tin Thin Films Including Phase Transformation Effects. *ECS Transactions* **2013**, *53* (30), 131-142.
81. Ding, N.; Xu, J.; Yao, Y. X.; Wegner, G.; Fang, X.; Chen, C. H.; Lieberwirth, I., Determination of the diffusion coefficient of lithium ions in nano-Si. *Solid State Ionics* **2009**, *180* (2), 222-225.
82. Ruffo, R.; Hong, S. S.; Chan, C. K.; Huggins, R. A.; Cui, Y., Impedance Analysis of Silicon Nanowire Lithium Ion Battery Anodes. *The Journal of Physical Chemistry C* **2009**, *113* (26), 11390-11398.
83. Bruce, P. G.; Scrosati, B.; Tarascon, J.-M., Nanomaterials for Rechargeable Lithium Batteries. *Angewandte Chemie International Edition* **2008**, *47* (16), 2930-2946.
84. Derrien, G.; Hassoun, J.; Panero, S.; Scrosati, B., Nanostructured Sn-C Composite as an Advanced Anode Material in High-Performance Lithium-Ion Batteries. *Advanced Materials* **2007**, *19* (17), 2336-2340.
85. Kepler, K. D.; Vaughey, J. T.; Thackeray, M. M., Li_xCu₆Sn₅ (0 < x < 13): An Intermetallic Insertion Electrode for Rechargeable Lithium Batteries. *Electrochemical and Solid-State Letters* **1999**, *2* (7), 307-309.

86. Fransson, L. M. L.; Vaughey, J. T.; Benedek, R.; Edström, K.; Thomas, J. O.; Thackeray, M. M., Phase transitions in lithiated Cu_2Sb anodes for lithium batteries: an in situ X-ray diffraction study. *Electrochemistry Communications* **2001**, *3* (7), 317-323.
87. Wu, Y., *Lithium-Ion Batteries: Fundamentals and Applications*. CRC Press: Boca Raton, 2015.
88. Bryngelsson, H.; Eskhult, J.; Nyholm, L.; Edström, K., Thin films of Cu_2Sb and Cu_9Sb_2 as anode materials in Li-ion batteries. *Electrochimica Acta* **2008**, *53* (24), 7226-7234.
89. Courtney, I. A.; Dahn, J. R., Electrochemical and In Situ X-Ray Diffraction Studies of the Reaction of Lithium with Tin Oxide Composites. *Journal of The Electrochemical Society* **1997**, *144* (6), 2045-2052.
90. Miyachi, M.; Yamamoto, H.; Kawai, H.; Ohta, T.; Shirakata, M., Analysis of SiO Anodes for Lithium-Ion Batteries. *Journal of The Electrochemical Society* **2005**, *152* (10), A2089-A2091.
91. George, C.; Morris, A. J.; Modarres, M. H.; De Volder, M., Structural Evolution of Electrochemically Lithiated MoS_2 Nanosheets and the Role of Carbon Additive in Li-Ion Batteries. *Chemistry of Materials* **2016**, *28* (20), 7304-7310.
92. Idota, Y.; Kubota, T.; Matsufuji, A.; Maekawa, Y.; Miyasaka, T., Tin-Based Amorphous Oxide: A High-Capacity Lithium-Ion-Storage Material. *Science* **1997**, *276* (5317), 1395-1397.
93. Clark, J. B.; Hastie, J. W.; Kihlberg, L. H. E.; Metselaar, R.; Thackeray, M. M., Definitions of terms relating to phase transitions of the solid state (IUPAC Recommendation 1994). **1994**, *66* (3), 577-594.
94. Augustyn, V., Tuning the interlayer of transition metal oxides for electrochemical energy storage. *Journal of Materials Research* **2016**, *32* (1), 2-15.
95. Reddy, M. V.; Subba Rao, G. V.; Chowdari, B. V. R., Metal Oxides and Oxysalts as Anode Materials for Li Ion Batteries. *Chemical Reviews* **2013**, *113* (7), 5364-5457.
96. Pham-Cong, D.; Choi, J. H.; Yun, J.; Bandarenka, A. S.; Kim, J.; Braun, P. V.; Jeong, S. Y.; Cho, C. R., Synergistically Enhanced Electrochemical Performance of Hierarchical $\text{MoS}_2/\text{TiNb}_2\text{O}_7$ Hetero-nanostructures as Anode Materials for Li-Ion Batteries. *ACS Nano* **2017**, *11* (1), 1026-1033.
97. Naguib, M.; Come, J.; Dyatkin, B.; Presser, V.; Taberna, P.-L.; Simon, P.; Barsoum, M. W.; Gogotsi, Y., MXene: a promising transition metal carbide anode for lithium-ion batteries. *Electrochemistry Communications* **2012**, *16* (1), 61-64.
98. Ohzuku, T.; Iwakoshi, Y.; Sawai, K., Formation of Lithium-Graphite Intercalation Compounds in Nonaqueous Electrolytes and Their Application as a Negative Electrode for a Lithium Ion (Shuttlecock) Cell. *Journal of The Electrochemical Society* **1993**, *140* (9), 2490-2498.
99. Goodenough, J. B.; Kim, Y., Challenges for Rechargeable Li Batteries. *Chemistry of Materials* **2010**, *22* (3), 587-603.
100. An, S. J.; Li, J.; Daniel, C.; Mohanty, D.; Nagpure, S.; Wood, D. L., The state of understanding of the lithium-ion-battery graphite solid electrolyte interphase (SEI) and its relationship to formation cycling. *Carbon* **2016**, *105*, 52-76.
101. Goodenough, J. B., Energy storage materials: A perspective. *Energy Storage Materials* **2015**, *1*, 158-161.
102. Dunn, B.; Kamath, H.; Tarascon, J.-M., Electrical Energy Storage for the Grid: A Battery of Choices. *Science* **2011**, *334* (6058), 928-935.
103. Slater, M. D.; Kim, D.; Lee, E.; Johnson, C. S., Sodium-Ion Batteries. *Advanced Functional Materials* **2013**, *23* (8), 947-958.
104. Yabuuchi, N.; Kubota, K.; Dahbi, M.; Komaba, S., Research Development on Sodium-Ion Batteries. *Chemical Reviews* **2014**, *114* (23), 11636-11682.
105. Kim, S.-W.; Seo, D.-H.; Ma, X.; Ceder, G.; Kang, K., Electrode Materials for Rechargeable Sodium-Ion Batteries: Potential Alternatives to Current Lithium-Ion Batteries. *Advanced Energy Materials* **2012**, *2* (7), 710-721.
106. Jache, B.; Adelhalm, P., Use of Graphite as a Highly Reversible Electrode with Superior Cycle Life for Sodium-Ion Batteries by Making Use of Co-Intercalation Phenomena. *Angewandte Chemie International Edition* **2014**, *53* (38), 10169-10173.
107. Wenzel, S.; Hara, T.; Janek, J.; Adelhalm, P., Room-temperature sodium-ion batteries: Improving the rate capability of carbon anode materials by templating strategies. *Energy & Environmental Science* **2011**, *4* (9), 3342-3345.

108. Senguttuvan, P.; Rouse, G.; Seznec, V.; Tarascon, J.-M.; Palacín, M. R., Na₂Ti₃O₇: Lowest Voltage Ever Reported Oxide Insertion Electrode for Sodium Ion Batteries. *Chemistry of Materials* **2011**, *23* (18), 4109-4111.
109. Xiong, H.; Slater, M. D.; Balasubramanian, M.; Johnson, C. S.; Rajh, T., Amorphous TiO₂ Nanotube Anode for Rechargeable Sodium Ion Batteries. *The Journal of Physical Chemistry Letters* **2011**, *2* (20), 2560-2565.
110. Alcántara, R.; Jaraba, M.; Lavela, P.; Tirado, J. L., NiCo₂O₄ Spinel: First Report on a Transition Metal Oxide for the Negative Electrode of Sodium-Ion Batteries. *Chemistry of Materials* **2002**, *14* (7), 2847-2848.
111. Darwiche, A.; Sougrati, M. T.; Fraisse, B.; Stievano, L.; Monconduit, L., Facile synthesis and long cycle life of SnSb as negative electrode material for Na-ion batteries. *Electrochemistry Communications* **2013**, *32*, 18-21.
112. Kim, J.-S.; Kim, D.-Y.; Cho, G.-B.; Nam, T.-H.; Kim, K.-W.; Ryu, H.-S.; Ahn, J.-H.; Ahn, H.-J., The electrochemical properties of copper sulfide as cathode material for rechargeable sodium cell at room temperature. *Journal of Power Sources* **2009**, *189* (1), 864-868.
113. Kim, J.-S.; Ahn, H.-J.; Ryu, H.-S.; Kim, D.-J.; Cho, G.-B.; Kim, K.-W.; Nam, T.-H.; Ahn, J. H., The discharge properties of Na/Ni₃S₂ cell at ambient temperature. *Journal of Power Sources* **2008**, *178* (2), 852-856.
114. Zhu, C.; Kopold, P.; Li, W.; van Aken, P. A.; Maier, J.; Yu, Y., A General Strategy to Fabricate Carbon-Coated 3D Porous Interconnected Metal Sulfides: Case Study of SnS/C Nanocomposite for High-Performance Lithium and Sodium Ion Batteries. *Advanced Science* **2015**, *2* (12), 1500200.
115. Sauvage, F.; Laffont, L.; Tarascon, J. M.; Baudrin, E., Study of the Insertion/Deinsertion Mechanism of Sodium into Na_{0.44}MnO₂. *Inorganic Chemistry* **2007**, *46* (8), 3289-3294.
116. West, K.; Zachau-Christiansen, B.; Jacobsen, T.; Skaarup, S., Sodium insertion in vanadium oxides. *Solid State Ionics* **1988**, *28-30*, 1128-1131.
117. Kikkawa, S.; Miyazaki, S.; Koizumi, M., Deintercalated NaCoO₂ and LiCoO₂. *Journal of Solid State Chemistry* **1986**, *62* (1), 35-39.
118. Abraham, K. M., Intercalation positive electrodes for rechargeable sodium cells. *Solid State Ionics* **1982**, *7* (3), 199-212.
119. Nishijima, M.; Gocheva, I. D.; Okada, S.; Doi, T.; Yamaki, J.-i.; Nishida, T., Cathode properties of metal trifluorides in Li and Na secondary batteries. *Journal of Power Sources* **2009**, *190* (2), 558-562.
120. Barker, J.; Saidi, M. Y.; Swoyer, J. L., A Sodium-Ion Cell Based on the Fluorophosphate Compound NaVPO₄F. *Electrochemical and Solid-State Letters* **2003**, *6* (1), A1-A4.
121. Plashnitsa, L. S.; Kobayashi, E.; Noguchi, Y.; Okada, S.; Yamaki, J.-i., Performance of NASICON Symmetric Cell with Ionic Liquid Electrolyte. *Journal of The Electrochemical Society* **2010**, *157* (4), A536-A543.
122. Fleischmann, S.; Tolosa, A.; Presser, V., Design of carbon/metal oxide hybrids for electrochemical energy storage. *Chemistry – A European Journal* **2018**, (doi:10.1002/chem.201800772).
123. Vilatela, J. J.; Eder, D., Nanocarbon Composites and Hybrids in Sustainability: A Review. *ChemSusChem* **2012**, *5* (3), 456-478.
124. Kickelbick, G., Introduction to Hybrid Materials. In *Hybrid Materials*, Wiley-VCH Verlag GmbH & Co. KGaA: 2007; pp 1-48.
125. Fleischmann, S.; Zeiger, M.; Jäckel, N.; Krüner, B.; Lemkova, V.; Widmaier, M.; Presser, V., Tuning pseudocapacitive and battery-like lithium intercalation in vanadium dioxide/carbon onion hybrids for asymmetric supercapacitor anodes. *Journal of Materials Chemistry A* **2017**, *5* (25), 13039-13051.
126. Gómez-Romero, P.; Sanchez, C., *Functional Hybrid Materials*. Wiley: 2006.
127. Fleischmann, S.; Tolosa, A.; Zeiger, M.; Krüner, B.; Peter, N. J.; Grobelsek, I.; Quade, A.; Kruth, A.; Presser, V., Vanadia-titania multilayer nanodecoration of carbon onions via atomic layer deposition for high performance electrochemical energy storage. *Journal of Materials Chemistry A* **2017**, *5* (6), 2792-2801.

128. Fleischmann, S.; Leistenschneider, D.; Lemkova, V.; Krüner, B.; Zeiger, M.; Borchardt, L.; Presser, V., Tailored Mesoporous Carbon/Vanadium Pentoxide Hybrid Electrodes for High Power Pseudocapacitive Lithium and Sodium Intercalation. *Chemistry of Materials* **2017**, *29* (20), 8653-8662.
129. Wang, X.; Yushin, G., Chemical vapor deposition and atomic layer deposition for advanced lithium ion batteries and supercapacitors. *Energy & Environmental Science* **2015**, *8* (7), 1889-1904.
130. Zeiger, M.; Ariyanto, T.; Krüner, B.; Peter, N. J.; Fleischmann, S.; Etzold, B. J. M.; Presser, V., Vanadium pentoxide/carbide-derived carbon core-shell hybrid particles for high performance electrochemical energy storage. *Journal of Materials Chemistry A* **2016**, *4* (48), 18899-18909.
131. Lim, E.; Kim, H.; Jo, C.; Chun, J.; Ku, K.; Kim, S.; Lee, H. I.; Nam, I.-S.; Yoon, S.; Kang, K.; Lee, J., Advanced Hybrid Supercapacitor Based on a Mesoporous Niobium Pentoxide/Carbon as High-Performance Anode. *ACS Nano* **2014**, *8* (9), 8968-8978.
132. Lim, E.; Lim, W.-G.; Jo, C.; Chun, J.; Kim, M.-H.; Roh, K. C.; Lee, J., Rational design of Li_3VO_4 @carbon core-shell nanoparticles as Li-ion hybrid supercapacitor anode materials. *Journal of Materials Chemistry A* **2017**, *5* (39), 20969-20977.
133. Mehrotra, R. C., Synthesis and reactions of metal alkoxides. *Journal of Non-Crystalline Solids* **1988**, *100* (1), 1-15.
134. Burwell Jr, R. L., Section 1 - Definitions and terminology. In *Manual of Symbols and Terminology for Physicochemical Quantities and Units—Appendix II*, Pergamon: 1976; pp 74-86.
135. Hench, L. L.; West, J. K., The sol-gel process. *Chemical Reviews* **1990**, *90* (1), 33-72.
136. Alemán, J. V.; Chadwick, A. V.; He, J.; Hess, M.; Horie, K.; Jones, R. G.; Kratochvíl, P.; Meisel, I.; Mita, I.; Moad, G.; Penczek, S.; Stepto, R. F. T., Definitions of terms relating to the structure and processing of sols, gels, networks, and inorganic-organic hybrid materials (IUPAC Recommendations 2007). *Pure and Applied Chemistry* **2007**, *79* (10), 1801.
137. Flory, P. J., *Principles of Polymer Chemistry*. Cornell University Press: 1953.
138. Yoldas, B. E., Preparation of glasses and ceramics from metal-organic compounds. *Journal of Materials Science* **1977**, *12* (6), 1203-1208.
139. Bradley, D. C.; Chakravarti, B. N.; Wardlaw, W., 460. Normal alkoxides of quinquevalent niobium. *Journal of the Chemical Society (Resumed)* **1956**, (0), 2381-2384.
140. Brinker, C. J.; Scherer, G. W., *Sol-gel Science: The Physics and Chemistry of Sol-gel Processing*. Academic Press: 1990.
141. Doeuff, S.; Henry, M.; Sanchez, C.; Livage, J., Hydrolysis of titanium alkoxides: Modification of the molecular precursor by acetic acid. *Journal of Non-Crystalline Solids* **1987**, *89* (1), 206-216.
142. Peng, S.; Li, L.; Kong Yoong Lee, J.; Tian, L.; Srinivasan, M.; Adams, S.; Ramakrishna, S., Electrospun carbon nanofibers and their hybrid composites as advanced materials for energy conversion and storage. *Nano Energy* **2016**, *22* (Supplement C), 361-395.
143. Tran, C.; Kalra, V., Fabrication of porous carbon nanofibers with adjustable pore sizes as electrodes for supercapacitors. *Journal of Power Sources* **2013**, *235* (0), 289-296.
144. Presser, V.; Zhang, L. F.; Niu, J. J.; McDonough, J.; Perez, C.; Fong, H.; Gogotsi, Y., Flexible Nanofelts of Carbide-Derived Carbon with Ultra-high Power Handling Capability. *Advanced Energy Materials* **2011**, *1* (3), 423-430.
145. Cheng, K.-K.; Hsu, T.-C.; Kao, L.-H., Carbon nanofibers prepared by a novel co-extrusion and melt-spinning of phenol formaldehyde-based core/sheath polymer blends. *Journal of Materials Science* **2011**, *46* (6), 1870-1876.
146. Atchison, J. S.; Schauer, C. L., Fabrication and characterization of electrospun semiconductor nanoparticle-polyelectrolyte ultra-fine fiber composites for sensing applications. *Sensors (Basel)* **2011**, *11* (11), 10372-10387.
147. Liu, G.; Ding, J.; Qiao, L.; Guo, A.; Dymov, B. P.; Gleeson, J. T.; Hashimoto, T.; Saijo, K., Polystyrene-block-poly(2-cinnamoyl ethyl methacrylate) Nanofibers—Preparation, Characterization, and Liquid Crystalline Properties. *Chemistry – A European Journal* **1999**, *5* (9), 2740-2749.
148. Ondarçuhu, T.; Joachim, C., Drawing a single nanofibre over hundreds of microns. *EPL (Europhysics Letters)* **1998**, *42* (2), 215.
149. Ma, P. X.; Zhang, R., Synthetic nano-scale fibrous extracellular matrix. *Journal of Biomedical Materials Research* **1999**, *46* (1), 60-72.

150. Feng, L.; Li, S.; Li, H.; Zhai, J.; Song, Y.; Jiang, L.; Zhu, D., Super-Hydrophobic Surface of Aligned Polyacrylonitrile Nanofibers. *Angewandte Chemie International Edition* **2002**, *41* (7), 1221-1223.
151. Huang, Z.-M.; Zhang, Y. Z.; Kotaki, M.; Ramakrishna, S., A review on polymer nanofibers by electrospinning and their applications in nanocomposites. *Composites Science and Technology* **2003**, *63* (15), 2223-2253.
152. Cooley, J. F. Electrical method of dispersing fluids. 1903.
153. Formhals, A. Artificial thread and method of producing same. 1940.
154. Formhals, A. Method and apparatus for spinning. 1944.
155. Formhals, A. Production of artificial fibers from fiber forming liquids. 1943.
156. Reneker, D.; Chun, I., Nanometre diameter fibres of polymer, produced by electrospinning. *Nanotechnology* **1996**, *7*, 216-223.
157. Doshi, J.; Reneker, D. H., Electrospinning process and applications of electrospun fibers. *Journal of Electrostatics* **1995**, *35* (2-3), 151-160.
158. Taylor, G., Disintegration of Water Drops in an Electric Field. *Proceedings of the Royal Society of London. Series A. Mathematical and Physical Sciences* **1964**, *280* (1382), 383-397.
159. Meli, L.; Miao, J.; Dordick, J. S.; Linhardt, R. J., Electrospinning from room temperature ionic liquids for biopolymer fiber formation. *Green Chemistry* **2010**, *12* (11), 1883-1892.
160. Yalcinkaya, B.; Yener, F.; Jirsak, O.; Cengiz-Callioglu, F., On the Nature of Electric Current in the Electrospinning Process. *Journal of Nanomaterials* **2013**, *2013*, 10.
161. Rayleigh, L., On The Instability Of Jets. *Proceedings of the London Mathematical Society* **1878**, *s1-10* (1), 4-13.
162. Shin, Y. M.; Hohman, M. M.; Brenner, M. P.; Rutledge, G. C., Electrospinning: A whipping fluid jet generates submicron polymer fibers. *Applied Physics Letters* **2001**, *78* (8), 1149-1151.
163. Li, Z.; Wang, C., Effects of Working Parameters on Electrospinning. In *One-Dimensional nanostructures*, Springer: Heidelberg, 2013; pp 15-28.
164. Li, Z.; Wang, C., Introduction of Electrospinning. In *One-Dimensional nanostructures*, Springer Heidelberg, 2013; pp 1-13.
165. Wang, H.-G.; Yuan, S.; Ma, D.-L.; Zhang, X.-B.; Yan, J.-M., Electrospun materials for lithium and sodium rechargeable batteries: from structure evolution to electrochemical performance. *Energy & Environmental Science* **2015**, *8* (6), 1660-1681.
166. Xianwen, M.; Hatton, T. A.; Gregory, C. R., A Review of Electrospun Carbon Fibers as Electrode Materials for Energy Storage. *Current Organic Chemistry* **2013**, *17* (13), 1390-1401.
167. Zhang, W.-J., A review of the electrochemical performance of alloy anodes for lithium-ion batteries. *Journal of Power Sources* **2011**, *196* (1), 13-24.
168. Chou, S.-L.; Pan, Y.; Wang, J.-Z.; Liu, H.-K.; Dou, S.-X., Small things make a big difference: binder effects on the performance of Li and Na batteries. *Physical Chemistry Chemical Physics* **2014**, *16* (38), 20347-20359.
169. Tolosa, A.; Fleischmann, S.; Grobelsek, I.; Quade, A.; Lim, E.; Presser, V., Binder-free hybrid titanium-niobium oxide/carbon nanofiber mats for lithium-ion battery electrodes. *ChemSusChem* **2018**, *11* (1), 159-170.
170. Tolosa, A.; Krüner, B.; Fleischmann, S.; Jäckel, N.; Zeiger, M.; Aslan, M.; Grobelsek, I.; Presser, V., Niobium carbide nanofibers as a versatile precursor for high power supercapacitor and high energy battery electrodes. *Journal of Materials Chemistry A* **2016**, *4* (41), 16003-16016.
171. Tolosa, A.; Krüner, B.; Jäckel, N.; Aslan, M.; Vakifahmetoglu, C.; Presser, V., Electrospinning and electrospraying of silicon oxycarbide-derived nanoporous carbon for supercapacitor electrodes. *Journal of Power Sources* **2016**, *313*, 178-188.
172. Tolosa, A.; Widmaier, M.; Krüner, B.; Griffin, J.; Presser, V., Continuous silicon oxycarbide fiber mats with tin nanoparticles as high capacity anode for lithium-ion batteries. *Sustainable Energy & Fuels* **2018**, (2), 215-228.
173. Levitt, A. S.; Knittel, C. E.; Vallett, R.; Koerner, M.; Dion, G.; Schauer, C. L., Investigation of nanoyarn preparation by modified electrospinning setup. *Journal of applied polymer science* **2017**, *134* (19), 44813.

174. S., L. A.; Richard, V.; Genevieve, D.; L., S. C., Effect of electrospinning processing variables on polyacrylonitrile nanoyarns. *Journal of Applied Polymer Science* **2018**, *135* (25), 46404.

Appendixes

Appendix A: Supporting Information to Chapter 3.1

Electrospinning and electrospraying of silicon oxycarbide-derived nanoporous carbon for supercapacitor electrodes

Appendix B: Supporting Information to Chapter 3.2

Niobium carbide nanofibers as a versatile precursor for high power supercapacitor and high energy battery electrodes

Appendix C: Supporting Information to Chapter 3.3

Binder-free hybrid titanium-niobium oxide/carbon nanofiber mats for lithium-ion battery electrodes

Appendix D: Supporting Information to Chapter 3.4

Continuous silicon oxycarbide fiber mats with tin nanoparticles as high capacity anode for lithium-ion batteries

Appendix E: Supporting Information to Chapter 3.5

Electrospun hybrid vanadium oxide/carbon fiber mats for lithium and sodium-ion battery electrodes

Appendix A: Supporting Information to Chapter 3.1

Electronic Supplementary Information

Electrospinning and electrospraying of silicon oxycarbide-derived nanoporous carbon for supercapacitor electrodes

Aura Tolosa,^{a,b} Benjamin Krüner,^{a,b} Nicolas Jäckel,^{a,b} Mesut Aslan,^a

Cekdar Vakifahmetoglu,^{c,*} Volker Presser^{a,b,*}

^a INM - Leibniz Institute for New Materials, 66123 Saarbrücken, Germany.

^b Department of Materials Science and Engineering, Saarland University, 66123 Saarbrücken, Germany.

^c Department of Mechanical Engineering, Istanbul Kemerburgaz University, 34217 Istanbul, Turkey.

* Corresponding authors. E-mail: cekdar.vakifahmetoglu@kemerburgaz.edu.tr; Tel: +90-2126040100 & E-mail: volker.presser@leibniz-inm.de; Tel: +49-6819300177

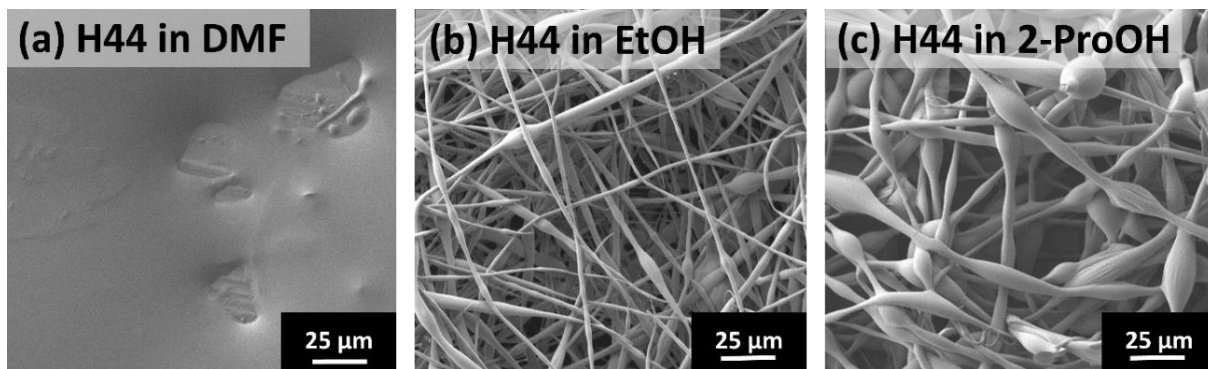


Fig. S1: Scanning electron micrographs of 60 mass% H44 in DMF (a), ethanol (EtOH) (b) and isopropanol (2-ProOH) (c).

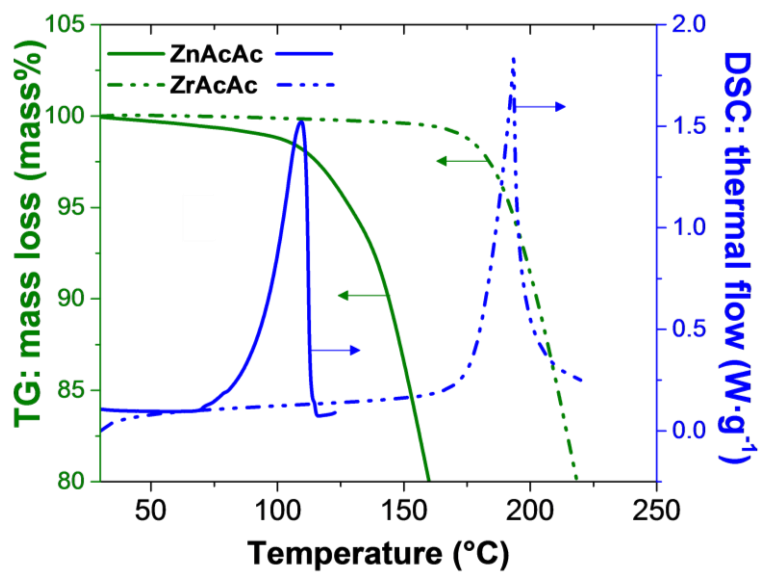


Fig. S2: Thermogravimetric (TG) and differential scanning calorimetry (DSC) analysis of ZrAcAc and ZnAcAc.

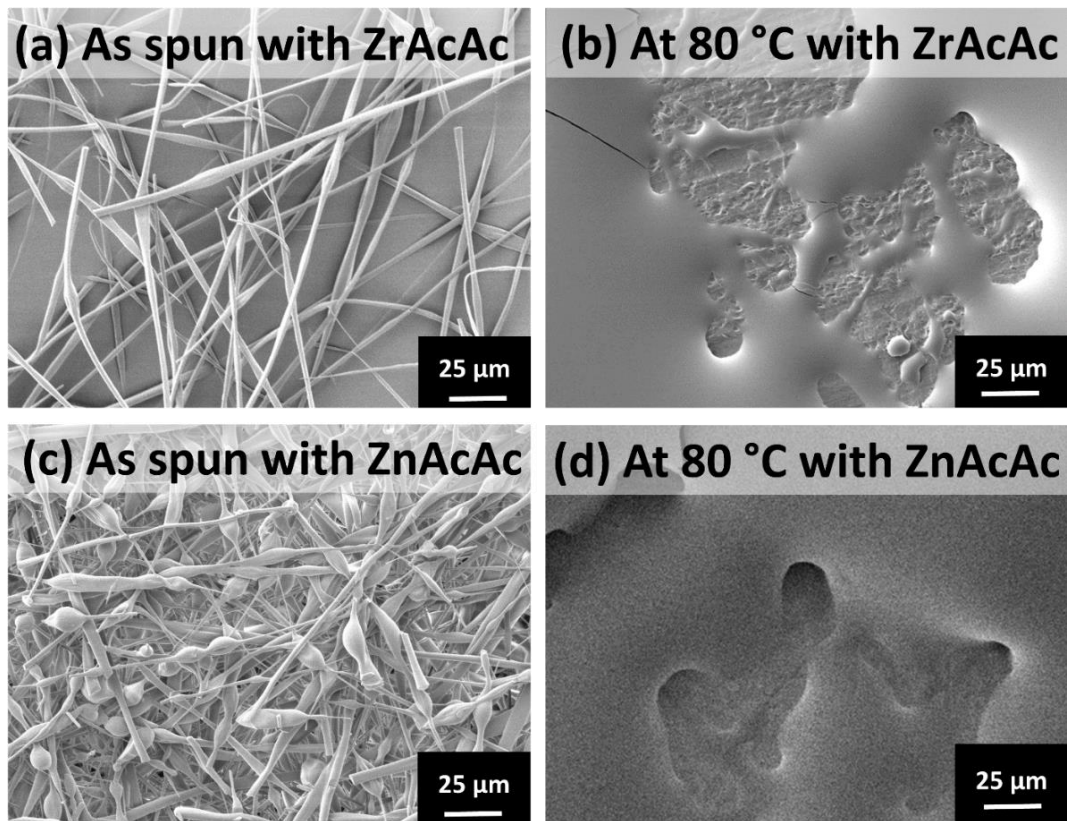


Fig. S3: Scanning electron micrographs of as spun H44 fibers with 0.05 parts of ZrAcAc (a) and ZnAcAc (b), relative to silicone resin, and after heating at 80 °C with ZrAcAc (c) and ZnAcAc (d).

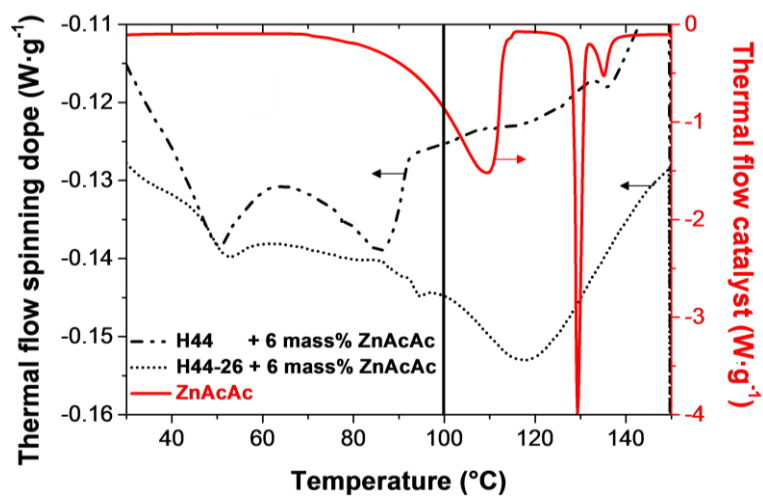


Fig. S4: Differential scanning calorimetry curves of spinning dopes prepared with H44 and H44-26 compared with ZnAcAc.

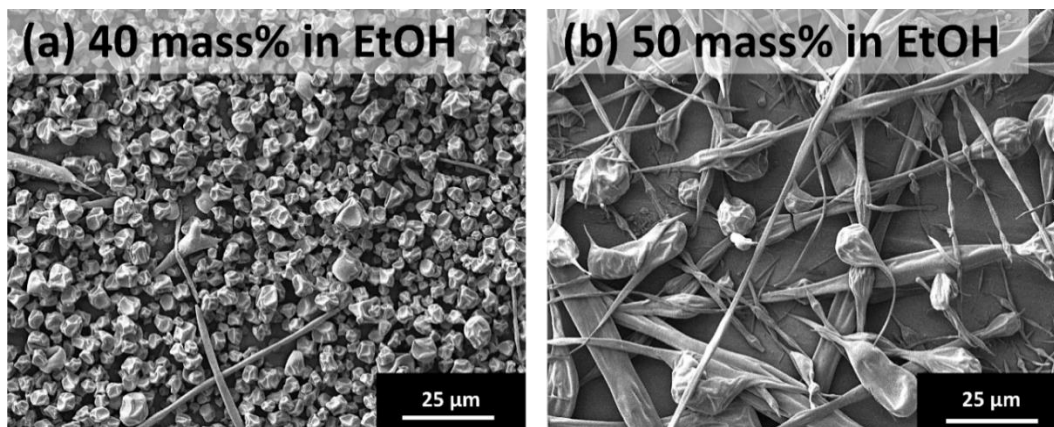


Fig. S5: Scanning electron micrographs of H44-26 in ethanol with 40 mass% (a) and 50 mass% (b) polymer concentration relative to ethanol.

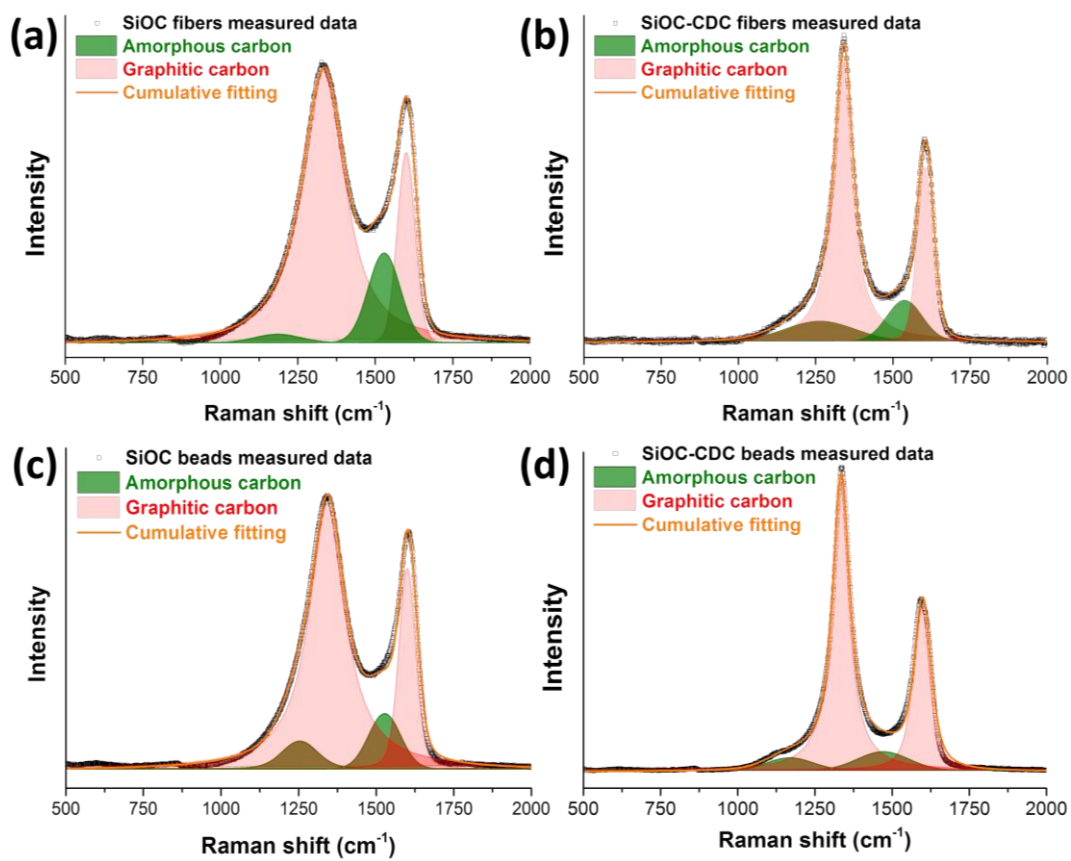


Fig. S6: Peak fitting applied to Raman spectra of SiOC (a) and SiOC-CDC (b) fibers, and SiOC (c) and SiOC-CDC (d) beads. Peak fitting using four Voigt peaks.

Appendix B: Supporting Information to Chapter 3.2

Electronic Supplementary Information

NIBIUM CARBIDE NANOFIBERS AS A VERSATILE PRECURSOR FOR HIGH POWER SUPERCAPACITOR AND HIGH ENERGY BATTERY ELECTRODES

Aura Tolosa,^{1,2} Benjamin Krüner,^{1,2} Simon Fleischmann,² Nicolas Jäckel,^{1,2} Marco Zeiger,^{1,2}

Mesut Aslan,¹ Ingrid Grobelsek,¹ and Volker Presser^{1,2,*}

¹ *INM - Leibniz Institute for New Materials, 66123 Saarbrücken, Germany*

² *Department of Materials Science and Engineering, Saarland University, 66123 Saarbrücken, Germany*

* *Corresponding author's eMail: volker.presser@leibniz-inm.de*

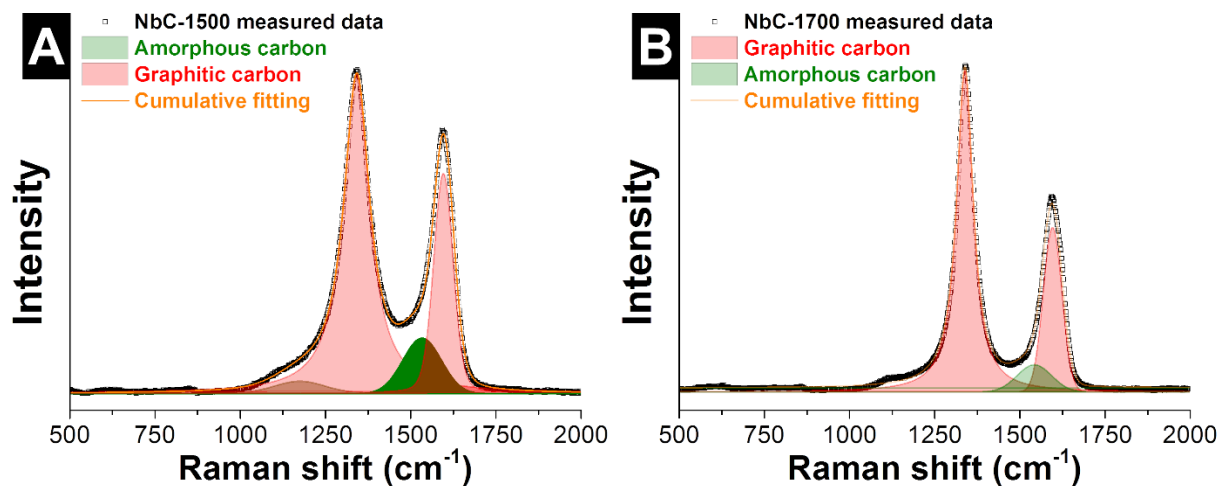


Figure S1: Peak fitting (four Voigt peaks) results for Raman spectra of (A) NbC/C composite fibers synthesized at 1500 °C and (B) 1700 °C.

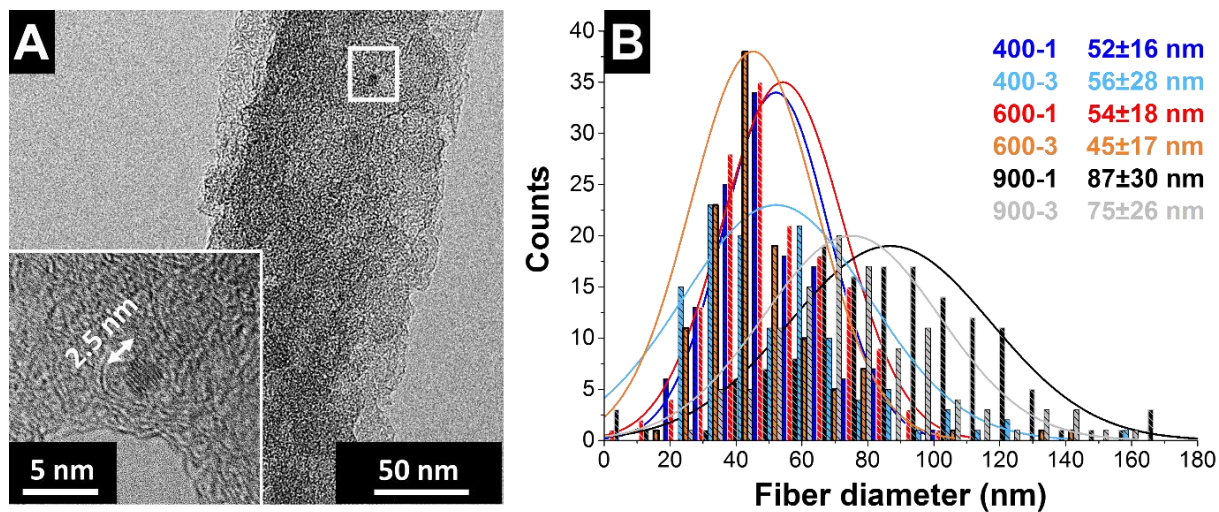


Figure S2: (A) TEM micrograph of NbC-CDC fibers synthesized at 400 °C and 3 h, where some residual NbC crystals are observed in the inset. (B) Fiber diameter distribution of NbC-CDC nanofibers with different synthesis temperatures (400, 600, or 900 °C) and chlorine gas treatment durations (1 h or 3 h).

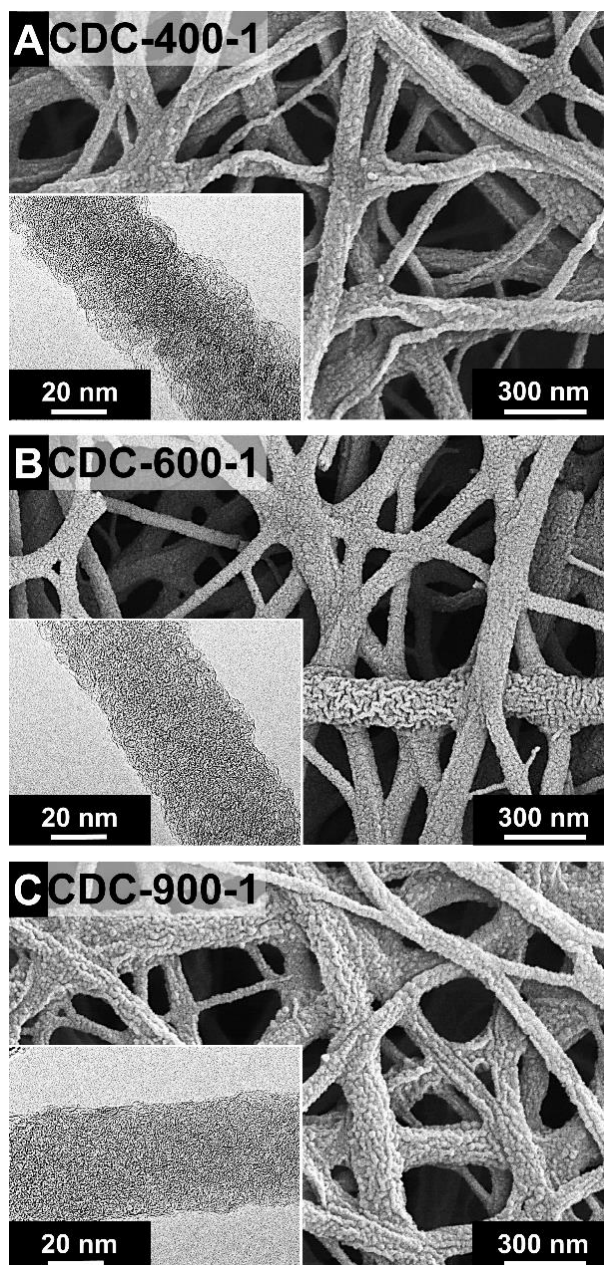


Figure S3: SEM and TEM micrographs (inset) of NbC-CDC fibers synthesized by chlorine gas treatment for 1 h at 400 °C (A), 600 °C (B) and 900 °C (C).

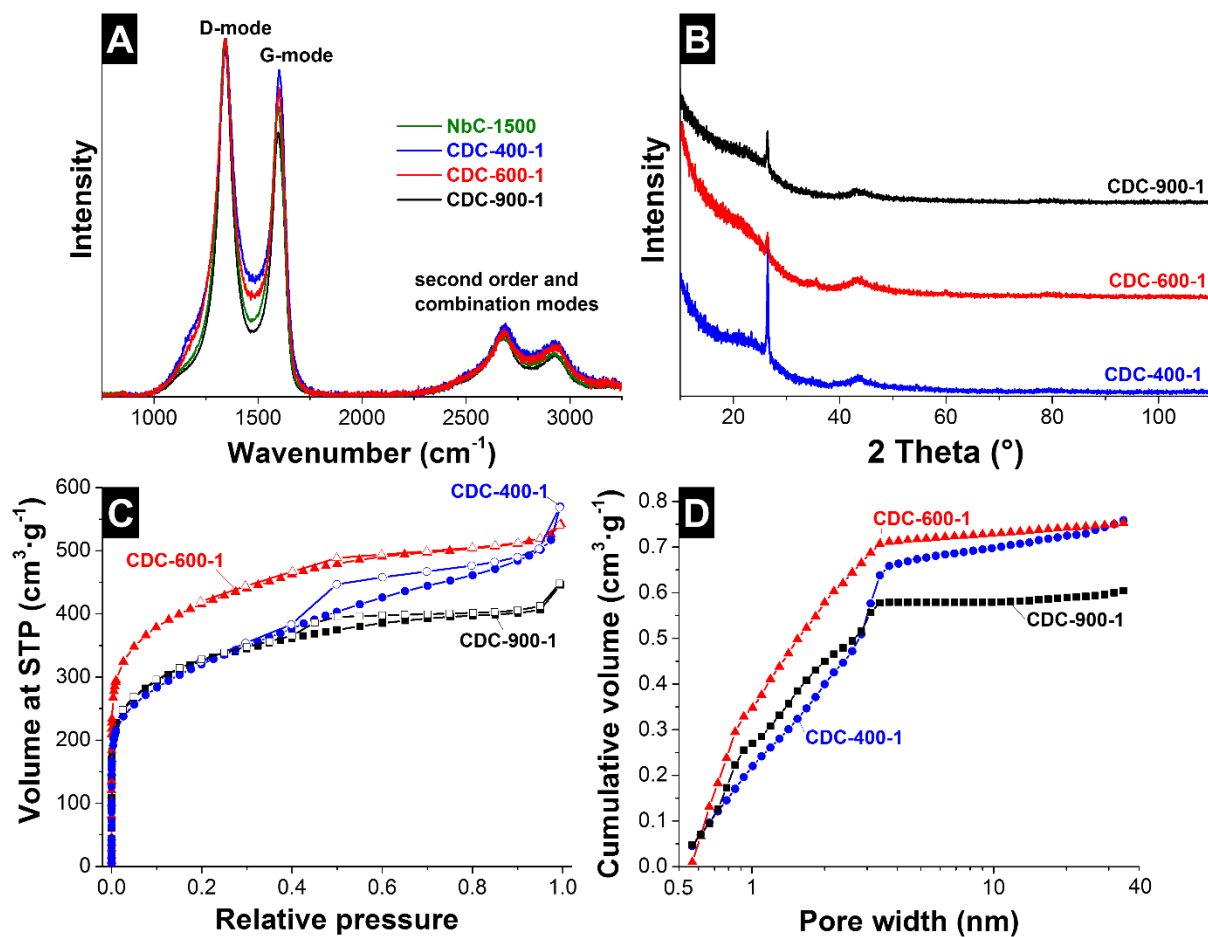


Figure S4: Structural characterization of NbC-CDC fibers synthesized by chlorine treatment for 1 h: (A) Raman spectra and (B) XRD diffractograms. (C) Nitrogen gas sorption isotherms at -196°C (STP: standard temperature pressure, and (D) corresponding cumulative pore volume distribution obtained from QSDFT data analysis.

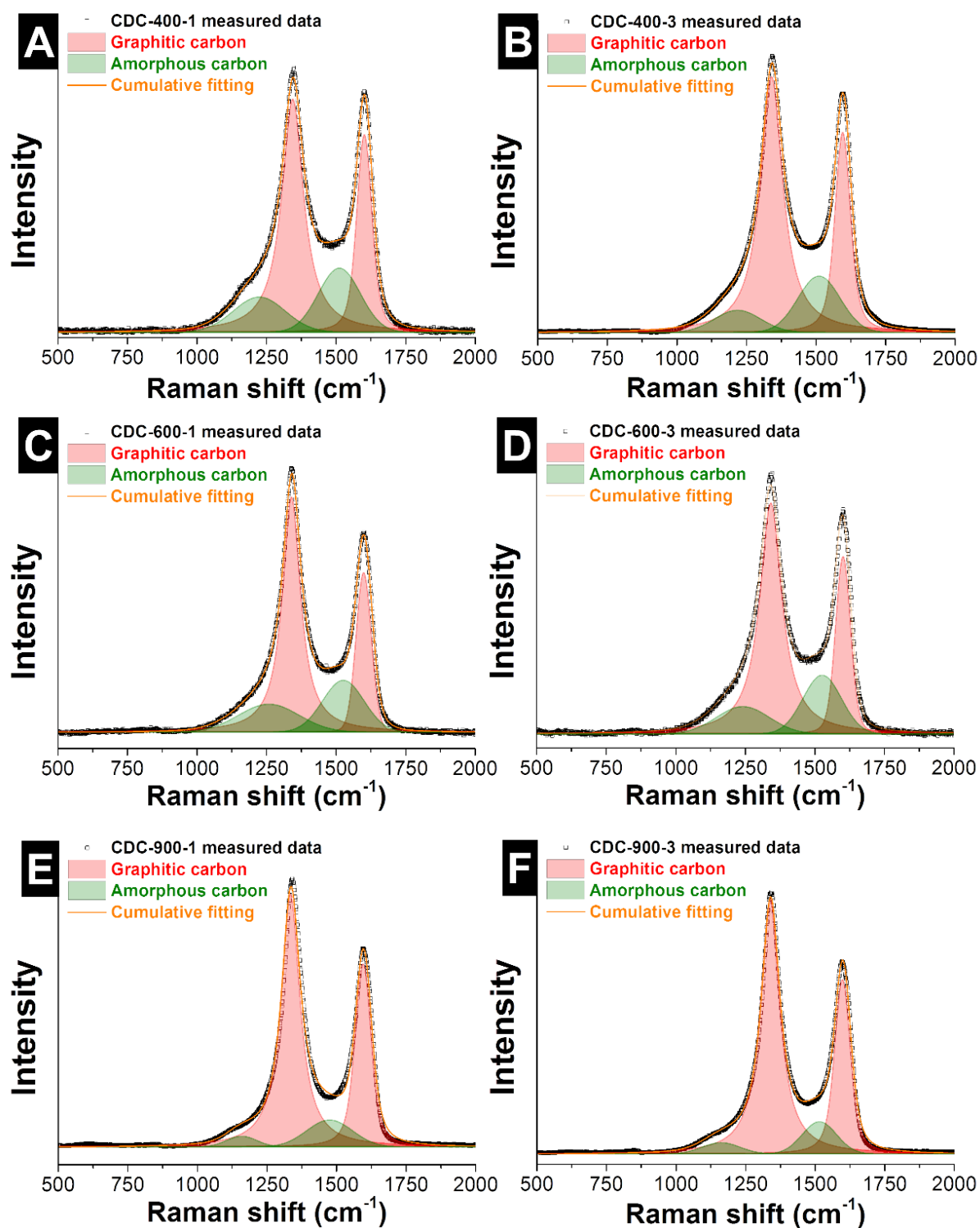


Figure S5: Results of four Voigt peak fitting for Raman spectra of NbC-CDC fibers synthesized. Samples after thermal chlorine gas treatment at (A-B) 400 °C, (C-D) 600 °C, and (E-F) 900 °C for (A,C,E) 1 h or (B,D,F) 3 h.

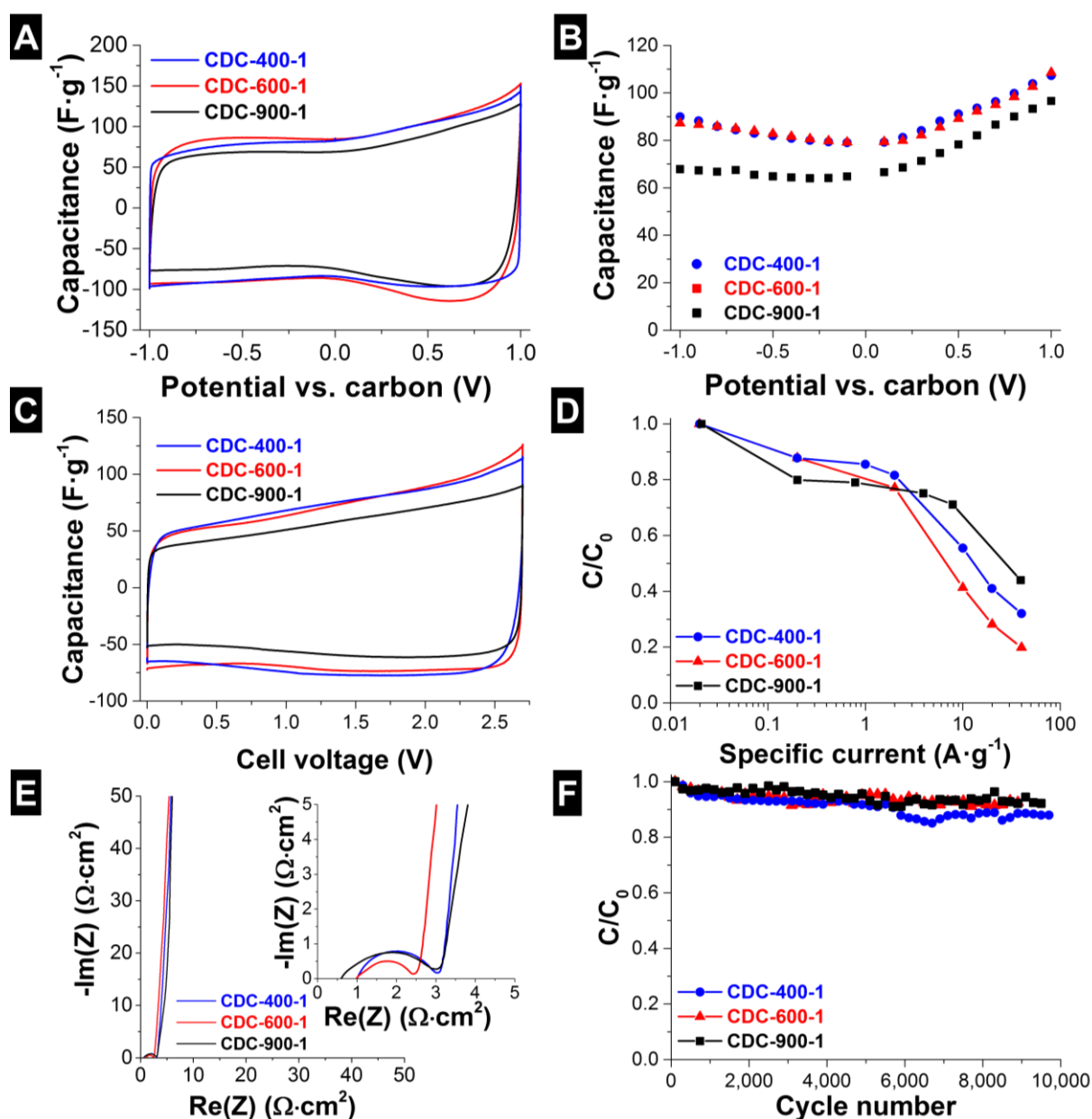


Figure S6: Electrochemical characterization of chlorine treated samples for 1 h in 1 M TEA-BF₄ in ACN. Half-cell measurements with (A) cyclic voltammetry at 10 mV·s⁻¹ and (B) GCPL at 2 A·g⁻¹. Characterization for full-cell with (C) cyclic voltammetry at 10 mV·s⁻¹, (D) galvanostatic charge/discharge power handling up to 2.5 V cell voltage between 0.02-40 A·g⁻¹, (E) EIS at 0 V, and (F) galvanostatic charge/discharge cycling stability up to 2.5 V at 1 A·g⁻¹ for 10,000 cycles.

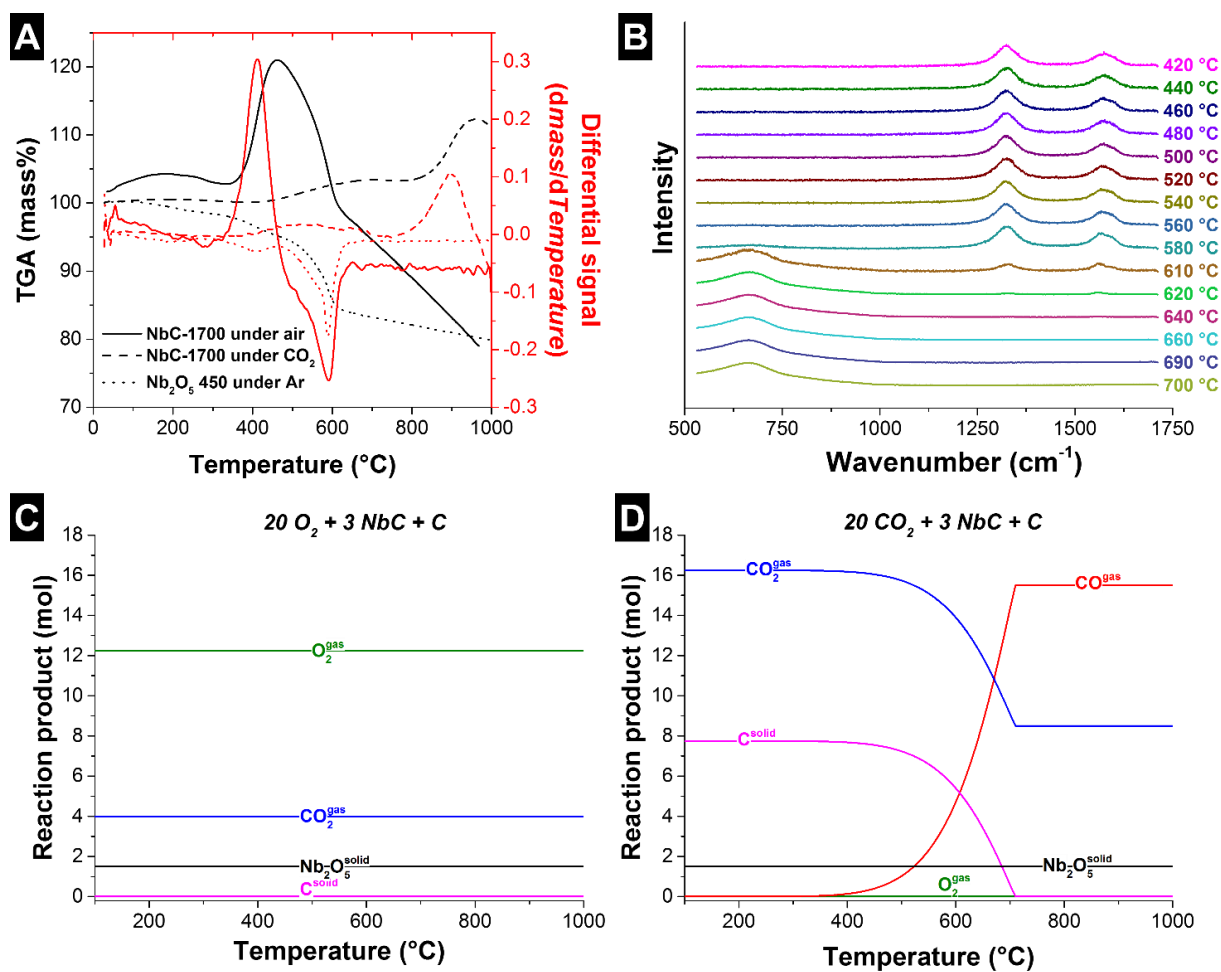


Figure S7: (A) TGA and DTG of NbC-1700 fibers under air and CO₂ at 5 °C·min⁻¹, and TGA and DTG of Nb₂O₅-450 fibers under Argon. (B) In situ Raman spectra of NbC-1700 fibers under treatment in air at 5 °C·min⁻¹. Thermodynamic calculations with FACTSAGE of reaction products from NbC/C (C) in air (simplified as oxygen) and (D) in CO₂.

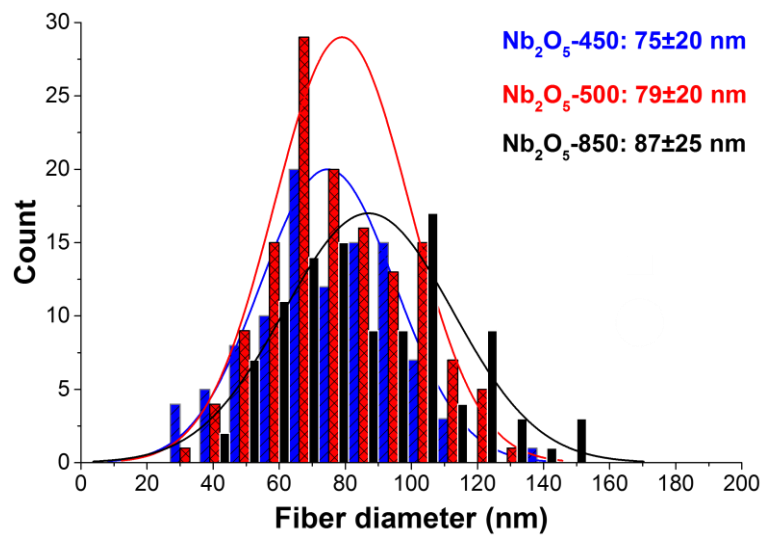


Figure S8: Fiber diameter distribution of Nb₂O₅/C hybrid fibers.

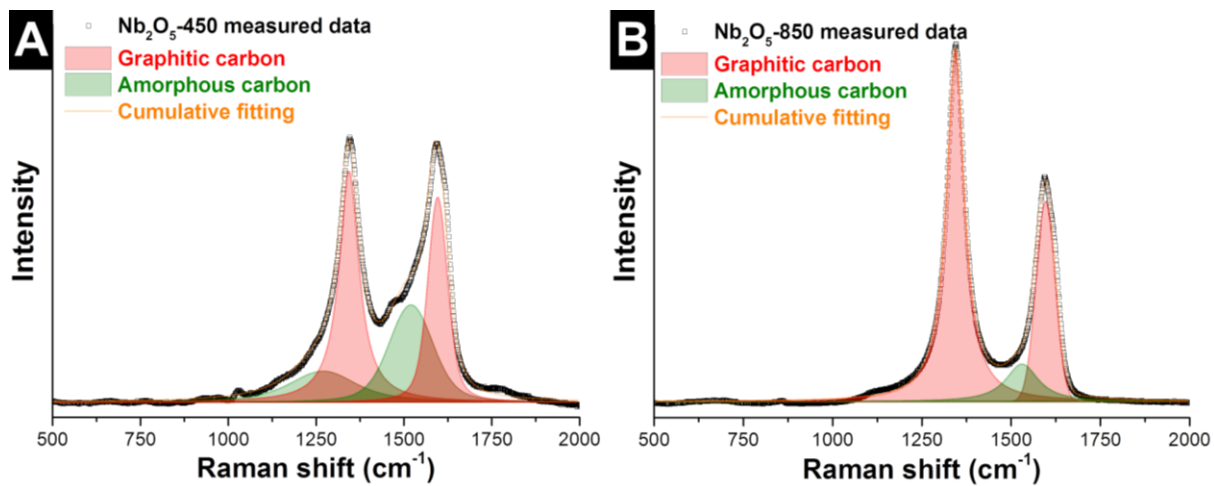


Figure S9: Four Voigt peak fitting results of Raman spectra of (A) Nb₂O₅-450 and (B) Nb₂O₅-850.

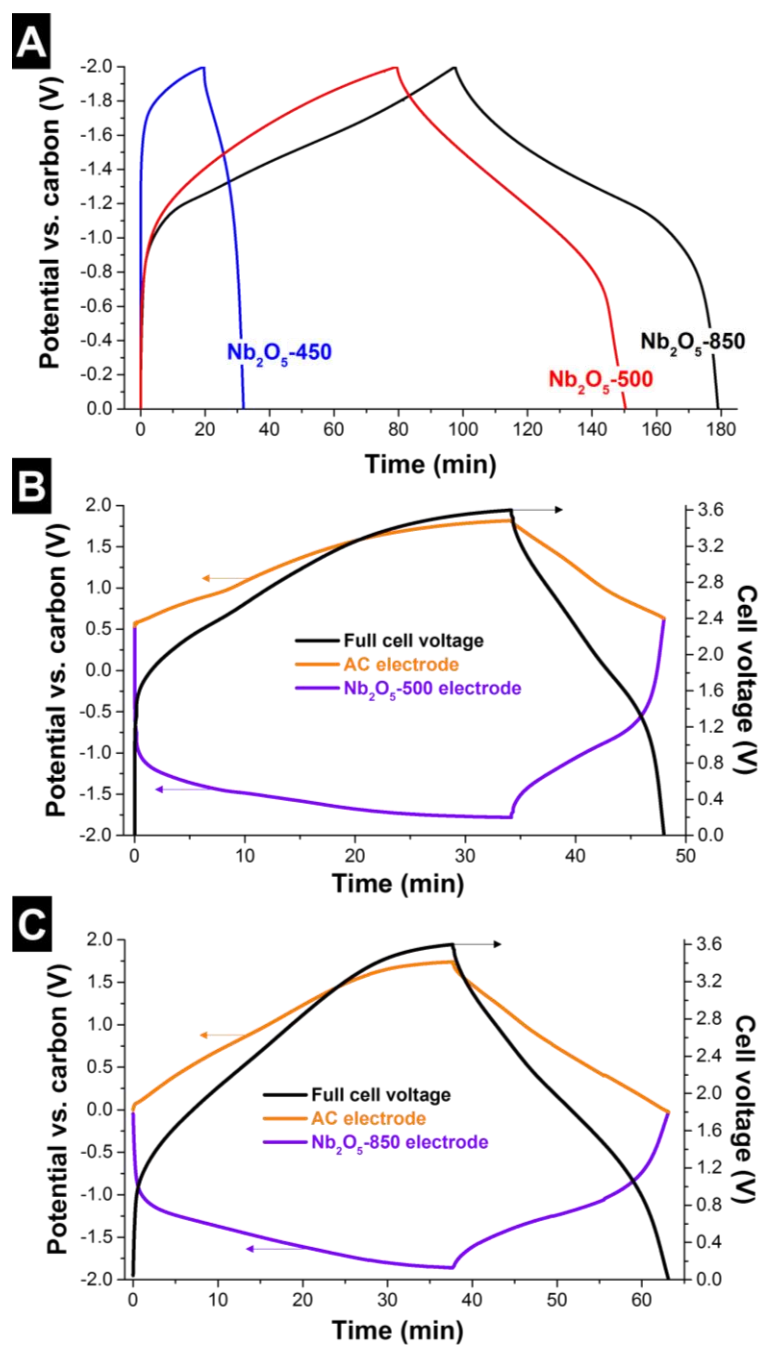


Figure S10: (A) Electrochemical characterization of Nb₂O₅/C hybrid fibers for half-cell configuration by GCPL at 0.1 A·g⁻¹ in LiClO₄ 1 M in EC/DMC (B) Full-cell measurements with a spectator reference electrode to monitor the potential development at the positive and negative electrode separately. The cell voltage is increased to 3.6 V at 0.1 A·g⁻¹, while observing the potential of the negative electrode (Nb₂O₅ electrode) and the positive electrode (AC electrode) through an AC reference electrode.

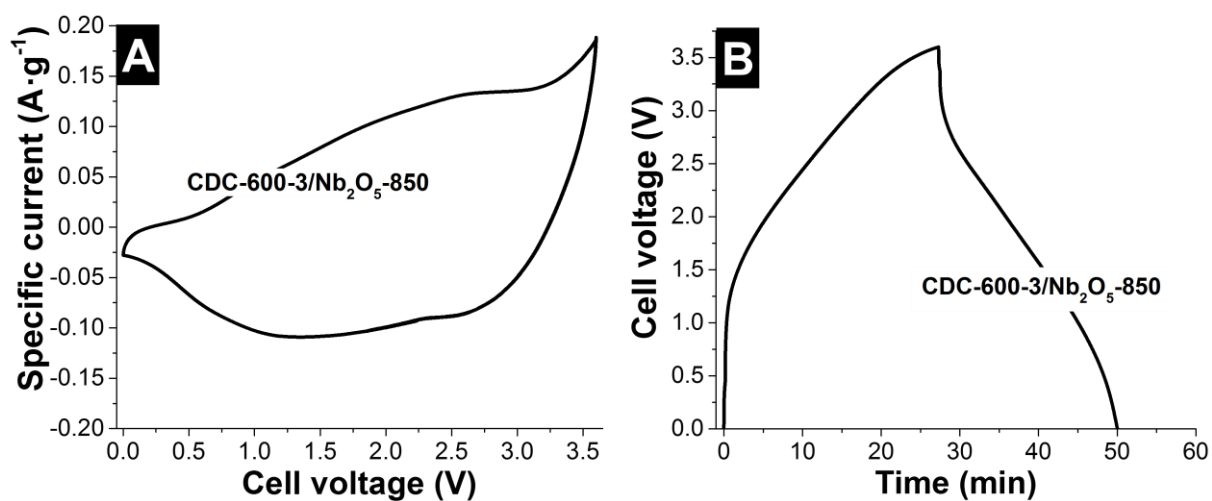


Figure S11: (A) Electrochemical characterization of CDC-600-3/Nb₂O₅-850 hybrid full-cell configuration by cyclic voltammetry at 1 mV·s⁻¹, (B) and by GCD to 3.6 V cell voltage at 0.1 A·g⁻¹ in LiClO₄ 1 M in EC/DMC. The cell used a Nb₂O₅-850 negative electrode and a CDC-600-3 positive electrode.

Table S1: EDX results of NbC-CDCs fibers and measured mass change after chlorine gas treatment.

Sample	Mass change	C (mass%)	O (mass%)	Nb (mass%)	Cl (mass%)
NbC-1500	-	24.8±0.6	2.3±0.5	73.9±0.9	
CDC-400-1	-75%	96.8±0.2	2.8±0.2	0.2±0.0	0.2±0.0
CDC-400-3	-78%	96.1±0.2	2.6±0.2	0.6±0.1	0.7±0.1
CDC-600-1	-74%	98.6±0.2	0.8±0.3	0.1±0.0	0.5±0.1
CDC-600-3	-74%	97.9±0.3	1.7±0.2	0.2±0.0	0.2±0.1
CDC-900-1	-79%	98.0±0.3	1.2±0.1	0.1±0.0	0.7±0.1
CDC-900-3	-72%	98.3±0.4	0.9±0.2	0.3±0.0	0.5±0.1

Table S2: Peak fitting of Raman spectra from NbC-CDCs fibers.

Sample	D-mode	G-mode	I _D /I _G - ratio	FWHM (cm ⁻¹)	
	(cm ⁻¹)	(cm ⁻¹)		D-mode	G-mode
NbC-1500	1342	1598	2.1	80.2±0.6	68.0±0.8
CDC-400-1	1345	1603	2.1	96.2±0.8	66.0±0.7
CDC-400-3	1343	1603	2.3	98.4±0.6	67.0±1.0
CDC-600-1	1341	1601	2.7	90.2±3.6	65.2±0.9
CDC-600-3	1340	1597	2.6	87.1±6.7	64.2±0.9
CDC-900-1	1335	1597	2.0	82.8±3.6	69.9±1.4
CDC-900-3	1335	1596	2.1	81.6±0.4	68.2±0.7

Table S3: Peak fitting of Raman spectra from Nb₂O₅/C fibers.

Sample	D-mode	G-mode	I _D /I _G - ratio	FWHM (cm ⁻¹)	
	(cm ⁻¹)	(cm ⁻¹)		D-mode	G-mode
NbC-1700	1340	1598	1.9	59.2±0.1	65.4±0.0
Nb ₂ O ₅ -450	1346	1599	1.5	69.7±6.5	67.2±1.2
Nb ₂ O ₅ -500	1354	1584	-	-	-
Nb ₂ O ₅ -850	1346	1599	2.5	60.9±0.2	64.1±0.9

Appendix C: Supporting Information to Chapter 3.3

Supporting Information

Binder-Free Hybrid Titanium–Niobium Oxide/Carbon Nanofiber Mats for Lithium-Ion Battery Electrodes

Aura Tolosa,^[a, b] Simon Fleischmann,^[a, b] Ingrid Grobelsek,^[a] Antje Quade,^[c] Eunho Lim,^[a] and Volker Presser^{*[a, b]}

cssc_201701927_sm_miscellaneous_information.pdf

SUPPORTING INFORMATION

Binder-free hybrid titanium-niobium oxide/carbon nanofiber mats for lithium-ion battery electrodes

**Aura Tolosa,^{1,2} Simon Fleischmann,^{1,2} Ingrid Grobelsek,¹
Antje Quade,³ Eunho Lim,¹ Volker Presser^{1,2,*}**

¹ *INM - Leibniz Institute for New Materials, 66123 Saarbrücken, Germany*

² *Department of Materials Science and Engineering, Saarland University, 66123 Saarbrücken, Germany*

³ *Leibniz Institute for Plasma Science and Technology, 17489 Greifswald, Germany*

* *Corresponding author's eMail: volker.presser@leibniz-inm.de*

1. Schematic illustration of the synthesis procedure

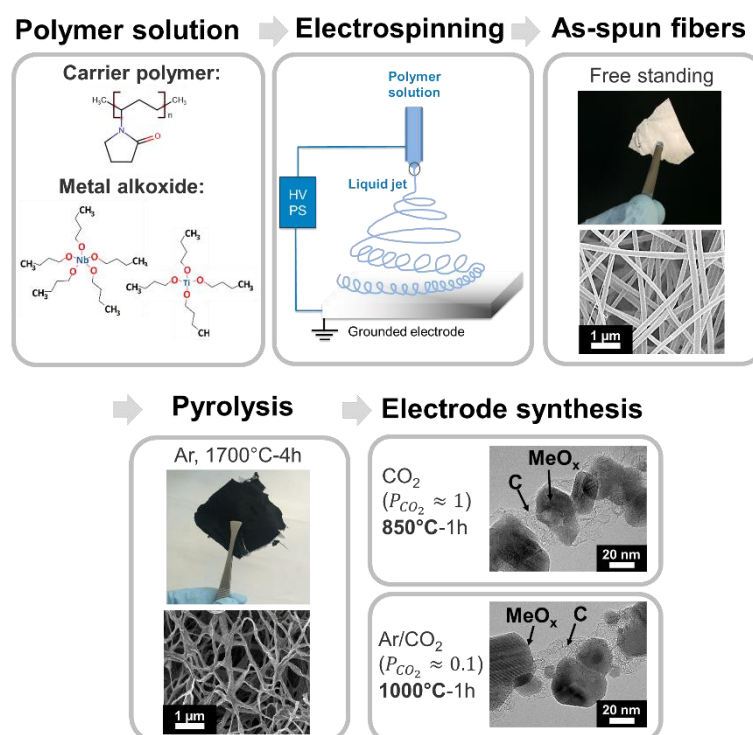


Figure S1: Schematic representation of the synthesis steps.

2. Characterization of metal carbide/carbon fibers

After thermal annealing in argon, the fiber shape is maintained with an average diameter of 69 ± 30 nm (**Figure S2A-B**), and metal carbide crystals surrounded by graphitic carbon are formed. The metal carbide/carbon fibers are named according to the Ti:Nb ratio used as NbC_x , TiNb_2C_x , and TiNb_6C_x . The amount of free carbon in the fibers was determined by TGA and the fiber elemental composition was determined by EDX (**Table S1**). After pyrolysis, the metal carbide samples present around 19 mass% of free carbon and the molar ratio between Ti:Nb corresponds to the ratio used for the spinning dope preparation, 1:2 and 1:6, for TiNb_2C_x and TiNb_6C_x , respectively. Raman spectra (*Supporting Information*, **Figure S2D**) of the metal carbide/carbon fibers showed characteristic peaks for incompletely graphitized carbon, namely the D-mode at $1341\text{-}1344\text{ cm}^{-1}$ and the G-mode at $1594\text{-}1598\text{ cm}^{-1}$.¹ In addition, we see carbon-related combination modes and overtones between 2500 cm^{-1} and 3000 cm^{-1} . The D- and G-mode relate sp^2 -hybridized carbon; the G-mode is related to the bond stretching of pairs of sp^2 -hybridized carbon atoms in rings and chains,¹ and the D-mode is due to the activation of the breathing modes of six carbon atoms rings when a defect is present.² The results of the Raman peak analysis are presented in **Table S2**.

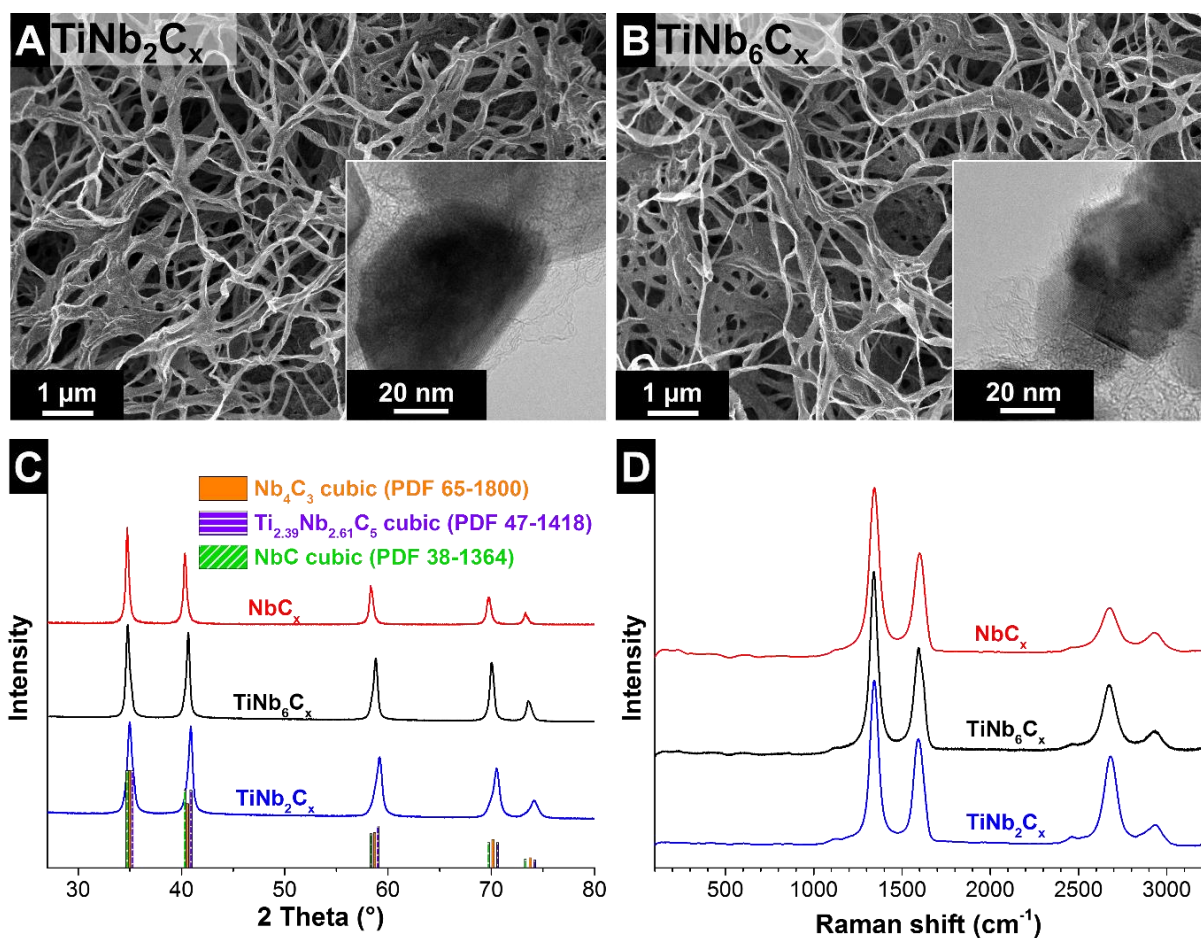


Figure S2: SEM and TEM micrographs (inset) of metal carbide/carbon fibers synthesized at 1700 °C in argon atmosphere with different Ti:Nb molar ratios, 1:2 (A) and 1:6 (B). X-ray diffraction pattern and literature values for diffraction peak positions (C), and Raman spectra (D).

Table S1: Elemental analysis by EDX and results of the free carbon content calculated from TGA. Data below the detection limit are marked as non-detectable (n.d.).

Material	EDX results (mass%)				TGA C _{free} (mass%)
	Ti	Nb	C	O	
NbC _x	n.d.	70.3±5.1	27.6±3.5	2.0±0.4	18.1
TiNb ₆ C _x	5.2±0.5	57.9±4.6	35.0±5.0	1.9±0.3	18.8
TiNb ₂ C _x	13.2±1.2	50.8±3.5	33.9±4.5	2.1±0.7	19.4

Table S2: Results of the Raman peak analysis, by peak deconvolution.

Sample	D-mode (cm ⁻¹)		G-mode (cm ⁻¹)		I _D /I _G -ratio
	Position	FWHM	Position	FWHM	
NbC_x	1344	62	1598	70	1.9
TiNb₆C_x	1341	52	1595	66	1.8
TiNb₂C_x	1343	50	1594	66	1.7

The crystalline metal carbide was characterized by XRD (**Figure S2C, Table S3**). The Nb fibers exhibit crystal sizes of ca. 45 nm consisting of cubic $Fm\bar{3}m$ niobium carbide (lattice parameter $a=4.47$ Å). For the TiNb₆ and TiNb₂ samples, cubic $Pm\bar{3}m$ Nb₄C₃ and cubic $Fm\bar{3}m$ Ti_{2.39}Nb_{2.61}C₅ (lattice parameter $a=4.45$ Å and $a=4.43$ Å, respectively) are formed, leading to a shift of the peak positions to higher 2θ angles. Presenting the same crystal structure, the smaller lattice parameter results from the lower atomic radius of titanium (1.40 Å) compared to niobium (1.46 Å).

Table S3: Rietveld analysis of the XRD pattern for the metal carbide/carbon fibers.

Material	Crystal phase	Domain size (nm)	Content (mass%)
NbC_x	NbC cubic $Fm\bar{3}m$ (PDF-38-1364)	45	100
	Lattice parameter $a=0.447$ nm		
TiNb₆C_x	Nb ₄ C ₃ cubic $Pm\bar{3}m$ (PDF-65-1800)	34	87
	Lattice parameter $a=0.445$ nm		
	NbC cubic $Fm\bar{3}m$ (PDF-38-1364)	30	13
	Lattice parameter $a=0.447$ nm		
TiNb₂C_x	Ti _{2.39} Nb _{2.61} C ₅ cubic $Pm\bar{3}m$ (PDF-47-1418)	28	82
	Lattice parameter $a=0.443$ nm		
	Nb ₄ C ₃ cubic $Fm\bar{3}m$ (PDF-65-1800)	24	18
	Lattice parameter $a=0.445$ nm		

3. Supplementary material characterization

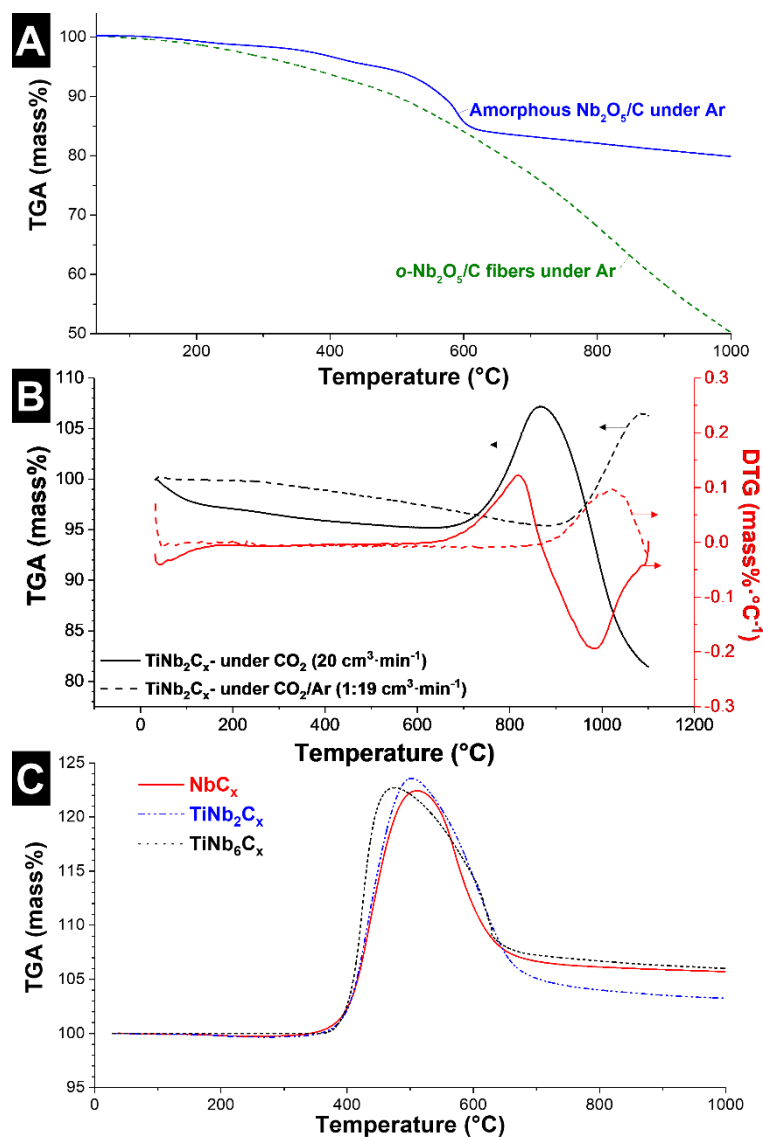


Figure S3: Thermogravimetric analysis of composite fiber containing $\text{Nb}_2\text{O}_5/\text{carbon}$ fibers (either amorphous or crystalline $o\text{-Nb}_2\text{O}_5$) under Ar (A), TiNb_2C_x under oxidizing atmospheres with different partial pressure of CO_2 (B), and metal carbide/carbon fibers under air for characterization of the carbon content (C).

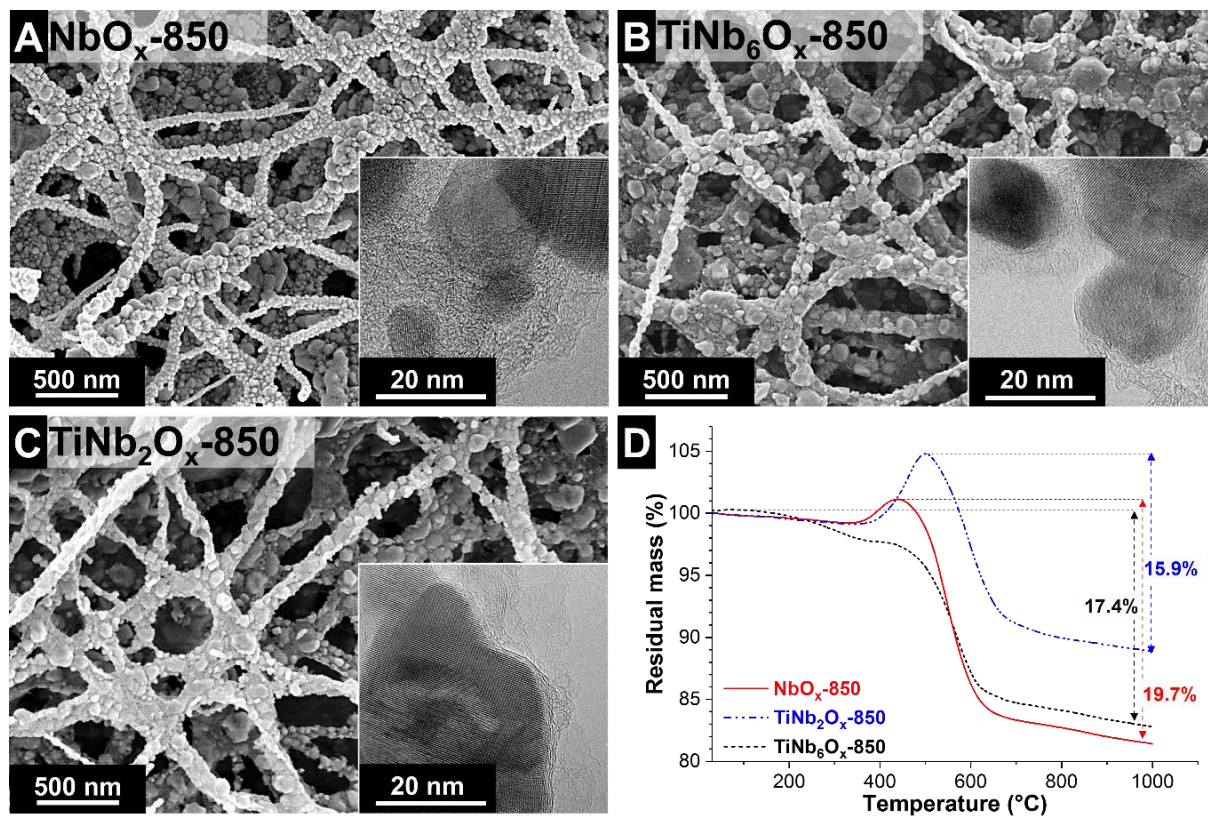


Figure S4: SEM and TEM micrographs (inset) of metal oxide/carbon fibers synthesized at 850 °C containing different Ti:Nb molar ratios, 0:1 (A), 1:6 (B) and 1:2 (C). Thermogravimetric analysis of the composite fiber under air for characterization of the carbon content (D).

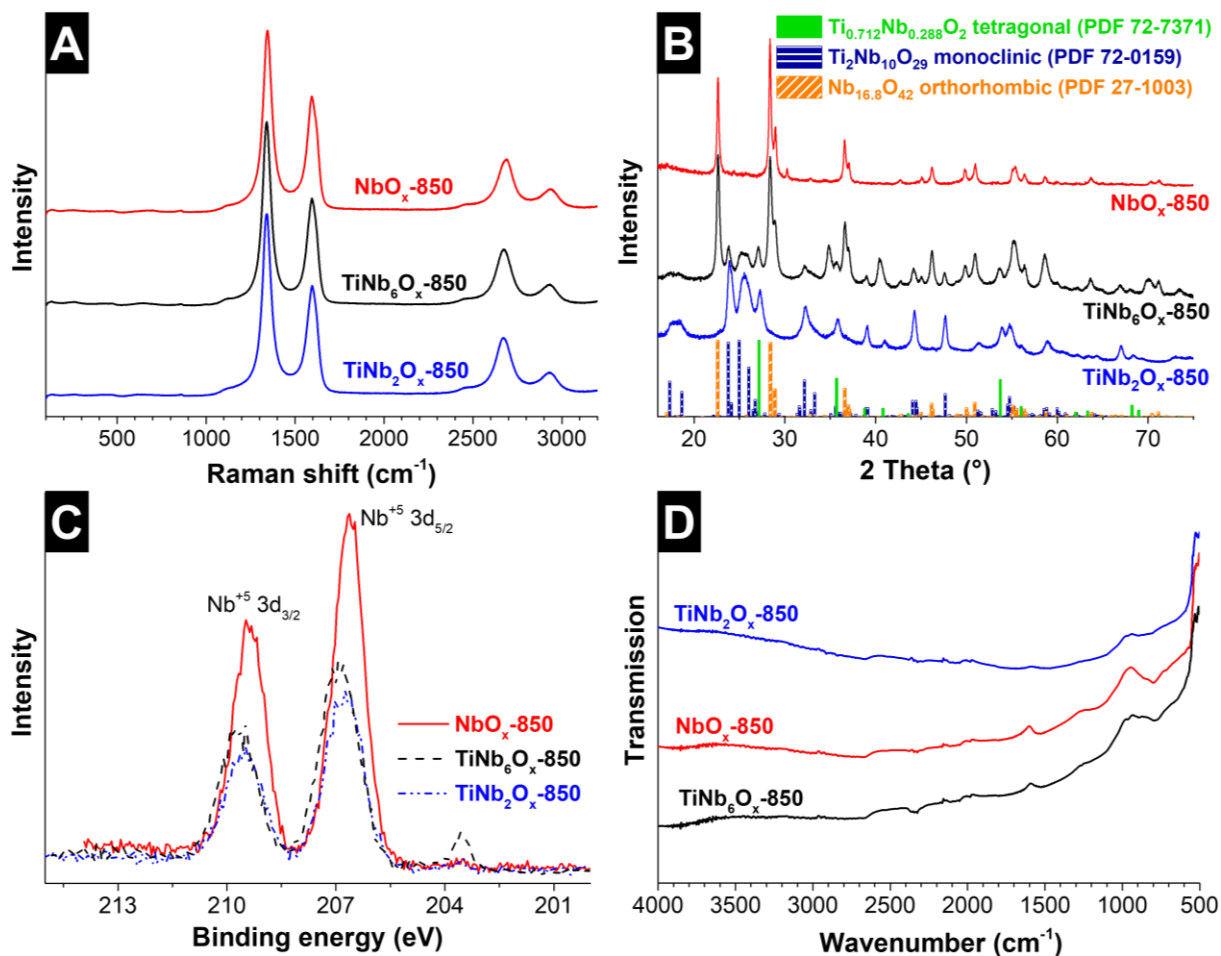


Figure S5: Chemical and structural characterization of the metal oxide/carbon fibers synthesized at 850 $^\circ\text{C}$ under CO_2 . Raman spectra (A), X-ray diffraction pattern and literature values for diffraction peak positions (B), high resolution X-ray photoelectron spectra of Nb 3d (C), and Fourier transform infrared spectra (D).

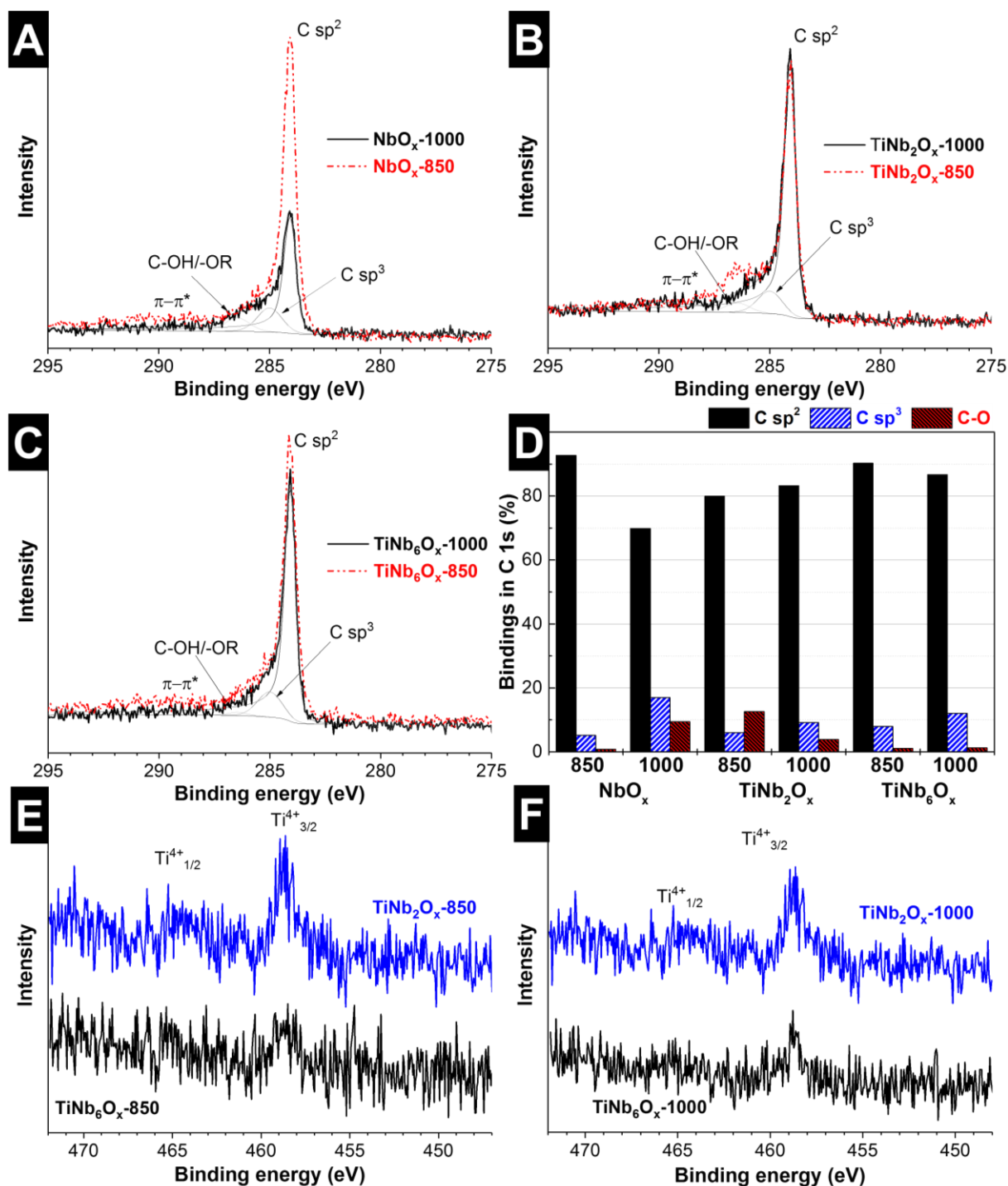


Figure S6: X-ray photoelectron spectra of the metal oxide/carbon hybrid fibers. High resolution measurements of C 1s (A-C) and content of chemical bindings of C 1s (D). High resolution measurements of Ti 2p (E-F).

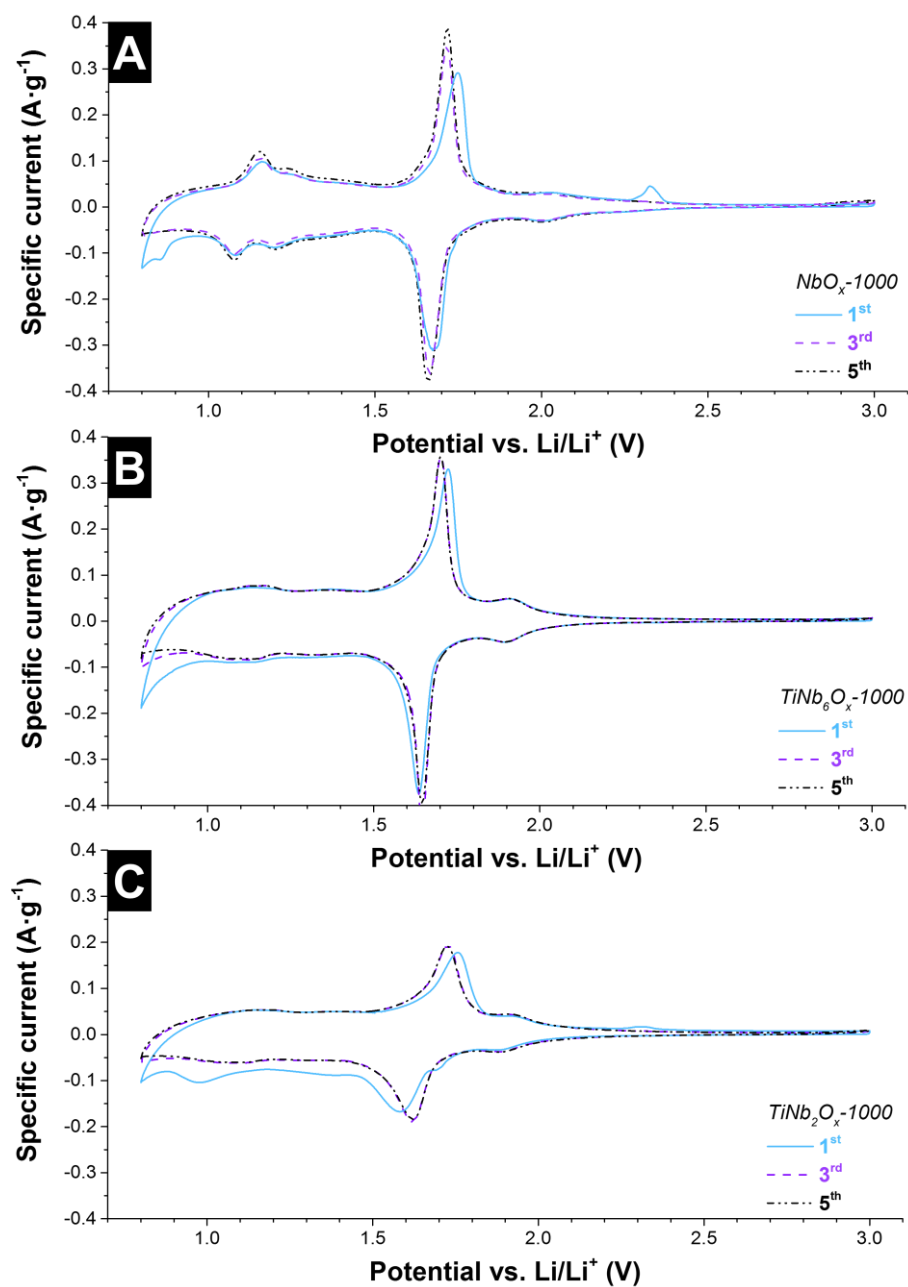


Figure S7: First five cycles by cyclic voltammetry at $0.1\text{ mV}\cdot\text{s}^{-1}$ in half-cell configuration of metal oxide/carbon hybrid nanofibers synthesized at $1000\text{ }^\circ\text{C}$ (A-C).

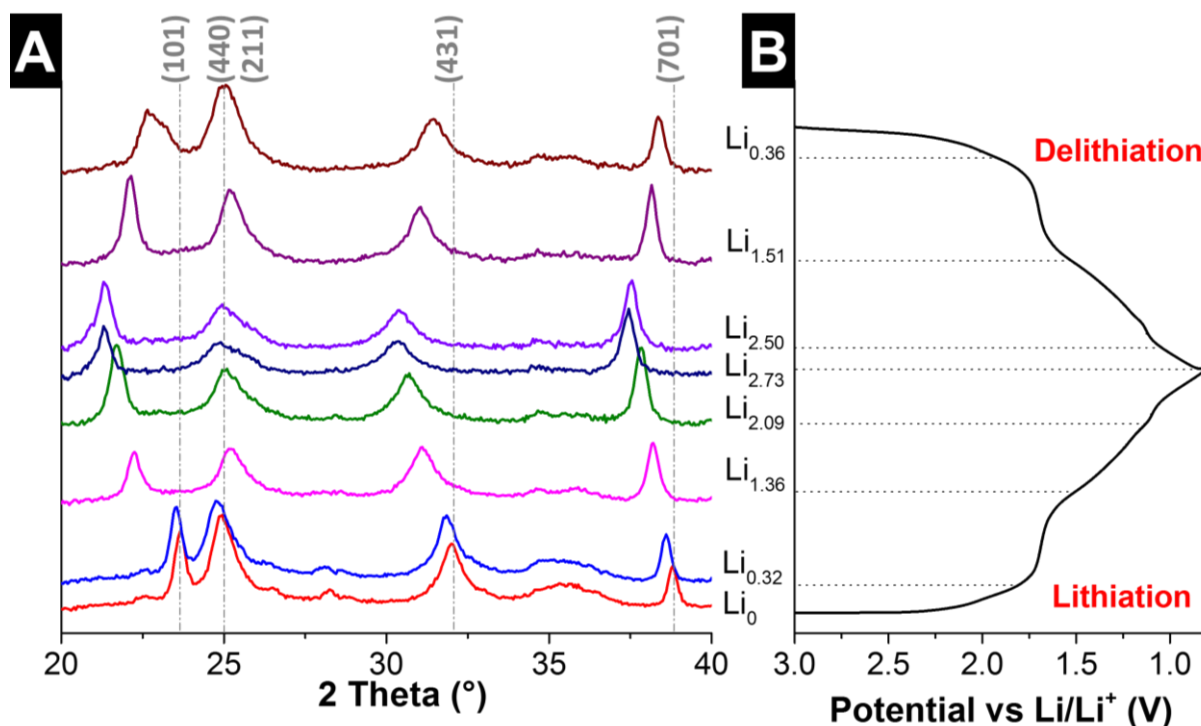


Figure S8: In situ XRD patterns for the sample NbO_x-1000, collected by chronoamperometry at different voltage steps, during lithiation and delithiation; and h-indexes for Nb₂O₅ tetragonal I4/mmm (PDF-72-1484) (A). For comparison, voltage profile during galvanostatic cycling at 0.025 A·g⁻¹ (B), and calculated Li_xNb₂O₅ at the different voltage steps used for in situ XRD. The x value for Li_xNb₂O₅ was calculated according to the results obtained after 5 cycles of galvanostatic cycling at 0.025 A·g⁻¹.

4. Carbon free content calculations

This section presents details about the calculations of the free carbon content based on the TGA results, exemplified for the sample TiNb₂.

Carbon free content in the metal carbide/carbon fibers

In the following equations m corresponds to mass, η to mol, and M to molar mass. Taking as an example the sample TiNb₂C_x, the metal carbide/carbon fibers are oxidized under air completely above 700 °C (**Figure S9A**), removing the initial carbon free (m_C^0) and leading to metal oxide. According to the TGA results, starting from 100 g (100 mass%) of metal carbide/carbon, after oxidation we will have 103.3 g (103 mass%) of metal oxide.

$$m_{TiC} + m_{NbC} + m_C^o = 100 \text{ g}$$

$$m_{TiO_2} + m_{Nb_2O_5} = 103.3 \text{ g}$$

From the EDX results, we confirmed that the molar amount of Ti:Nb in this sample corresponds to 1 mol of Ti: 2 mol of Nb.

$$1 \cdot \eta_{Ti} = 2 \cdot \eta_{Nb} \quad ; \quad 1 \cdot \eta_{TiO_2} = 1 \cdot \eta_{Nb_2O_5}$$

$$M_{TiO_2} \cdot \eta_{TiO_2} + M_{Nb_2O_5} \cdot \eta_{Nb_2O_5} = 103.3 \text{ g}$$

$$(M_{TiO_2} + M_{Nb_2O_5}) \cdot \eta_{Nb_2O_5} = 103.3 \text{ g}$$

$$\eta_{Nb_2O_5} = \frac{103.3 \text{ g}}{\left(79.9 \frac{\text{g}}{\text{mol}} + 265.8 \frac{\text{g}}{\text{mol}}\right)}$$

$$\eta_{Nb_2O_5} = 0.30 \text{ mol} \quad ; \quad \eta_{Nb} = 2 \cdot 0.30 \text{ mol} = 0.60 \text{ mol}$$

$$\eta_{TiO_2} = 0.30 \text{ mol} \quad ; \quad \eta_{Ti} = 0.30 \text{ mol}$$

The amount of titanium and niobium in the metal oxide are the same which were present in the metal carbide.

$$\eta_{Nb} = 0.60 \text{ mol} \quad ; \quad \eta_{NbC} = 0.60 \text{ mol}$$

$$\eta_{Ti} = 0.30 \text{ mol} \quad ; \quad \eta_{TiC} = 0.30 \text{ mol}$$

$$m_{TiC} + m_{NbC} + m_C^o = 100 \text{ g}$$

$$M_{TiC} \cdot \eta_{TiC} + M_{NbC} \cdot \eta_{NbC} + m_C^o = 100 \text{ g}$$

$$59.9 \frac{\text{g}}{\text{mol}} \cdot 0.30 \text{ mol} + 104.9 \frac{\text{g}}{\text{mol}} \cdot 0.60 \text{ mol} + m_C^o = 100 \text{ g}$$

$$m_C^o = 19.4 \text{ g} \quad ; \quad \%m_C^o = 19.4 \text{ mass\%}$$

As a result, we see that the metal carbide/carbon hybrid fibers contained 19.4 mass% of free carbon.

Carbon free content in the metal oxide/carbon fibers

Taking as an example the sample $TiNb_2O_x$, the metal oxide/carbon fibers are oxidized under air completely above 600 °C (**Figure S9B**), removing completely the free carbon of the metal oxide (m_C^f). According to the TGA results, starting from 100 g (100 mass%) of metal oxide/carbon, after oxidation we will have 88.2 g (88.2 mass%) of metal oxide, and all the carbon has been removed, corresponding to the $\%m_C^f = 11.8 \text{ mass\%}$.

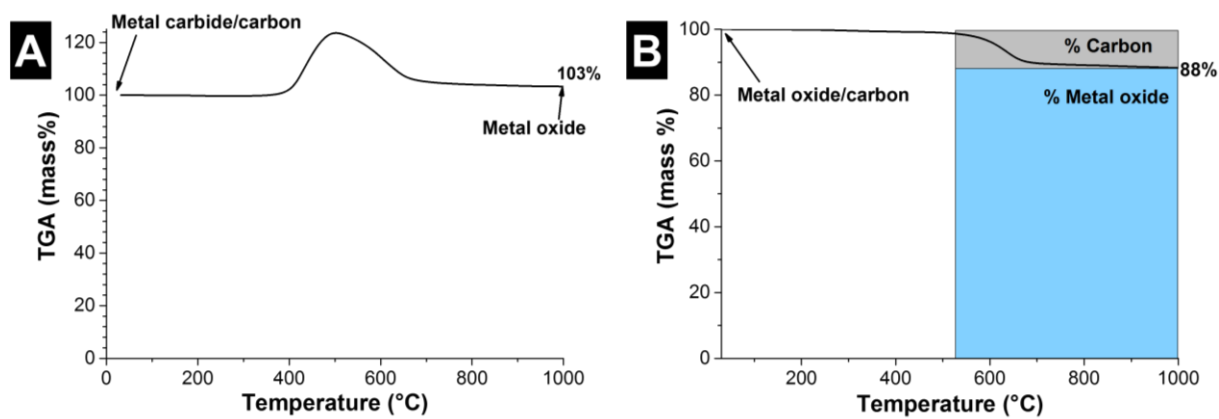


Figure S9: TGA of the metal carbide/carbon (sample TiNb₂C_x) (A) and metal oxide/carbon fibers (sample TiNb₂O_x) (B) under air for carbon content calculations.

References

- [1] A. C. Ferrari, J. Robertson *Physical Review B*. **2001**, *64*, 075414-075411 - 075414-075417.
- [2] A. C. Ferrari, D. M. Basko *Nature Nanotechnology*. **2013**, *8*, 235-246.

Appendix D: Supporting Information to Chapter 3.4

SUPPORTING INFORMATION

Continuous silicon oxycarbide fiber mats with tin nanoparticles as high capacity anode for lithium-ion batteries

Aura Tolosa,^{1,2} Mathias Widmaier,^{2,3} Benjamin Krüner,^{1,2}

John M. Griffin,⁴ and Volker Presser^{1,2*}

¹ *INM – Leibniz Institute for New Materials, Campus D2 2, 66123 Saarbrücken, Germany*

² *Department of Materials Science and Engineering, Saarland University, Campus D2 2, 66123 Saarbrücken, Germany*

³ *Robert Bosch GmbH, Robert-Bosch-Campus 1, 71272 Renningen, Germany*

⁴ *Department of Chemistry, Lancaster University, Lancaster, LA1 4YB, United Kingdom*

* *Corresponding author's eMail: volker.presser@leibniz-inm.de*

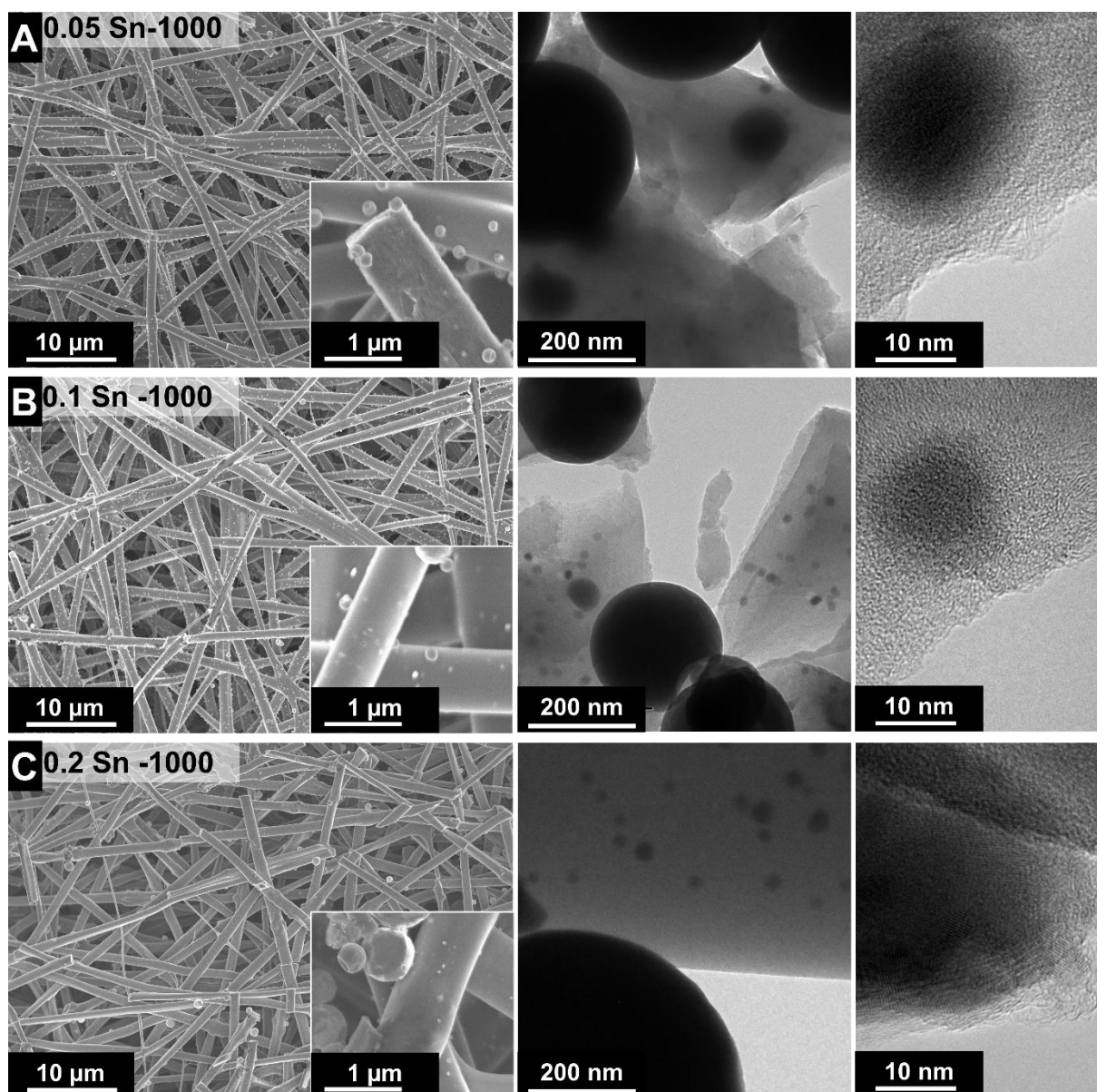


Figure S1: SEM and TEM micrographs (inset) of the SiOC fibers synthesized at 1000 °C, containing different amounts of Sn: 0.05 (A), 0.1 (B), and 0.2 (C).

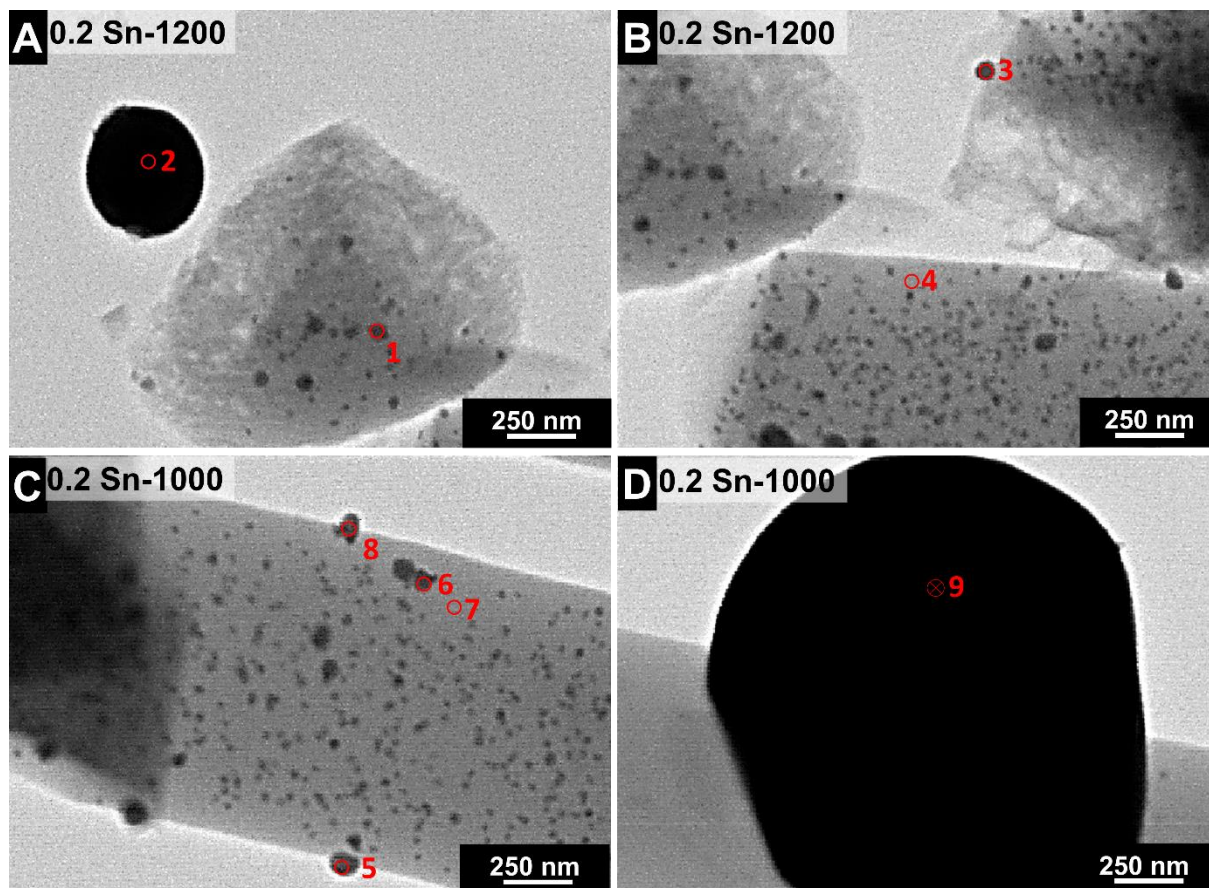


Figure S2: TEM micrographs corresponding to EDX point analysis, for the samples containing 0.2 Sn synthesized at 1200 °C (A-B) and 1000 °C (C-D).

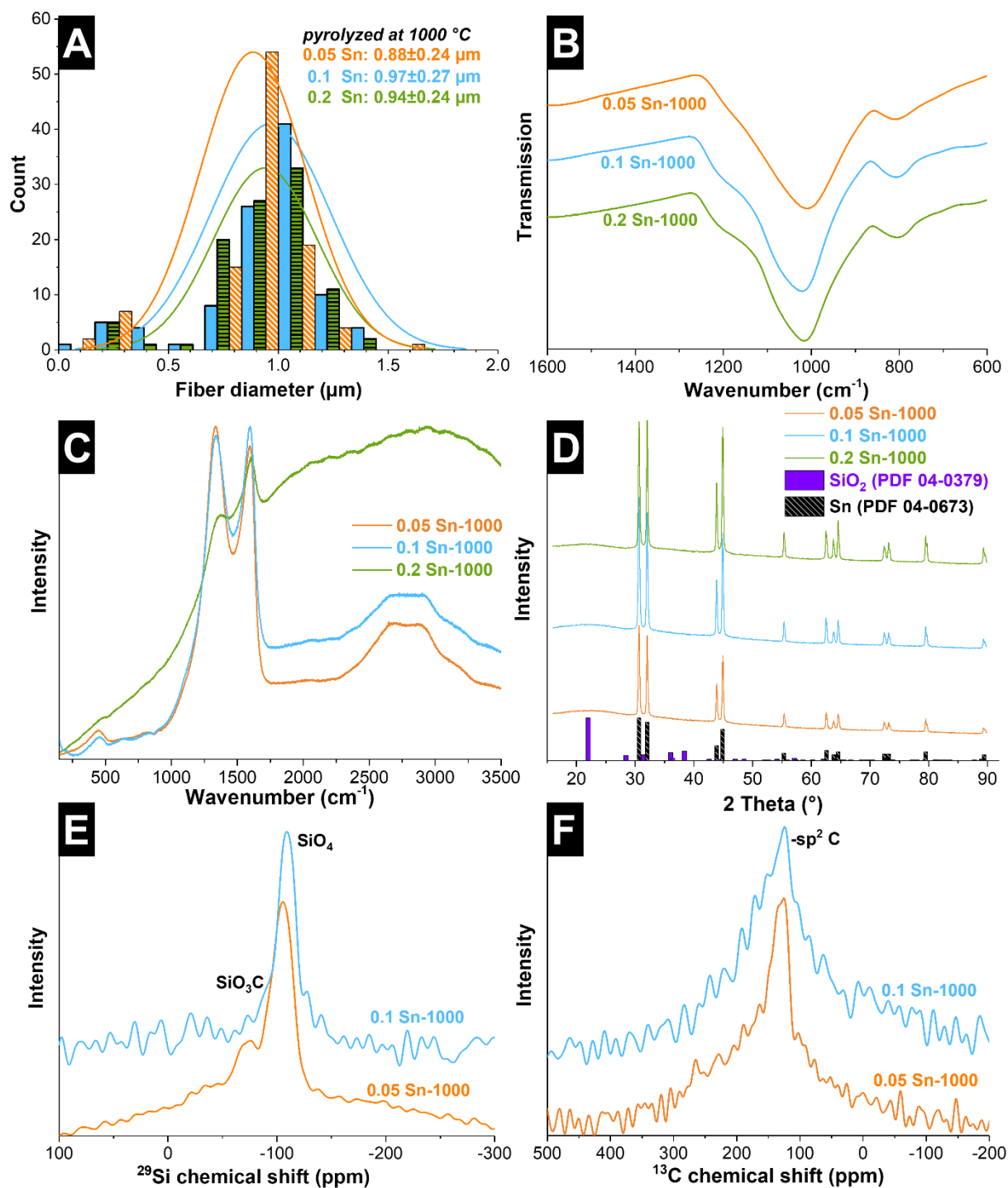


Figure S3: Material characterization of fibers synthesized at 1000 °C. Fiber diameter distribution (A), Fourier transform infrared spectra (B), Raman spectra (C), X-ray diffraction pattern and literature values for diffraction peak positions (D), solid-state ²⁹Si NMR (E), and ¹³C NMR (F).

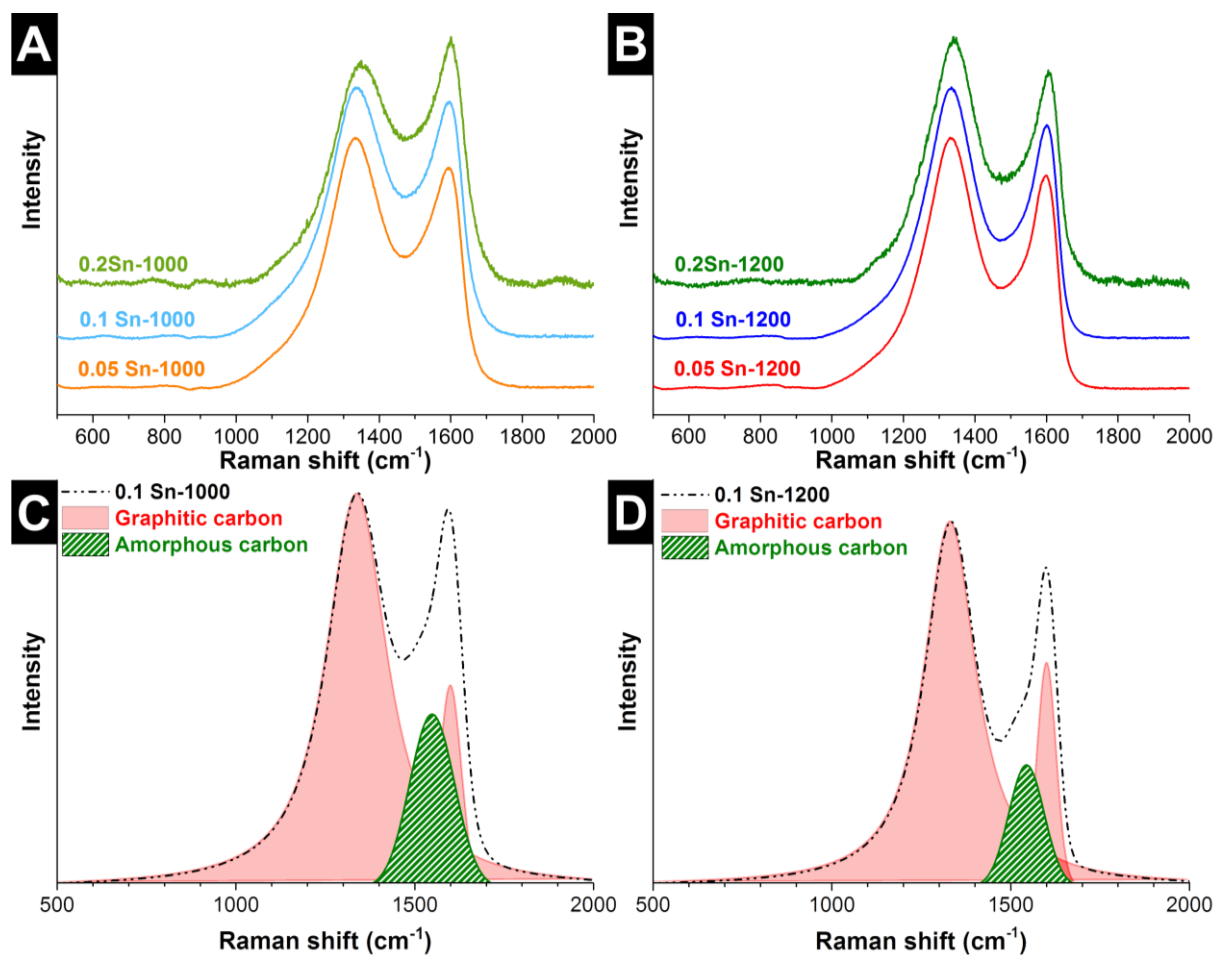


Figure S4: Comparative Raman spectra for the samples synthesized at 1000 °C (A) and 1200 °C (B) after background normalization. Representation of peak deconvolution of the samples containing 0.1 Sn synthesized at 1000 °C (C) and 1200 °C (D).

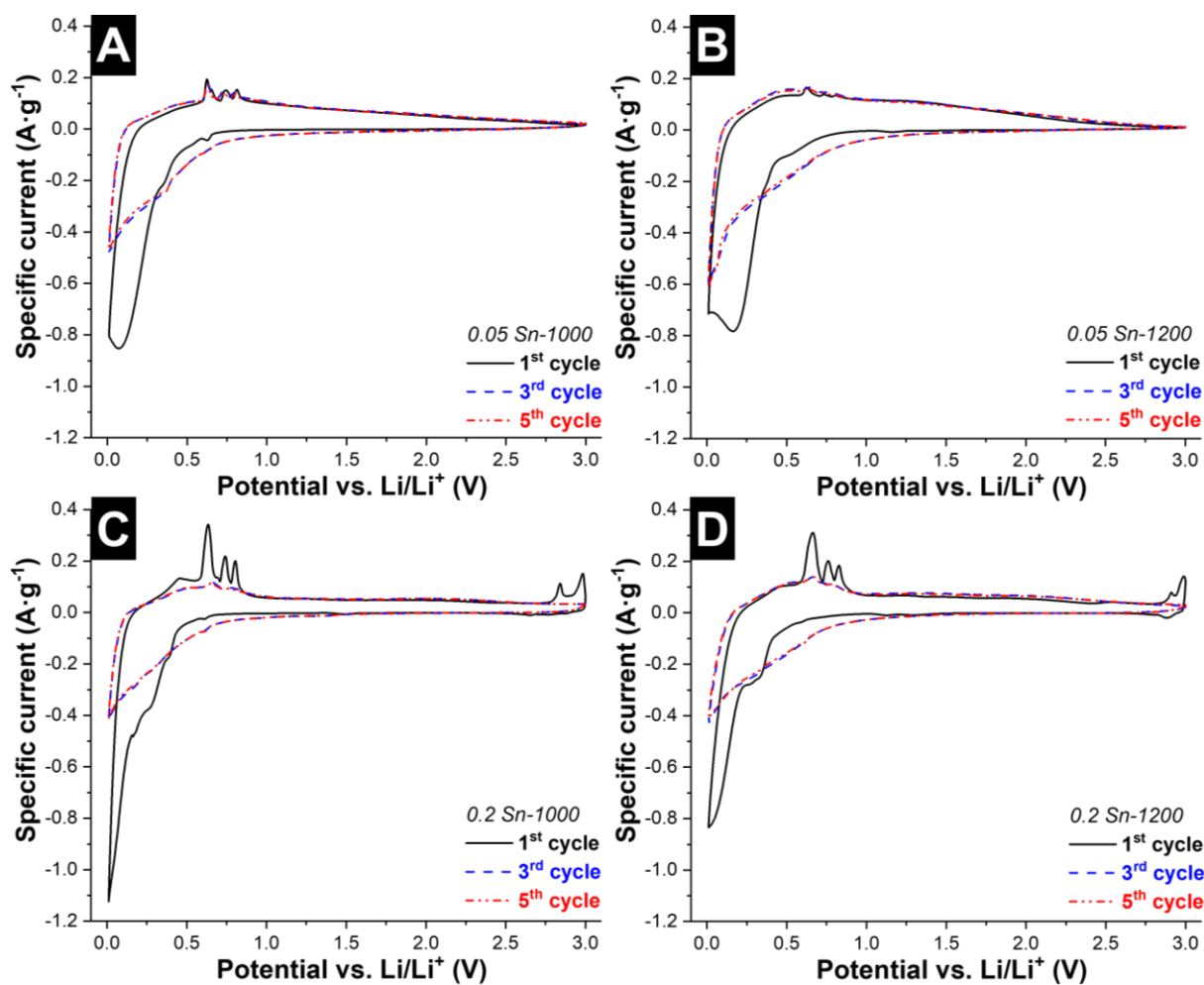


Figure S5: Initial five cycles at 0.1 mV·s⁻¹ for the samples containing 0.05 Sn (A-B) and 0.2 Sn (C-D) synthesized at 1000 °C (A, C) and 1200 °C (B, D).

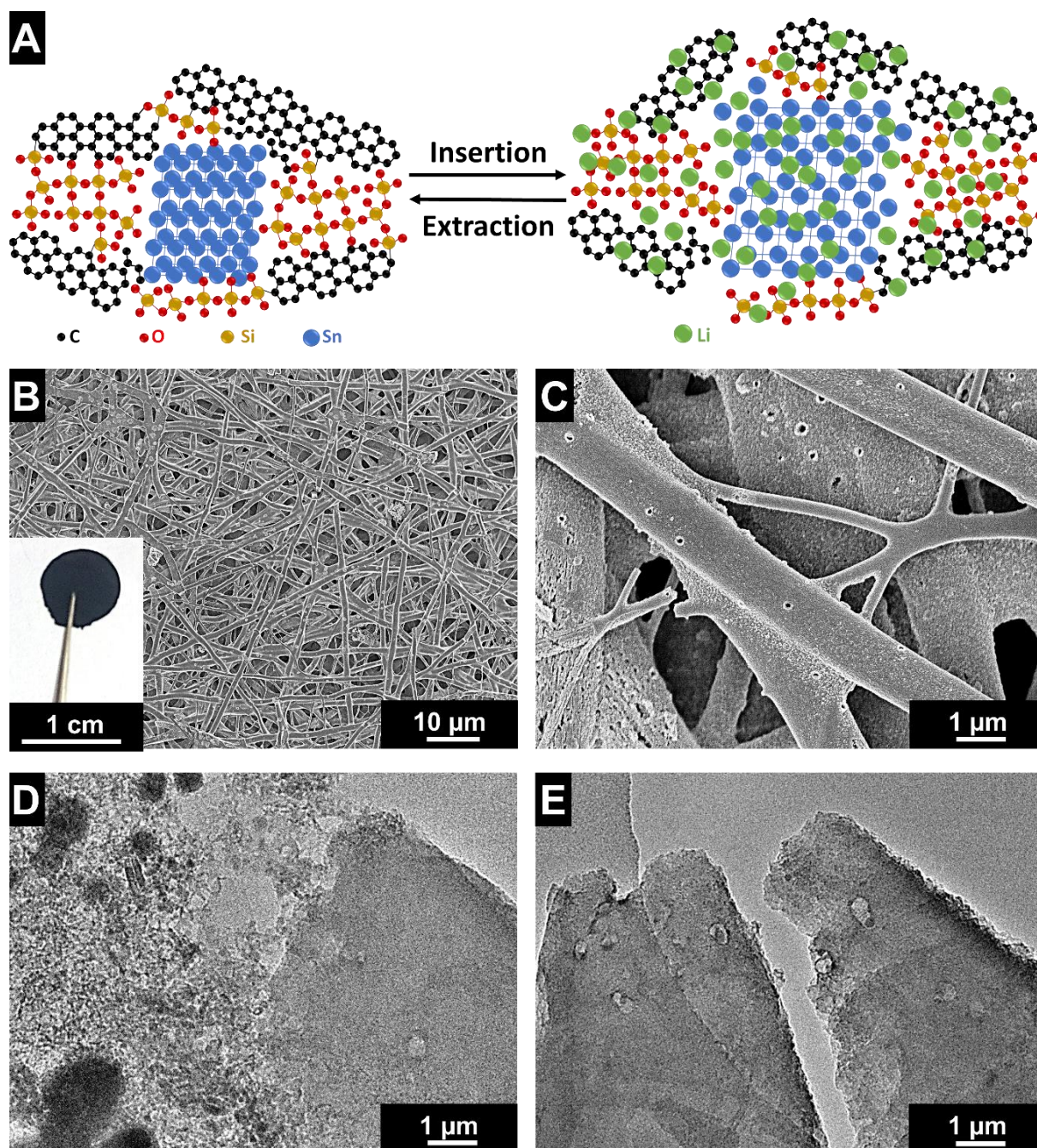


Figure S6: Schematic representation of lithium insertion and extraction in the hybrid material Sn/SiOC (A). Scanning electron micrographs and photograph (*inset*) (B, C), and transmission electron micrographs of the sample 0.05 Sn-1200 after GCPL for 100 cycles (D, E).

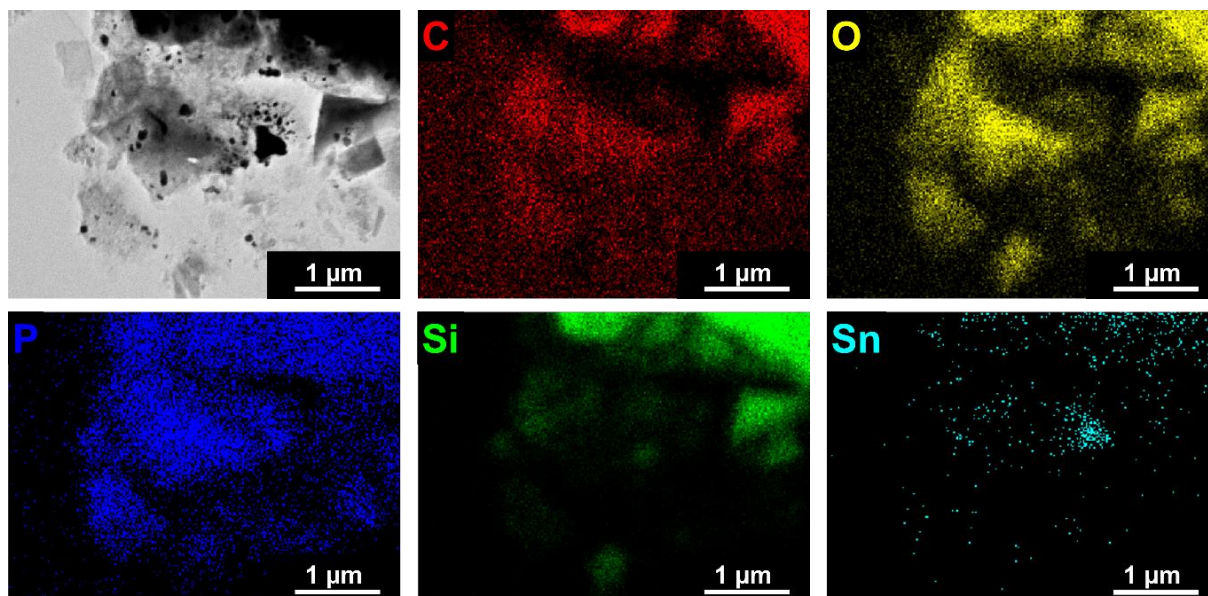


Figure S7: Element mapping analysis of the sample 0.05 Sn-1200 after GCPL for 100 cycles, from EDX analysis during TEM imaging.

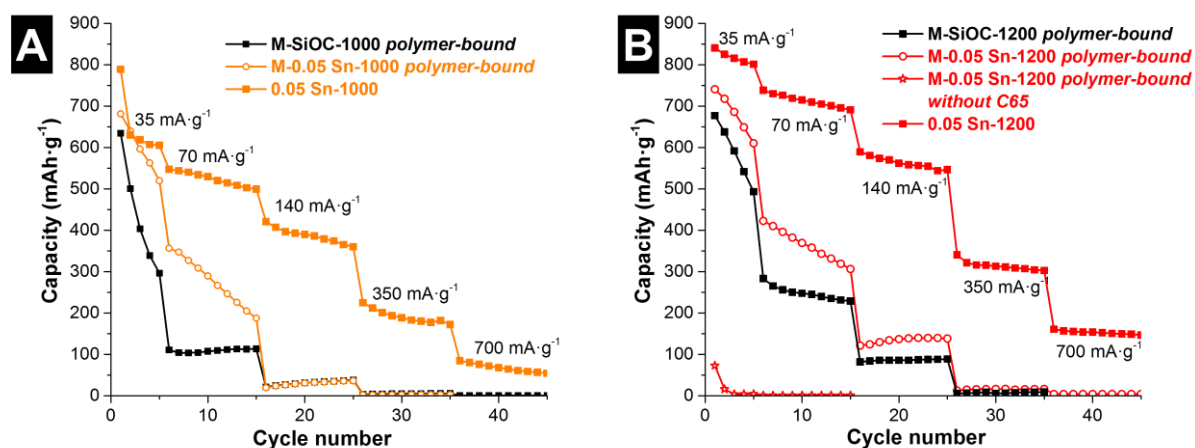


Figure S8: Electrochemical performance of free-standing electrodes. Comparison between polymer-bound electrodes and fiber mats synthesized at 1000 °C (A) and 1200 °C (B).

Table S1: EDX results (all values in at%) from the point analysis during TEM imaging.

Spot	C	O	Si	Sn
1	20.9	39.7	36.5	2.9
2	26.8	5.1	3.0	65.1
3	8.6	15.9	53.5	22.0
4	27.8	32.7	39.5	0.0
5	44.0	22.2	17.4	16.4
6	35.0	33.3	26.6	5.1
7	28.9	38.8	32.1	0.2
8	51.5	28.5	12.0	8.0
9	7.1	4.5	2.6	85.8

Table S2: Simplified calculated composition based on EDX and ICP-AES results, and calculated theoretical capacity.

Sample	Calculated composition (mass%)			Capacity (mAh·g ⁻¹)
	Sn	SiO ₂	C _{free}	
0.05 Sn-1000	6.2	55.7	38.1	1197
0.1 Sn-1000	10.4	56.1	33.5	1229
0.2 Sn-1000	22.1	53.1	24.8	1259
0.05 Sn-1200	6.4	54.2	39.4	1178
0.1 Sn-1200	10.7	54.6	34.7	1210
0.2 Sn-1200	21.9	55.7	22.4	1295

Table S3: Sheet resistance of the polymer-bound electrodes compared to the fiber mat electrodes.

Sample	Sheet resistance (Ω·cm)
M-SiOC-1000 (<i>polymer-bound</i>)	9.67 ± 0.91
M-0.05 Sn-1000 (<i>polymer-bound</i>)	3.57 ± 1.01
0.05 Sn-1000 (<i>fiber mat</i>)	0.71 ± 0.10
M-SiOC-1200 (<i>polymer-bound</i>)	2.79 ± 0.32
M-0.05 Sn-1200 (<i>polymer-bound</i>)	3.54 ± 0.38
0.05 Sn-1200 (<i>fiber mat</i>)	0.28 ± 0.05

Appendix E: Supporting Information to Chapter 3.5

SUPPORTING INFORMATION

Electrospun hybrid vanadium oxide/carbon fiber mats for lithium and sodium-ion battery electrodes

Aura Tolosa,^{1,2} Simon Fleischmann,^{1,2}

Ingrid Grobelsek,¹ Volker Presser^{1,2,*}

¹ *INM - Leibniz Institute for New Materials, 66123 Saarbrücken, Germany*

² *Department of Materials Science and Engineering, Saarland University, 66123 Saarbrücken, Germany*

* *Corresponding author's eMail: volker.presser@leibniz-inm.de*

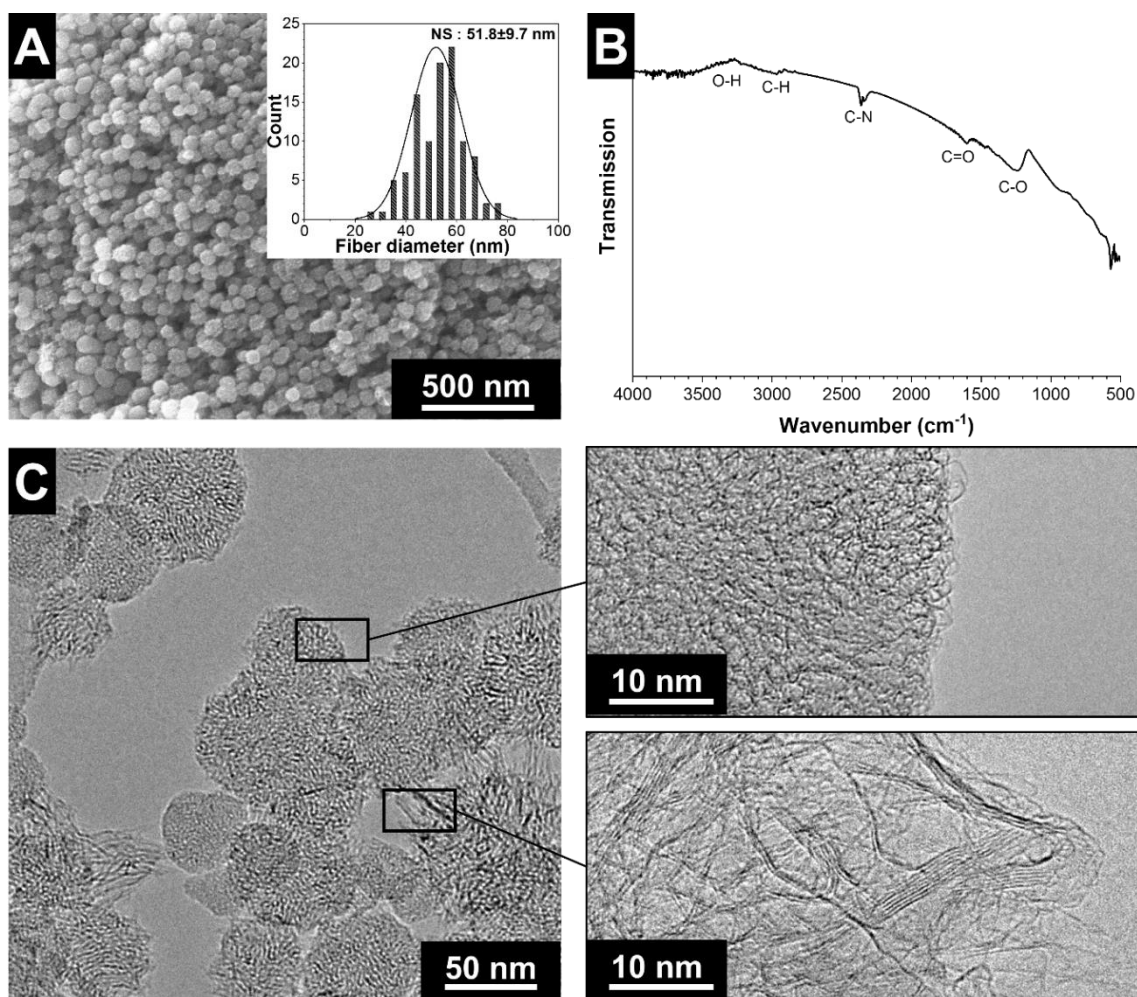


Figure S1: Characterization of graphitic carbon nanohorn particles (NS). Scanning electron micrograph with particle size distribution (A), Fourier-transform infrared spectra (B), and transmission electron micrographs (C).

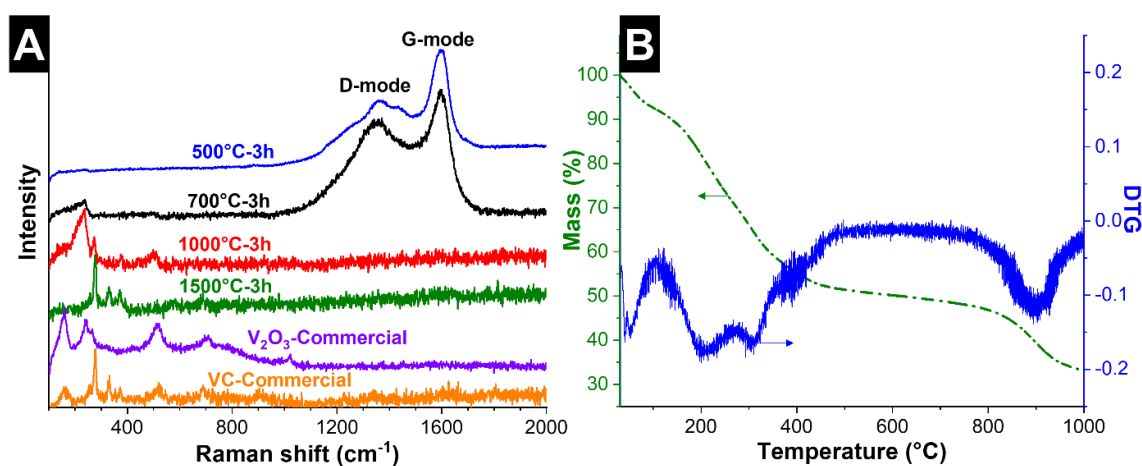


Figure S2: Raman spectra of fibers pyrolyzed at 500-1500 $^{\circ}\text{C}$ (A). For comparison, also the Raman spectra of commercially available V_2O_3 and VC particles are presented. (B) Thermogravimetric analysis of the fibers during pyrolysis under argon at $5^{\circ}\text{C}\cdot\text{min}^{-1}$. DTG is the first derivative of the thermogram data.

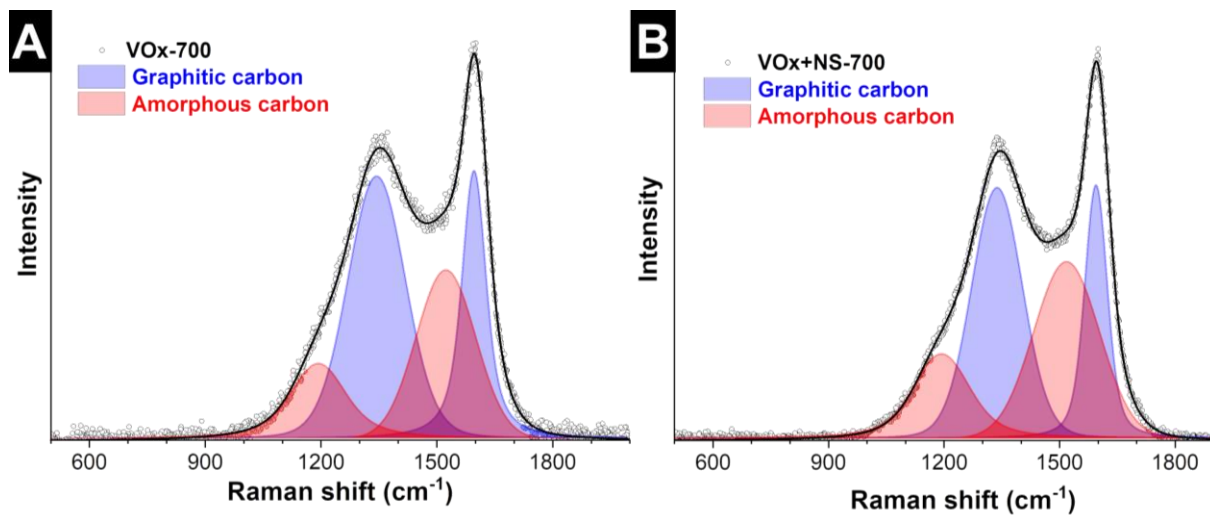


Figure S3: Peak deconvolution by 4 Voigt peak fitting for fibers after pyrolysis at 700 °C without (A) and with NS (B).

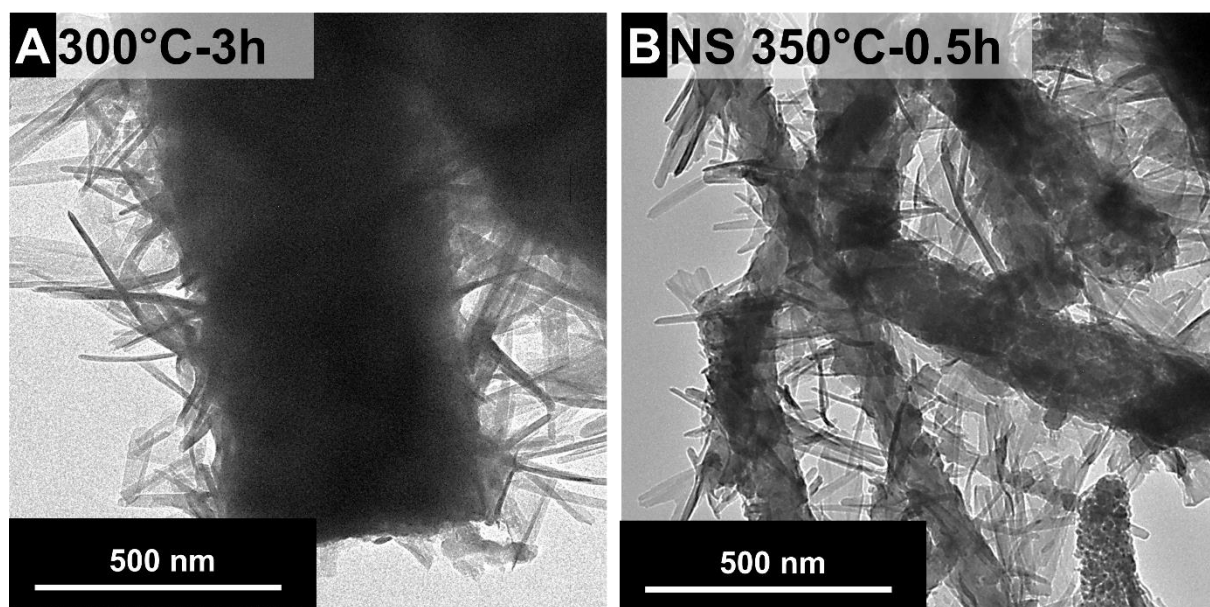


Figure S4: Transmission electron micrographs of samples after treatment under oxidizing atmospheres. The presence of vanadium oxide nanostructures was common in the sample without NS at 300 °C for 3 h (A) and with NS at 350 °C for 30 min (B).

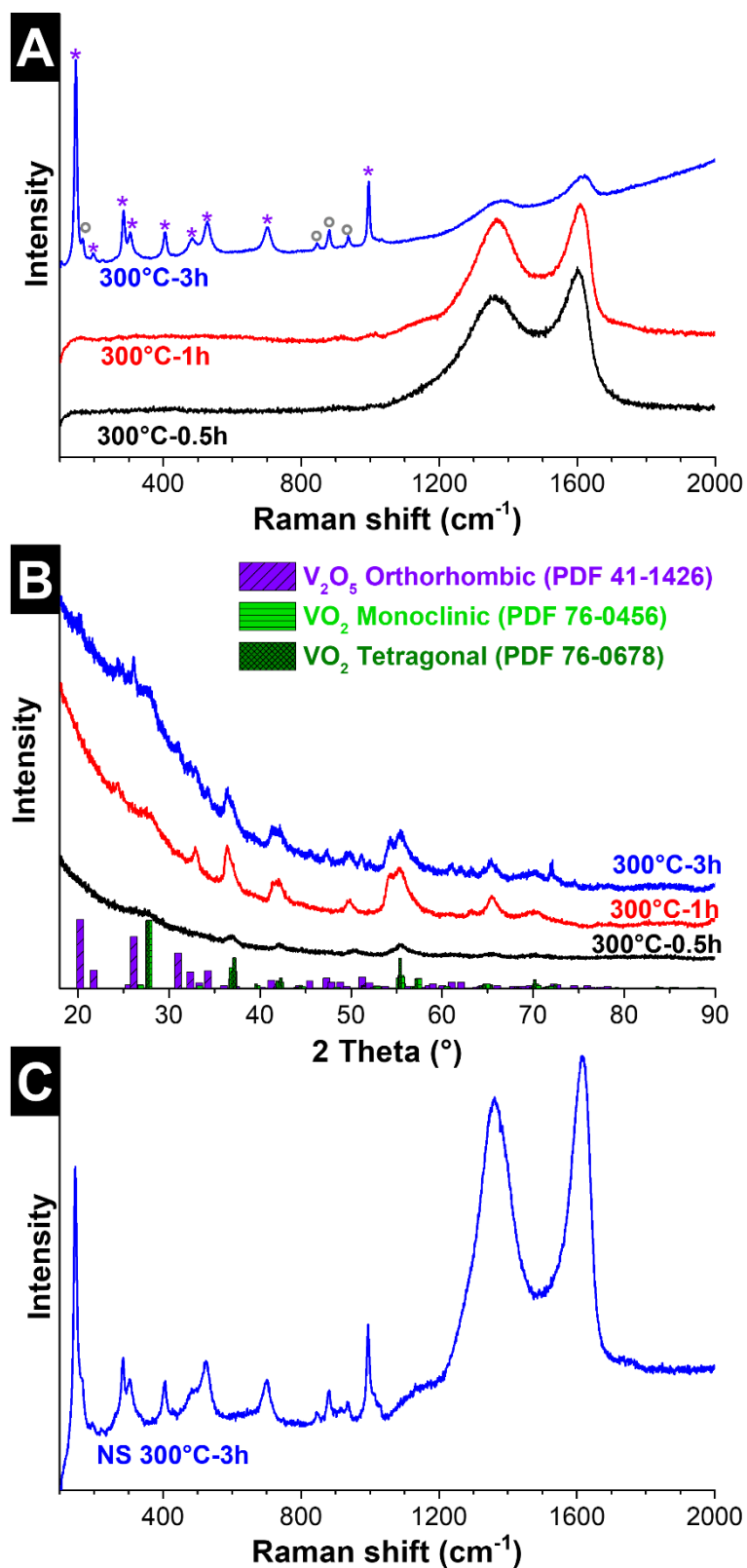


Figure S5: Raman spectra (A) and X-ray diffractograms of fibers without NS synthesized under oxidizing atmospheres at 300 °C. Raman spectra of fibers with NS synthesized under oxidizing atmospheres (C).

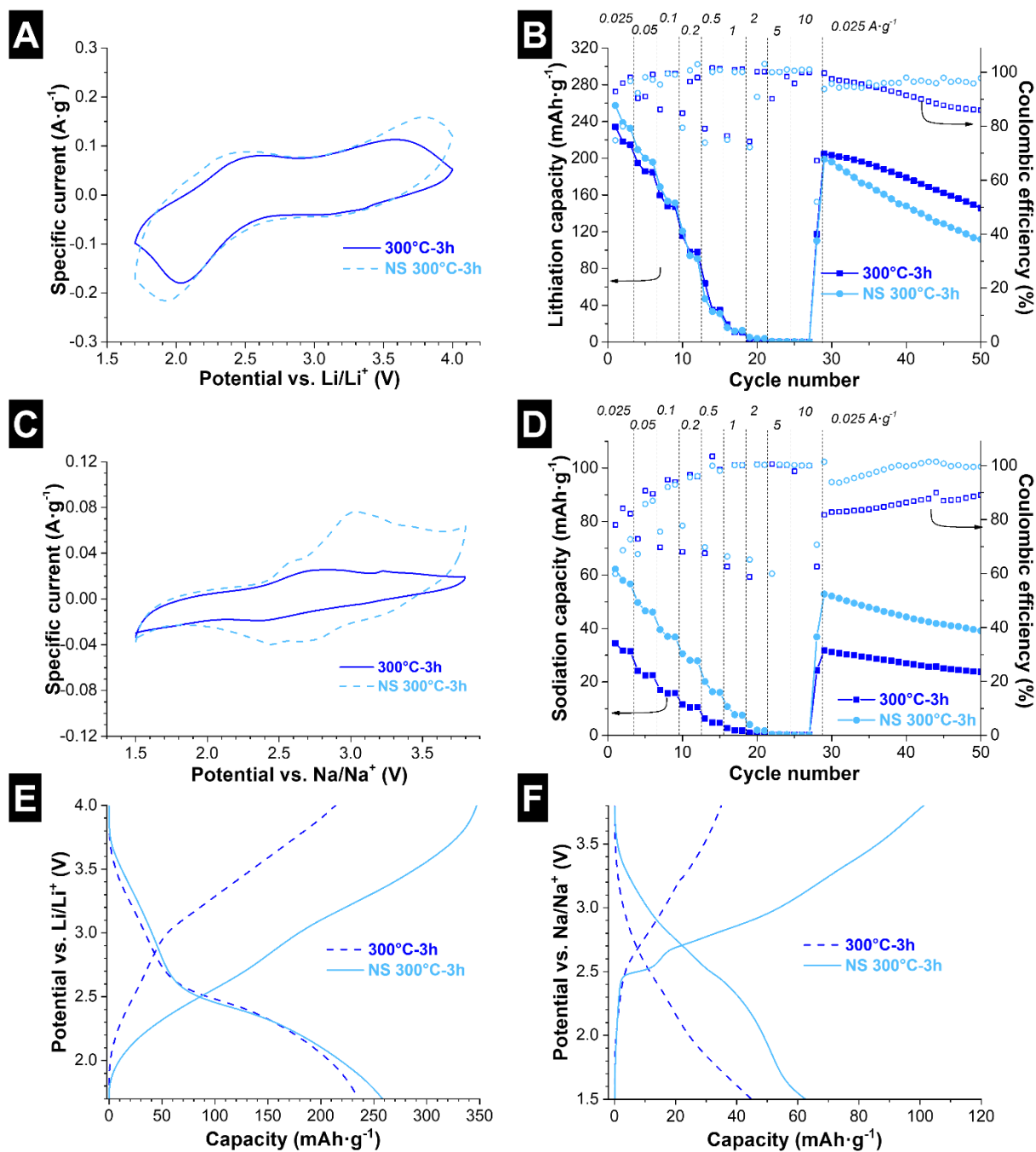


Figure S6: Cyclic voltammogram of the 5th cycle at 0.1 mV·s⁻¹ of the fibers synthesized at 300 °C for 3 h, tested as a free-standing cathode for lithium-ion batteries (A) and sodium-ion batteries (C). Discharge capacity and Coulombic efficiency by galvanostatic cycling at rates of 0.025-10 A·g⁻¹, tested as a cathode for lithium-ion batteries (B) and sodium-ion batteries (D). Galvanostatic curves for delithiation/lithiation (E) and desodiation/sodiation (F) for the first cycle at 0.025 A·g⁻¹. All gravimetric values consider the entire electrode mass (that is: vanadium oxide and carbon).

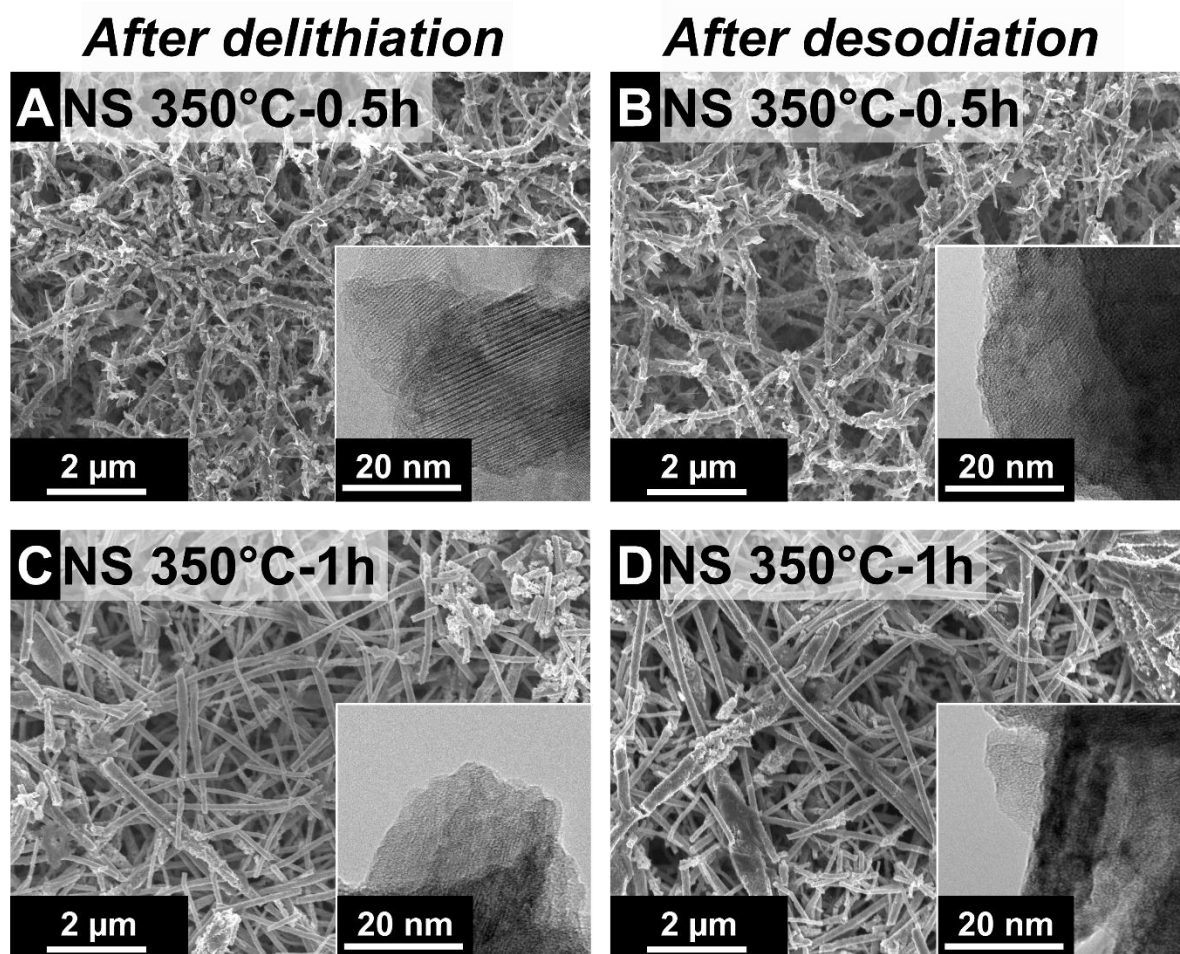


Figure S7: Scanning and transition electron micrographs of the electrodes after cyclic testing for LIBs (A, C) and for NIBs (B, D).

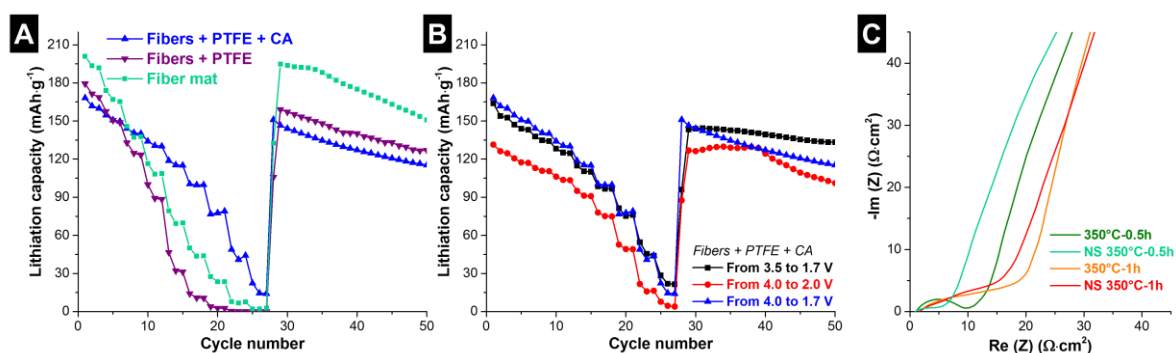


Figure S8: Discharge capacity by galvanostatic cycling at rates of $0.025\text{--}10\text{ A}\cdot\text{g}^{-1}$, tested as a cathode for lithium-ion batteries (A, B), capacity values are normalized to the complete electrode mass. Comparison between fiber mats, and polymer-bound fibers with and without conductive additives (A). Comparison between different voltage operation ranges (B). Nyquist plot for fiber mats tested as cathode for sodium-ion batteries (C).

Table S1: Detailed information of the Rietveld analysis of the XRD pattern for the vanadium oxide/carbon fibers after treatment under air/Ar.

Sample	Crystal phase	Refined lattice parameter / ICSD Data (nm)	Preferred orientation	Domain size (nm)	Content (mass%)
300°C-0.5h	VO ₂ tetragonal <i>P4₂/mmm</i> (PDF-76-0678)	$a=0.455 / 0.460-0.452, c=0.286 / 0.288-0.285$	[2 1 1] → 0.24	8	66
	V ₂ O ₃ rhombohedral <i>R$\bar{3}c$</i> (PDF-85-1411)	$a=0.493 / 0.501-0.490, c=1.404 / 1.394-1.400$	[0 3 0] → 0.60 [1 1 6] → 0.30	13	26
300°C-1h	VO ₂ monoclinic <i>P12₁/c1</i> (PDF-76-0456)	$a=0.574 / 0.576-0.574, b=0.453 / 0.454-0.452, c=0.534 / 0.538-0.537, \theta=12.284 / 12.265-12.261$	[3 1 0] → 0.10	3	53
	V ₄ O ₉ orthorhombic <i>Pnma</i> (PDF-71-2248)	$a=1.728 / 1.793, b=0.361 / 0.363, c=1.025 / 0.940.$	[0 2 0] → 0.53 [3 0 5] → 0.08	6	33
300°C-3h	V ₃ O ₇ monoclinic <i>C12/c1</i> (PDF-71-0454)	$a=2.188 / 2.192, b=0.367 / 0.368, c=1.830 / 1.834, \theta=9.581 / 9.561$		32	24
	V ₂ O ₅ orthorhombic <i>Pmmn</i> (PDF-41-1426)	$a=1.145 / 1.154-1.150, b=0.436 / 0.438-0.434, c=0.355 / 0.357-0.354$	[1 0 1] → 0.80	65	54
	V ₂ O ₃ rhombohedral <i>R$\bar{3}c$</i> (PDF-71-0280)	$a=0.494 / 0.501-0.490, c=1.392 / 1.394-1.400$	[1 1 0] → 0.15 [1 1 6] → 0.80	63	12
350°C-0.5h	VO ₂ monoclinic <i>P12₁/c1</i> (PDF-76-0456)	$a=0.574 / 0.575-0.574, b=0.454 / 0.454-0.452, c=0.537 / 0.538-0.537, \theta=12.286 / 12.265-12.261$	[2 -3 -1] → 0.60 [2 -1 -2] → 0.35	16	49
	VO ₂ tetragonal <i>P4₂/mmm</i> (PDF-76-0678)	$a=0.453 / 0.460-0.452, c=0.287 / 0.288-0.285$	[2 1 1] → 0.35 [3 1 0] → 0.40	10	22
	V ₄ O ₉ orthorhombic <i>Pnma</i> (PDF-71-2248)	$a=1.688 / 1.793, b=0.361 / 0.363, c=0.993 / 0.940$	[0 1 1] → 0.35 [3 1 4] → 0.19	6	15
	V ₂ O ₃ rhombohedral <i>R$\bar{3}c$</i> (PDF-01-1203)	$a=0.492 / 0.501-0.490, c=1.398 / 1.394-1.400$	[0 2 4] → 0.70	6	14
350°C-1h	V ₂ O ₅ orthorhombic <i>Pmmn</i> (PDF-41-1426)	$a=1.150 / 1.154-1.150, b=0.437 / 0.438-0.434, c=0.356 / 0.357-0.354$		82	69
	V ₃ O ₇ monoclinic <i>C12/c1</i> (PDF-71-0454)	$a=2.192 / 2.191, b=0.368 / 0.367, c=1.833 / 1.834, \theta=9.568 / 9.561,$		115	26
350°C-3h	V ₂ O ₅ orthorhombic <i>Pmmn</i> (PDF-41-1426)	$a=1.151 / 1.154-1.150, b=0.438 / 0.438-0.434, c=0.356 / 0.357-0.354.$		79	98

Aura Monserrat Tolosa Rodríguez, M. Sc.

Curriculum Vitae

PhD Student (Materials science), Chemical engineer



Date of birth: January 21st, 1990 (Bogota, Colombia)

Nationality: Colombian

Family status: Unmarried

ACADEMIC BACKGROUND

- **(10/2014) Master of Science** in Advance Materials in Science and Engineering, AMASE
Main emphasis in polymer and composites
1st year: Politecnico University of Catalunya, Barcelona, Spain
2nd year: Saarland University & Leibniz Institute for New Materials, Saarbrücken, Germany
(Energy Materials Group, Prof. Volker Presser)
Title: „Novel processing route to obtain ultra-fine SiOC fibers by electrospinning” (2.0)
- **(03/2012) Bachelor** in Chemical Engineering
University of los Andes, Bogota, Colombia (Process Safety Group, Prof. Felipe Munoz)
Title: „Comparative study of blast models for unconfined vapor cloud explosions, for the characterization of damage in industrial structures” (1.0)

PROFESSIONAL EXPERIENCE

(Since 2014) INM-Leibniz Institut for New Materials, Saarbrücken, Germany

- **PhD student** - Energy Materials Group, since 12/2014
- **Master student** - Energy Materials Group, 04/2014 – 10/2014

(2008-2011) University of the Andes, Bogotá, Colombia

- **Student intern and bachelor student** - Process Safety Group, 08/2010 – 12/2011
- **Student Intern** - Energy Conversion Group, 01 – 12/2011
- **Student Intern** - Alternative Energy Sources Group, 08 – 12/2008, 08/2009 – 06/2010

(2008-2012) Supermercado la Despensa, Bogotá, Colombia

- **Full-time co-administrator** - 01/2012 – 08/2012
- **Part-time co-administrator** - 01/2010 – 12/2011
- **Part-time cashier** - 01/2008-12/2009

STUDENT SUPERVISION

- **(2018) Master Thesis** (Hybrid vanadium pentoxide/carbon hybrid nanofibers; Mathias Baltes, Saarland University)
- **(2016) Internship** (Enhancement of electrochemical performance of non-woven mat electrodes via vapor deposition of aluminum current collector; Samuel Alcantar, University of California Santa Barbara)
- **(2015) Master Project** (Highly porous carbide-derived carbon nanofibers as electrodes for supercapacitors, Thomas Antonie Espinoza, Saarland University)

SCIENTIFIC QUALIFICATIONS AND EXPERTISE

Materials synthesis techniques

- Electrospinning
- Sol-gel synthesis
- Hydrothermal synthesis

Materials characterization techniques

- Transmission and scanning electron microscopy
- Infrared, Raman and energy dispersive X-ray spectroscopy
- Electrochemical characterization
- Thermogravimetric analysis and differential scanning calorimetry
- Rheometrie
- Gas sorption analysis
- X-ray diffraction

IT knowledge

- ORIGIN
- MATLAB
- DEV C++
- SOLID EDGE ST2
- FLACS
- ANSYS WORKBENCH
- ASPEN SUITE

AWARDS AND HONORS

- **Scholarship** EU Erasmus LLL (LifeLong Learning) for the Master in Advance Materials in Science and Engineering (AMASE), 09/2013-09/2014
- **Scholarship** for studies in chemical engineering bachelor, National University of Colombia 12/2006 (Rejected)
- **Statewide classification** Among the top 0.1%. School examination ICFES 2006-II (Comparable to Schweizerische Maturitätsprüfung Matura)
- **Finalist** at National Chemistry Olympiad, National University of Colombia 09/2006

TEACHING EXPERIENCE

- **2016-2017 Summer term:** Exercises “Thermodynamics” (Prof. Volker Presser, Materials Science and Engineering department, Saarland University)
- **2011-Winter term:** Computational training in “Plants design” (Prof. Felipe Munoz, Chemical Engineering department, University of los Andes)
- **2011-Summer and winter term:** Exercises and practical training in “Thermodynamics” (Prof. Gregorio Porras, Mechanical Engineering department, University of los Andes)
- **2009-2010 Winter term:** Exercises and practical training “Unit operations” (Prof. Rocio Sierra, Prof. Felipe Munoz and Prof. Gustavo Rodríguez, Chemical Engineering department, University of los Andes)
- **2008 Winter term:** Exercises and practical training “Phase and chemical equilibrium” (Prof. Rodrigo Gomez, Chemical Engineering department, University of los Andes)

PUBLICATIONS

- J-1. Casco ME, Badaczewski F, Grätz S, **Tolosa A**, Presser V, Smarsly B, Borchardt L. MECHANOCHEMICAL SYNTHESIS OF POROUS CARBON AT ROOM TEMPERATURE WITH A HIGHLY ORDERED SP² MICROSTRUCTURE. *Carbon*, 2018, DOI: 10.1016/j.carbon.2018.06.068
- J-2. Krüner B, Odenwald C, Jäckel N, **Tolosa A**, Kickelbick G, Presser V. SILICON OXYCARBIDE BEADS FROM CONTINUOUSLY PRODUCED POLYSILSESQUIOXANE AS STABLE ANODE MATERIAL FOR LITHIUM-ION BATTERIES. *ACS Applied Energy Materials*, 2018, 1 (6), 2961-2970.
- J-3. Krüner B, Schreiber A, **Tolosa A**, Quade A, Badaczewski F, Pfaff T, Smarsly B, Presser V. NITROGEN-CONTAINING NOVOLAC-DERIVED CARBON BEADS AS ELECTRODE MATERIAL FOR SUPERCAPACITORS. *Carbon*, 2018, 132, 220-231.
- J-4. Fleischmann S, **Tolosa A**, Presser V. DESIGN OF CARBON/METAL OXIDE HYBRIDS FOR ELECTROCHEMICAL ENERGY STORAGE. *Chemistry A European Journal*, 2017, DOI: 10.1002/chem.201800772.
- J-5. Srimuk P, Lee J, **Tolosa A**, Kim C, Aslan M, Presser V. TITANIUM DISULFIDE: A PROMISING LOW-DIMENSIONAL ELECTRODE MATERIAL FOR SODIUM ION INTERCALATION FOR SEAWATER DESALINATION. *Chemistry of Materials*, 2017, 29 (23), 9964-9973.
- J-6. **Tolosa A**, Fleischmann S, Grobelsek I, Quade A, Lim E, Presser V. BINDER-FREE HYBRID TITANIUM-NIOBIUM OXIDE/CARBON NANOFIBER MATS FOR LITHIUM-ION BATTERY ELECTRODES. *ChemSusChem*, 2017, 11 (1), 159-170.
- J-7. Choudhury S, Srimuk P, Raju K, **Tolosa A**, Fleischmann S, Zeiger M, Ozoemena K I, Borchardt L, Presser V. CARBON ONION / SULFUR HYBRID CATHODES VIA INVERSE VULCANIZATION FOR LITHIUM SULFUR BATTERIES. *Sustainable Energy & Fuels*, 2017; 2 (1), 133-146
- J-8. **Tolosa A**, Widmaier M, Krüner B, Griffin J, Presser V. CONTINUOUS SILICON OXYCARBIDE FIBER MATS WITH TIN NANOPARTICLES AS HIGH CAPACITY ANODE FOR LITHIUM-ION BATTERIES. *Sustainable Energy Fuels*, 2017, 2 (1), 215-228.

- J-9. Choudhury S, Krüner B, Massuti-Ballester P, **Tolosa A**, Prehal C, Grobelsek I, Paris O, Borchardt L, Presser V. MICROPOROUS NOVOLAC-DERIVED CARBON BEADS/SULFUR HYBRID CATHODE FOR LITHIUM-SULFUR BATTERIES. *Journal of Power Sources*, 2017, 357, 198-208.
- J-10. Krüner B, Odenwald C, **Tolosa A**, Schreiber A, Aslan M, Kickelbick G, Presser V. CARBIDE-DERIVED CARBON BEADS WITH TUNABLE NANOPORES FROM CONTINUOUSLY PRODUCED POLYSILSESQUOXANES FOR SUPERCAPACITOR ELECTRODES. *Sustainable Energy & Fuels*, 2017, 1 (7), 1588-1600.
- J-11. Lee J, **Tolosa A**, Krüner B, Jackel N, Fleischmann S, Zeiger M, Kim D, Presser V. ASYMMETRIC TIN-VANADIUM REDOX ELECTROLYTE FOR HYBRID ENERGY STORAGE WITH NANOPOROUS CARBON ELECTRODES. *Sustainable Energy & Fuels*, 2017, 1(2), 299-307.
- J-12. Srimuk P, Zeiger M, Jäckel N, **Tolosa A**, Krüner B, Fleischmann S, Grobelsek I, Aslan M, Shvartsev B, Suss ME, Presser V. ENHANCED PERFORMANCE STABILITY OF CARBON/TITANIA HYBRID ELECTRODES DURING CAPACITIVE DEIONIZATION OF OXYGEN SATURATED SALINE WATER. *Electrochimica Acta*, 2017, 224, 314-328.
- J-13. Fleischmann S, **Tolosa A**, Zeiger M, Krüner B, Peter NJ, Grobelsek I, Quade A, Kruth A, Presser V. VANADIA-TITANIA MULTILAYER NANODECORATION OF CARBON ONIONS VIA ATOMIC LAYER DEPOSITION FOR HIGH PERFORMANCE ELECTROCHEMICAL ENERGY STORAGE. *Journal of Materials Chemistry A*, 2016, 5 (6), 2792-2801.
- J-14. Srimuk P, Kaasik F, Krüner B, **Tolosa A**, Fleischmann S, Jackel N, Tekeli MC, Aslan M, Suss ME, Presser V. MXENE AS A NOVEL INTERCALATION-TYPE PSEUDOCAPACITIVE CATHODE AND ANODE FOR CAPACITIVE DEIONIZATION. *Journal of Materials Chemistry A*, 2016, 4 (47), 18265-18271.
- J-15. Srimuk P, Ries L, Zeiger M, Fleischmann S, Jackel N, **Tolosa A**, Krüner B, Aslan M, Presser V. HIGH PERFORMANCE STABILITY OF TITANIA DECORATED CARBON FOR DESALINATION WITH CAPACITIVE DEIONIZATION IN OXYGENATED WATER. *RSC Advances*, 2016, 6 (108), 106081-106089.
- J-16. Zeiger M, Fleischmann S, Krüner B, **Tolosa A**, Thiele S, Presser V. INFLUENCE OF CARBON SUBSTRATE ON THE ELECTROCHEMICAL PERFORMANCE OF CARBON/MANGANESE OXIDE HYBRIDS IN AQUEOUS AND ORGANIC ELECTROLYTES. *ASC Advances*, 2016, 6 (109), 107163-107179.
- J-17. **Tolosa A**, Krüner B, Fleischmann S, Jäckel N, Zeiger M, Aslan M, Grobelsek I, Presser V. NIOBIUM CARBIDE NANOFIBERS AS A VERSATILE PRECURSOR FOR HIGH POWER SUPERCAPACITOR AND HIGH ENERGY BATTERY ELECTRODES. *Journal of Materials Chemistry A*, 2016, 4, 16003-16016.
- J-18. Lee J, Krüner B, **Tolosa A**, Sathyamoorthi S, Kim D, Choudhury S, Kum-Hee S, Presser V. TIN/VANADIUM REDOX ELECTROLYTE FOR BATTERY-LIKE ENERGY STORAGE CAPACITY COMBINED WITH SUPERCAPACITOR-LIKE POWER HANDLING. *Energy and Environmental Science*, 2016, 9 (11), 3392-3398.
- J-19. Busom J, Schreiber A, **Tolosa A**, Jäckel N, Grobelsek I, Peter NJ, Presser V. SPUTTERING OF SUB-MICROMETER ALUMINUM LAYERS AS COMPACT, HIGH-PERFORMANCE, LIGHT-WEIGHT CURRENT COLLECTOR FOR SUPERCAPACITORS. *Journal of Power Sources*, 2016, 329, 432-440.

- J-20. Krüner B, Lee J, Jäckel N, **Tolosa A**, Presser V. SUB-MICROMETER NOVOLAC-DERIVED CARBON BEADS FOR HIGH PERFORMANCE SUPERCAPACITORS AND REDOX ELECTROLYTE ENERGY STORAGE. *ACS Applied Materials and Surfaces*, 2016, 8 (14), 9104-9115.
- J-21. **Tolosa A**, Krüner B, Jäckel N, Aslan M, Vakifahmetoglu C, Presser V. ELECTROSPINNING AND ELECTROSPRAYING OF SILICON OXYCARBIDE-DERIVED NANOPOROUS CARBON FOR SUPERCAPACITOR ELECTRODES. *Journal of Power Sources*, 2016, 31, 178-188.
- J-22. Jäckel N, Weingarth D, Schreiber A, Krüner B, Zeiger M, **Tolosa A**, Aslan M, Presser V. PERFORMANCE EVALUATION OF CONDUCTIVE ADDITIVES FOR ACTIVATED CARBON SUPERCAPACITORS IN ORGANIC ELECTROLYTE. *Electrochimica Acta* 2016, 191, 284-298.
- J-23. Atchison JS, Zeiger M, **Tolosa A**, Funke LM, Jäckel N, Presser V. ELECTROSPINNING OF ULTRAFINE METAL OXIDE/CARBON AND METAL CARBIDE/CARBON NANOCOMPOSITE FIBERS. *RSC Advances*, 2015, 5 (45), 35683-35692.

ORAL PRESENTATIONS

- T-1. **Tolosa A**, Fleischmann S, Grobelsek I, Presser V. “Hybrid Ti-Nb₂O₅/C electrospun nanofibers as Li-ion battery electrodes”. 2018 MRS Spring Meeting, Phoenix (United States of America); April 6th, 2018.
- T-2. **Tolosa A**, Krüner B, Fleischmann S, Aslan M, Presser V. “Electrospinning for high power electrochemical energy storage”. BMBF Junior Investigation Workshop Energy Research, Dresden (Germany), November 23rd, 2016.
- T-3. **Tolosa A**, Krüner B, Fleischmann S, Aslan M, Presser V. “Electrospun microporous carbon fibers and niobia/carbon hybrid nanofibers for energy storage”. *Electrospinning for Energy*, Montpellier (France); June 24th, 2016.
- T-4. **Tolosa A**, Aslan M, Krüner B, Jäckel N, Presser V. “Electrospun nanofibers for energy storage applications”. German-Estonian Workshop in Future capacitive technologies, Tartu (Estonia), December 11th, 2015.
- T-5. **Tolosa A**, Aslan M, Jäckel N, Krüner B, Presser V. “Electrospun microporous carbon fibers and carbon hybrid fibers for electrochemical applications“. Uds-ECUST Summer School on Materials Science and Chemistry, Sarbrücken (Germany), October 6th, 2015.
- T-6. **Tolosa A**, Presser V. “We like to spin – Electrospun nanofibers for energy storage”. Joint BMBF Junior Investigator Workshop at INM, Saarbrücken (Germany), September 27th, 2015.
- T-7. **Tolosa A**, Jäckel N, Krüner B, Vakifahmetoglu C, Presser V. “Novel route for cost effective production of ultra-fine SiOC by electrospinning”. 14th International Conference of the European Ceramic Society, Toledo (Spain), June 26th, 2015.
- T-8. **Tolosa A**, Aslan M, Jäckel N, Krüner B, Presser V. “Electrospun microporous carbon hybrid fibers for electrochemical applications”. 8th EEIGM International Conference on Advanced Materials Research, Valencia (Spain), June 12th, 2015.
- T-9. **Tolosa A**. “Energy Materials Group”. Kick off Meeting, CREATE-Net, Montevideo (Uruguay), March 20th, 2015.

- T-10. **Tolosa A**, Atchison JS, Zeiger M, Presser V. “Ultrafine carbon and carbon hybrid fibers for electrochemical applications”. Inter disziplinärer Workshop ENREKON-Presser Group, Augsburg (Germany), February 19th, 2015.
- T-11. **Tolosa A**, Atchison JS, Jäckel N, Zeiger M, Vakifahmetoglu C, Presser V. “Novel processing route to obtain ultra-fine high purity low cost SiOC fibers by electrospinning”. DGM Tag Nachwuchsforum, Darmstadt (Germany), September 22th, 2014.

POSTERS

- P-1. **Tolosa A**, Fleischmann S, Grobelsek I, Presser V. “Continuous hybrid fibers: highways for rapid electron transport in battery electrodes”. Doktorandentag of the Faculty of Natural Sciences and Technology, Saarland University, Saarbrücken (Germany), November 15th, 2017.
- P-2. **Tolosa A**, Krüner B, Fleischmann S, Aslan M, Presser V. “Niobium carbide nanofibers as a precursor for supercapacitor and battery electrodes”. 1.Jahrestagung der Fachgruppe Chemie und Energie, Jena (Germany), Oktober 6-7th, 2016.
- P-3. **Tolosa A**, Krüner B, Fleischmann S, Aslan M, Presser V. “Niobium carbide nanofibers as a precursor for supercapacitor and battery electrodes”. Materials Science and Engineering MSE, Darmstadt (Germany), September 27-29th, 2016.
- P-4. **Tolosa A**, Atchison JS, Vakifahmetoglu C, Presser V. “Novel processing route to obtain SiOC fibers by electrospinning”. 2nd International INM/UdS Poster Symposium, Saarbrücken (Germany), August 14th, 2014.